Functionalised Nanoparticles for Molecular Imaging

Natasha Ann Keasberry

Thesis submitted in partial fulfilment of the requirements for the Degree of Doctor of Philosophy

Supervisor: Prof. N. J. Long

Department of Chemistry

Imperial College London

Declaration

The work described in this thesis was carried out between October 2010 and February 2014 at the Department of Chemistry, Imperial College London. The entire body of this work is my own unless stated otherwise, through cited reference or other acknowledgement, and has not been previously submitted for a degree at this or any other university.

Statement of Copyright

The copyright of this thesis rests with the author and is made available under a Creative Commons Attribution Non-Commercial No Derivatives licence. Researchers are free to copy, distribute or transmit the thesis on the condition that they attribute it, that they do not use it for commercial purposes and that they do not alter, transform or build upon it. For any reuse or redistribution, researchers must make clear to others the licence terms of this work.

Acknowledgements

Firstly, I would like to thank my supervisor, Professor Nick Long for the opportunity to carry out my research at Imperial, and for his support and advice during the course of my PhD. There were many frustrating times but he always managed to pull me through them. I am also very grateful to the Brunei government for funding my project.

Thanks also goes to Juan for his guidance during the project, for helping me with all the tricky nanoparticle syntheses and infuriating characterisation techniques, Graeme for his DOTA syntheses expertise (and all the tedious T_1 and T_2 NMR measurements!), and Taka for all the assistance with the biological assays and protocols.

To the members of the Long group – it has been a great 4 years. I've enjoyed my time in the Long lab and office and am glad to have gotten to know each and every one of you. Special mention though goes to a handful of people. Myra – our long conversations about anything and everything kept me sane. To Mike and Andy – labs was definitely a lot more fun and interesting having you both on our side of the lab, with Mike quizzing me on Absolute Radio music, and all the reddit/movie/music/hot women discussions with Andy. Bowie with our shared love for baking and always with her words of encouragement when I was frustrated with labs. James, it's been great quoting Friends and HIMYM with you (sometimes for no reason at all) – I've loved the laughs.

Special thanks to Pete Haycock in NMR who had his fair share of running T_1/T_2 measurements and other samples I had trouble with. I would also like to acknowledge John Barton and Lisa Haigh for mass spectrometry analyses.

Finally, I would like to thank my parents and sister Vanessa for believing in me and reminding me that I could do this. And Simon, thank you for your patience when I get upset with work and for supporting me through the tears and long hours. I love you guys.

Abstract

This thesis describes the synthesis of iron oxide nanoparticles for use as contrast agents in biomedical imaging, specifically for MRI. The limitations of single imaging modalities can be overcome by the synergistic combination of two or more imaging techniques, e.g. the low sensitivity but high resolution of MRI complements the high sensitivity but low resolution of PET. The large surface area of superparamagnetic iron oxide nanoparticles (SPION) allows relatively simple functionalisation. The large size of a single combined nanoparticle MRI/PET probe would slow down *in vivo* movement, diminishing radioactivity before reaching its target. Pre-targeting using a magnetic nanoparticle followed by the injection of the radio-labelled molecule at the correct time will ensure radioactivity remains sufficiently high. Thus, the investigation of dual-modality probe development is also a focus of the thesis.

Chapter 2 discusses the preparation of iron oxide nanoparticles with a core diameter of 6 nm via the high temperature thermal decomposition of iron salts. Direct modification to the surface of the nanoparticles was carried out using various small molecules with differing anchoring groups, the most successful being sodium alendronate, a bisphosphonate ligand.

Chapter 3 describes the further functionalisation of the nanoparticles. One way this was achieved was by the incorporation of PEG chains of different lengths to increase water solubility and biocompatibility. Functionalisation with a strained alkyne for eventual *in vitro/in vivo* copper-free cycloaddition with an azide group was also achieved. The PET moiety was designed to be a ^{68}Ga-azido-DOTA complex. Prior to radiolabelling with gallium-68, the copper-free cyclised resultant nanoparticles were characterised by the use of lanthanide analogues (Eu, Tb and Gd). Eu and Tb allowed for fluorescence spectroscopy, while the Gd allowed for relaxivity measurements to be carried out. Unexpected fluorescence results were observed for the Eu and Tb analogues.

The Gd-NP conjugates are further investigated in Chapter 4. Combination of both a T_1 and T_2 moiety results in changes to the relaxivity of the resultant nanoparticle which can act as a dual-weighted MRI probe. The relaxivities are found to vary with modifications to the nanoparticle construct.

Finally, preliminary *in vitro* experiments with macrophages were carried out to investigate whether there was significant preferential uptake between M1 and M2 macrophages. A single-chain variable fragment (scFv) specific to Fractalkine, a chemokine important in the progression of atherosclerosis was prepared, for use as a targeting moiety towards the imaging of vulnerable plaque.

Abbreviations

°C	degrees Celsius
γ	gyromagnetic ratio
ΔJ	difference in angular momentum levels
λ_{em}	emission wavelength
λ_{ex}	excitation wavelength
µ	micro-
ν	frequency
τ	luminescence lifetime
acac	acetylacetonate
ATR	attenuated total reflectance
B_0	magnetic field
BP	bisphosphonate
BSA	bovine serum albumin
CA	contrast agent
CT	computed tomography
d	doublet
D	distance between two PEG molecules on nanoparticle surface
Da	Dalton
dd	doublet of doublets
DCM	dichloromethane
DLS	dynamic light scattering
DMF	dimethylformamide
DMSO	dimethyl sulfoxide
DOTA	1,4,7,10-Tetraazacyclododecane-1,4,7,10-tetraacetic acid
DO3A-^{t}Bu	1,4,7-Tris(*tert*-butoxycarbonylmethyl)-1,4,7,10-tetraazacyclododecane
DTPA	diethylene triamine pentaacetic acid

E	energy
EDC	1-Ethyl-3-(3-dimethylaminopropyl)carbodiimide
ELISA	enzyme-linked immunosorbent assay
ESI	electrospray ionisation
Et	ethyl
FID	free induction decay
h	Planck's constant
IONP	iron oxide nanoparticle
IR	infrared
kDa	kilodalton
LDL	low density lipoprotein
Ln	lanthanide
M	Molar
m	multiplet
m	spin quantum number
m/*z*	mass /charge ratio
MALDI	matrix-assisted laser desorption/ionisation
Me	methyl
mins	minutes
mmol	millimoles
MPS	mononuclear phagocyte system
MRI	magnetic resonance imaging
MS	mass spectrometry
mV	millivolts
M_w	molecular weight
NHS	N-hydroxysuccinimide
NMR	nuclear magnetic resonance

NOTA	1,4,7-Triazacyclonane-1,4,7-triacetic acid
NP	nanoparticle
OCT	optical coherence tomography
PBS	phosphate buffered saline
PBS (-)	phosphate buffered saline without magnesium or calcium
PEG	polyethylene glycol
PET	positron emission tomography
ppm	parts per million
q	quartet
q	hydration state
QD	quantum dots
r_1	longitudinal relaxivity constant
R_1	longitudinal relaxation rate
r_2	transverse relaxivity constant
R_2	transverse relaxation rate
R_F	Flory radius
RT	room temperature
S_0	singlet ground state
S_1	singlet triplet state
SAP	square antiprismatic
scFv	single chain variable fragment
SDS-PAGE	sodium dodecyl sulphate – polyacrylamide gel electrophoresis
SPECT	single-photon emission computed tomography
SPION	superparamagnetic iron oxide nanoparticle
SQUID	superconducting quantum interference device
t	triplet
T_1	spin-lattice/longitudinal relaxation

T_2	spin-spin/transverse relaxation
$t_{½}$	circulation half-time
^{t}Bu	*tert*-butyl
TBDMS	*tert*-butyl dimethyl silyl
TEM	transmission electron microscopy
TGA	thermogravimetric analysis
THF	tetrahydrofuran
Ts	tosyl
TSAP	twisted square antiprismatic
US	ultrasound
UV-Vis	ultraviolet-visible

List of Compounds

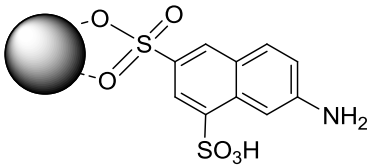

NP-S1

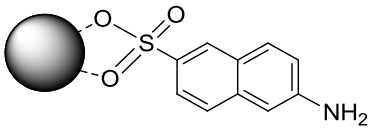

NP-S2

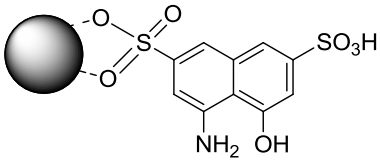

NP-S3

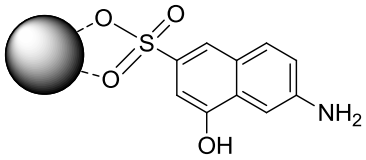

NP-S4

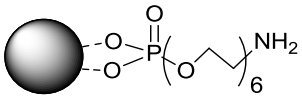

NP1

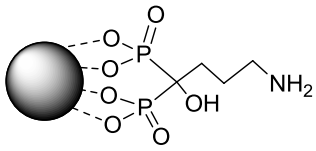

NP2

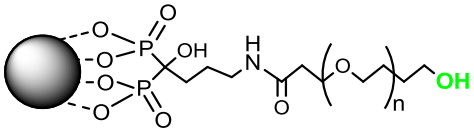

NP3 n = 12
NP4 n = 58
NP5 n = 96

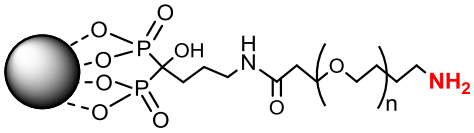

NP6 n = 12
NP7 n = 58
NP8 n = 96

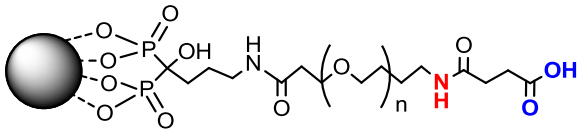

NP9 n = 12
NP10 n = 58
NP11 n = 96

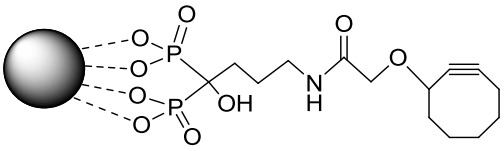

NP12

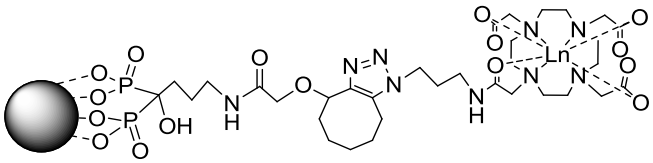

NP13 Ln = Eu
NP14 Ln = Tb
NP15 no Ln

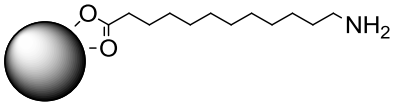

NP16

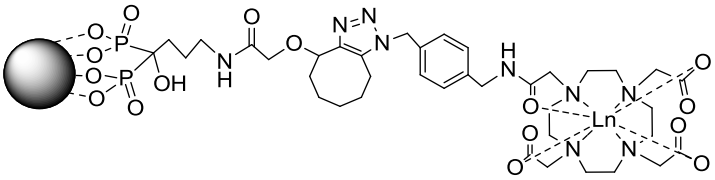

NP17 Ln = Eu
NP18 Ln = Tb
NP19 Ln = Gd
NP20 no Ln

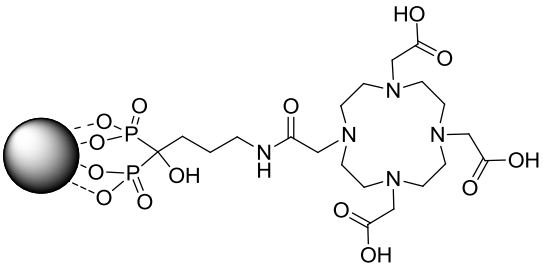

NP21

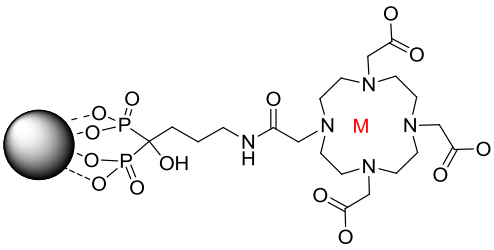

NP22 M = Gd
NP23 M = Mn
NP24 M = Zn

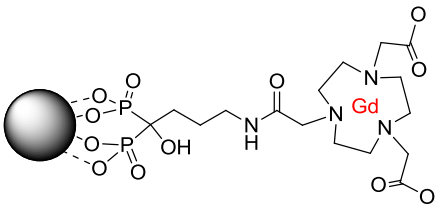

NP25

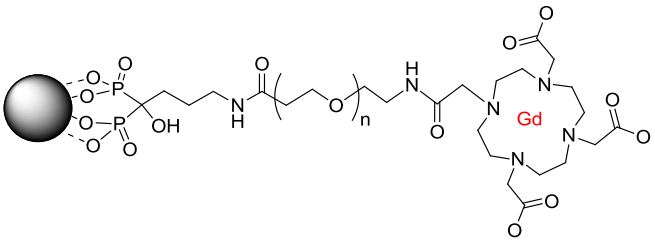

NP26 n = 6
NP27 n = 96

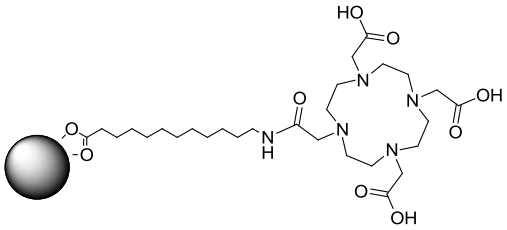

NP28

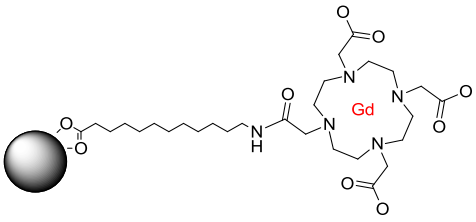

NP29

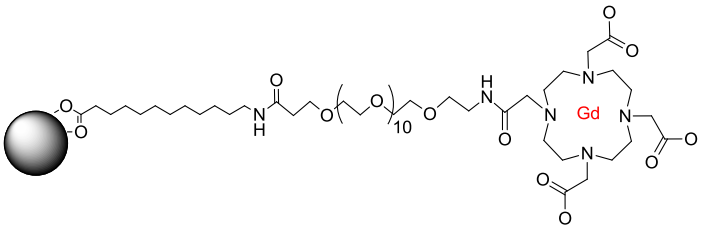

NP30

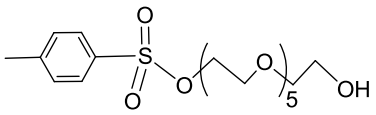

1

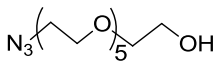

2

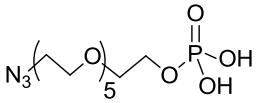

3

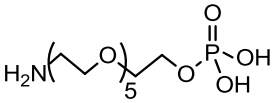

4

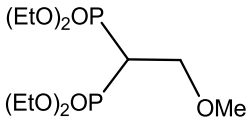

5

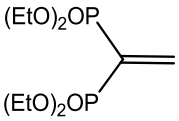

6

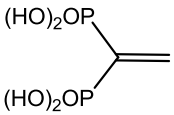

7

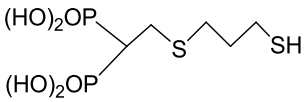

8a

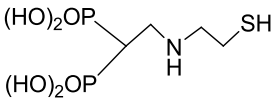

8b

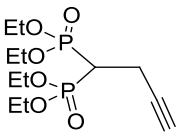

9

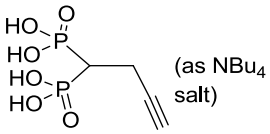

10

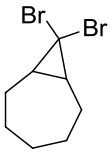

11

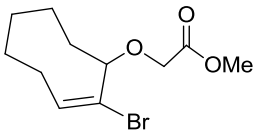

12

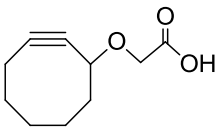

13

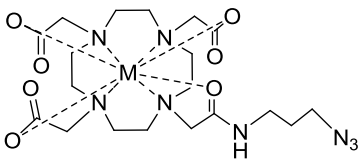

14 M = Eu
15 M = Tb
16 M = Gd
17 M = Ga

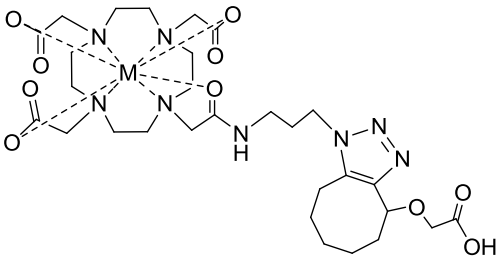

18 M = Eu
19 M = Tb
20 M = Gd
21 M = Ga

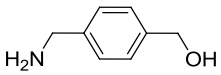

22

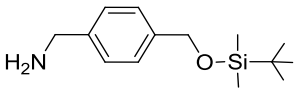

23

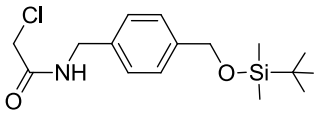

24

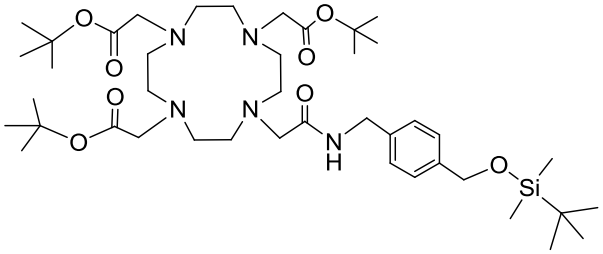

25

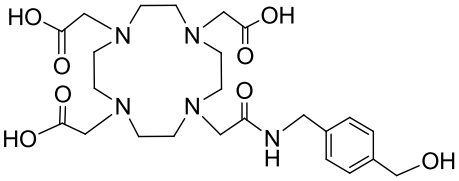

26

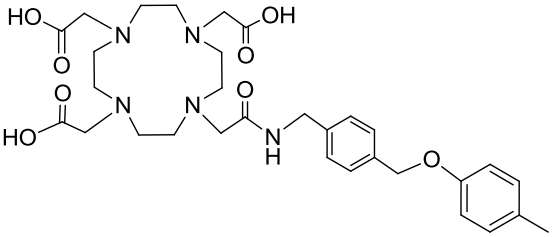

27

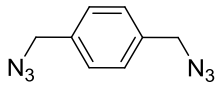

28

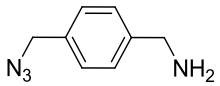

29

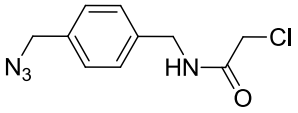

30

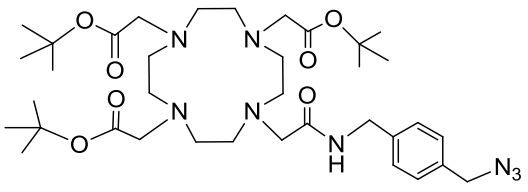

31

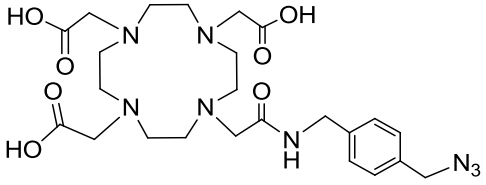

32

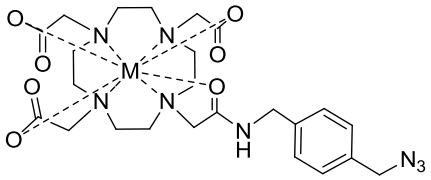

33 M = Eu
34 M = Tb
35 M = Gd

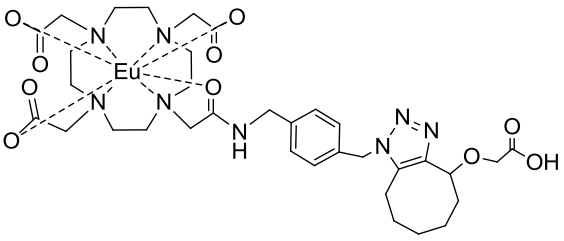

36 M = Eu
37 M = Tb
38 M = Gd

Table of Contents

CHAPTER 1

INTRODUCTION

1 Introduction

This chapter introduces the reader firstly to molecular imaging and a general overview of nanoparticles, especially for use in the medical and imaging field. This leads to a brief explanation of magnetic resonance imaging and the contrast agents in use, specifically iron oxide nanoparticles, which will be the focus within this project. Some background into how the surface of the nanoparticles is functionalised is also described in this chapter but will be discussed in further detail in Chapter 3. Dual modal imaging is also briefly described here as one of the targets in this project is to design a dual modal MRI/PET imaging agent utilising Ga-68 as the PET moiety. A specific application of the nanoparticles is in the imaging of plaque and this is introduced at the end of this chapter, with a more detailed discussion in Chapter 5.

1.1 Molecular Imaging

The combination of information and expertise from various scientific disciplines, including chemistry, physics, engineering, biology, as well as many others, has brought about an innovative technology, known as molecular imaging. Historically, the traditional method of *in vivo* imaging was to simply image anatomy, and detect structural anomalies to detect diseases.[1] Molecular imaging differs from traditional imaging by using probes that can interact with a particular target or pathway in the body and allowing any abnormalities in these systems to be detected. This will in turn allow for the earlier detection, diagnosis and potential treatment of the disease.[2–4] Research into non-invasive *in vivo* imaging technology has received an abundance of attention over the last decade or so in order to bring about better understanding of the cellular and molecular processes of diseases in the human body. Different imaging modalities exist, among them are magnetic resonance imaging (MRI), positron emission tomography (PET), single photon emission computed tomography (SPECT), optical and ultrasound imaging.[5] PET and SPECT imaging rely on radionuclides to produce an image which exposes the patient to radiation. In all the imaging techniques, the interaction of tissue with various forms of energy is what is exploited to produce an image of the body. These imaging modalities differ from each other in the following main aspects, a) spatial resolution, b) depth penetration, c) type of energy used to obtain the image, and d) sensitivity – the ability to detect the probe relative to the background. This is tabulated below (**Table 1.1**).

Imaging Modality	Type of energy used	Spatial resolution	Depth penetration	Sensitivity
Positron emission tomography (PET)	high energy γ rays	1 – 2 mm	no limit	pM
Single photon emission computed tomography (SPECT)	low energy γ rays	1 – 2 mm	no limit	pM
Magnetic resonance imaging (MRI)	radiowaves	25 – 100 µm	no limit	mM
Optical imaging	visible to NIR light	2 – 4 mm	≈ 1 cm	nM - pM
Ultrasound	high-frequency sound	50 – 500 µm	mm to cm	-
Computed tomography (CT)	X-rays	50 – 200 µm	no limit	-

Table 1.1 General characteristics of the main imaging modalities (modified from ref[5])

Each imaging modality has its own advantages for a specific application but each also has its own drawbacks; for example, MRI gives high resolution images but is not very sensitive, while PET has high sensitivity but poor resolution. Therefore, a combination of two or even more imaging modalities could improve the quality of the image obtained when they are synergistically combined. Many examples of dual- or multi-modality imaging agents already exist in the literature but this is not exhaustive and more work can be done to synthesise these contrast agents for various applications. This will be discussed further in Section 1.4 of this chapter.

Nanoparticles have been in existence for centuries, being produced by volcanic eruptions, weathering or microbial processes.[6] Organic compounds such as proteins, viruses and polysaccharides, or inorganic ones such as metals, iron oxides, and aluminosilicates are all naturally occurring nanoparticles.[7] The field of nanomaterials has expanded in recent years to include those which are produced in a modern synthetic laboratory and there is a wide range of nanoparticle systems that are being developed and that are in use in the imaging and medical field today. One of the criteria for this application is that these nanoparticles have to be between 1 and 1000 nm in diameter. Together with the excellent properties of nanoparticles such as the high surface area to mass ratio, and relative ease of functionalising the nanoparticles to either introduce new properties or modify existing ones, nanoparticles have the potential of bringing significant advances in the prevention, diagnosis and treatment of diseases. Nanoparticles are currently being exploited in a wide variety of applications, including imaging, drug delivery, photothermal therapy, and biosensors. The use of nanomaterials in the medical field for the diagnosis and treatment of disease has been termed nanomedicine.[8] Nanoparticle systems which include polymeric and magnetic nanoparticles,

liposomes, micelles, dendrimers and carbon nanotubes have all been investigated for biomedical use.[9,10]

Contrast agents have been utilised to enhance image quality and improve the visibility of features that would otherwise be difficult to detect.[11] Nanoparticles have been used as contrast agents in various imaging modalities. This is made either by loading the contrast agent onto a nanocarrier, or having the nanoparticle act as the contrast agent themselves. One of the more well-known examples of the latter is the use of iron oxide nanoparticles as a contrast agent in magnetic resonance imaging (MRI).[12] Gold nanoparticles as an X-ray contrast agent,[13] quantum dots in fluorescence imaging,[14] microbubbles loaded with nanoparticles on the surface for use as ultrasound contrast agent,[15] and radiolabelled nanoparticles for combined PET and CT imaging,[16] are some other examples where nanoparticle systems have been utilised as contrast agents.

1.2 Magnetic Resonance Imaging (MRI)

MRI is a non-invasive imaging technique that uses the behaviour of proton spins in the body under an external magnetic field to produce an image of the internal organs and tissues.[17] The contrast in the images produced is the result of different spin relaxation rates (spin-lattice relaxation, T_1 and spin-spin relaxation, T_2) of water molecules in different tissues.[18]

MRI uses the principle of nuclear magnetic resonance (NMR) to image nuclei in the body; the most frequently used being the hydrogen nucleus as water is abundant in the body. Protons have a magnetic moment that is proportional to their angular momentum, and the constant of proportionality is given by the gyromagnetic ratio γ. When protons are placed in a magnetic field, they change their energy states and their spins are separated into two energy levels (called the Zeeman effect, **Figure 1.1**) - the higher energy level being the spins aligning anti-parallel to the magnetic field, and the lower energy level being the spins aligning parallel to the magnetic field which is the preferred state. The spins cancel each other out which results in no net magnetisation.

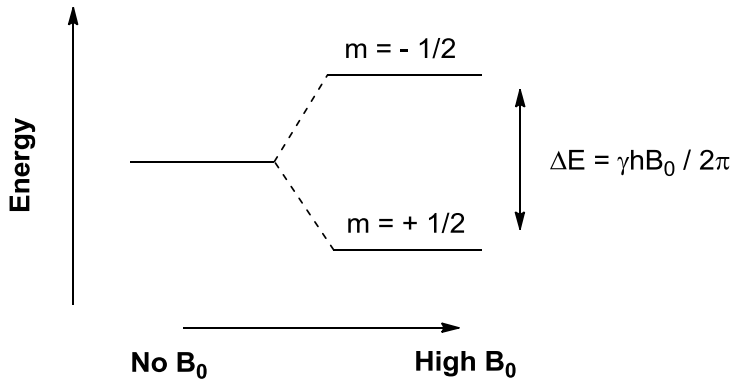

Figure 1.1 Energy levels of spins states for the hydrogen nucleus where E is the energy, B_0 is the magnetic field, γ is the gyromagnetic ratio, m is the spin quantum number, h is Planck's constant and ν is the frequency at which resonant transitions occur.

The net magnetisation can be defined as a vector in the Z-axis, with the protons precessing around the direction of the external magnetic field B_0 at the Larmor frequency. There are more spins aligned with B_0 than there are in the other direction and so the vector is represented in the positive z-direction (**Figure 1.2**).

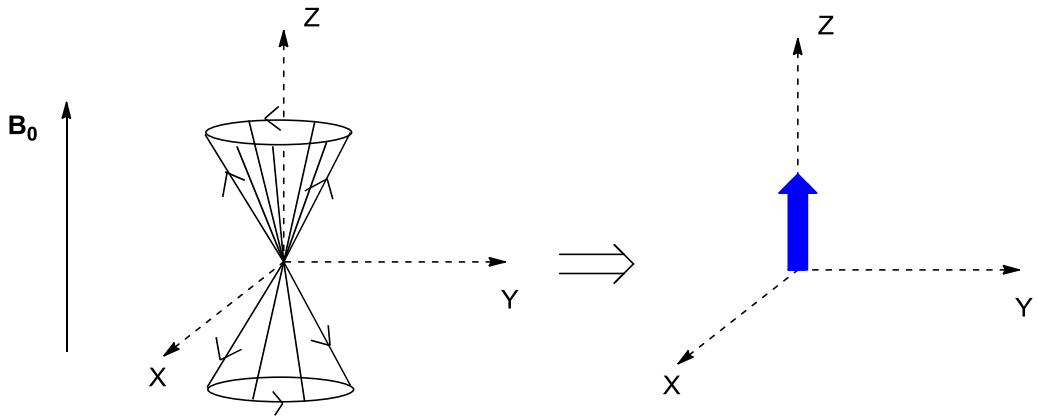

Figure 1.2 Protons precess around the applied magnetic field, resulting in a net magnetisation vector in the z-axis.

As the protons are resting in an external magnetic field with no external stimuli to induce changes in the spin states, a signal related to the relaxation of the spin states cannot be obtained. Therefore for a signal to be measured, there needs to be a change in energy from the equilibrium state. This is achieved via a radiofrequency pulse which when applied causes the net magnetisation vector to change direction as energy is absorbed, either 90^o or 180^o to the Z-axis.

When the radiofrequency pulse is switched off, the magnetisation vector relaxes back to the ground state. This can occur in two ways as shown in **Figure 1.3**: i) spin-lattice relaxation (which has a time constant T_1) whereby the vector realigns back to its original position in the Z-axis, and ii) spin-spin relaxation (which has a time constant T_2) where the magnetisation in the X-Y plane returns to its net value of zero until the signal decays with time. The magnetisation and decay of the induced signal over time is called free induction decay (FID).

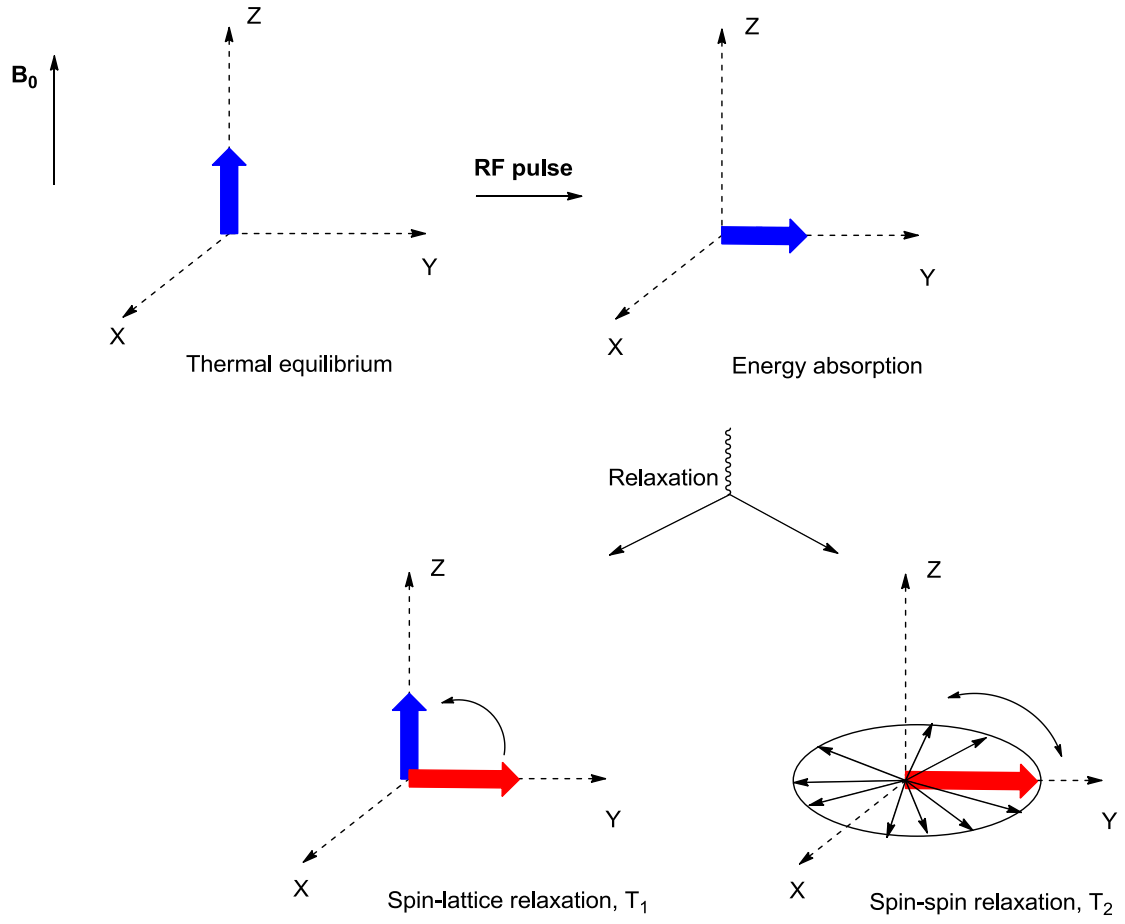

Figure 1.3 Spin-lattice (T_1) and spin-spin (T_2) relaxation processes which occur after the RF pulse is switched off.

Once the electrical signals are recorded, computer software parameters can manipulate the information to ascertain the position of the nuclei in the body in order to obtain a contrasted image. An advantage of MRI over other imaging modalities is its ability to produce high quality images with high spatial resolution in the millimetre range.[19] There is also no need to use ionising radiation unlike X-rays and CT scanning.[19] However, MRI has very low sensitivity compared to PET and SPECT which can impair the amount of contrast in the images.[20] To overcome this, exogenous substances or contrast agents have been developed that can increase the relaxation rate of local water protons.

1.2.1 Contrast agents for MRI

As MRI signal intensity is a result of proton relaxation rates (both the longitudinal, $1/T_1$ and transverse rates, $1/T_2$), increasing $1/T_1$ should brighten the image while increasing $1/T_2$ should darken the image. Contrast agents are able to alter the relaxation rate of protons in the body which improves the MRI signal intensity. The most commonly used MRI contrast agents in a clinical setting contain paramagnetic gadolinium (T_1 contrast agents), which brighten the image in the regions where the agent accumulates.[21,22]

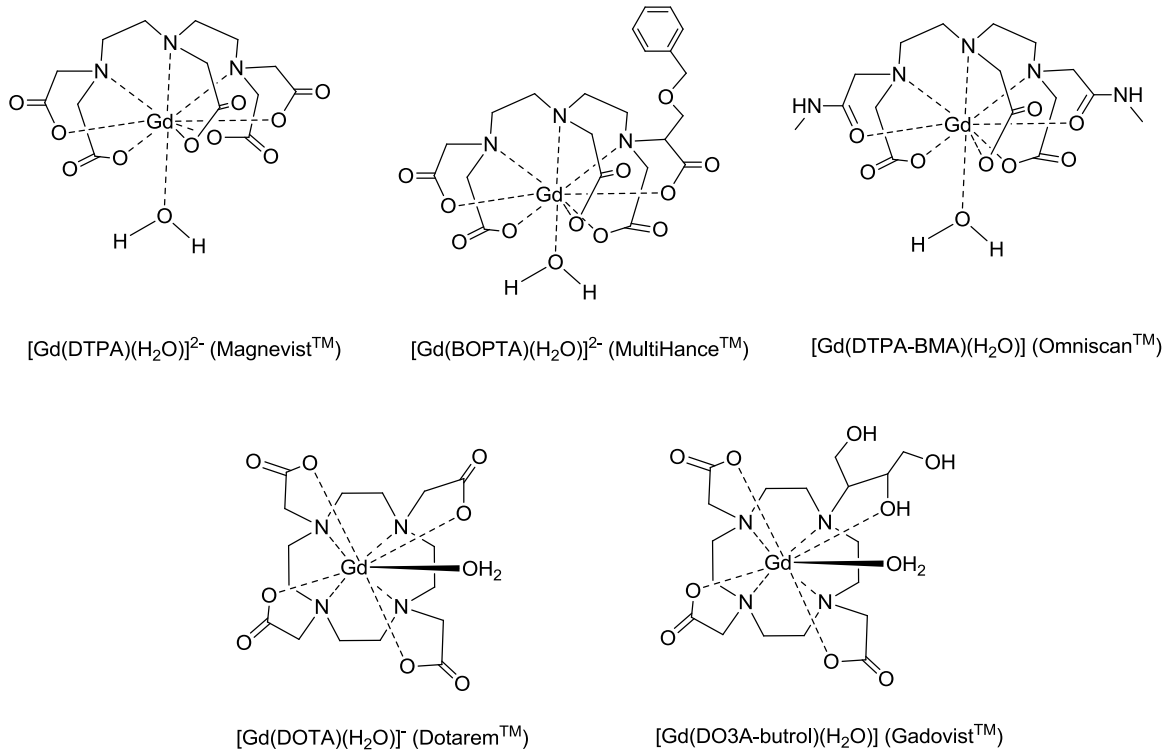

Figure 1.4 Examples of clinically-approved contrast agents containing Gd bound by DOTA and DTPA chelators.

Gadolinium contrast agents utilise gadolinium (III) which has 7 unpaired electrons. Free Gd^{3+} is highly toxic – it is similar in size to Ca^{2+} which is abundant in the body and therefore competes with Ca^{2+} for calcium-binding enzymes and calcium channels, disrupting biological processes.[23,24] It, therefore, has to be strongly coordinated to a chelator in order to be used *in vivo.* However, the complex still needs to have one or more vacant coordination sites to allow a water molecule to bind. The most common chelators have been acyclic DTPA (diethylene triamine pentaacetic acid) and macrocylic DOTA (1,4,7,10-tetraazacyclododecane-N,N',N'',N'''-tetraacetic acid), or derivatives of them (**Figure 1.4**), which allow for water coordination. The much shorter distance between the bound water molecule

and Gd(III) ion allows the protons to experience a much stronger paramagnetic effect compared to the non-coordinated water molecules which results in enhanced relaxivity and greater image contrast.

Superparamagnetic iron oxide nanoparticles (SPION) have also found use in molecular and cellular imaging as T_2 contrast agents, which conversely results in a darkened image.[25] SPIONs have a higher relaxation value and are removed more slowly by the renal system compared to gadolinium-containing contrast agents. They are currently being investigated as an attractive choice for molecular imaging.[26–28] There are a few clinically approved iron oxide nanoparticles, such as Feridex and Resovist, for use as MRI contrast agents, however they are much less popular than the T_1 agents, and have been discontinued. SPIONs have primarily been used to image the liver, spleen and lymph nodes as this is where they accumulate, but are rapidly removed from circulation by the mononuclear phagocyte system (MPS).[29] Target-specific applications require a long blood residence time therefore SPIONs have to be coated with functionalised coatings such as polyethylene glycol (PEG) or dextran to enhance their biocompatibility in order to be used in this application.[30] The goal is then to functionalise the nanoparticle surfaces to enable targeting for molecular imaging and cell tracking, however this is not trivial.

1.2.2 Iron oxide nanoparticles as MRI contrast agents

Magnetic iron oxide nanoparticles exist in many forms in nature, but the three most common ones are magnetite (Fe_3O_4), maghemite (γ-Fe_2O_3) and hematite (α-Fe_2O_3).[31] However, magnetite and maghemite are focused on for the purposes of imaging as hematite is only weakly ferromagnetic.[32] Magnetite has a higher proportion of Fe^{2+} therefore it can potentially oxidise to maghemite in air or at low pH in the absence of oxygen if the nanoparticles are bare.[33] Both have spinel structures, however magnetite has a higher saturation magnetisation than maghemite particles of the same size.[33,34] The magnetic properties of the iron oxide nanoparticles are strongly dependant on the crystallinity of the material and this can change depending on the method of synthesis.[35,36] In order to utilise iron oxide nanoparticles as MRI contrast agents, the particles need to have good relaxivities which is achieved by having a highly crystalline core.[37,38]

Iron oxide nanoparticles as contrast agents are made up of an iron oxide core, and capped with a passivating layer which is usually a stealth layer of polymers (PEG or dextran) for biocompatibility and to prevent aggregation. These can be functionalised for further attachment of an optical moiety,

a radioligand, biological molecules such as antibodies, or even drugs - for use as dual-modal imaging agents, disease-specific target or therapeutics respectively (**Figure 1.5**).

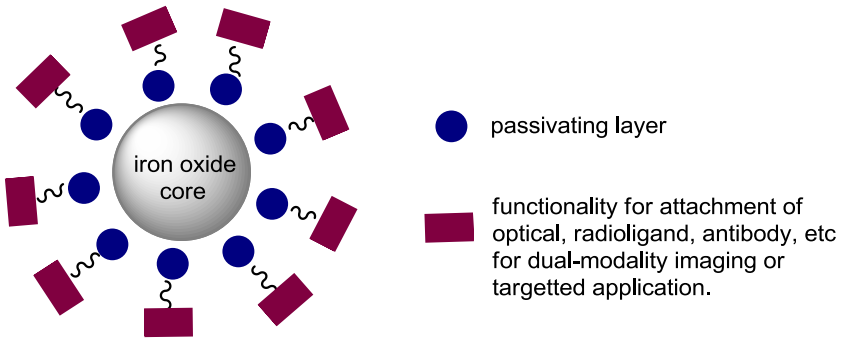

Figure 1.5 Simplified representation of general iron oxide nanoparticle structure.

Nanoparticles have been separated into three different classes according to their size: i) micrometer-sized paramagnetic iron oxide (MPIO, up to several micrometers), ii) superparamagnetic iron oxide (SPIO, up to hundreds of nanometers), iii) ultrasmall superparamagnetic iron oxide (USPIO, less than 50 nm).[39] The ideal size for *in vivo* delivery of nanoparticles is 10-100 nm although this is dependent on the application.[40] Smaller nanoparticles are removed too quickly by the kidneys while larger nanoparticles are isolated by the MPS.

There are numerous chemical methods that can be used to synthesise superparamagnetic nanoparticles. These include co-precipitation, thermal decomposition, microemulsions, sol-gel syntheses and hydrothermal reactions among others.[41–43] The difficulty faced in synthesising these nanoparticles is in obtaining a monodisperse population of appropriate size.

The simplest and most common method of synthesising magnetic nanoparticles is by the classical literature method of co-precipitation.[44–48] This involves ageing stoichiometric amounts of ferrous and ferric salts in aqueous media to produce the iron oxides. This occurs in two stages; nucleation and growth.[49–52] A disadvantage of the co-precipitation method is that particle size control is limited as the control of the crystal growth is due to kinetic factors. The nanoparticles produced by this method have a large size distribution due to the nucleation and growth steps occurring simultaneously. Nucleation to produce the seed crystals occurs rapidly when the reaction solution reaches supersaturation, and then simultaneous slow growth of the crystals on the surface of the seeds occurs.[38] This results in particles of varying sizes. Hence, to produce narrowly dispersed iron oxide nanoparticles, the process of nucleation should be separated from growth.[53]

Narrowly dispersed nanoparticles with a good size control can be achieved by the high-temperature decomposition of iron organic precursors such as $Fe(CO)_5$, $Fe(acac)_3$ or $Fe(Cup)_3$ [Cup = Cupferron - N-nitroso-N-phenyl hydroxylamine] in the presence of organic solvents and surfactants.[54] The products of this type of synthesis have been shown to deliver higher relaxivities due to improved crystallinity.[38] The co-precipitation and thermal decomposition methods are the two most commonly used to prepare iron oxide nanoparticles for biomedical applications.[55]

To prevent aggregation of the nanoparticles, the iron oxide cores have to be capped with a stabilising agent.[29] These can be monomeric (carboxylates, phosphates), inorganic (silica, gold) or polymeric (PEG, dextran). The capping moieties are not usually covalently-bound to the iron oxide core. For example, hydrogen bonding between the hydroxyl groups of dextran and the surface of the iron oxide has been postulated.[30] This means that the capping layer may be easily stripped *in vivo*, resulting in aggregation and/or clearance from the body. The commonly used molecules to stabilise SPIONs in the literature have been surfactants such as oleic acid and alkane phosphonic acids.[56] These molecules are amphiphilic and result in highly stable nanoparticles that are dispersible in organic solvents. But this is not ideal as these SPIONs require further functionalisation to impart water solubility before use in biological applications. Polymeric coatings such as dextran are ideal molecules as they impart biocompatibility to the iron oxide nanoparticles.[57] This enables the SPIONs to be used in biological systems and remain stable in water at neutral pH and physiological salinity. The polymer coating can also allow further functionalisation of the SPION surface with drugs, fluorescent compounds or even PET/SPECT reporters for therapeutic and bimodal imaging purposes.

1.3 Functionalisation of nanoparticle surfaces

1.3.1 Capping agents as stabilisers

As previously mentioned, there are different capping agents that have been used in the literature – monomeric, inorganic and polymeric. Monomeric stabilisers utilise functional groups such as carboxylates and phosphates to bind to the surface of the iron oxide core. These molecules are usually citric acid or other organic acids which bind to the iron oxide core via the oxygen atoms of the acids. Inorganic materials such as silica and gold provide a binding site on the nanoparticle surface for biological ligands. For example, with a silica surface, the silanol groups on the surface allow reaction of specific ligands to the particles, via hydrolysis and condensation of an organosilane.[58,59]

Natural and synthetic polymeric capping agents such as dextran and polyvinyl alcohol (PVA) have been the most widely used as they are biocompatible and biodegradable.[60] However, they are not covalently linked to the iron oxide core and may be easily stripped *in vivo*, therefore inducing aggregation.[61]

An alternative direct method of functionalising the nanoparticle surface has been developed by Herranz *et al*, and involves synthesising oleic-acid capped SPIONs by the high temperature decomposition route but then oxidising the double bond of the oleic acid to form azelaic acid which has a higher water solubility.[62] The terminal carboxylic acid group was then reacted with amines in water to show that the nanoparticles can be functionalised further in aqueous medium (**Scheme 1.1**).

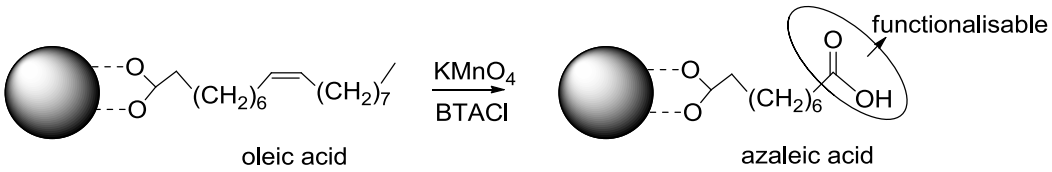

Scheme 1.1 Synthesis of hydrophilic nanoparticles by oxidation of the double bond in the oleic acid using potassium permanganate ($KMnO_4$) and benzyltrimethyl-ammonium chloride (BTACl).

Silica and gold are the two more exploited materials to be used as coatings for iron oxide nanoparticles. Silica is advantageous as it is relatively inert which improves chemical stability.[63,64] The silica surface is usually deposited by three main methods, a) the Stöber process, b) emulsion method, and c) from a silicic acid solution. Gold coating is also highly useful as gold-thiol interactions can be utilised to further functionalise the nanoparticle surface. Gold surfaces have been deposited on iron oxide nanoparticles by literature protocols such as the thermal decomposition of gold compounds over a pre-made iron oxide nanoparticle,[65,66] or by a reverse-micelle approach.[67] Coating of iron oxide nanoparticles will be further discussed in Chapter 2.

Surfactants such as oleic acid chains are good at stabilising the iron oxide nanoparticles in organic solvents but their coordinating bonds are labile.[29] Exchanging carboxylic acid anchors for a molecule containing a phosphonate group that can more strongly coordinate to the iron on the surface of the core will greatly improve the stability of the nanoparticles over a larger pH and temperature range.[34,68–71]

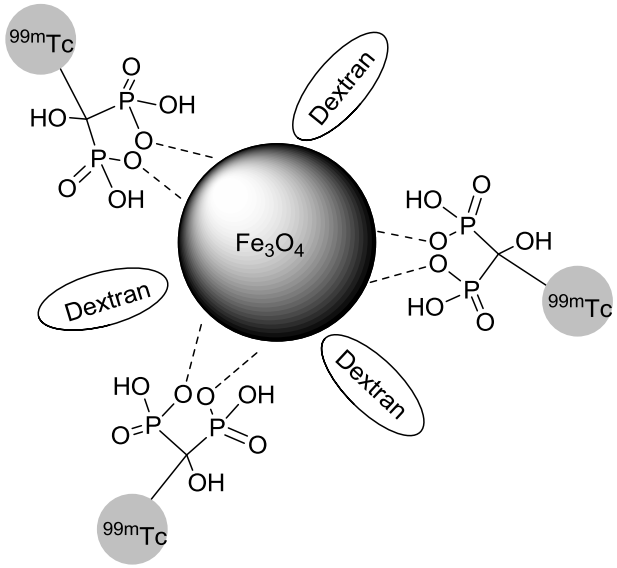

Figure 1.6 Simplified diagram of 99mTc-containing bisphosphonate iron oxide conjugate for dual modality SPECT-MR imaging.

Daou *et al* have carried out studies on the phosphonate interaction with iron oxide nanoparticles and have also shown that nanoparticles with phosphonates exhibit higher magnetisation.[68–70] A recent paper by Torres *et al* have also successfully shown that ^{99m}Tc-containing bisphosphonate ligands can directly bind to the iron oxide core of dextran coated nanoparticles (**Figure 1.6**).[72] Other recent papers by Motte *et al* have also used bisphosphonates as capping agents for SPIONs.[73] This will be expanded upon in Chapter 2.

1.3.2 Surface modification for functionality

Nanoparticles that have not been functionalised with a targeting moiety will be taken up by macrophages in the body and this has so far limited their use to imaging organs such as the liver, spleen and lymph nodes. Targeting moieties such as antibodies, proteins or peptides can be bioconjugated via mediators (such as NHS ester) to form a covalent link between them.

Surface modification using covalent linkages is usually used to attach components which will remain a part of the contrast agent. These are typically radioligands and fluorophores, as opposed to drugs. The conjugation of radioligands and fluorophores to MRI contrast agents to give dual-modality imaging agents will be discussed further below.

1.3.3 Site-targeted contrast agents for imaging of diseases

Early contrast agents in clinical use were not specifically designed to recognise specific targets such as receptors or cell markers. These contrast agents were still termed "tissue-specific" due to their accumulation in tissues and organs via phagocytosis or endocytosis, ending up in the liver, kidneys (via MPS) or lymph nodes.[74,75] Other contrast agents which were not quite tissue-specific, but had long blood residence times due to either their high molecular weights or by binding to serum albumin, were called blood pool contrast agents.[76,77]

In order for highly specific targets to be recognised and induce a different signal intensity to that of non-targeted tissue, contrast agents require conjugation to a ligand for selective receptor binding.[78] This can be an antibody, peptide, protein or other biological molecule to act as a targeting agent towards receptors in a diseased organ or cells in order to image a specific disease or pathway. A large proportion of targeted contrast agents in the literature has been for MRI, ultrasound and optical or fluorescence imaging, as much of the initial work to create these targeted contrast agents was to simply conjugate the relevant probe with an antibody. In the case of MRI, this was initially achieved by the direct conjugation of an antibody to the Gd chelate. However, this method is challenging due to the low sensitivity of MRI which makes the target detection difficult.[79]

Several different conjugation techniques have been developed to overcome this. One way to do this is by employing a two-step avidin-biotin conjugation. The HER-2/*neu* receptor is a known marker in breast cancer cells and Artemov *et al* demonstrated targeted imaging by pre-labelling the receptor with biotin conjugated anti-HER-2/*neu* antibodies.[80] The gadolinium contrast agent complexed to avidin specifically binds to the biotin-antibodies generating a positive T_1 contrasted MRI image. Others have used lipid or micelle based nanoparticles carrying high payloads of Gd chelates embedded in the lipid membrane.[81] Increasing the relaxivity of Gd-based contrast agents to obtain larger signal intensity, or utilising iron oxide nanoparticles to generate a negative contrast, have also been successful approaches. Zhao *et al* have used specific phosphate binding proteins which target apoptotic cells conjugated to SPIO to image cell death and have shown *in vivo* that tumours treated with chemotherapy showed a shift in MR signal.[82] This would be a useful way to monitor cancer response to therapy.

Other imaging modalities besides MRI have also seen attempts to produce targeted contrast agents. Microbubbles have been labelled with various antibodies and peptides for the ultrasound imaging of specific diseases or events. Conjugation of a microbubble to a P-selectin specific ligand or antibody has been shown by Klibanov *et al* to effectively image inflammation.[83] Tumour angiogenesis has also been successfully imaged with selective uptake of microbubbles conjugated to integrin-binding

Knottin peptides.[84] Price *et al* and Song *et al* have both separately shown that targeted microbubbles can be used for drug delivery, with destruction of the bubbles at the intended specific site releasing the drug.[85,86] Fluorescence-based targeted contrast agents for tumour imaging have also been demonstrated. Conjugation of a tumour receptor-specific peptide to a dye resulted in tumour retention compared to negligible uptake by non-tumour-specific dyes.[87,88]

1.4 Dual- or Multi-modality Imaging

No single imaging modality is faultless – each has its limits and because of this, combining two or more imaging agents within one probe is becoming increasingly explored. Of the various combinations of imaging modalities, MRI/optical imaging has been the most well-developed, especially the functionalisation of gadolinium chelates with fluorophores or even quantum dots.[89] Other modalities that have been combined are PET/optical, SPECT/optical and MRI/PET.

Even though multimodality imaging has been used clinically to obtain a greater understanding of disease processes, different agents have been used for each modality. Dual-modal imaging cannot simply be addressed by adding two separate classes of contrast agents together as each can have different pharmacokinetic properties. Therefore, a multi-functional probe that can be detected by two or more imaging modalities simultaneously would be extremely beneficial.[90]

Multimodality imaging was initially carried out by using two separate probes and acquiring two separate images, then overlapping/fusing the images to obtain a more in-depth picture of the disease and its processes. This is termed software fusion. However, this is not always ideal as this method requires two separate machines and therefore moving the patient into a different position. Coupled with the involuntary movement of the organs, images obtained (especially MR images) can result in artefacts and cause difficulties when fusing images. To overcome this, a single probe which incorporates two or more imaging modalities and the ability to acquire the images using a single machine/instrument allows the patient to remain in the same/similar position while the image is acquired.[91–93]

In the early 1990s, Hasegawa *et al* at the University of San Francisco, pioneered a CT scanner that was placed in tandem with a SPECT camera.[94] Their success led to the eventual commercial scanners by GE Healthcare (SPECT/CT) and Siemens Molecular Imaging (PET/CT in 1998).

A combined scanner would facilitate seamless production of fused images, and improve acquisition times. It also offers more accurate images which provide an advantage during surgery, which

requires accurate localisation of the image (for example guided biopsies where sampling error can be reduced). Ultimately, it should offer the simplicity and convenience that fusion software cannot. A combined PET/CT scanner also gives the additional benefit of providing low-noise attenuation correction with the prospect of improved PET scan quality and quantitative accuracy. Combined scanners have an advantage in therapy as they allow for more efficient therapy planning and accurate monitoring of the therapy administered compared to just using a single imaging modality.[95,96]

With a combined scanner, the image can be obtained using two separate contrast agents, a dual-modal probe, or even with just one contrast agent.

The advantages of using a single dual-modal probe over two separate contrast agents are:

a) A single probe helps to ensure the same pharmacokinetics throughout.
b) Allows for complementary anatomic, functional and molecular information to be obtained.
c) The body's clearance mechanism is not put under additional stress to remove the probes (compared to using two separate probes).
d) Dual-imaging probe gives the assurance that the signal obtained by both modalities comes from the same molecule.

The main disadvantages of dual-modal imaging are that the concentration of the different contrast agents to be used can vary by 3 orders of magnitude.[95] It may not be as simple as coupling two separate modalities together (especially for MRI which is not sensitive and therefore requires a large amount of contrast agent, but PET which is very sensitive needs only a small amount of the radionuclide). Also, the dual-modal instruments, especially for PET/MRI have been difficult to design and combine due to the interference between the separate components (for example, the magnets for the MRI can interfere with the photodetector on PET). This results in acquisition of images that are difficult to align.

Although combined scanners are likely to improve the accuracy of image fusion, some inaccuracies still exist, for example, related to respiratory chest movement differences between fast CT and slower PET acquisitions. As the PET and CT scans are not acquired simultaneously, the risk of patient movement between scans will still remain.

Optical/PET (SPECT) has also been looked into due to the high detection sensitivity of both imaging modalities. Optical imaging's depth penetration is limited by the energy being absorbed and scattered by tissue. PET/SPECT on the other hand, is not limited by tissue depth. When combined,

the optical data provides high-throughput imaging of molecular and functional events while the nuclear imaging provides quantitative data. Also, optical imaging is relatively low cost and flexible enough to be integrated into existing PET or SPECT systems. A fused PET/optical image would provide the information on where the probe has been localised (by PET), while the optical data would report the probe activity.

Following on from the success of PET/CT scanners, the combination of PET with MRI was a logical progression and can offer several advantages, the greatest of which is that it would theoretically provide the "perfect" spatial combination of molecular/functional PET and anatomic/functional MRI.[20] Compared with PET/CT, PET/MRI has the added advantage of greatly reducing radiation exposure (both PET and CT use radiation). However, a combined PET/MRI scanner faces a technical challenge in terms of space constraints. Also, PET detectors use photomultiplier tubes to acquire the images which are affected by the magnets of the MRI component.

Another advantage of MRI/PET over CT/PET is that MRI/PET images can be acquired simultaneously while CT/PET images are taken sequentially, lengthening scan times. CT/PET also require two different breathing protocols, which causes artefacts and therefore affect the accuracy of the images and attenuation correction. MRI also has several other advantages over CT – MRI has excellent soft-tissue contrast and does not use ionising radiation.

One of the more popular combinations of dual-modal imaging is to combine MRI and optical imaging, with small molecules being the simplest concept but challenging to synthesise.[95] There are various examples of MRI/optical probes of different combinations of signalling components in the literature. The majority of these have incorporated Gd-chelates and have primarily been synthesised by manipulating the chelate structures to include an organic fluorophore. For example, fluorescein covalently attached to Gd-DO3A has been shown to be an effective dual-modality probe (**Figure 1.7**).[97] The fluorescein moiety was attached via the reaction of fluorescein isothiocyanate to an amino group on the macrocycle. Other organic fluorophores such as rhodamine have also been investigated.[98]

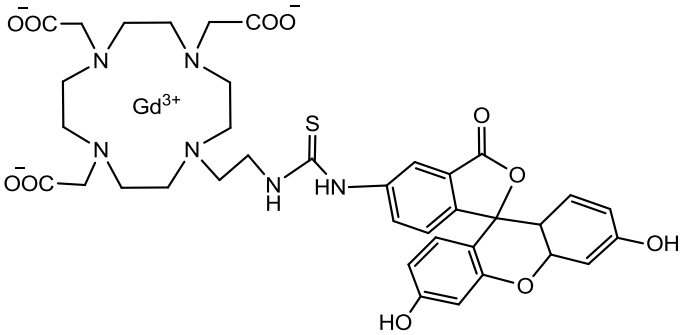

Figure 1.7 Structure of Gd-DO3A-ethylthioreido-fluorescein.

Another example of an MRI/optical probe features gadolinium-functionalised quantum dots on dye-doped silica.[99] Quantum dots have been known to have solubility and toxicity issues which may prove problematic. This can be overcome by introducing passivating ligands before use *in vitro*. However, the silica shells are inert and can hold a large amount of Gd ions which enhances the relaxivity.

Aside from gadolinium chelates, iron oxide nanoparticles have also been functionalised with optical agents. Similar to the functionalisation of gadolinium chelates by simple conjugation with fluorescent moieties, iron oxides can be modified for MRI/optical imaging by coupling to fluorophores such as rhodamine,[100,101] indolequinones,[102] dansyl[103] and Cy5.5.[104–106] These examples have all shown bimodal imaging capabilities. There are many examples of core/shell structures as a means to introduce optical probes onto iron oxide nanoparticles, however not all have been shown to act as a dual modal MRI/optical probe in a biological setting. One of the more popular methods to form these core/shell systems is to coat the iron oxide core with a silica shell and subsequently trap the fluorophore such as rhodamine or terbium complexes, within the silica shell,[107,108] or to deposit the optical moiety such as a quantum dot as another layer onto the silica shell.[109] Quantum dots can also be directly grown around the iron oxide core,[110] and this method has also been used to coat iron oxides with inorganic luminescent shells such as LaF_3CeTb, and Y_2O_3:Eu.[111,112] However, the core/shell structures usually have large sizes, making them less suitable for use in biological imaging despite having both magnetic and optical capabilities. Therefore, simple conjugation of organic dyes have remained the more attractive way of forming dual modal MRI/optical agents, especially with Cy5.5 due to the desirable wavelength emission of Cy5.5 for biological applications (675 λ_{ex}/694 λ_{em}).

1.4.1 PET/MR imaging

With respect to this project, dual-modal MRI/PET imaging is an area of exciting development. PET is a technique that can be used to detect chemical changes in the body before the disease symptoms become apparent.[113–115] Radioisotopes with a short half-life such as ^{11}C and ^{18}F are less suited for PET/MRI dual-modality probes due to the time restrictions on the synthesis and purification of the probes as well as their compatibility with long-lived biological molecules. Isotopes such as ^{64}Cu, ^{68}Ga and ^{124}I have longer half-lives that make them more ideal for PET/MRI systems.

There have not been many examples of dual-modal MRI/PET imaging agents, simply due to the difficulties in combining an MRI and PET probe together and overcoming the question of concentration (as previously discussed). Nanoparticles have been the predominant MRI contrast agent used in the development of this field as they are the perfect scaffold to integrate different imaging modalities onto a single platform.[116] ^{64}Cu has been more widely chosen as the radioisotope to be investigated due to its well-established coordination chemistry which allows for a more varied approach to chelation enabling further linkages to nanoparticles, other imaging agents, peptides and other biological molecules.[117]

Examples of dual modal MRI/PET probes from the literature include work by Glaus *et al,* who have shown that their SPIO core coated with micelles composed of functionalised PEGylated lipids, and modified with DOTA for ^{64}Cu labelling have dual imaging capabilities.[118] These have been different to previous probes where the particles were coated with more traditional polymer and carbohydrate based molecules (**Figure 1.8**) such as those by Lee *et al* [119] and Nahrendorf *et al*.[120] Lee *et al* have further shown that their system, which includes conjugation to an RGD peptide that targets tumours results in a tumour-specific probe. Nahrendorf *et al* went further and conjugated a fluorophore which gave a trimodal probe. They also showed that these probes can be used for the imaging of atherosclerotic plaque from their biodistribution results and PET/CT scans which show accumulation of the probe in the arteries of the diseased mice, corroborated by *in vivo* MRI and *ex vivo* fluorescence imaging.

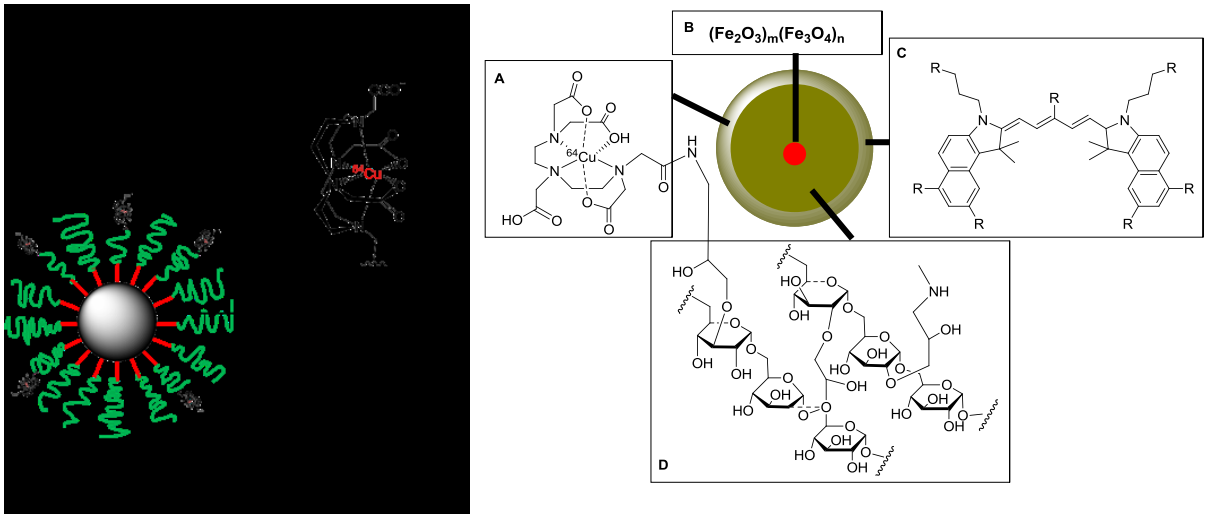

Figure 1.8 Left: Micelle-coated ^{64}Cu-conjugated IONP as synthesised by Glaus *et al,* image adapted from ref [118]. Right: Nahrendorf's IONP (B) coated with dextran (D) and labelled with a fluorophore (C) and ^{64}Cu (A), image adapted from ref [120].

There have been even fewer examples of iron oxide nanoparticles conjugated to ^{68}Ga for use in MRI/PET imaging. Gallium-68 has several advantages over copper-64 and so would be an ideal radioisotope to label dual MRI/PET probes. Gallium-68 is produced by a readily available generator as opposed to the cyclotron-produced copper-64, and the positron efficiency of ^{68}Ga (89 %) is much higher than ^{64}Cu (17.4 %).[121]

An example of ^{68}Ga conjugated to silica nanoparticle with cobalt ferrite core is shown below (**Figure 1.9**).[122] The triple modality MRI/PET/NIRF probe consists of 50 nm sized silica nanoparticles with amino and PEG coating and a NIRF dye encapsulating a cobalt ferrite core. The ^{68}Ga-NOTA complex was chelated to the amine surface. However, this probe has not been functionalised to be target-specific. Another example by Stelter *et al* used the same principle but incorporated a transfection agent for cell labelling.[123]

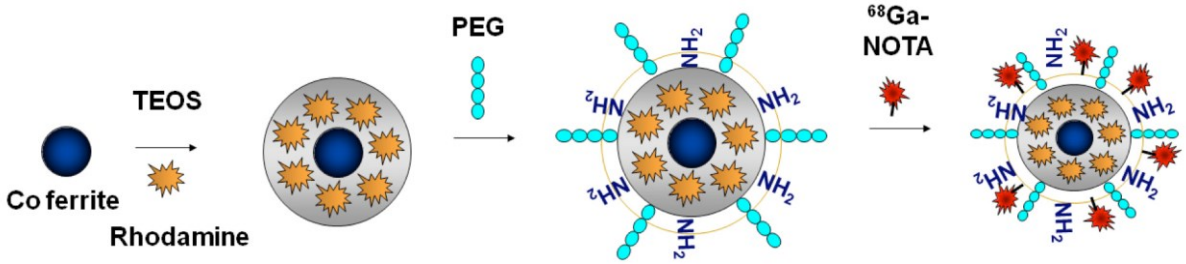

Figure 1.9 Diagram showing the synthesis of PET/MRI/fluorescent triple modality molecular probe based on silica nanoparticles with cobalt ferrite core. TEOS - tetraethyl orthosilicate; NOTA - 1,4,7-triazacyclonane-1,4,7-triacetic acid [Image from ref [122]].

The use of DOTA and NOTA ligands to chelate metal ions has been extensively researched therefore these would seem logical ligands to use for binding Ga(III). Although NOTA has a slightly higher log K value for Ga (30.1)[124] than DOTA (21.3)[125], NOTA has not yet been approved for clinical use. Within this project, the PET moiety (gallium-DOTA) will be attempted to be conjugated to the nanoparticle via the copper-free azide-alkyne cycloaddition reaction. The dual-modal contrast agent would be assembled *in vivo* as the large size of a single pre-combined nanoparticle MRI/PET probe would slow down *in vivo* movement, diminishing radioactivity before reaching its target. Pre-targeting using a magnetic nanoparticle followed by the injection of the radio-labelled molecule at the correct time will ensure radioactivity remains sufficiently high. Therefore, a pre-targeting concept whereby the magnetic nanoparticle is first injected, followed by the injection of the radio-labelled molecule at the correct time will be attempted to ensure radioactivity remains sufficiently high. This will be discussed further in Chapter 3.

1.5 Applications specific to this project

Iron oxide nanoparticles are currently being extensively researched for use in target-specific applications. These include cancer imaging and inflammation in atherosclerosis, among others, and have already been briefly introduced in previous sections.[126–128] Nanoparticles are optimal for targeted imaging because of their large surface area capable of conjugating biological molecules such as antibodies and proteins. In theory, it would be possible to image any disease state, or an event, as long as the specific target (receptor or cell marker) to be imaged is known. In the body, this amounts to a large collection of diseases, receptors and cell markers, and hence antibodies, peptides and proteins that can be conjugated to contrast agents.

An immediate application of the nanoparticles synthesised in this project is in cardiovascular plaque imaging and was carried out in collaboration with the Bioengineering Department at Imperial College London. Cardiovascular disease (CVD) is one of the leading causes of deaths in the UK. The causes of CVD are varied, although atherosclerosis and hypertension are two of the more common ones. Atherosclerosis is a condition where the walls of the arteries harden and the lumen narrows, due to the formation of atherosclerotic plaque. Atherosclerotic plaque has been shown to play a significant role towards the development of acute coronary syndrome (ACS). Post-mortem examinations of patients who have suffered heart attacks indicate that the plaques become vulnerable in ACS leading to blood clots and eventually heart attacks.[129] The main factor that

contributes to plaque progression and vulnerable plaque formation is inflammation which is regulated by a chemokine network. By imaging the key proteins during vulnerable plaque formation, it is hoped that at-risk patients can be diagnosed earlier.

1.5.1 Atherosclerosis

Atherosclerosis is a vascular disease where the artery wall thickens (stenosis) and hardens due to the presence of atheromatous plaque. Atherosclerosis was initially thought to be predominantly caused by high concentrations of lipids in the artery wall. However, even after lifestyle and diet changes, and the use of pharmaceutical drugs to control cholesterol concentrations, it remains one of the leading causes of death in many industrialised countries.[130,131] Therefore, the composition and morphology of plaque in the arteries are more important factors than luminal stenosis when determining whether a cardiovascular event will occur.[132,133] It is now widely accepted that atherosclerosis is a disease that is a result of inflammation.[134–138]

There are two types of plaque (illustrated in **Figure 1.10**): a) stable plaque, which has a small and hard fatty core with a thick fibrous cap, and where the atheroma grows to eventually restrict blood flow due to reduction in the lumen diameter; and b) unstable (or vulnerable) plaque, consisting of a larger and soft fatty core with a thin fibrous cap, which is susceptible to rupture. When a vulnerable plaque ruptures, a clot can form elsewhere in the body that can either slow or stop blood flow, leading to tissue death. The two most commonly recognised situations where a clot from vulnerable plaque disruption results in tissue death, is a heart attack (artery blockage in the heart) and stroke (artery blockage in the brain).

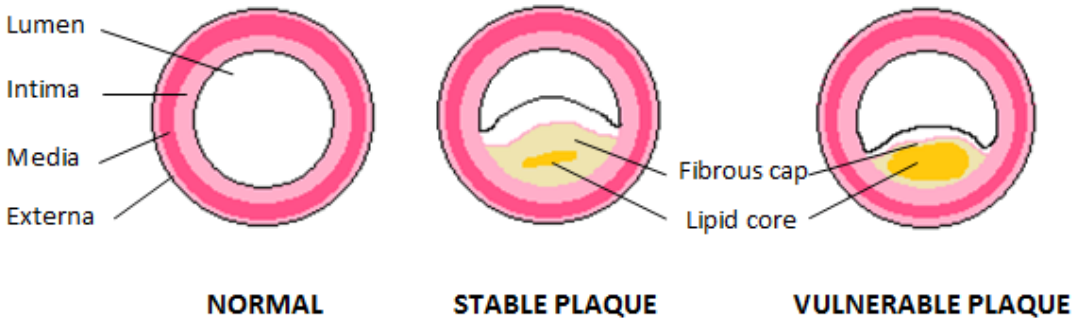

Figure 1.10 Simplified illustration of stable and vulnerable plaque. Stable plaques have a small, hard lipid core with a thick fibrous cap, while vulnerable plaques have a larger lipid core, with a thin and fragile fibrous cap.[139]

The process for the formation of plaque in the arteries is not fully understood, but the general consensus is that plaque is formed as a result of inflammatory processes in the endothelial cells of the artery wall due to the presence of irritants. The presence of these irritants arises from factors such as diabetes, smoking, a high fat diet, hypertension, and even some bacterial infections, which results in foreign materials such as free radicals and lipids in the blood stream.

Arteries are made up of three layers, the intima, media and externa. The intima layer further consists of a layer of cells called the endothelium, supported by an internal elastic lamina, which help to maintain the smoothness of the inside of the arterial wall, thus keeping a good flow of blood. As people age, endothelial dysfunction (or damage) is aggravated by any one or a combination of the following: elevated low density lipoprotein (LDL) levels; infections from microorganisms such as the herpes virus; genetic mutation; free radicals from hypertension, diabetes, or smoking.[140–142] This allows the endothelium to be more permeable to LDL, thus starting the atherosclerotic process. Macrophages are dispatched to the site of inflammation, and upon recognition of the LDLs as exogenous, they internalise them and turn into foam cells.[143]

When this inflammatory response fails to remove the irritants, the inflammation can continue indefinitely. As the inflammatory response repeats itself, more macrophages and T-cells migrate to and accumulate within the plaque.[144,145] At the same time, a high concentration of LDL in the blood stream results in the LDL accumulating in the intima to form fatty streaks. The smooth muscle cells of the tunica media start migrating to the intima, forming a fibrous cap over the fatty streak. The combination of the fatty core and the fibrous cap is known as an atherosclerotic plaque. The artery wall can compensate for the presence of the lesion for some time, so that the lumen remains unchanged. This is known as "remodelling".[146] Eventually, the artery wall becomes so severely damaged that it cannot compensate for the large size of the plaque, which now obtrudes far into the lumen, and obstructs blood flow. As the disease progresses, macrophages, endothelial cells and smooth muscle cells within the plaque die from apoptosis or necrosis.[147] This results in a large lipid-necrotic core and a thinner fibrous cap that is more fragile and prone to rupture.[148]

1.5.2 Vulnerable Plaque

The deviation to form vulnerable plaque has been found to be directly correlated to a vast number of macrophages at the site of inflammation. When the foam cells and other components of the plaque die, various chemical factors are triggered and released which sustain the inflammatory process, thus increasing the numbers of macrophages even more. These macrophages have been

known to produce proteinases and free radicals that can degrade tissue as well as prevent the formation of stable fibrous cap, leading to wall damage and plaque rupture.[149–151] The total amount of macrophages that is found within the plaque has been correlated to an increased risk of plaque rupture.[143]

Even with the advances in medical treatments for cardiovascular disease, a large number of patients who appear healthy die suddenly without any prior symptoms.[152,153] A large proportion of these sudden deaths have been attributed to the presence of vulnerable plaque. Vulnerable plaque differs from stable plaque and has been defined by several groups to generally have a thin fibrous cap that is <65 µm thick and a large lipid core that is infiltrated by macrophages.[154] It is more difficult to detect by traditional imaging methods due to these differences in composition and morphology between the stable and vulnerable plaque.

1.5.3 Imaging of vulnerable plaque

In order to prevent the worst-case scenarios of heart attacks and strokes when a vulnerable plaque ruptures, earlier diagnosis of vulnerable plaque in high-risk patients (such as those with a family history of heart disease) is required. Commonly used methods to image plaque are by ultrasound (US), optical coherence tomography (OCT), computed tomography (CT) and conventional angiography. These methods typically detect atherosclerosis by evaluating the physical characteristics of the arterial walls, especially the considerable narrowing of the lumen.[132] However, these conventional techniques have low resolutions and do not allow for the accurate determination of the presence of thin fibrous caps to distinguish between stable and vulnerable plaque and therefore are less than reliable for imaging vulnerable plaque.[139]

Several methods for imaging atherosclerosis and vulnerable plaque have been reported in the literature, mostly on small animal models for practical purposes. Atherosclerosis is a chronic inflammatory disease, where the inflammatory cells such as macrophages play a significant role at every stage of the disease. Many examples in the literature have used these markers in the inflammatory processes, as well as other biological targets such as apoptosis,[155–157] to image atherosclerosis, most commonly with radioisotope imaging. A relatively straightforward method is to use radiolabelled LDL to visualise their accumulation in plaque,[158–160] as well as tracking monocytes (precursors to macrophages) labelled with ^{111}In-oxine, a clinically approved radiotracer.[161] A less direct method that has been shown to successfully image plaque in mice, is by imaging a specific

receptor, LOX-1 that binds to oxidised LDL.[162,163] Macrophages in plaque have also been imaged by following the uptake of ^{18}F-FDG, as macrophages have a high metabolic rate.[164]

So far, the methods to image plaque involve the use of radiotracers, and although they may determine the presence of the relevant criteria for vulnerable plaque, PET/SPECT imaging does not provide complementary local tissue confirmation of the vulnerable plaque. MR imaging is better suited to imaging plaque, and vulnerable plaque in particular, as the excellent soft-tissue contrast allows for composition and morphology of plaque vulnerability, not just luminal stenosis.[165] After the discovery that SPIONs were spontaneously taken up by macrophages in plaque, first in rabbits,[166–169] and then later in humans,[170] MR imaging of plaque using nanoparticles as contrast agents began to develop in earnest. By attaching targeting moieties to nanoparticles,[171,172] which enable even more selective uptake by macrophages in plaque, MRI offers a very promising method for *in vivo* targeted imaging of plaque. However, even with MR imaging (with and without the use of contrast agents), not all the vulnerable plaque criteria can be evaluated at the same time by one single MR technique. Therefore, combined imaging will be required in order to assess multiple plaque features for a truly useful clinical evaluation.

1.6 Aims

Magnetic iron oxide nanoparticles as MRI contrast agents have been researched extensively. However, the formation of a single dual-modal MRI/PET contrast agent incorporating iron oxide nanoparticles has been less heavily explored, and is therefore an area that would be interesting to investigate. An application of the dual-modal MRI/PET probe would be to image vulnerable plaque, by targeting a cytokine protein that is expressed in the endothelial cells of the arteries.

Taking all of this into consideration, the aims of this project are briefly outlined below:

1. To synthesise iron oxide nanoparticle with a high magnetisation, high crystallinity and low size dispersion. Different synthesis methods will be explored and the nanoparticles from each method characterised.
2. To coat the nanoparticle surface with a suitable ligand that will render the resultant nanoparticle water-soluble, and examine their stability at physiological conditions.
3. Functionalise the nanoparticles with suitably reactive functional groups to allow the surface to be decorated further with:
    a. PEG molecules for biocompatibility;

   b. Alkyne for copper-free alkyne-azide cycloaddition reaction to assemble a dual-modal MRI/PET imaging agent *in vivo*.

4. Study the physical characteristics of the functionalised nanoparticles.
5. Conjugate the nanoparticles to an antibody to enable the targeting and imaging of vulnerable plaque in atherosclerosis.

1.7 References

1. M. Rudin and R. Weissleder, *Nat. Rev. Drug Discov.*, 2003, **2**, 123–31.
2. P. J. Cassidy and G. K. Radda, *J. R. Soc. Interface*, 2005, **2**, 133–44.
3. L. Ottobrini, P. Ciana, A. Biserni, G. Lucignani, and A. Maggi, *Mol. Cell Endocrinol.*, 2006, **246**, 69–75.
4. R. Weissleder and U. Mahmood, *Radiology*, 2001, **219**, 316–33.
5. T. F. Massoud and S. S. Gambhir, *Gene. Dev.*, 2003, **17**, 545–80.
6. F. J. Heiligtag and M. Niederberger, *Mater. Today*, 2013, **16**, 262–271.
7. J. R. Lead and K. J. Wilkinson, *Environ. Chem.*, 2006, **3**, 159.
8. V. Wagner, A. Dullaart, A.-K. Bock, and A. Zweck, *Nat. Biotechnol.*, 2006, **24**, 1211–7.
9. K. Cho, X. Wang, S. Nie, Z. G. Chen, and D. M. Shin, *Clin. Cancer Res.*, 2008, **14**, 1310–6.
10. S. Parveen, R. Misra, and S. K. Sahoo, *Nanomed.*, 2012, **8**, 147–66.
11. L. Smith, Z. Kuncic, K. Ostrikov, and S. Kumar, *J. Nanomater.*, 2012, **2012**, 1–7.
12. C. Fang and M. Zhang, *J. Mater. Chem.*, 2009, **19**, 6258–6266.
13. J. F. Hainfeld, D. N. Slatkin, T. M. Focella, and H. M. Smilowitz, *Brit. J. Radiol.*, 2006, **79**, 248–53.
14. B. A. Kairdolf, A. M. Smith, T. H. Stokes, M. D. Wang, A. N. Young, and S. Nie, *Annu. Rev. Anal. Chem.*, 2013, **6**, 143–62.
15. S. Fokong, B. Theek, Z. Wu, P. Koczera, L. Appold, S. Jorge, U. Resch-Genger, M. van Zandvoort, G. Storm, F. Kiessling, and T. Lammers, *J. Control. Release*, 2012, **163**, 75–81.
16. G. Ting, C.-H. Chang, and H.-E. Wang, *Anticancer Res.*, 2009, **29**, 4107–4118.
17. W. S. Hinshaw, P. A. Bottomley, and G. N. Holland, *Nature*, 1977, **270**, 722–723.
18. M. A. Brown and R. C. Semelka, *MRI: Basic Principles and Applications*, John Wiley and Sons, 4th edn., 2010.
19. M. Bottrill, L. Kwok, and N. J. Long, *Chem. Soc. Rev.*, 2006, **35**, 557–571.
20. B. J. Pichler, A. Kolb, T. Nagele, and H.-P. Schlemmer, *J. Nucl. Med.*, 2010, **51**, 333–336.
21. P. Caravan, J. J. Ellison, T. J. McMurry, and R. B. Lauffer, *Chem. Rev.*, 1999, **99**, 2293–2352.
22. E. Toth and A. Merbach, Eds., *The Chemistry of Contrast Agents in Medical Magnetic Resonance Imaging*, Wiley, 2001.
23. A. D. Sherry, P. Caravan, and R. E. Lenkinski, *J. Magn. Reson. Imaging*, 2009, **30**, 1240–1248.
24. H. Ersoy and F. J. Rybicki, *J. Magn. Reson. Imaging*, 2007, **26**, 1190–1197.
25. W. J. Rogers, C. H. Meyer, and C. M. Kramer, *Nat. Clin. Pract. Card.*, 2006, **3**, 554–562.
26. Y.-X. Wang, S. Hussain, and G. Krestin, *Eur. Radiol.*, 2001, **11**, 2319–2331.
27. T. K. Jain, M. K. Reddy, M. A. Morales, D. L. Leslie-Pelecky, and V. Labhasetwar, *Mol. Pharm.*, 2008, **5**, 316–327.
28. H. Ai, C. Flask, B. Weinberg, X. T. Shuai, M. D. Pagel, D. Farrell, J. Duerk, and J. Gao, *Adv. Mater.*, 2005, **17**, 1949–1952.
29. S. Laurent, D. Forge, M. Port, A. Roch, C. Robic, L. Vander Elst, and R. N. Muller, *Chem. Rev.*, 2008, **108**, 2064–2110.
30. M. Rudin, *Molecular Imaging: Basic Principles And Applications In Biomedical Research*, Imperial College Press, 2005.
31. R. M. Cornell and U. Schwertmann, *The Iron Oxides: Structure, Properties, Reactions, Occurrences and Uses*, Wiley-VCH, Weinheim, 2nd ed., 2003.
32. A. S. Teja and P.-Y. Koh, *Prog. Cryst. Growth Ch.*, 2009, **55**, 22–45.

33. R. L. Rebodos and P. J. Vikesland, *Langmuir*, 2010, **26**, 16745–16753.
34. C. Boyer, M. R. Whittaker, V. Bulmus, J. Liu, and T. P. Davis, *NPG Asia Mater.*, 2010, **2**, 23–30.
35. D. Margulies, F. Parker, M. Rudee, F. Spada, J. Chapman, P. Aitchison, and A. Berkowitz, *Phys. Rev. Lett.*, 1997, **79**, 5162–5165.
36. D. Margulies, F. Parker, F. Spada, R. Goldman, J. Li, R. Sinclair, and A. Berkowitz, *Phys. Rev. B*, 1996, **53**, 9175–9187.
37. R. Frison, G. Cernuto, A. Cervellino, O. Zaharko, G. M. Colonna, A. Guagliardi, and N. Masciocchi, *Chem. Mater.*, 2013, **25**, 4820–4827.
38. J. Xie, G. Liu, H. S. Eden, H. Ai, and X. Chen, *Acc. Chem. Res.*, 2011, **44**, 883–892.
39. H. Bin Na, I. C. Song, and T. Hyeon, *Adv. Mater.*, 2009, **21**, 2133–2148.
40. V. I. Shubayev, T. R. Pisanic Ii, and S. Jin, *Adv. Drug Deliv. Rev.*, 2009, **61**, 467–477.
41. A. B. Chin and I. I. Yaacob, *J. Mater. Process. Tech.*, 2007, **191**, 235–237.
42. C. Albornoz and S. E. Jacobo, *J. Magn. Magn. Mater.*, 2006, **305**, 12–15.
43. J. Wan, X. Chen, Z. Wang, X. Yang, and Y. Qian, *J. Cryst. Growth*, 2005, **276**, 571–576.
44. I. Martínez-Mera, M. E. Espinosa-Pesqueira, R. Pérez-Hernández, and J. Arenas-Alatorre, *Mater. Lett.*, 2007, **61**, 4447–4451.
45. S. A. Morrison, C. L. Cahill, E. E. Carpenter, S. Calvin, and V. G. Harris, *J. Nanosci. Nanotechno.*, 2005, **5**, 1323–1344.
46. Y. Sun, M. Ma, Y. Zhang, and N. Gu, *Colloid Surf. A*, 2004, **245**, 15–19.
47. J. Qiu, R. Yang, M. Li, and N. Jiang, *Mater. Res. Bull.*, 2005, **40**, 1968–1975.
48. S.-J. Lee, J.-R. Jeong, S.-C. Shin, J.-C. Kim, and J.-D. Kim, *J. Magn. Magn. Mater.*, 2004, **282**, 147–150.
49. R. Boistelle and J. P. Astier, *J. Cryst. Growth*, 1988, **90**, 14–30.
50. T. Sugimoto, *Chem. Eng. Technol.*, 2003, **26**, 313–321.
51. H.-C. Schwarzer and W. Peukert, *Chem. Eng. Commun.*, 2004, **191**, 580–606.
52. N. M. Gribanov, E. E. Bibik, O. V Buzunov, and V. N. Naumov, *J. Magn. Magn. Mater.*, 1990, **85**, 7–10.
53. P. Tartaj, M. P. Morales, S. Veintemillas-Verdaguer, T. Gonzalez-Carreño, C. J. Serna, and K. H. J. Buschow, in *Handbook of Magnetic Materials*, Elsevier, 2006, vol. Volume 16, pp. 403–482.
54. W. Wu, Q. He, and C. Jiang, *Nanoscale Res. Lett.*, 2008, **3**, 397–415.
55. J. Gallo, N. J. Long, and E. O. Aboagye, *Chem. Soc. Rev.*, 2013, **42**, 7816–33.
56. Y. Sahoo, A. Goodarzi, M. T. Swihart, T. Y. Ohulchanskyy, N. Kaur, E. P. Furlani, and P. N. Prasad, *J. Phys. Chem. B*, 2005, **109**, 3879–3885.
57. K. G. Paul, T. B. Frigo, J. Y. Groman, and E. V Groman, *Bioconjugate Chem.*, 2004, **15**, 394–401.
58. A. Ulman, *Chem. Rev.*, 1996, **96**, 1533–1554.
59. Q. Liu, Z. Xu, J. A. Finch, and R. Egerton, *Chem. Mater.*, 1998, **10**, 3936–3940.
60. L. Meng Meng, K. Do Kyung, A. J. El Haj, and J. Dobson, *IEEE T. Nanobiosci.*, 2008, **7**, 298–305.
61. N. Kohler, C. Sun, A. Fichtenholtz, J. Gunn, C. Fang, and M. Zhang, *Small*, 2006, **2**, 785–792.
62. F. Herranz, M. P. Morales, A. G. Roca, R. Vilar, and J. Ruiz-Cabello, *Contrast Media Mol. I.*, 2008, **3**, 215–222.
63. K. Woo, J. Hong, and J.-P. Ahn, *J. Magn. Magn. Mater.*, 2005, **293**, 177–181.
64. G. A. van Ewijk, G. J. Vroege, and A. P. Philipse, *J. Magn. Magn. Mater.*, 1999, **201**, 31–33.
65. L. Wang, J. Luo, M. M. Maye, Q. Fan, Q. Rendeng, M. H. Engelhard, C. Wang, Y. Lin, and C.-J. Zhong, *J. Mater. Chem.*, 2005, **15**, 1821.
66. J. Gallo, I. García, D. Padro, B. Arnáiz, and S. Penadés, *J. Mater. Chem.*, 2010, **20**, 10010.

67. J. Lin, W. Zhou, A. Kumbhar, J. Wiemann, J. Fang, E. E. Carpenter, and C. J. O'Connor, *J. Solid State Chem.*, 2001, **159**, 26–31.
68. T. J. Daou, S. Begin-Colin, J. M. Grenèche, F. Thomas, A. Derory, P. Bernhardt, P. Legaré, and G. Pourroy, *Chem. Mater.*, 2007, **19**, 4494–4505.
69. T. J. Daou, J. M. Grenèche, G. Pourroy, S. Buathong, A. Derory, C. Ulhaq-Bouillet, B. Donnio, D. Guillon, and S. Begin-Colin, *Chem. Mater.*, 2008, **20**, 5869–5875.
70. T. J. Daou, G. Pourroy, J. M. Greneche, A. Bertin, D. Felder-Flesch, and S. Begin-Colin, *Dalton Trans.*, 2009, 4442–4449.
71. A. Hofmann, S. Thierbach, A. Semisch, A. Hartwig, M. Taupitz, E. Ruhl, and C. Graf, *J. Mater. Chem.*, 2010, **20**, 7842–7853.
72. R. Torres Martin de Rosales, R. Tavaré, A. Glaria, G. Varma, A. Protti, and P. J. Blower, *Bioconjugate Chem.*, 2011, **22**, 455–465.
73. L. Motte, F. Benyettou, C. de Beaucorps, M. Lecouvey, I. Milesovic, and Y. Lalatonne, *Faraday Discuss.*, 2011, **149**, 211–225.
74. D. Artemov, *J. Cell. Biochem.*, 2003, **90**, 518–24.
75. H.-J. Weinmann, W. Ebert, B. Misselwitz, and H. Schmitt-Willich, *Eur. J. Radiol.*, 2003, **46**, 33–44.
76. U. Schmiedl, M. Ogan, H. Paajanen, M. Marotti, L. E. Crooks, A. C. Brito, and R. C. Brasch, *Radiology*, 1987, **162**, 205–210.
77. Z. M. Bhujwalla, D. Artemov, K. Natarajan, E. Ackerstaff, and M. Solaiyappan, *Neoplasia*, 2001, **3**, 143–53.
78. J. W. M. Bulte and D. L. Kraitchman, *NMR Biomed.*, 2004, **17**, 484–99.
79. A. M. Morawski, G. A. Lanza, and S. A. Wickline, *Curr. Opin. Biotech.*, 2005, **16**, 89–92.
80. D. Artemov, N. Mori, R. Ravi, and Z. M. Bhujwalla, *Cancer Res.*, 2003, **63**, 2723–2727.
81. B. den Adel, L. M. van der Graaf, I. Que, G. J. Strijkers, C. W. Löwik, R. E. Poelmann, and L. van der Weerd, *Contrast Media Mol. I.*, 2012, **8**, 63–71.
82. M. Zhao, D. A. Beauregard, L. Loizou, B. Davletov, and K. M. Brindle, *Nat. Med.*, 2001, **7**, 1241–4.
83. A. L. Klibanov, *Invest. Radiol.*, 2006, **41**, 354–362.
84. J. K. Willmann, R. H. Kimura, N. Deshpande, A. M. Lutz, J. R. Cochran, and S. S. Gambhir, *J. Nucl. Med.*, 2010, **51**, 433–40.
85. R. J. Price, D. M. Skyba, S. Kaul, and T. C. Skalak, *Circulation*, 1998, **98**, 1264–1267.
86. J. Song, J. C. Chappell, M. Qi, E. J. VanGieson, S. Kaul, and R. J. Price, *J. Am. Coll. Cardiol.*, 2002, **39**, 726–731.
87. S. Achilefu, R. B. Dorshow, J. E. Bugaj, and R. Rajagopalan, *Invest. Radiol.*, 2000, **35**, 479–85.
88. J. E. Bugaj, S. Achilefu, R. B. Dorshow, and R. Rajagopalan, *J. Biomed. Opt.*, 2001, **6**, 122–33.
89. L. Frullano and T. Meade, *J. Biol. Inorg. Chem.*, 2007, **12**, 939–949.
90. M. Moseley and G. Donnan, *Stroke*, 2004, **35**, 2632–2634.
91. D. Townsend and S. Cherry, *Eur. Radiol.*, 2001, **11**, 1968–1974.
92. D. W. Townsend, *Phys. Med. Biol.*, 2008, **53**, R1.
93. J. Culver, W. Akers, and S. Achilefu, *J. Nucl. Med.*, 2008, **49**, 169–172.
94. B. Hasegawa, H. R. Tang, A. J. Da Silva, K. H. Wong, K. Iwata, and M. C. Wu, *Nucl. Instrum. Meth. A*, 2001, **471**, 140–144.
95. A. Louie, *Chem. Rev.*, 2010, **110**, 3146–3195.
96. S. R. Cherry, A. Y. Louie, and R. E. Jacobs, *P. IEEE*, 2008, **96**, 416–438.

97. A. Mishra, J. Pfeuffer, R. Mishra, J. Engelmann, A. K. Mishra, K. Ugurbil, and N. K. Logothetis, *Bioconjugate Chem.*, 2006, **17**, 773–780.
98. M. M. Hüber, A. B. Staubli, K. Kustedjo, M. H. B. Gray, J. Shih, S. E. Fraser, R. E. Jacobs, and T. J. Meade, *Bioconjugate Chem.*, 1998, **9**, 242–249.
99. D. Gerion, J. Herberg, R. Bok, E. Gjersing, E. Ramon, R. Maxwell, J. Kurhanewicz, T. F. Budinger, J. W. Gray, M. A. Shuman, and F. F. Chen, *J. Phys. Chem. C*, 2007, **111**, 12542–12551.
100. S. S. Banerjee and D.-H. Chen, *Nanotechnology*, 2009, **20**, 185103.
101. J. J. Gallagher, R. Tekoriute, J.-A. O'Reilly, C. Kerskens, Y. K. Gun'ko, and M. Lynch, *J. Mater. Chem.*, 2009, **19**, 4081.
102. N. Hirata, K. Tanabe, A. Narita, K. Tanaka, K. Naka, Y. Chujo, and S. Nishimoto, *Bioorgan. Med. Chem.*, 2009, **17**, 3775–81.
103. C.-M. Cheng, P.-Y. Chu, K.-H. Chuang, S. R. Roffler, C.-H. Kao, W.-L. Tseng, J. Shiea, W.-D. Chang, Y.-C. Su, B.-M. Chen, Y.-M. Wang, and T.-L. Cheng, *Cancer Gene Ther.*, 2009, **16**, 83–90.
104. M. J. Pittet, F. K. Swirski, F. Reynolds, L. Josephson, and R. Weissleder, *Nat. Protoc.*, 2006, **1**, 73–9.
105. M. F. Kircher, U. Mahmood, R. S. King, R. Weissleder, and L. Josephson, *Cancer Res.*, 2003, **63**, 8122–8125.
106. L. Josephson, M. F. Kircher, U. Mahmood, Y. Tang, and R. Weissleder, *Bioconjugate Chem.*, 2002, **13**, 554–560.
107. A. T. Heitsch, D. K. Smith, R. E. Patel, D. Ress, and B. A. Korgel, *J. Solid State Chem.*, 2008, **181**, 1590–1599.
108. Z. Ma, D. Dosev, M. Nichkova, R. K. Dumas, S. J. Gee, B. D. Hammock, K. Liu, and I. M. Kennedy, *J. Magn. Magn. Mater.*, 2009, **321**, 1368–1371.
109. V. Salgueiriño-Maceira, M. A. Correa-Duarte, M. A. López-Quintela, and J. Rivas, *J. Nanosci. Nanotechno.*, 2009, **9**, 3684–3688.
110. S. T. Selvan, P. K. Patra, C. Y. Ang, and J. Y. Ying, *Angew. Chem. Int. Ed.*, 2007, **46**, 2448–52.
111. H. He, M. Y. Xie, Y. Ding, and X. F. Yu, *Appl. Surf. Sci.*, 2009, **255**, 4623–4626.
112. Z. Y. Ma, D. Dosev, M. Nichkova, S. J. Gee, B. D. Hammock, and I. M. Kennedy, *J. Mater. Chem.*, 2009, **19**, 4695–4700.
113. J. S. Fowler and A. P. Wolf, *Acc. Chem. Res.*, 1997, **30**, 181–188.
114. M. E. Phelps, *P. Natl. Acad. Sci. USA*, 2000, **97**, 9226–9233.
115. P. W. Miller, N. J. Long, R. Vilar, and A. D. Gee, *Angew. Chem. Int. Ed.*, 2008, **47**, 8998–9033.
116. D. Patel, A. Kell, B. Simard, B. Xiang, H. Y. Lin, and G. Tian, *Biomaterials*, 2011, **32**, 1167–76.
117. C. J. Anderson and R. Ferdani, *Cancer Biother. Radio.*, 2009, **24**, 379–93.
118. C. Glaus, R. Rossin, M. J. Welch, and G. Bao, *Bioconjugate Chem.*, 2010, **21**, 715–722.
119. H.-Y. Lee, Z. Li, K. Chen, A. R. Hsu, C. Xu, J. Xie, S. Sun, and X. Chen, *J. Nucl. Med.*, 2008, **49**, 1371–9.
120. M. Nahrendorf, H. Zhang, S. Hembrador, P. Panizzi, D. E. Sosnovik, E. Aikawa, P. Libby, F. K. Swirski, and R. Weissleder, *Circulation*, 2008, **117**, 379–87.
121. Z.-B. Li, K. Chen, and X. Chen, *Eur. J. Nucl. Med. Mol. I.*, 2008, **35**, 1100–1108.
122. K. W. Kang, *Open Nucl. Med. J.*, 2010, **2**, 153–156.

123. L. Stelter, J. Pinkernelle, R. Michel, R. Schwartländer, N. Raschzok, M. Morgul, M. Koch, T. Denecke, J. Ruf, H. Bäumler, A. Jordan, B. Hamm, I. Sauer, and U. Teichgräber, *Mol. Imaging Biol.*, 2010, **12**, 25–34.
124. V. Kubíček, J. Havlíčková, J. Kotek, G. Tircsó, P. Hermann, E. Tóth, and I. Lukeš, *Inorg. Chem.*, 2010, **49**, 10960–10969.
125. E. T. Clarke and A. E. Martell, *Inorg. Chim. Acta*, 1991, **181**, 273–280.
126. J. R. McCarthy and R. Weissleder, *Adv. Drug Deliv. Rev.*, 2008, **60**, 1241–51.
127. M. Liong, J. Lu, M. Kovochich, T. Xia, S. G. Ruehm, A. E. Nel, F. Tamanoi, and J. I. Zink, *ACS Nano*, 2008, **2**, 889–96.
128. S. J. Shin, J. R. Beech, and K. A. Kelly, *Integr. Biol.*, 2013, **5**, 29–42.
129. H.-K. Yip, C.-J. Wu, H.-W. Chang, C.-H. Yang, K.-H. Yeh, S. Chua, and M. Fu, *Chest*, 2004, **126**, 1417–1422.
130. P. Libby, P. M. Ridker, and G. K. Hansson, *Nature*, 2011, **473**, 317–25.
131. J. Shepherd, S. M. Cobbe, I. Ford, C. G. Isles, A. R. Lorimer, P. W. Macfarlane, J. H. McKillop, and C. J. Packard, *New Engl. J. Med.*, 1995, **333**, 1301–1308.
132. T. Saam, T. S. Hatsukami, N. Takaya, B. Chu, H. Underhill, W. S. Kerwin, J. Cai, M. S. Ferguson, and C. Yuan, *Radiology*, 2007, **244**, 64–77.
133. R. A. Vogel, *Clin. Cardiol.*, 1997, **20**, 426–432.
134. R. Ross, *New Engl. J. Med.*, 1999, **340**, 115–126.
135. R. Ross and J. A. Glomset, *New Engl. J. Med.*, 1976, **295**, 369–377.
136. R. Ross and J. A. Glomset, *Science*, 1973, **180**, 1332–1339.
137. R. Ross, *Nature*, 1993, **362**, 801–9.
138. R. Ross, *New Engl. J. Med.*, 1986, **314**, 488–500.
139. D. Vancraeynest, A. Pasquet, V. Roelants, B. L. Gerber, and J.-L. J. Vanoverschelde, *J. Am. Coll. Cardiol.*, 2011, **57**, 1961–79.
140. G. N. Levine, J. F. Keaney, and J. A. Vita, *New Engl. J. Med.*, 1995, **332**, 512–21.
141. S. P. Glasser, A. P. Selwyn, and P. Ganz, *Am. Hear. J.*, 1996, **131**, 379–84.
142. D. Steinberg, S. Parthasarathy, T. E. Carew, J. C. Khoo, and J. L. Witztum, *New Engl. J. Med.*, 1989, **320**, 915–24.
143. G. K. Hansson, *New Engl. J. Med.*, 2005, **352**, 1685–1695.
144. L. Jonasson, J. Holm, O. Skalli, G. Bondjers, and G. K. Hansson, *Arter. Thromb. Vas.*, 1986, **6**, 131–138.
145. A. C. van der Wal, P. K. Das, D. Bentz van de Berg, C. M. van der Loos, and A. E. Becker, *Lab. Invest.*, 1989, **61**, 166–70.
146. S. Glagov, E. Weisenberg, C. K. Zarins, R. Stankunavicius, and G. J. Kolettis, *New Engl. J. Med.*, 1987, **316**, 1371–1375.
147. T. D. Littlewood and M. R. Bennett, *Curr. Opin. Lipidol.*, 2003, **14**, 469–75.
148. E. Falk, *J. Am. Coll. Cardiol.*, 2006, **47**, C7–12.
149. C. B. Jones, D. C. Sane, and D. M. Herrington, *Cardiovasc. Res.*, 2003, **59**, 812–23.
150. P. R. Moreno, E. Falk, I. F. Palacios, J. B. Newell, V. Fuster, and J. T. Fallon, *Circulation*, 1994, **90**, 775–778.
151. A. C. van der Wal, A. E. Becker, C. M. van der Loos, and P. K. Das, *Circulation*, 1994, **89**, 36–44.
152. R. J. Myerburg, A. Interian, R. M. Mitrani, K. M. Kessler, and A. Castellanos, *Am. J. Cardiol.*, 1997, **80**, 10F–19F.
153. D. P. Zipes and H. J. J. Wellens, *Circulation*, 1998, **98**, 2334–2351.

154. A. P. Burke, A. Farb, G. T. Malcom, Y. Liang, J. Smialek, and R. Virmani, *New Engl. J. Med.*, 1997, **336**, 1276–1282.
155. F. D. Kolodgie, A. Petrov, R. Virmani, N. Narula, J. W. Verjans, D. K. Weber, D. Hartung, N. Steinmetz, J. L. Vanderheyden, M. A. Vannan, H. K. Gold, C. P. M. Reutelingsperger, L. Hofstra, and J. Narula, *Circulation*, 2003, **108**, 3134–9.
156. S. Isobe, S. Tsimikas, J. Zhou, S. Fujimoto, M. Sarai, M. J. Branks, A. Fujimoto, L. Hofstra, C. P. Reutelingsperger, T. Murohara, R. Virmani, F. D. Kolodgie, N. Narula, A. Petrov, and J. Narula, *J. Nucl. Med.*, 2006, **47**, 1497–1505.
157. L. Hofstra, I. H. Liem, E. A. Dumont, H. H. Boersma, W. L. van Heerde, P. A. Doevendans, E. DeMuinck, H. Wellens, G. J. Kemerink, C. P. Reutelingsperger, and G. A. Heidendal, *Lancet*, 2000, **356**, 209–212.
158. J. M. Rosen, S. P. Butler, G. E. Meinken, T. S. T. Wang, R. Ramakrishnan, S. C. Srivastava, P. O. Alderson, and H. N. Ginsberg, *J. Nucl. Med.*, 1990, **31**, 343–350.
159. A. M. Lees, R. S. Lees, F. J. Schoen, J. L. Isaacsohn, A. J. Fischman, K. A. McKusick, and H. W. Strauss, *Arter. Thromb. Vas.*, 1988, **8**, 461–470.
160. S. Vallabhajosula, M. Paidi, J. J. Badimon, N.-A. Le, S. J. Goldsmith, V. Fuster, and H. N. Ginsberg, *J. Nucl. Med.*, 1988, **29**, 1237–1245.
161. M. F. Kircher, J. Grimm, F. K. Swirski, P. Libby, R. E. Gerszten, J. R. Allport, and R. Weissleder, *Circulation*, 2008, **117**, 388–95.
162. S. Ishino, T. Mukai, Y. Kuge, N. Kume, M. Ogawa, N. Takai, J. Kamihashi, M. Shiomi, M. Minami, T. Kita, and H. Saji, *J. Nucl. Med.*, 2008, **49**, 1677–85.
163. D. Li, A. R. Patel, A. L. Klibanov, C. M. Kramer, M. Ruiz, B.-Y. Kang, J. L. Mehta, G. A. Beller, D. K. Glover, and C. H. Meyer, *Circulation*, 2010, **3**, 464–72.
164. J. H. F. Rudd, *Circulation*, 2002, **105**, 2708–2711.
165. T. Saam, T. S. Hatsukami, H. Underhill, W. S. Kerwin, and M. S. Ferguson, 2007, **244**.
166. S. G. Ruehm, C. Corot, P. Vogt, S. Kolb, and J. F. Debatin, *Circulation*, 2001, **103**, 415–422.
167. S. A. Schmitz, M. Taupitz, S. Wagner, K. J. Wolf, D. Beyersdorff, and B. Hamm, *J. Magn. Reson. Imaging*, 2001, **14**, 355–61.
168. S. A. Schmitz, S. E. Coupland, R. Gust, S. Winterhalter, S. Wagner, M. Kresse, W. Semmler, and K. J. Wolf, *Invest. Radiol.*, 2000, **35**, 460–471.
169. S. A. Schmitz, M. Taupitz, S. Wagner, S. E. Coupland, R. Gust, A. Nikolova, and K. J. Wolf, *Invest. Radiol.*, 2002, **37**, 405–411.
170. M. E. Kooi, V. C. Cappendijk, K. B. J. M. Cleutjens, A. G. H. Kessels, P. J. E. H. M. Kitslaar, M. Borgers, P. M. Frederik, M. J. A. P. Daemen, and J. M. A. van Engelshoven, *Circulation*, 2003, **107**, 2453–8.
171. S. A. Wickline, A. M. Neubauer, P. M. Winter, S. D. Caruthers, and G. M. Lanza, *J. Magn. Reson. Imaging*, 2007, **25**, 667–80.
172. R. Weissleder, M. Nahrendorf, and M. J. Pittet, *Nat. Mater.*, 2014, **13**, 125–38.

CHAPTER 2

Magnetic nanoparticle preparation and ligand exchanges

2 Magnetic nanoparticle preparation and ligand exchanges

2.1 Introduction

This chapter discusses the various methods of iron oxide nanoparticle synthesis and their characterisation. As previously mentioned in Chapter 1, there are multiple ways to synthesise iron oxide nanoparticles. Several methods were attempted to synthesise the core nanoparticles to determine the method that best produces nanoparticles with a narrow polydispersity, and high crystallinity. The bulk nanoparticles synthesised here were via the high temperature thermal decomposition of an iron precursor, and are not soluble in polar solvents, so exchanging the initial coating for a different ligand which will allow the resultant nanoparticles to be resuspended in water, or DMSO/ethanol/methanol (which can be diluted with water) would be most ideal. The ligands chosen for exchange were based on functional groups that have been shown to have a strong affinity for the nanoparticle surface. Carboxylate anchors (the most commonly used chemical group) were not compared as there are already plentiful examples in the literature.[1] Furthermore, as the bulk core nanoparticles are synthesised with oleic acid which has a carboxylate unit as the anchor, it was thought best to replace the oleic acid with a ligand that has a stronger binding affinity for the nanoparticle surface, instead of replacing a carboxylate for another carboxylate. Phosphates and bisphosphonates[2,3] were then the first choice as nanoparticle coating groups. Another type of functional group, sulfonates, was also investigated as an anchor for ligands to cap the nanoparticles. Only a few examples in the literature utilise sulfonates as capping ligands for iron oxide nanoparticles, especially for small molecules containing the sulfonate group. One example of such a ligand system is described by Portet *et al*.[4] However, the resultant nanoparticles were not stable in water for very long.

Within this chapter, the different methods explored to synthesise the core nanoparticles will be described, alongside an explanation of the results of the ligands exchanges carried out.

2.2 Synthesis of bulk core iron oxide nanoparticles

As previously discussed in the introduction chapter, there are many literature preparations of iron oxide nanoparticles. Co-precipitation of iron salts in a basic medium is the most common method of nanoparticle preparation in the literature, and was one of the methods attempted here. Other methods of syntheses attempted were the hydrothermal synthesis method and the high temperature thermal decomposition of iron salts. Several methods were attempted in order to

determine which method was most favourable and which produced nanoparticles with a narrow size distribution and high crystallinity.

2.2.1 Hydrothermal syntheses

The first method to be attempted was the hydrothermal method of synthesis.[5,6] This is usually carried out by heating an iron salt at a relatively high temperature and pressure in a Parr reactor. Two protocols were attempted using two different iron salts, with one having a citric acid coating to stabilise the nanoparticles, and another using n-decylamine (**Scheme 2.1**).

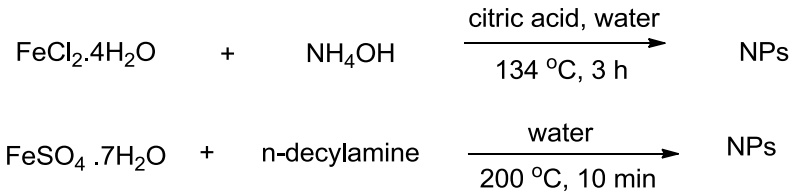

Scheme 2.1 The hydrothermal synthesis of iron oxide nanoparticles via iron salts such as $FeCl_2$ and $FeSO_4$.

The citrate-coated nanoparticles has a better appearance in solution compared to the decylamine stabilised nanoparticles and were therefore imaged by transmission electron microscopy (TEM). As seen in **Figure 2.1**, the citrate-coated nanoparticles are unfortunately highly aggregated, with the organic ligand coating forming a layer around several nanoparticle cores. Therefore the hydrothermal method of synthesis proved difficult to obtain reproducible nanoparticles with the desired characteristics.

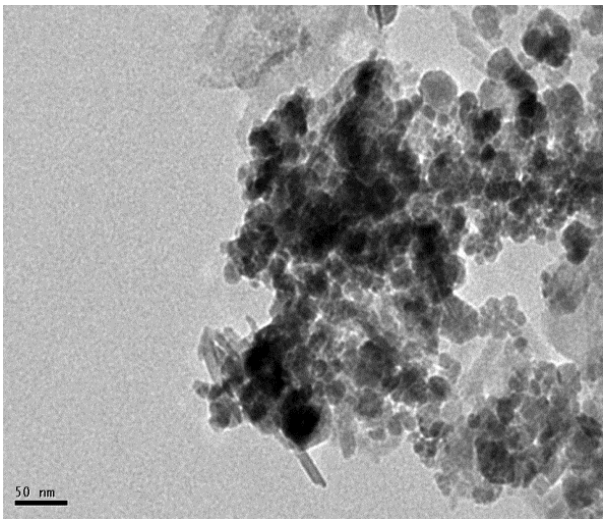

Figure 2.1 TEM image of highly aggregated citrate coated NP from the hydrothermal reaction of $FeCl_2$.

2.2.2 Co-precipitation of iron salts

The co-precipitation method involves combining a mixture of aqueous Fe^{2+}/Fe^{3+} salts in the presence of a base such as NH_4OH at either room temperature or slightly elevated temperature. This method is advantageous as it allows for large-scale production of iron oxide nanoparticles, up to 40 g.[7] Between pH 8 and 14, and at a stoichiometric ratio of 2:1 (Fe^{3+}/Fe^{2+}) in a non-oxidising environment, the thermodynamics of the reaction indicates that complete precipitation of Fe_3O_4 (magnetite) should occur (**Scheme 2.2**). [1]

$$Fe^{2+} + 2Fe^{3+} + 8OH^- \longrightarrow Fe_3O_4 + 4H_2O$$

Scheme 2.2 Reaction scheme for the co-precipitation of iron to form Fe_3O_4.

Fe_3O_4 however, is not very stable and is sensitive to oxidation, transforming into γ-Fe_2O_3 (maghemite) in the presence of oxygen. This can be prevented by protecting the surface of the nanoparticle through the addition of a capping ligand (such as citrate, or polymers such as dextran or polyvinyl alcohol).

In this work, a literature co-precipitation method was attempted.[8] $FeCl_2$ and $FeCl_3$ were stirred together in degassed deionised water under nitrogen. Under mild heating, aqueous ammonia was added and the nanoparticles precipitated immediately. The nanoparticles were isolated by a magnet and resuspended in ethanol. Citric acid was also added in another attempt but this gave the same results as the bare nanoparticles. The bare and citrate coated nanoparticles were both a cloudy suspension. TEM images of the nanoparticles (**Figure 2.2**) show that the shape of the particles are not consistently spherical, and form aggregates. This was as expected as the nanoparticles in solution were not homogenous.

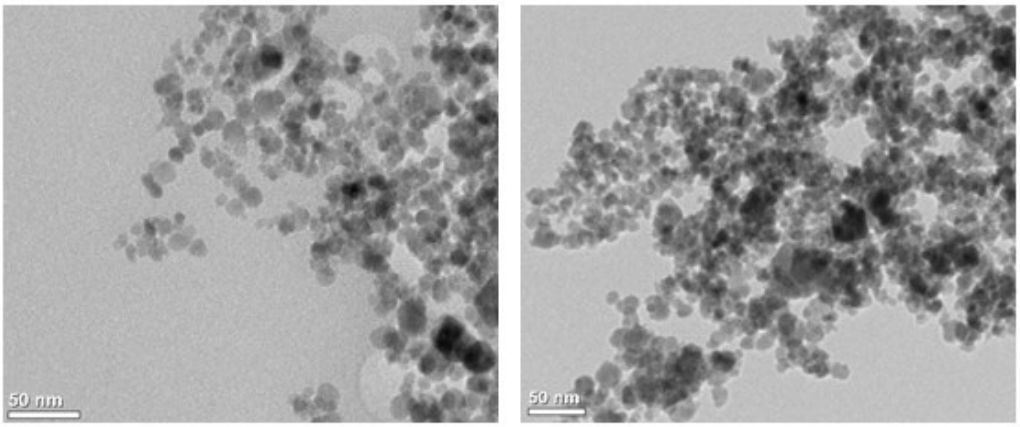

Figure 2.2 TEM images of iron oxide nanoparticles obtained via the co-precipitation of iron salts. The particles were highly aggregated, and were inconsistent in shape.

2.2.3 Silica shell coated iron oxide core

Silica is one of the preferred inorganic coatings for iron oxide nanoparticles as it has a high biostability, low toxicity, and the exposed silanol groups on the surface would allow for further versatile functionalisation, for example with amine groups.[9] It was hoped that the availability of amine groups would then allow for straightforward chemistry for building a water-soluble surface, especially through the use of peptide coupling reactions with carboxylic acids to form stable amide bonds. There are several protocols in the literature to produce a silica shell coated iron oxide nanoparticle.[8,10]

Typical methods for synthesising a core-shell iron oxide-silica nanoparticle usually involve the synthesis of the magnetic core, followed by layering on a surface of silica. The silica shell is usually deposited via either the Stöber method or a microemulsion process.[11–15] The Stöber method has primarily been used for the preparation of silica nanoparticles and involves stirring a solution of tetraethyl orthosilicate in water, and a low M_W alcohol such as ethanol, and ammonia. Varying the type of alcohol and the reaction volumes will produce silica particles of varying sizes. In the case of silica nanoparticle synthesis, the Stöber method produces particles with a less than ideal size distribution. When this process is applied to the formation of silica shells in core-shell systems, it usually results in a multi-core assembly with a non-uniform thickness of the silica surrounding several cores.[13] An alternative to the Stöber method that has had success in the literature is an inverse microemulsion or water-in-oil microemulsion system.[16–19] These systems employ a surfactant to lower the interfacial tension between the water component and the oil component, resulting in the formation of a stable single-phase system.[20] Like the Stöber method, the microemulsion system has also been used to form core-shell iron oxide-silica nanoparticles.[21–23] As with the silica nanoparticles, when the microemulsion method is used to produce the core-shell nanoparticles, it results in multi-cored nanoparticles which increases the overall size and hence reduces the stability of the particles in solution.[22]

A literature preparation of a core-shell iron oxide-silica nanoparticle which aimed to eliminate the multi-core problem was attempted.[10] The iron oxide nanoparticles were synthesised via the co-precipitation method above and used immediately after for the deposition of the silica shell. The silica coating appeared to have been successful as two distinct structures were observed in the TEM image (**Figure 2.3**, below). However, the nanoparticles were in a multicore assembly with the silica shell surrounding several cores. This was repeated several times with the same results each time. The synthesis of single core-shell systems may be more complicated than suggested by literature and therefore this route was not carried forward.

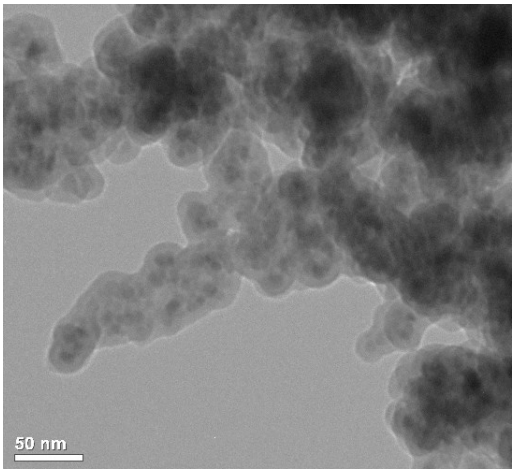

Figure 2.3 TEM image of the silica-coated iron oxide nanoparticles. The darker spots are the iron oxide nanoparticles and the lighter areas surrounding the nanoparticles are the silica shell.

2.2.4 High temperature thermal decomposition

Nanoparticle preparation via the high temperature thermal decomposition of iron (**Scheme 2.2**) gives a very narrow size dispersion and high crystallinity, both of which are important for a good contrast agent with high relaxivity properties.[24] The protocol followed was one from literature and was chosen due to the simplicity and convenience of carrying out the reaction in an organic solution whilst being able to tune the size of the nanoparticles with ease, simply by varying the reaction conditions or by seed-mediated growth.[24]

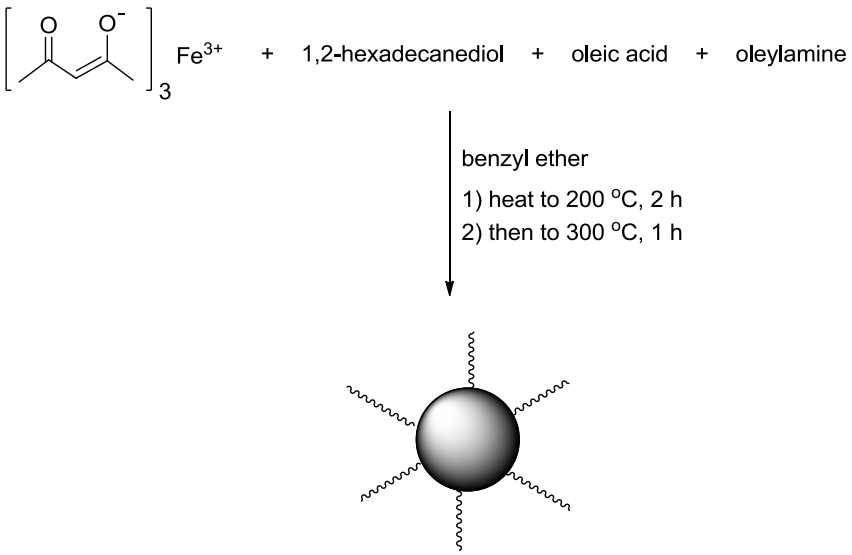

Scheme 2.2 Scheme showing the synthesis of iron oxide nanoparticles via the high temperature decomposition of $Fe(acac)_3$.

The synthesis of 6 nm nanoparticles involved heating the reaction mixture to 200 °C for 2 hours, then at 300 °C for 1 hour. Over this time, the mixture turned black suggesting the formation of nanoparticles. Once cooled, addition of ethanol precipitated the nanoparticles. Isolation by centrifugation or by a magnet, resulted in a black pellet which could be resuspended in a non-polar solvent. The nanoparticles were washed by repeated addition of methanol, ethanol and acetone to precipitate the particles out of a solution in hexane followed by centrifugation or magnetic sorting. Final addition of hexane resuspended the nanoparticles for storage in the freezer.

Characterisation of the oleic acid-capped nanoparticles was by TEM, infrared spectroscopy (IR), X-ray diffraction (XRD), and superconducting quantum interference device (SQUID). Analytical data for XRD and magnetic measurements (SQUID) were obtained with assistance from PDRAs in the Long group, Nazila Kamaly and Juan Gallo.

The IR spectrum was obtained neat on an attenuated total reflectance (ATR) plate. The spectrum confirmed the presence of the oleic acid ligands on the surface of the nanoparticles through the C=O stretches which appear around 1500 cm^{-1} (**Figure 2.4**). This stretch indicates that the carboxylic groups are bound to the nanoparticle surface as the infrared stretch has shifted slightly from that of free carboxylic acids (1700 cm^{-1}).

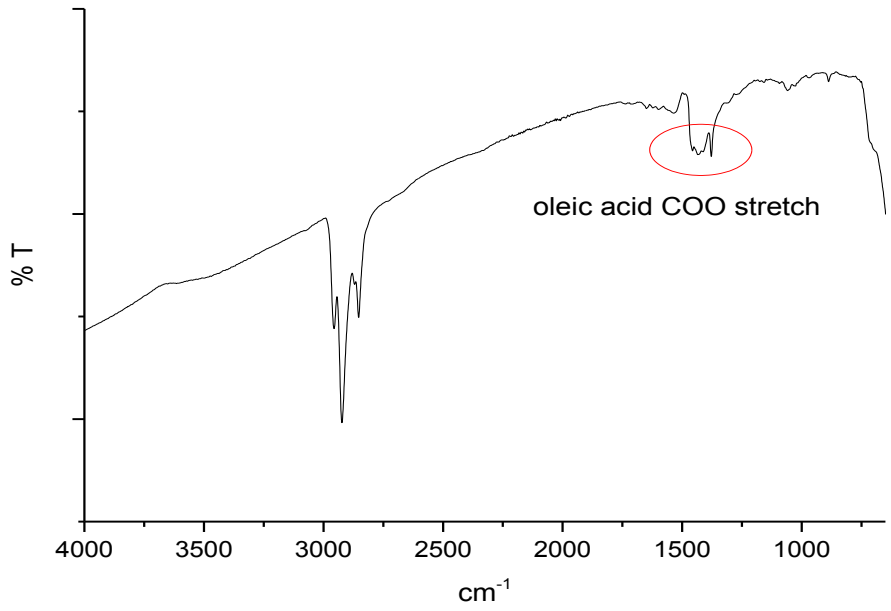

Figure 2.4 Infrared spectrum of bulk oleic acid coated iron oxide nanoparticles (neat, ATR plate).

TEM micrographs (**Figure 2.5 A, B**) showed a narrow distribution of spherical NPs, with the average size of approximately 6.1 nm (based on 500 measurements, **Figure 2.5 E**). Using TEM, a selected area electron diffraction (SAED) pattern was obtained and the composition of magnetite was confirmed based on measured lattice spacings from the rings in the diffraction pattern, which compared to known lattice spacings for bulk Fe_3O_4 along with their respective hkl indexes (**Figure 2.5 C**). XRD obtained on solid Fe_3O_4 NPs shows several peaks corresponding to the interplanar spacings 111, 220, 311, 400, 511 and 400 comparable to standard peaks (JCPDS, 01-075-0449, Inorganic Crystal Structure Database), confirming the correct reflection peaks for the inverse cubic spinel Fe_3O_4 structure (**Figure 2.5 D**). In addition, energy-dispersive X-ray spectroscopy (EDXS) of a sample of the nanoparticles confirmed the presence of iron (**Figure 2.5 F**).

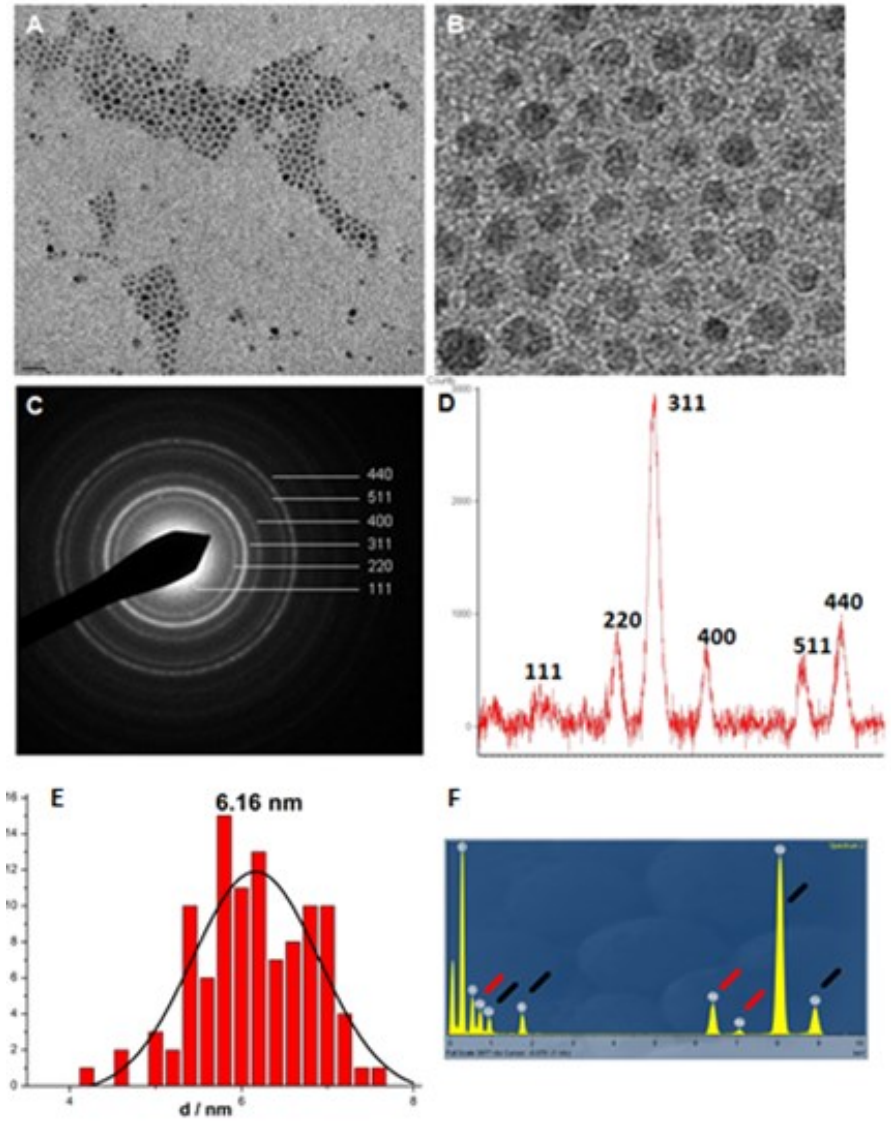

Figure 2.5 A: TEM micrograph of as-prepared Fe_3O_4 nanoparticles (oleic acid capped) (scale bar = 20 nm); **B**: enlarged area from A; **C**: SAED showing lattice ring patterns; **D**: XRD diffractogram with indexed peak positions and relative intensities; **E:** Size distribution diagram of as prepared Fe_3O_4 nanoparticles; **F**: EDXS spectra of a sample of Fe_3O_4 nanoparticles. Red lines indicate Fe peaks; black lines show Cu and Si peaks coming from the sample holder.

The magnetic properties of the sample were measured by superconducting quantum interference device (SQUID). The normalised saturation (M_s) magnetisation for the Fe_3O_4 NPs was measured to be 68 emu/g (**Figure 2.6**) which is comparable to similar sized IONPs (30-60 emu/g).[25,26] Zerofield cooled (ZFC) and field cooled (FC) magnetisation data measured with a field of 100 Oe in the temperature range 0-400 K were obtained (**Figure 2.6**). In the ZFC measurement, with increasing temperature more particles re-orientate their magnetisation with the external field and the total magnetisation increases. This reaches a maximum at the blocking temperature (T_b) of 34 K, indicating magnetic interactions between the NPs are present (**Figure 2.6**). These results show that the synthesised IONPs exhibit superparamagnetic behaviour at room temperature with no hysteresis.

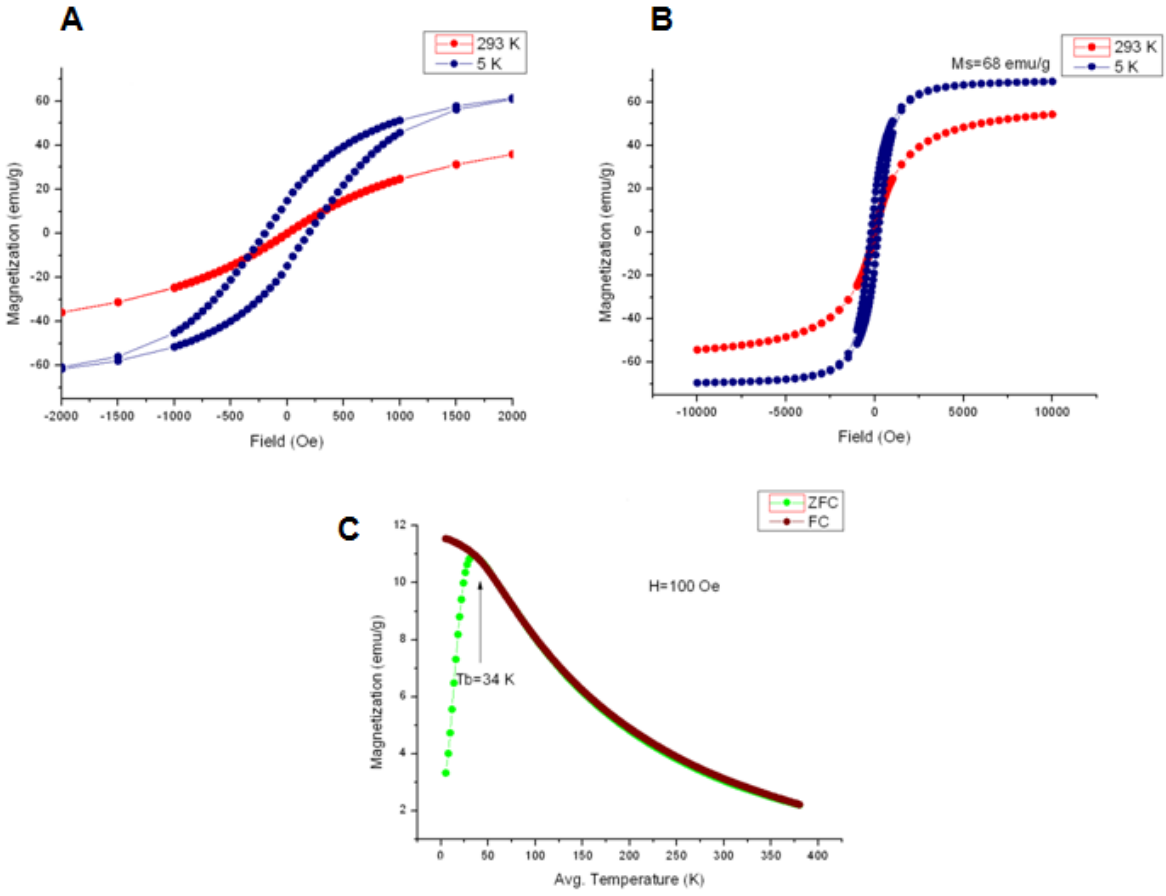

Figure 2.6 Magnetic measurements of Fe_3O_4 nanoparticles. **A and B,** room (red) and low temperature (5 K) (blue) magnetisation hysteresis. **C**, zero field cooled (ZFC) and field cooled (FC) magnetization measurements of the same sample.

2.2.5 Conclusion

The nanoparticles synthesised via the high temperature thermal decomposition of iron acetylacetonate produced particles with a good size distribution, well-controlled sizes, and

nanoparticles with a high crystallinity. This is highly advantageous over the other above mentioned methods of nanoparticle preparation (hydrothermal and co-precipitation). The nanoparticles synthesised by co-precipitation were highly aggregated which is undesirable. A disadvantage of the thermal decomposition method is that the nanoparticles are only soluble in apolar solvents thus requiring a ligand exchange step to further functionalise the nanoparticles. Nevertheless, the quality of the nanoparticles synthesised via thermal decomposition outweighs this added synthetic step and therefore all the bulk core nanoparticles synthesised for further functionalisation were synthesised via the high temperature thermal decomposition method.

2.3 Ligand exchange with small molecules

Naked iron oxide nanoparticles form agglomerates due to the lack of stabilising surface ligands. It is therefore essential to coat the nanoparticles with capping agents such as small molecules, polymers, or inorganic shells such as gold and silica. As previously described in chapter 1 (introduction), there are various capping agents already used in the literature.[1] In the previous section, work on the synthesis of silica shell coated iron oxide nanoparticles was attempted but this was not trivial for forming single core-shell systems. It was determined that the best method to synthesise the bulk core nanoparticles was via the high temperature thermal decomposition method and these particles are only soluble in non-polar solvents. In order to disperse the nanoparticles in polar solvents, it is necessary to replace the oleic acid/oleylamine coating. During the course of this PhD, the focus was primarily on small molecules such as phosphates, bisphosphonates and sulfonates, as these groups have been shown to have a stronger affinity for the nanoparticle surface than carboxylates.[1–3] Several bisphosphonate ligands were investigated, and as a comparison, a phosphate ligand was synthesised based on previous work within the group. As an alternative, sulfonate-type ligands were investigated as capping ligands for the nanoparticles. Sulfonates are rarely mentioned as anchoring units in the literature and this will be discussed below.

2.3.1 Sulfonates

Sulfonates have not been widely used as an anchoring group for capping ligands on nanoparticles and few examples exist in the literature. This could be because there are not many small molecule sulfonate ligands commercially and readily available, and it has not yet been shown to be as good an anchor as carboxylates and phosphates. One example in the literature where a sulfonate has been

incorporated with nanoparticles is a poly(sodium-4-styrene)sulfonate-iron oxide nanocomposite (**Figure 2.7**).[27] This magnetic suspension has been shown to have tunable low-field relaxivities, and was synthesised in a one-step co-precipitation procedure.

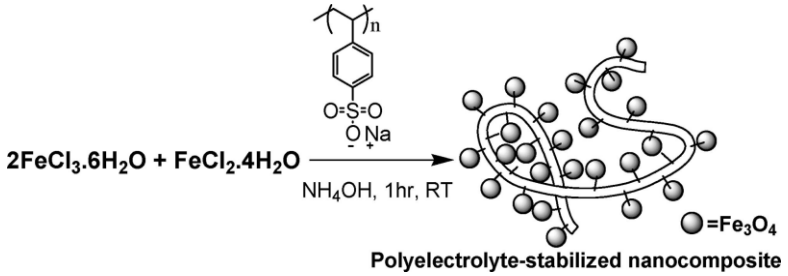

Figure 2.7 One-step synthesis of poly(sodium-4-styrene)sulfonate-iron oxide nanocomposite. Image from ref [27].

In another example, dodecylsulfonate, a surfactant, has also been shown to stabilise iron oxide nanoparticles.[28] Rafailovich *et al* have synthesised in one-step via sonolysis of the iron precursor and the surfactant. The infrared spectra confirmed the bonding of the sulfonic acid groups to the nanoparticle surfaces by ionic bonding, which was possible due to the direct reaction of the surfactant with the iron precursor. One example of a small molecule sulfonate ligand coating nanoparticles via ligand exchange is by Portet *et al* where he used a disulfonic acid.[4] Sulfonate 3 (**Figure 2.8**, **S3**) was the disulfonic acid Portet used and he found that the resultant nanoparticle was stable for greater than 4 weeks.[4] This was the starting point for the sulfonate ligands chosen to be investigated. The other sulfonates were chosen to have the same core naphthalene, but with some modifications. One modification was to compare a monosulfonic acid with the disulfonic acid, in order to determine if two sulfonate groups improve the stability compared to having just one sulfonate (**Figure 2.8**, **S4**). The other was to have only the amine group, with no extra hydroxyl group in the molecule (**Figure 2.8**, **S2**). After the ligand exchange, NP-sulfonate 1 is given the notation **NP-S1**, NP-sulfonate 2 as **NP-S2** and so forth.

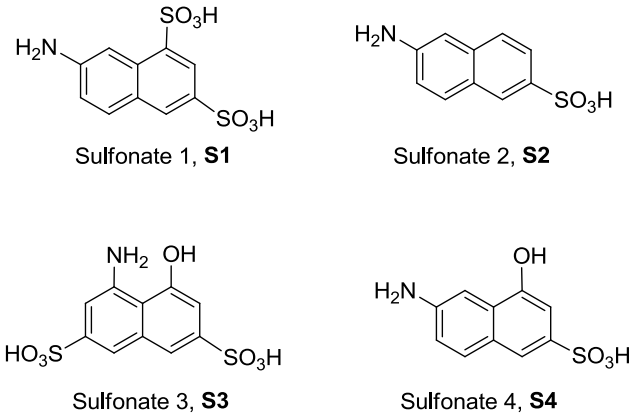

Figure 2.8 Structures of the sulfonate ligands which were used to coat the nanoparticles.

a) Ligand exchange with sulfonates

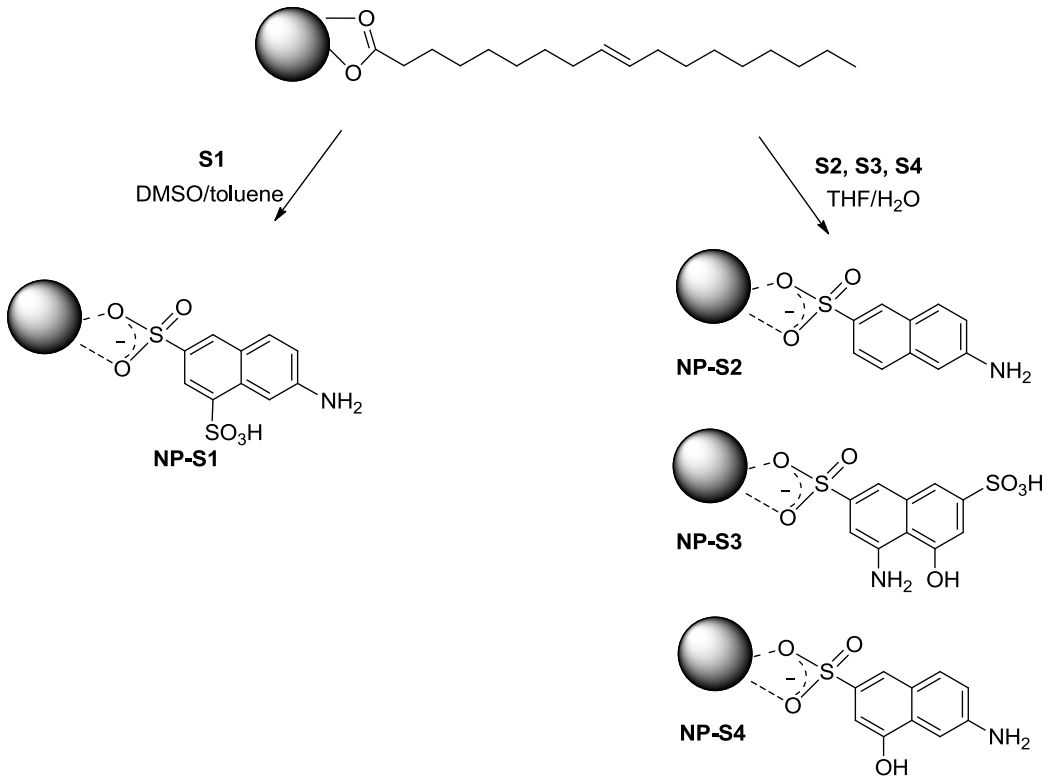

Scheme 2.3 Ligand exchanges of bulk nanoparticles with sulfonate ligands (**S1 to S4**) to give **NPS1 – NPS4**.

The ligand exchanges were carried out via a DMSO/toluene mixture (for **NP-S1**), or basic H_2O/THF mixture (**S2**, **S3** and **S4**) (**Scheme 2.3**). The DMSO/toluene system proved difficult to purify for **NP-S2, NP-S3** and **NP-S4** as removal of excess sulfonate ligand was difficult during workup therefore the basic H_2O/THF system was utilised. The ligands were dissolved in either DMSO or basic water, while the nanoparticles were suspended in toluene or THF. The mixtures were stirred for two days, at the end of which they were centrifuged and the supernatant was decanted off. In the case of the DMSO/toluene exchange for **NP-S1**, the black pellet was washed with DMSO to remove free ligand, and then magnetic separation was used to isolate the nanoparticles. In the case of the H_2O/THF exchange to give **NP-S2, NP-S3** and **NP-S4**, the black pellet was washed with basic water (with sonication) to remove any free ligand, then the magnetic particles were separated from the supernatant by a magnet. After the respective washings to remove any free ligands, all the nanoparticles were re-suspended in DMSO, and treated with a few drops of 1 M HCl, and sonicated. Precipitation with acetone or THF, followed by magnetic separation resulted in nanoparticles that were soluble in DMSO.

All the nanoparticles coated in the sulfonates were dispersible in DMSO, but not directly in water. The naphthalene backbone is quite hydrophobic which may explain the lack of solubility of the resultant nanoparticles. **S3** and **S4** however, have an extra OH group which could allow for hydrogen bonding and therefore may have aided in the better solubility of the **NP-S3** and **NP-S4**. In terms of stability of the nanoparticles, **NP-S1**, **NP-S3** and **NP-S4** were stable for several days in a solution of DMSO. **NP-S2** resulted in nanoparticles that settled after several days. In a more dilute solution (approximately 85 µg/mL NP) of DMSO however, this instability was less obvious, with precipitation of the nanoparticles taking weeks instead of days (**Figure 2.9**).

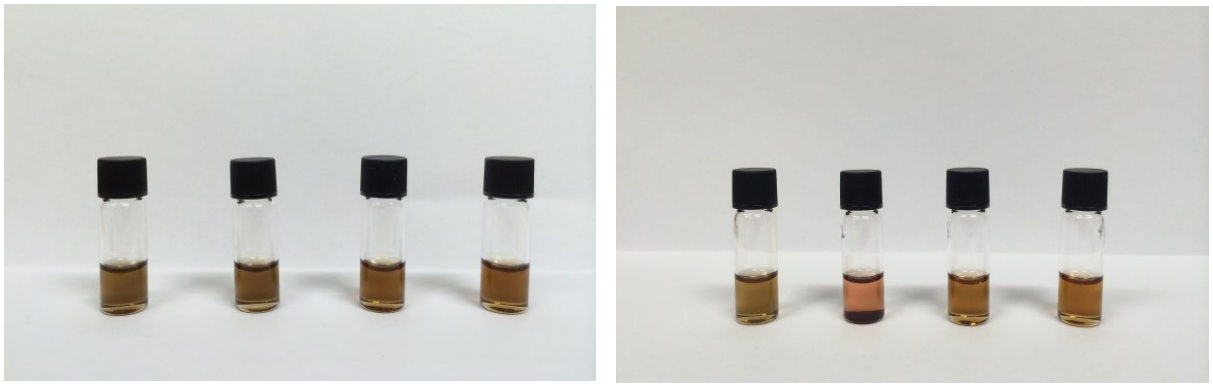

Figure 2.9 From left to right: diluted solutions (approximately 85 µg/mL NP) of **NP-S1, NP-S2, NP-S3, NP-S4** in DMSO. Left – solution of the nanoparticles at t = 0h. Right – solution of the nanoparticles after 2 weeks.

b) Characterisation of sulfonate coated nanoparticles

The sulfonate coated nanoparticles were characterised by TEM, IR, thermogravimetric analysis (TGA) and dynamic light scattering (DLS). Rhodamine coupling to the amine group on the surface was also carried out to determine the number of free amine groups available on the surface.

All the sulfonate ligands had almost identical infrared spectra, as the structures of the ligands are very similar. Hence, after ligand exchange, the nanoparticles coated with the ligands also had very similar spectra to each other (see **Figure 2.10** for IR spectrum of **NP-S1**). The sulfonate stretch, ν(S=O), for the ligand appears as sharp peaks around 1000 – 1200 cm^{-1}. The NP-sulfonate has a broad stretch in a similar region, and is indicative that the ligand exchange was successful.

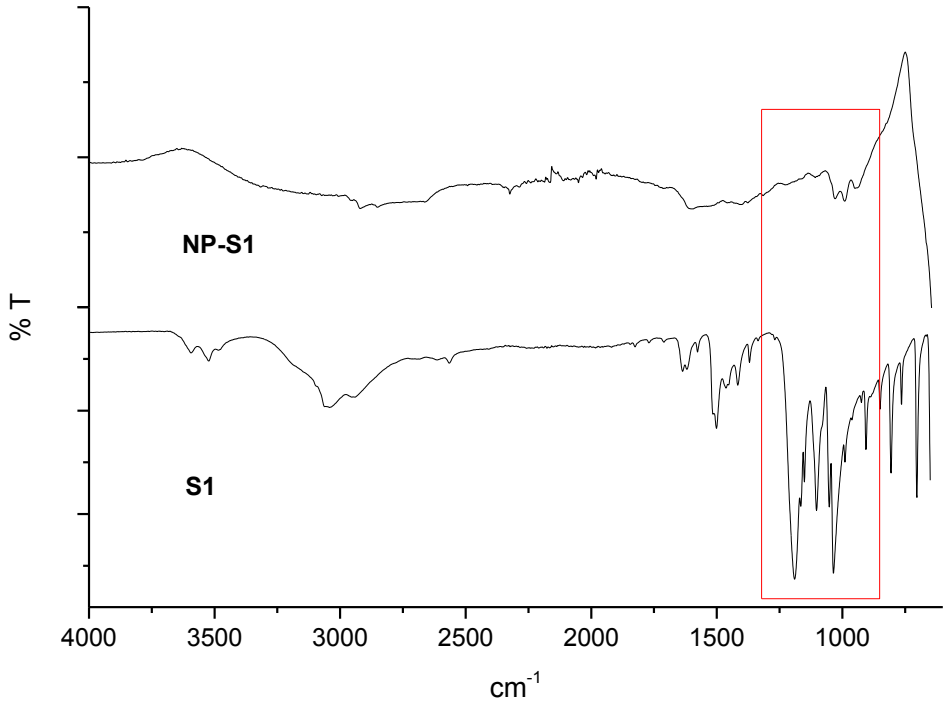

Figure 2.10 Infrared spectrum of **NP-S1** (top curve, neat, ATR plate) compared with the infrared spectrum of the **S1** (bottom curve, neat, ATR plate). The red box indicates region of the spectrum that contain stretches from the sulfonate functional group.

DLS measurements

The sulfonate coated nanoparticles were analysed by DLS measurements, in DMSO, with a glass cuvette, and their sizes tabulated below (**Table 2.1**). The sizes of the ligands are relatively small when considering typical bond lengths of approximately 1 – 2 nm, which would mean that on a core of 6 nm, the sulfonate coated nanoparticles should be roughly 10 nm (actual size). In a solvent, this size is expected to increase due to interaction between the nanoparticle and solvent. For **NP-S1, NP-S2** and **NP-S3**, hydrodynamic diameters were 19.5 nm, 15.2 nm and 14.4 nm respectively and were as expected.

Nanoparticle	Hydrodynamic diameter (nm)
NP-S1	19.5 ± 3.1
NP-S2	15.2 ± 5.6
NP-S3	14.4 ± 2.3
NP-S4	82.9 ± 153.5*

Table 2.1 Hydrodynamic diameters of the nanoparticles coated with the sulfonate ligands. *inconsistent results obtained for this sample.

DLS measurements for **NP-S4** gave inconsistent results however, even after repeat measurements, with very small sizes for some (< 10 nm) as well as very large sizes for others (> 100 nm). This could be due to the sample beginning to degrade, resulting in a mixture of aggregates and bare particles.

When a nanoparticle is surrounded by media, the solvent molecules interact with the particle's surface, and this influences the behaviour of the nanoparticles. The surface-solvent interaction forms an additional layer around the nanoparticle, and this is the hydrodynamic diameter. DLS measurements are also affected by the solvent the particles are in, as different solvents have different properties, such as viscosity. Therefore the outcome of the measurement will be different in DMSO compared to in water or other solvents. DLS measurements are also not accurate for ultrasmall nanoparticles such as these as the laser beam which hits the nanoparticles may be larger in diameter than the nanoparticles themselves, resulting in a large scatter of light and therefore introducing large errors.

TEM images:

The sulfonate coated nanoparticles were imaged by TEM and all showed similar particle morphology and size dispersion. A small drop of a dilute solution of the nanoparticle sample was deposited on a holey carbon copper grid. **Figure 2.11** below shows the TEM image for **NP-S1**. The nanoparticles are spherical in shape, retaining the same structure as the oleic acid capped nanoparticles prior to ligand exchange. There is also minimal aggregation as the particles are well dispersed on the TEM grid. Average size of the core was calculated to be 6.2 nm, based on 150 measurements.

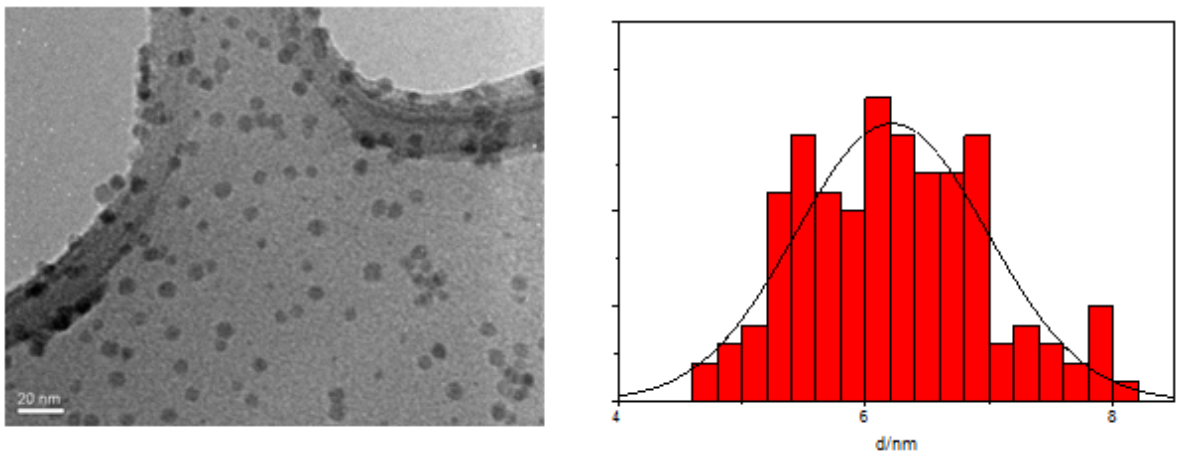

Figure 2.11 TEM image of **NP-S1**. The nanoparticles appear to be well dispersed, with minimal aggregation, and have an average size of approximately 6.2 nm.

TGA and rhodamine coupling:

TGA is a technique where the mass of a sample is monitored as it is heated in a controlled environment. A typical TGA run for the nanoparticles involves heating a concentrated solution of the sample in water (about 30 µL). A solid sample of the nanoparticle was difficult to obtain (drying of the sample leads to a sticky residue and therefore is difficult to handle and transfer between vessels and TGA pan). The program was then set to hold the temperature of the furnace at 120 °C for 30 min to drive off the solvent, leaving approximately 1 – 2 mg of dry nanoparticle sample. The temperature was then increased to 800 °C at a rate of 10 °C/min. At this stage, the mass loss as the sample is heated should correspond to the mass of ligands surrounding the nanoparticle. A curve of this section can then be plotted against temperature or time, and the initial mass lost due to solvent can be disregarded (**Figure 2.12**).

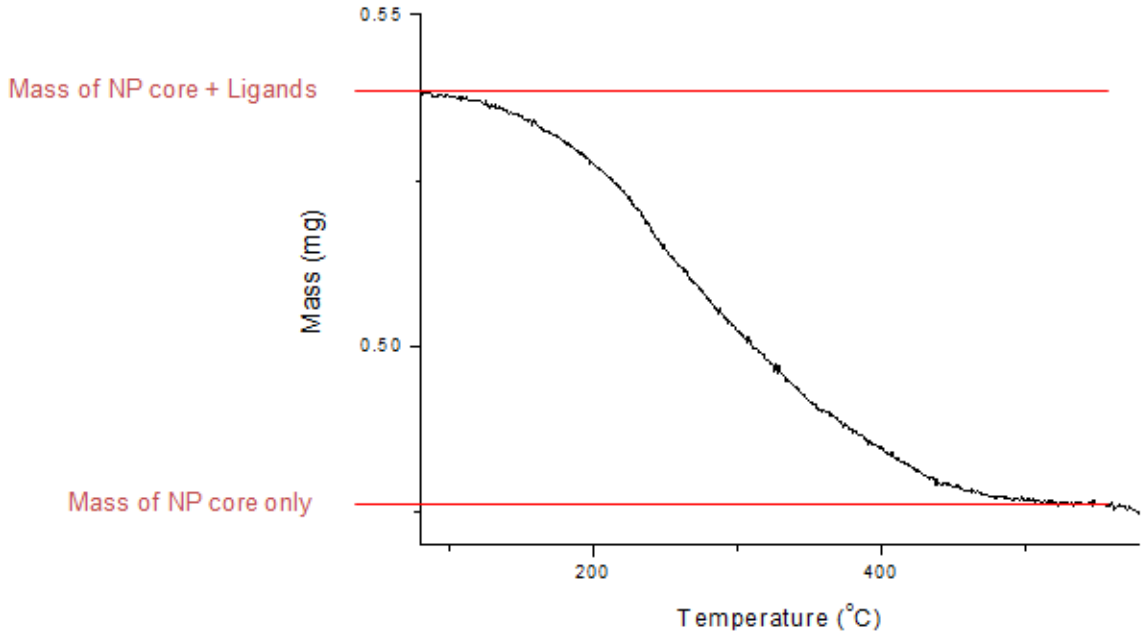

Figure 2.12 TGA curve showing the loss of mass from the sample of **NP-S1** (after solvent loss) against temperature.

From the TGA curve, the difference in mass after the loss of water when the sample is heated can then be used to calculate the number of ligands that coat the surface of one particle.[29] The total mass of ligands lost can be found by subtracting the end mass (mass of NP core only) from the starting mass (mass of NP core + ligands).

Assuming the NP is a sphere, the volume of the NP, V_{NP}, can be calculated:

$$V_{NP} = \frac{4}{3}\pi r^3 = 1.13 \times 10^{-19}\text{cm}^3$$

(where r = 3 nm on average based on the diameter of the core obtained from TEM images).

To find the M_W of the nanoparticle core (no ligands), the mass of 1 particle can be calculated from the density, d_{NP} (magnetite density: 5.15 g/cm^3)[30] and volume, V_{NP} (calculated) of the NP. The relationship between the mass of 1 particle to Avogadro's number gives the M_W of the core.

$$Mass\ of\ 1\ particle = d_{NP} \times V_{NP} = 5.82 \times 10^{-19}\text{g}$$
$$M_W = mass\ of\ 1\ particle \times Avogadro's\ number$$
$$= 350752.16\ \text{Da}$$

The number of moles of the core can then be calculated, knowing the mass of the core (mass at end of run, from TGA curve);

$$n(core) = \frac{m(core)}{M_W(core)}$$
$$= 1.47 \times 10^{-9}\text{mol}$$

The number of moles of ligands per nanoparticle can also be calculated, knowing the total mass of ligands lost from the TGA curve, and the M_W of the ligand (271.08, known).

$$n(ligand) = 1.79 \times 10^{-7}\text{mol}$$

From the number of moles of ligands per nanoparticle, and the number of moles of the core, the number of ligands per nanoparticle can be calculated from the relationship between the two.

$$no.\ of\ ligands\ per\ particle = \frac{n(ligand)}{n(core)}$$
$$= 121\ \text{ligands}$$

TGA of each nanoparticle sample was run three times, and the average of the combined runs calculated to obtain the average number of ligands per sample (**Table 2.2**). For these sulfonates, TGA measurements have not been carried out before in the literature. Based on the structure of the ligands, it would be expected that the binding of the ligands to the nanoparticle surface would be similar and thus the number of ligands on the surface would also be similar to each other. This is in agreement with the experimental results as a small range in the average number of ligands was determined (between 93.5 and 110.9).

Nanoparticle	Average number of ligands	Number of free amine groups
NP-S1	95.1 ± 40.1	130.56 ± 4.51
NP-S2	110.9 ± 28.8	130.08 ± 27.43
NP-S3	93.5 ± 12.6	124.55 ± 29.26
NP-S4	98.2 ± 17.0	145.02 ± 26.85

Table 2.2 Average number of ligands on nanoparticle surface calculated from TGA measurements, and average number of free amine groups available on the surface of sulfonate coated nanoparticles determined by indirect rhodamine quantification assay.

To determine the number of free amines on the nanoparticle surface, a known quantity of the sulfonate-coated nanoparticles were reacted with a known equivalence of 5(6)-carboxy-X-rhodamine N-succinimidyl ester (rhodamine-NHS) (**Scheme 2.4**). The amount of unreacted dye in the washing was then measured by UV-Vis spectroscopy and correlated to a calibration curve. The amount of reacted dye can then be calculated and related back to the number of amine groups that reacted.

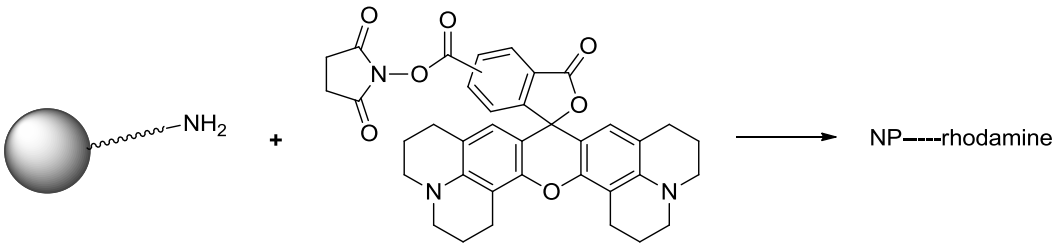

Scheme 2.4 Reaction between terminal amine group on NP and 5(6)-carboxy-X-rhodamine N-succinimidyl ester (rhodamine-NHS).

In a typical experiment, 0.5 mg of nanoparticles were reacted with 300 eq of rhodamine-NHS in DMSO. At the end of the reaction, the nanoparticles were precipitated out with THF and the supernatant was kept and then evaporated to remove the THF. The residue from the evaporated supernatant was dissolved in a known volume of water, and UV-Vis of an aliquot was recorded. Calculations revealed that there were between 130 and 145 amine groups available on average for **NP-(S1 to S4)** (**Table 2.2**). These values are similar to the number of ligands determined from the TGA data, within the error values obtained.

2.3.2 Phosphate

Following on from work by Dr Juan Gallo, PDRA in the Long group, a monophosphate-PEG_6-amine was synthesised. The commercial PEG (HO-PEG-azide) used by Dr Gallo for phosphorylation is not economically viable for large scale preparation, therefore a synthetic route to the desired compound from the less expensive hexaethylene glycol was explored (**Scheme 2.5**). (Current prices from Sigma-Aldrich, August 2014: £277.61/mmol of HO-$(PEG)_7$-azide (≥95 %), £1.59/mmol of hexaethylene glycol (97 %)).

a) Synthesis of phosphate-PEG-amine ligand

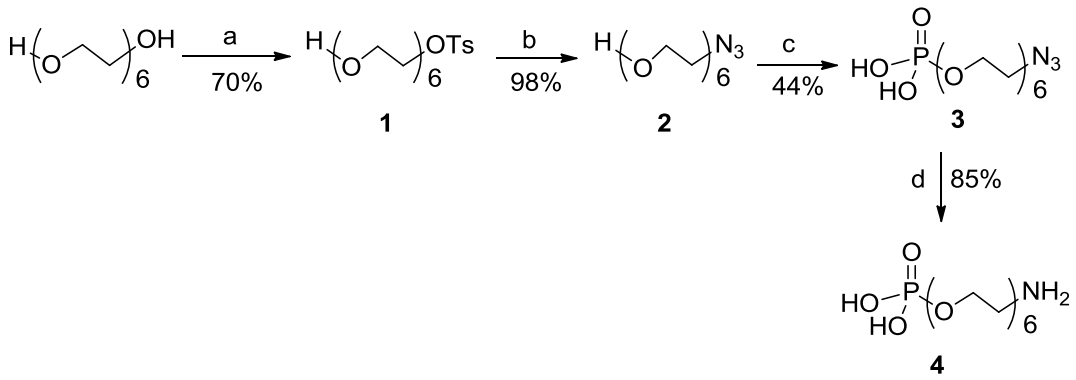

Scheme 2.5 Reaction scheme for the synthesis of monophosphate-PEG_6-amine. Reagents and conditions: a) TsCl, Ag_2O, DCM, 0 °C. b) NaN_3, MeCN, 60 °C. c) $POCl_3$, NEt_3, DCM, 0°C. d) $SiHEt_3$, Pd/C, MeOH, RT.

The reaction towards the novel phosphate-PEG-amine ligand (**4**), starts with the mono-protection of hexaethylene glycol using tosyl chloride. Substitution of the tosyl group with azide followed by phosphorylation of the terminal alcohol and subsequent reduction of the azide to the amine gave **4** in good yields.

In a 2003 paper by Hii *et al*,[31] it was shown that mono-protection with a tosyl group can be introduced to a symmetrical diol in the presence of silver(I) oxide and potassium iodide. A similar protection protocol using benzyl bromide and silver oxide to monoprotect symmetrical diols with high selectivity was presented in a paper by Bouzide and Sauve.[32] They proposed that the selectivity of the monobenzylation of the diol occurs due to the complexation of the oxygen atoms of the alcohol groups with the silver atom thus increasing the lability of the alcohol protons, especially the proton that is not involved in intramolecular hydrogen bonding (complex I, **Figure 2.13**). However, when there are more oxygen atoms in the molecule, such as in PEG, the additional oxygen atoms

also complex to the silver atom (complex II, **Figure 2.13**) which further improves the selectivity of the monoprotection. Bouzide and Sauve have proven this by comparing the poorer selectivity observed using aliphatic diols with oligoethylene glycols.[32] This mechanism would also explain the selectivity with the tosyl reaction. The reaction to form **1** gave a 70 % yield after purification by column chromatography. Characterisation by ^{1}H NMR, mass spectrometry and elemental analysis confirmed the successful synthesis of the compound and were in accordance with the literature.[31]

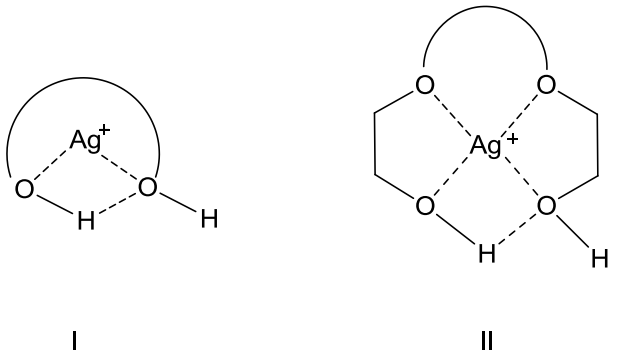

Figure 2.13 Complex I shows the complexation of the silver atom to the oxygen atoms in aliphatic diols. Complex II shows the chelation of the silver atom to the other oxygen atoms in oligoethylene glycols.

Subsequent reactions to substitute the Ts group with an azide (**2**), then phosphorylation of the untouched OH group (**3**) were carried out based on known organic synthetic reactions; tosyl groups are known to be excellent leaving groups for substitution with azides,[33,34] and the introduction of a phosphate group was a modification of a literature method.[35] Both reactions were successful and were relatively simple to purify, requiring only an aqueous workup. Characterisation by ^{1}H NMR, ^{31}P{^{1}H} NMR (for **3**), mass spectrometry and elemental analysis confirmed the synthesis of **2** and **3**. The reduction of the azide to an amine group (**4**) was carried out using triethylsilane (TES) and Pd/C to generate H_2 gas *in situ*, a modification of a literature method.[36] This reaction occurs via a catalytic transfer of hydrogen where H_2 gas is replaced by a hydrogen donor with Pd/C as catalyst. Mandal *et al*[36] have shown that TES/Pd-C is a convenient method of hydrogenation – reactions are often completed in 10 minutes or less with excess TES and 10 – 20 % Pd/C in MeOH and require only room temperature conditions. The reaction proceeded well to give **4** in 85 % yield, with characterisation by ^{1}H NMR, ^{31}P{^{1}H} NMR and high resolution mass spectrometry.

b) Ligand exchange of bulk oleic acid capped nanoparticles with phosphate ligand

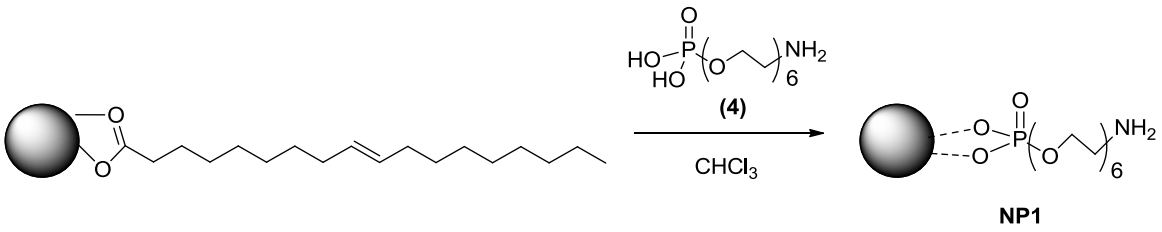

Scheme 2.6 Ligand exchange of bulk nanoparticles with ligand **4** to give **NP1**.

Ligand exchange of the nanoparticles with the monodentate ligand **4** was carried out via a single solvent system (**Scheme 2.6**), following the protocol for similar type ligands in the literature.[35] Both the nanoparticles and the ligand were dissolved in chloroform, then stirred for 2 days. At the end of this time, the reaction mixture was concentrated and the nanoparticles precipitated out with hexane, isolated by a magnet and the supernatant decanted. The particles were resuspended in DCM and again washed with hexane. This was repeated a total of three times. Finally the particles were suspended in ethanol. This solubility in a polar solvent suggests a successful ligand exchange. The nanoparticles appeared to be stable in solution for over three months (**Figure 2.14**).

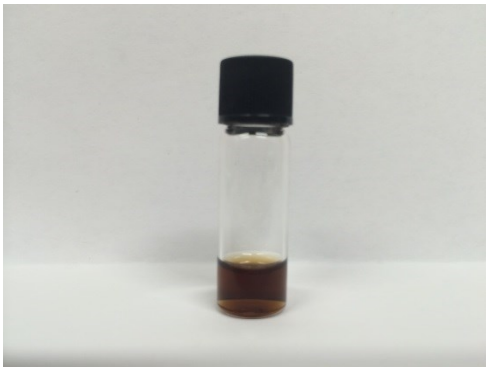

Figure 2.14 A sample of **NP1** in ethanol showing a clear solution with no precipitation or aggregation of the nanoparticles, after 3 months.

c) Characterisation of phosphate-capped nanoparticles (NP1)

Characterisation of the resultant nanoparticles was carried out by TEM imaging, TGA, DLS and IR spectroscopy. The infrared spectrum (**Figure 2.15**) shows a sharp stretch around 1100 cm^{-1} which is highly indicative of a phosphate P=O stretch, confirming the successful ligand exchange.

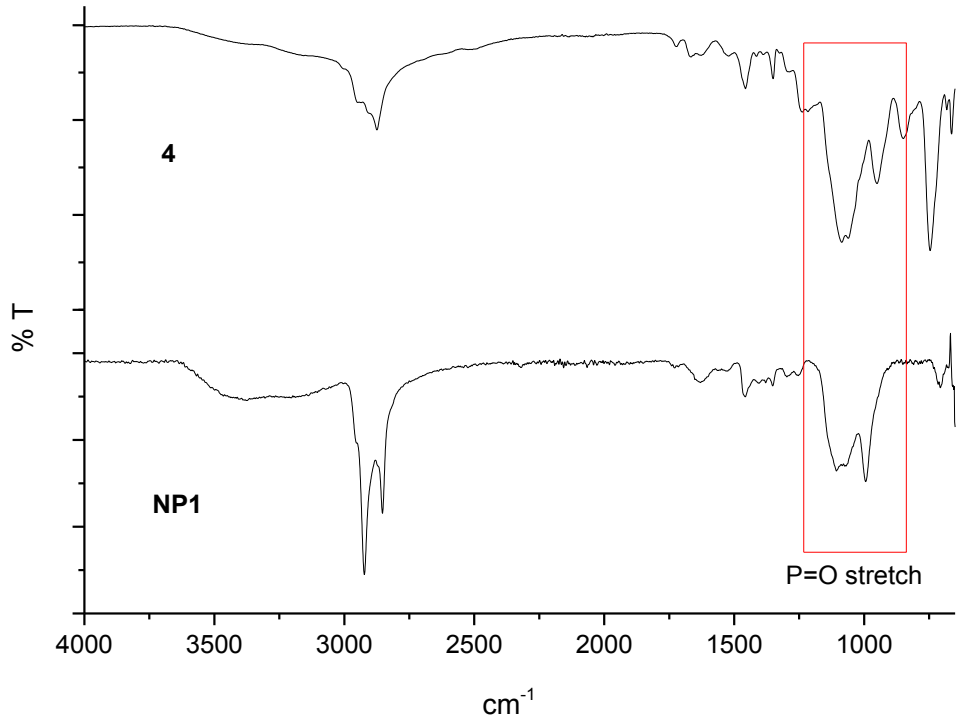

Figure 2.15 Infrared spectra of **4** (top) and **NP1** (bottom), both were run neat on ATR plate. The **NP1** spectrum retains a peak around 1100 cm^{-1}, indicative of a P=O stretch.

Comparison of the IR spectra of the ligand **4** and the nanoparticle **NP1** show that both have the P=O stretch around 1100 cm^{-1}. The P=O stretch in the nanoparticle was slightly broader than that of the free ligand due to binding of the phosphate to the nanoparticle surface, reducing the ability of the P=O to stretch as freely.

A 7 µL diluted solution of **NP1** in ethanol was deposited on a holey carbon copper grid and imaged by TEM. TEM image of **NP1** (**Figure 2.16**) shows that the particles were still highly mono-dispersed after the ligand exchange, and the average size of the iron oxide core was 7.2 nm, similar to that of the bulk oleic acid capped nanoparticles. The particles were spherical in shape and showed minimal aggregation.

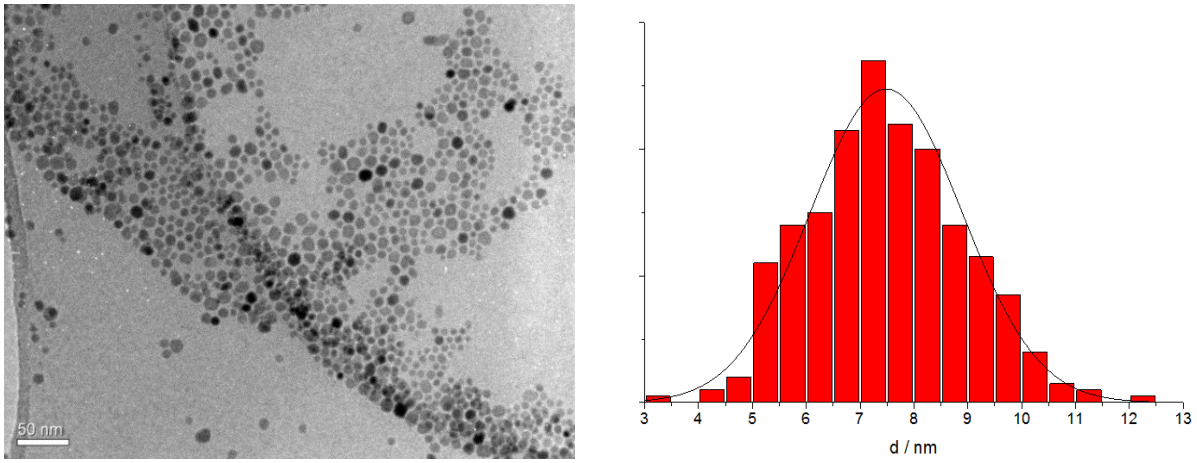

Figure 2.16 Left: TEM image of **NP1**. Right: Size distribution of the nanoparticles showing that the average core size was 7.2 nm.

TGA and rhodamine coupling:

After TGA analysis and similar calculations for **NP-(S1-S4)** applied to **NP1**, it was calculated that there were 1800 ligands on the surface of the nanoparticle. When compared to literature values of approximately 150 ligands for similar phosphate-type ligands (1.24 ligands/nm^2),[35] it suggests that the value of 1800 ligands for a 6 nm nanoparticle is incorrect. One explanation for this could be that the washing method in the workup was not ideal resulting in unbound ligand remaining and this would contribute to the high mass that was lost during the TGA.

Like the sulfonate coated nanoparticles, **NP1** samples were reacted with rhodamine-NHS to determine the number of free amines on the surface of the nanoparticle. From the calculations, the number of amine groups reacted was 239. This number is still higher than the expected number of ligands that should coat the nanoparticle surface (approximately 150), therefore confirming that there may still be free ligand in the sample that has not been completely removed during the washing step of the purification procedure. This is in agreement with the TGA results. Due to time constraints, further experimentation with workup procedures or the use of a different solvent system for the ligand exchange was not able to be carried out.

DLS measurements:

The average hydrodynamic diameter of **NP1** was 34.9 ± 6.2 nm in ethanol. Based on standard bond lengths, the size of the ligand is relatively small, at about 3 – 5 nm, and thus the expected

hydrodynamic size of the resultant nanoparticle would be approximately 15 – 20 nm, taking into account the hydration sphere around the nanoparticle. The recorded value however, is slightly higher than this. As previously discussed in the DLS measurements of sulfonate coated nanoparticles, hydrodynamic size measurements in DLS are affected by different solvents and their properties. This could explain why the hydrodynamic size is larger than expected, as the solvent sphere around the nanoparticle would change in different solvents. Another possibility in this case could be excess ligand remaining after workup, resulting in several ligand layers around the surface of the core (**Figure 2.17**). This would explain the unexpected values obtained in the TGA and rhodamine coupling reaction.

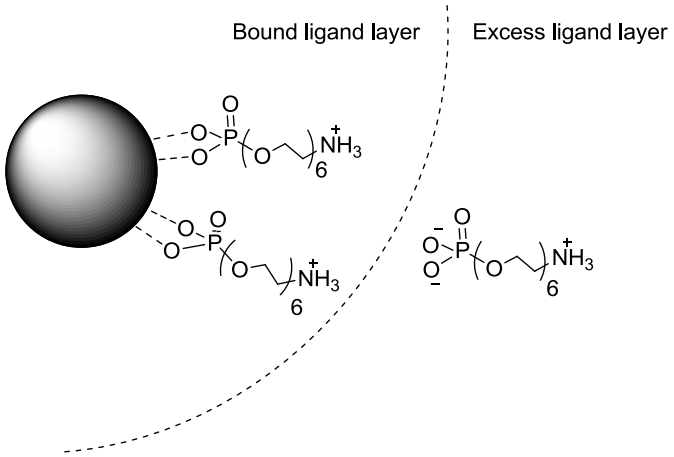

Figure 2.17 Excess ligand after workup that could result in a second layer on the nanoparticle surface.

2.3.3 Bisphosphonates

The primary focus of the ligand exchanges in this project has been on bisphosphonate ligands (BP) as there is precedent in the literature for bisphosphonate ligands being stronger capping ligands for nanoparticles compared to carboxylate and phosphate ligands.[2,3,37,38] To begin with, there is a wide range of commercially available bisphosphonate ligands, as they have been known to feature in bone drugs for the past 40 years. Hydroxyapatite is a modified calcium apatite mineral found in bone. The discovery that endogenous pyrophosphate was involved in the formation and dissolution of hydroxyapatite crystals led to the development of pyrophosphate analogues. These analogues were to be more stable and hydrolysis-resistant molecules that could prevent loss of bone mineral. This led to the identification of bisphosphonates where the P-C-P backbone replaced the labile P-O-P moiety in pyrophosphates and resulted in a large number of commercially available

bisphosphonates.[39–41] Examples of some commercially available bisphosphonates are presented in **Figure 2.18**.

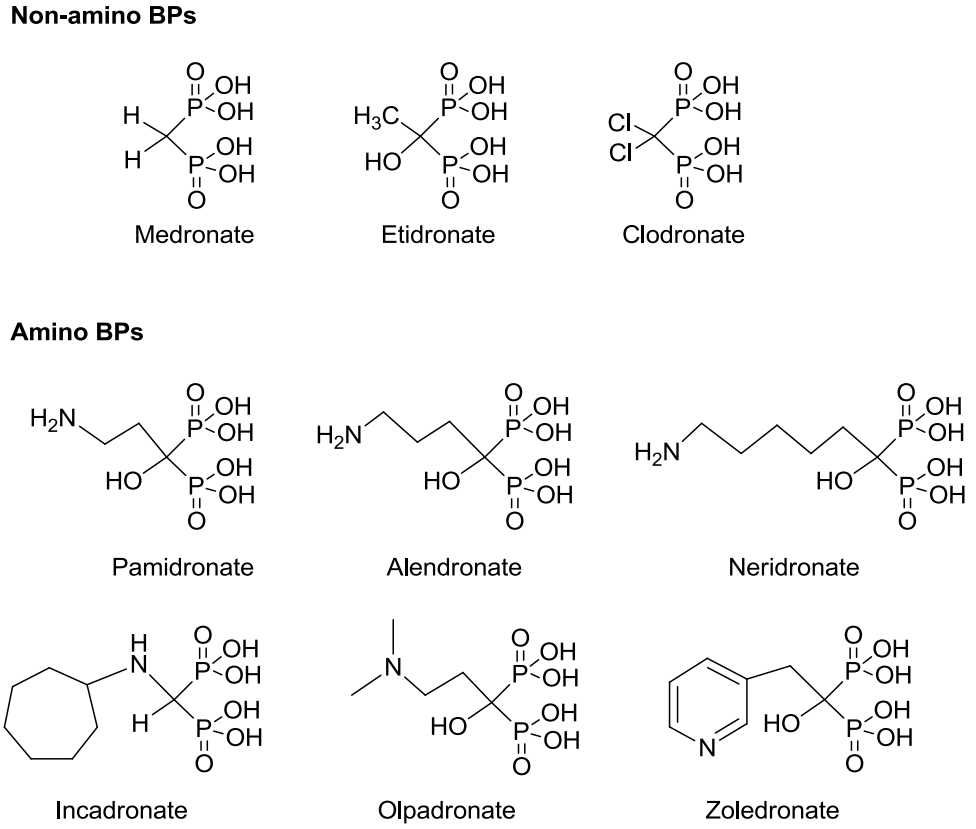

Figure 2.18 Examples of current BPs used in a clinical setting.

The general structure of bisphosphonates compared to pyrophosphate can be summarised below (**Figure 2.19**). The P-C-P moiety in the bisphosphonate was identified as being responsible for the strong affinity to hydroxyapatite, and the distance between the two phosphate oxygens was found to be ideal for Ca^{2+} binding.[42] The replacement of the central oxygen for a carbon allowed for the introduction and subsequent variation of R_1 and R_2 groups, which can alter the bisphosphonate affinity for bone, as well as their biological activity. The R_1 substituent has been found to play an important role in bone affinity. When R_1 is an OH group, participation of the hydroxyl group in Ca^{2+} hydroxyapatite binding results in a 'tridentate' mode of binding thus enhancing binding activity.[43] Therefore, having an OH group at the R_1 position is favoured.

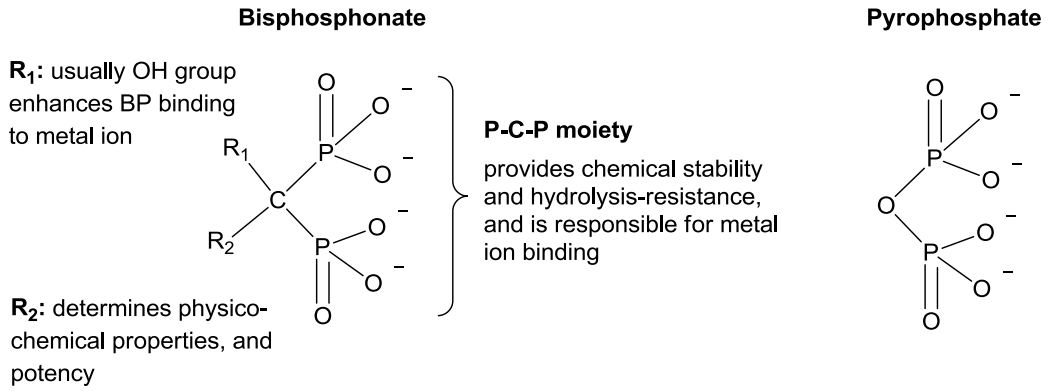

Figure 2.19 General structure of a bisphosphonate showing the functional properties of the separate moieties.

Modifications to the R_2 side chain also had an effect on hydroxyapatite affinity. Introduction of nitrogen-containing groups means the bisphosphonate has a high pKa value which remains protonated at physiological pH, resulting in an overall positive charge on the bisphosphonate-hydroxyapatite surface.[44] The opposite is observed when there are no nitrogen moieties resulting in repulsion between the bisphosphonate and hydroxyapatite, thus a lower affinity. The development of bisphosphonates can be divided into three phases: the non-nitrogen-containing, (alkyl) nitrogen-containing, and heterocyclic nitrogen-containing. Introduction of alkyl amines at the R_2 position enhanced the potency of bisphosphonates.[45] However, the distance of the nitrogen atom from the P-C-P backbone is also important with regards to potency. Lengthening of the alkyl chain from pamidronate to alendronate (**Figure 2.18**) saw an increase in potency, but increasing the chain beyond alendronate reduced it.[46] The introduction of heterocyclic nitrogen-containing rings, such as in zolendronate increased potency further.

Bisphosphonates have also been known to have a high affinity for other metals. Before its discovery as a bone drug, they were used as anticorrosive, anti-scaling and complexing agents.[47] There have been many examples in the literature where bisphosphonates form complexes with various metals. These include Ba(II),[48,49] Sr(II),[48,49] Mg(II),[48,49] Al(III),[50] Fe(III),[50] Cu(II),[51,52] Zn(II),[53] Ni(II),[54] Co(II),[54] UO_2(II)[55] and lanthanides such as Nd(III)[56] and Gd(III).[57] Phosphonic acids and bisphosphonates have also been known to bind strongly to metal oxide surfaces, including TiO_2,[58–62] ZrO_2,[58,59,63] Al_2O_3,[58,62,64] SiO_2,[60,62] Fe_2O_3/Fe_3O_4,[4,65–68] as well as rare earth metal oxides M_2O_3 where M = Eu, Er, Yb, and Gd.[66]

All these examples have shown that the bisphosphonate ligand is versatile as a ligand. From these examples, a few different bisphosphonates were investigated as coating ligands for iron oxide nanoparticles. Even though amine groups have primarily been chosen as the R_2 group in the commercial bisphosphonates due to the improved potency of the drug, it was decided to also

attempt the synthesis of an alkyne and thiol version in order to allow for further versatile functionalisation via 'click chemistry' in the case of the alkyne, or maleimides with the thiol. It was hoped that the P-C-P moiety would be sufficient for the binding activity required for BP-metal oxide interaction. For the purposes of nanoparticle coating in this project, the distance between the terminal functional group and the P-C-P backbone was not taken into consideration.

a) Alkyne and thiol BP

The alkyne BP and thiol BP chosen as the initial BP ligands were synthesised according to literature.[69–71] Following a literature survey of bisphosphonate synthesis, it was decided to synthesise a vinylidene bisphosphonate as the starting point towards the alkyne and thiol BP as it would provide the flexibility of synthesising other BPs via the same precursor, with modifications to the synthetic procedures that will be used to produce the initial alkyne and thiol BP. Several literature papers use the vinylidene BP as a precursor to other BPs.[69,70,72–74]

The vinylidene BP was synthesised over two steps following a literature method, starting with tetraethyl methylenebisphosphonate. This was reacted with diethylamine and paraformaldehyde to form a methoxymethylated intermediate **5** (**Scheme 2.7**). The intermediate was heated to reflux with a catalytic amount of *p*-toluenesulfonic acid monohydrate to give the vinylidene bisphosphonate ester **6** with the elimination of methanol.[70] The initial synthesis of **6** proved problematic as the reaction is driven by the elimination of methanol and in order to do this, the methanol produced has to be removed as the reaction progresses. This was accomplished in the literature via a Dean-Stark reflux. Another method using a Soxhlet apparatus was attempted, and proved to be a better method possibly due to the presence of CaH_2 in the Soxhlet chamber to remove methanol. Both **5** and **6** were characterised by ^{1}H and $^{31}P\{^{1}H\}$ NMR, and were in accordance with the literature.

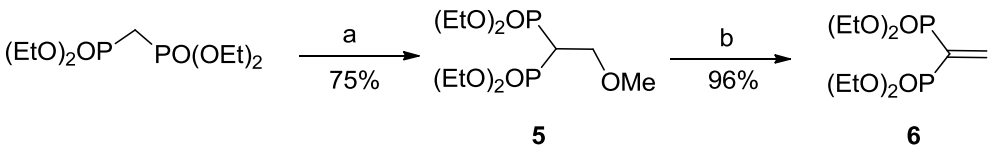

Scheme 2.7 Synthesis of vinylidene bisphosphonate ester **6**, intermediate towards the synthesis of thiol and alkyne bisphosphonic acid. Reagents and conditions: a) $HNEt_2$, $(HCOH)_n$, MeOH, reflux. b) $TsOH.H_2O$, toluene, reflux.

The next stage of the synthesis was to convert the phosphonate ester to the free acid **7** (**Scheme 2.8**). The majority of literature procedures use bromotrimethylsilane.[75,76] The work-up involves removing the organic solvent under vacuum and then extracting the residue into water and neutralising with 40 % aqueous tetrabutylammonium hydroxide to pH 4. This gives **7** as the tetrabutylammonium salt instead of the free acid. The solution was dried at 50 – 60 ^{o}C under vacuum. Characterisation was by ^{1}H and ^{31}P{^{1}H} NMR and was in accordance with the literature.

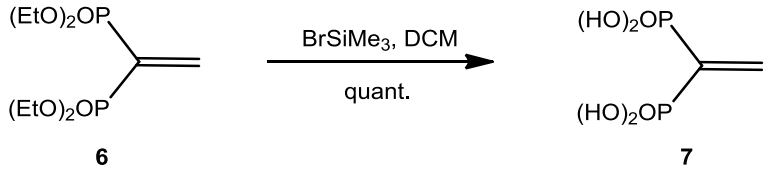

Scheme 2.8 Hydrolysis of the phosphonate ester **6** into the free acid **7**, with $BrSiMe_3$ in DCM at RT.

Thiol BP

The thiol BP **8a** was initially synthesised by the nucleophilic addition of 1,3-propane-dithiol (**Scheme 2.9**), in accordance with the literature.[70] However, this method proved problematic as the 1-butanol used in the reaction was difficult to remove, as observed when characterised by ^{1}H NMR spectroscopy.

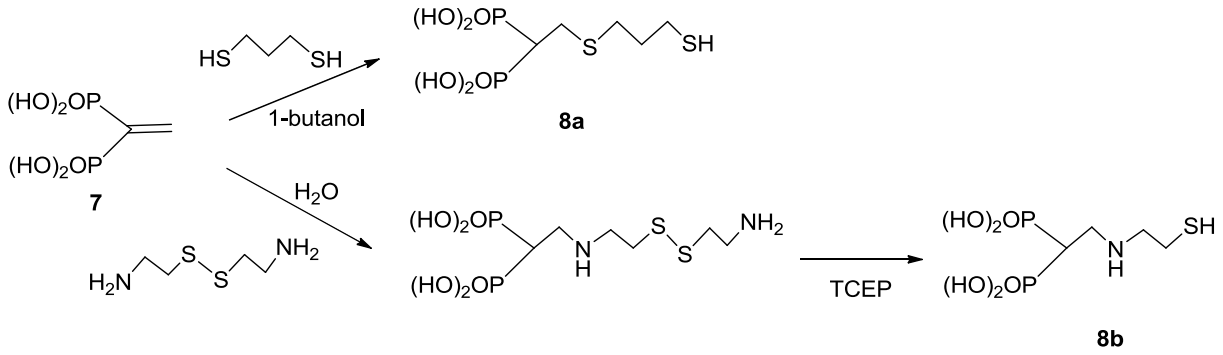

Scheme 2.9 Synthesis of thiol BP via 1,3-propane-dithiol (**8a** top) and cystamine (**8b** bottom).

In another method outlined by Alferiev *et al*, **7** was reacted with cystamine instead.[71] This gives a disulfide intermediate which was reduced with tris(2-carboxyethyl)phosphine (TCEP) to give **8b**, which was characterised by ^{1}H and ^{31}P{^{1}H} NMR and was in accordance with the literature.

8b was soluble in water and ligand exchange with the bulk nanoparticles was attempted using several different solvent systems. Initially, a biphasic hexane/water system containing the nanoparticles in hexane and the ligand in water was shaken using a shaker to mix. This resulted in the nanoparticles being formed in an emulsion-like layer between the water and hexane layers. The nanoparticles were separated from the solution for purification by a magnet and the supernatant was decanted. Unreacted ligand was subsequently removed by washing with water and acetone. The resulting nanoparticles were a suspension in water that unfortunately settled within 1-3 hours after isolation. A single phase solvent system was attempted next, with the ligand in water at basic conditions, and the nanoparticles in THF. After the ligand exchange, the resultant nanoparticles were washed with acetone and ethanol but the final product was still not well dispersed in water. Infrared spectroscopy of the nanoparticles recorded a P=O stretch at 1039 cm^{-1} which suggested that a successful ligand exchange had occurred. However, thiols themselves are not very water soluble due to poor hydrogen bonding and once on the nanoparticles, the ligands would have lost the water solubilising bisphosphonate group to surface binding thus rendering the nanoparticles poorly soluble in water.

Alkyne BP

The alkyne BP was synthesised via the reaction between vinylidene bisphosphonate ester **6** and sodium acetylenide, according to literature (**Scheme 2.10**).[69] Aqueous workup yielded **9** which was then reacted on with bromotrimethylsilane to reduce the esters to the free acid **10**. Both species were characterised by ^{1}H and $^{31}P\{^{1}H\}$ NMR and were in accordance with the literature.

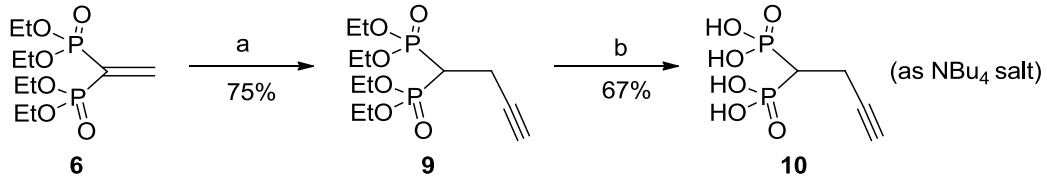

Scheme 2.10 Synthesis of alkyne BP. Reagents and conditions: a) sodium acetylenide, THF, -20 °C then RT. b) $BrSiMe_3$, DCM, 0 °C then RT.

Ligand exchange between **10** and bulk nanoparticles using the same method as that for **8b** was attempted. As with **8b**, the infrared spectrum of the nanoparticles was similar with a P=O stretch observed. However, the resultant nanoparticles were also not water soluble, likely due to the same

reasoning that the loss of the phosphonate group to metal oxide binding renders the nanoparticles insoluble in water.

b) Sodium alendronate

Due to the solubility difficulties encountered with the alkyne and thiol BP capped nanoparticles, a commercially available bisphosphonate ligand was then utilised. Sodium alendronate was chosen due to its water solubility, availability of a terminal amine group for further functionalisation, and was economically more attractive compared to the other alkyl amine BPs such as pamidronate. (Current prices from TCI-UK, August 2014: £1.38/mmol of sodium alendronate trihydrate (97 %), £97.37/mmol of disodium pamidronate hydrate).

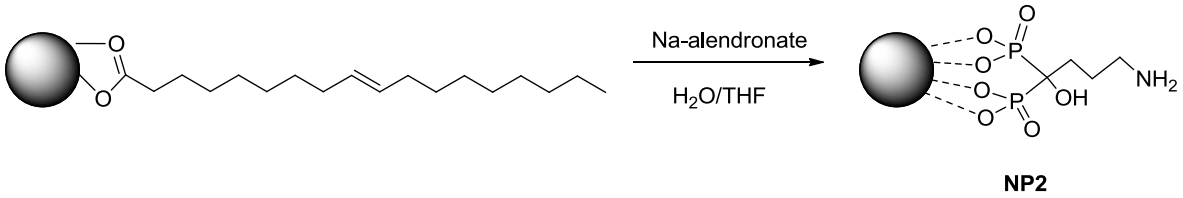

Scheme 2.11 Ligand exchange reaction between bulk nanoparticles and sodium alendronate ligand.

Ligand exchange of the oleic acid-capped nanoparticles with sodium alendronate was carried out in one phase in a miscible two solvent system of THF and water to give **NP2** (**Scheme 2.11**). In a typical experiment, a large excess of sodium alendronate (approximately 60 mg) was dissolved in water with the addition of 1M KOH to the solution to completely solvate the white solid alendronate and bring the solution to pH 9/10. Sodium alendronate is acidic and highly acidic conditions will degrade the iron oxide nanoparticles so it is essential that the solution is kept at a slightly basic pH. Approximately 1.5 mL of bulk oleic acid capped nanoparticles (from a 20 mL stock solution in hexane) dispersed in THF was then added and the mixture of the ligand and the nanoparticles stirred at room temperature for two days. After this, the nanoparticles were isolated by a magnet, the residue resuspended in water and precipitated with acetone followed by centrifugation. This washing step was repeated twice and finally the nanoparticles were resuspended in water, and stored with a few drops of 1 M KOH such that the nanoparticle solution is at pH 8/9.

Characterisation of bisphosphonate capped nanoparticles NP2:

Characterisation of the alendronate-capped nanoparticles **NP2** was done by IR, DLS, TEM and TGA. TEM images (**Figure 2.20**) shows negligible difference in size and morphology of the nanoparticle core before and after ligand exchange. The size of the core stays roughly the same, with only the nanoparticles arrangement on the grids changing due to the type of solvent they were suspended in before placement on the grids. Substitution of the oleic acid ligand with the alendronate would have no drastic effect on the core of the nanoparticles, which is what the TEM images capture.

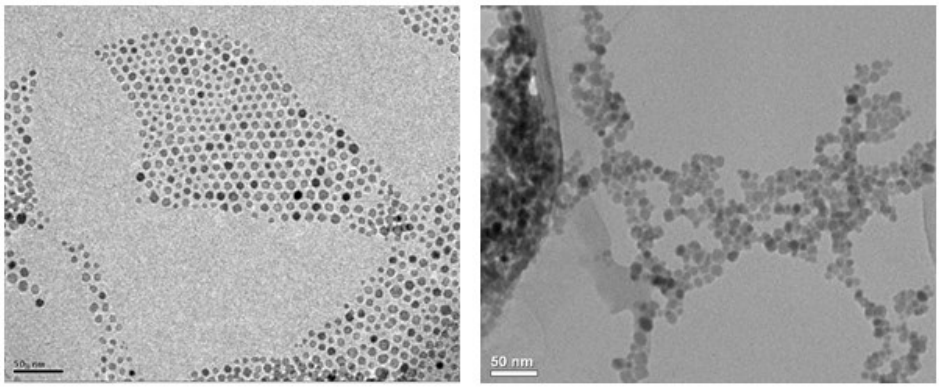

Figure 2.20 TEM images of the nanoparticles before (left) and after (right) ligand exchange with sodium alendronate.

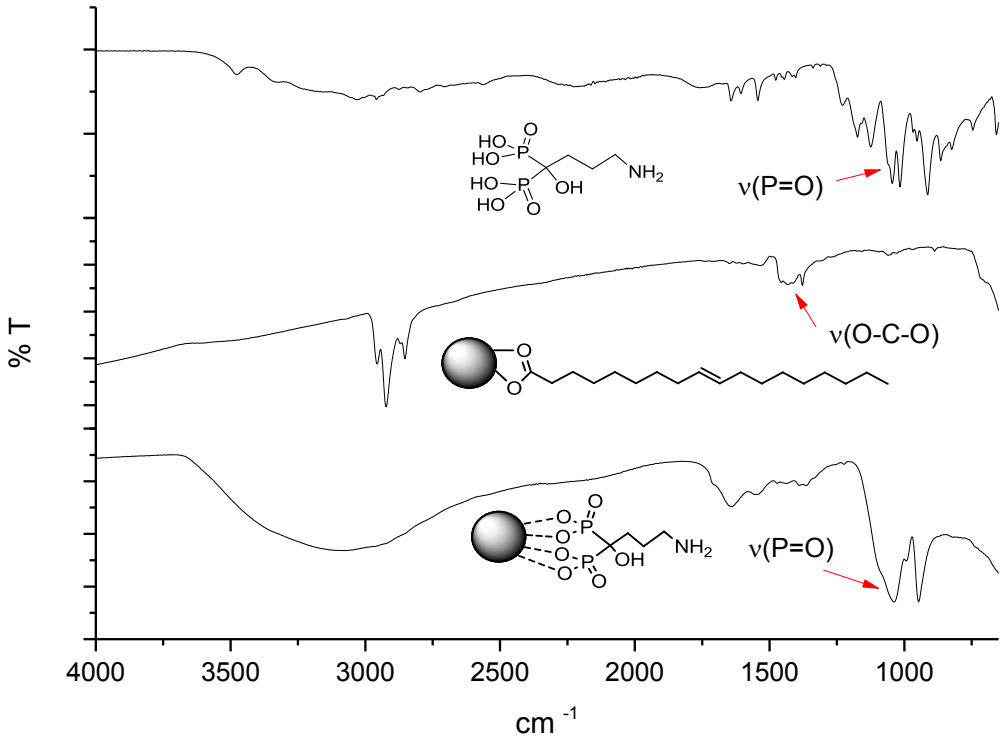

Figure 2.21 Infrared spectrum of the nanoparticles before and after the ligand exchange with sodium alendronate (neat, ATR plate). Top – sodium alendronate ligand, middle – oleic acid capped nanoparticles, bottom – alendronate capped nanoparticles **NP2**.

The nanoparticles were also characterised by infrared spectroscopy, run neat on an ATR plate (**Figure 2.21**). Functional groups with a strong stretching frequency, such as C-O in the carboxylic group of oleic acid, and the phosphonate resonance of the alendronate will have characteristic stretches. The IR of the alendronate capped nanoparticles show a strong P=O stretch at approximately 1100 cm^{-1} which was not present in the oleic acid capped particles.

From DLS measurements, the nanoparticles were found to have a hydrodynamic diameter average of 20.2 ± 5.2 nm and a charge of -25 mV in water at pH 7.4. Taking into consideration typical bond lengths for C-C, C-N and C-P bonds, the approximate size of the ligand would be around 1 nm. Coupled with the average core diameter of 6 – 7 nm, the approximate size of **NP2** should be in the region of 10 nm, and with the shell of water should theoretically give a total hydrodynamic diameter of approximately 20 nm. This is in agreement with the observed hydrodynamic diameter measured by DLS. Multiple layers of alendronate ligand as shown in **Figure 2.22** was found to not be present as the hydrodynamic diameter measured by DLS did not change with more washing steps.

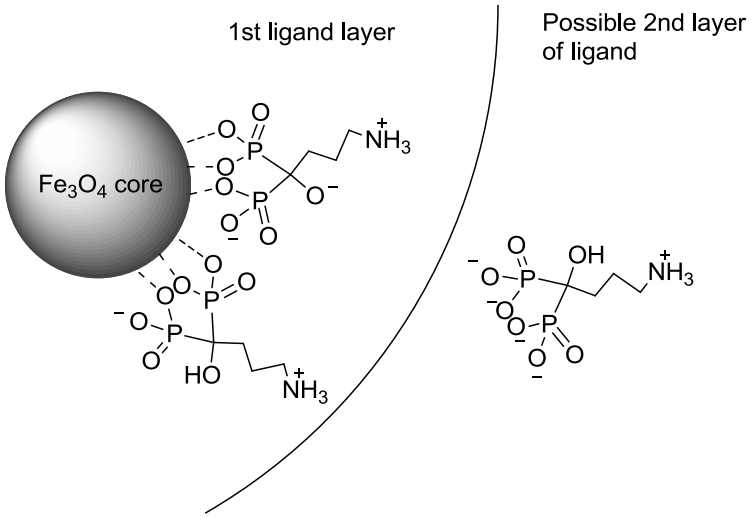

Figure 2.22 Diagram showing multiple layers of alendronate ligand on the NP core.

The negative surface charge of -25 mV in water at pH 7.4 is unexpected. The amine group on the alendronate has a pK_a of 12.2,[77] so at approximately pH 7 in water, the amine group should be protonated giving a positive charge. However the OH group which has a pK_a of less than 7 would still be deprotonated at pH 7. Surface charge of **NP2** was also measured at different pH to determine if acidic pH would protonate the amine and hydroxyl groups, resulting in a positive charge. This was indeed the case, as at highly acidic pH (around 2-3), the surface charge of the nanoparticles was +18.5 while at highly basic pH (around pH 10-11), the surface charge was -28.4. This confirms that the results obtained at pH 7 are as they should be.

TGA and rhodamine coupling:

TGA measurements were repeated three times for each batch of nanoparticles, and three different batches of nanoparticles were measured, for a total of nine readings (**Table 2.3**). This was to ensure the reproducibility of the data between different batches of **NP2** synthesised at different times. The average number of ligands overall was 116.

NP-alendronate (**NP2**) sample	Average no. of ligands
Batch 1	123.02 ± 39.78
Batch 2	108.42 ± 33.14
Batch 3	115.59 ± 33.99

Table 2.3 Table detailing the average number of ligands determined for each batch of NP-alendronate

The ligands on **NP2** were lost over a range of temperature, between 200 and 450 °C. According to literature, there are approximately 1.6 bisphosphonate ligand molecules per nm^2 of iron oxide nanoparticles for a nanoparticle core of approximately 6 nm diameter.[4] For these particles, this equates to about 180 bisphosphonate ligands on the surface. This theoretical value is not far from the average measured number of alendronic acid ligands (average 115 ± 30) which coat **NP2**.

Rhodamine coupling to **NP2** was performed similarly as before where 300 equivalents of rhodamine-NHS was reacted with 1 mg of **NP2** in water. After 3.5 h, the mixture was centrifuged and the supernatant's UV-Vis spectrum was measured. After repeating the rhodamine coupling six times, the absorbance at 554 nm (λ_{max}) correlated to an average of 145 amine groups reacted. These data suggest that the rhodamine coupling data correlates well with the number of ligands determined by TGA.

2.3.4 Further stability measurements

To assess stability of the nanoparticles at different physiological conditions, the nanoparticles **NP1** and **NP2** were suspended in various media. Both **NP1** (ethanol stock, diluted with water) and **NP2** (in water) were assessed in different concentrations of NaCl solution as well as in water at different pH. The sulfonate coated nanoparticles were not assessed in this way as they were already not very stable in the DMSO solution. In addition as the nanoparticles would eventually be used *in vivo,* the toxicity of the iron oxide nanoparticles in blood was investigated. This measurement to determine

possible toxicity of nanoparticles towards blood cells is important in order to maintain red blood cell integrity after administration of the nanoparticles.[78] All the nanoparticles after ligand exchange (**NP1**, **NP2** and sulfonate coated) were diluted with PBS and incubated with blood.

a) In H_2O at different pH over time

There are different pH conditions in different cells and regions of the body. To determine the stability of the particles at different pH, the nanoparticles were observed after addition to water at different pH, in the range from highly acidic (pH 1) to highly basic (pH 13). 100 µL of **NP1** and **NP2** were suspended in water at different pH (between 1 and 13, 1 mL each). Their stability in the respective pH was recorded at different time points (**Figure 2.23**).

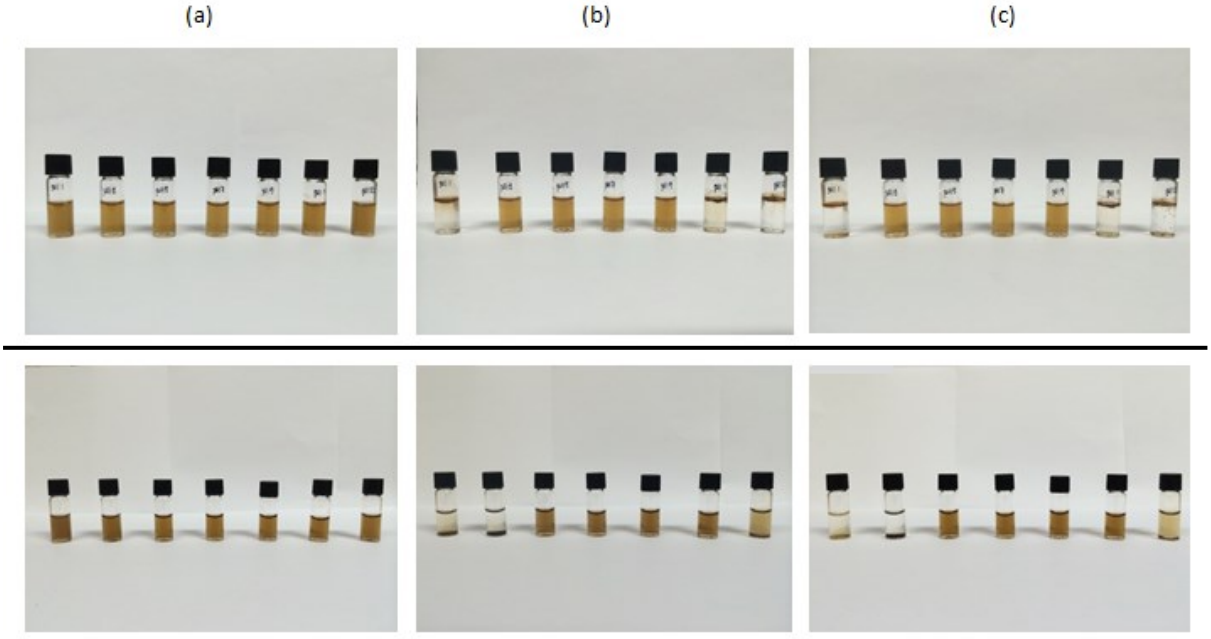

Figure 2.23 Nanoparticles in water at varying pH (from L to R: pH 1, 3, 5, 7, 9, 11, 13). a) at t = 0 h; b) t = 6 h; c) t = 24 h. Top set **NP1**, bottom set **NP2**.

Overall, **NP1** was more stable at lower pH range, compared to **NP2**, over a 24 hour period. The nanoparticles **NP1** were stable between pH 3 and 9, while **NP2** were stable between pH 5 and 11. This slight difference in range could be due to the different pKa's of the ligands on **NP1** and **NP2** which affects the stability of the particles as the functional groups are protonated and deprotonated in the respective pH. Instability at the lower acidic pH is as expected, as iron oxide nanoparticles

begin to be digested in a highly acidic environment. Instability at the higher basic pH is most likely due to charge repulsion between the particles, as the surface groups are deprotonated.

b) In NaCl solution

As the traditional method of delivering nanoparticles to a patient is via a saline solution, the stability of the nanoparticles in salt solutions of varying concentration was observed. Normal saline is 0.9 % NaCl solution, so an upper limit of 1.2 % was used. 100 µL of nanoparticles **NP1** and **NP2** were added to 0.5 mL of NaCl solutions of varying concentration between 0 % and 1.2 % NaCl. In **Figure 2.24**, the nanoparticles are seen to have precipitated out of solution after 1 h.

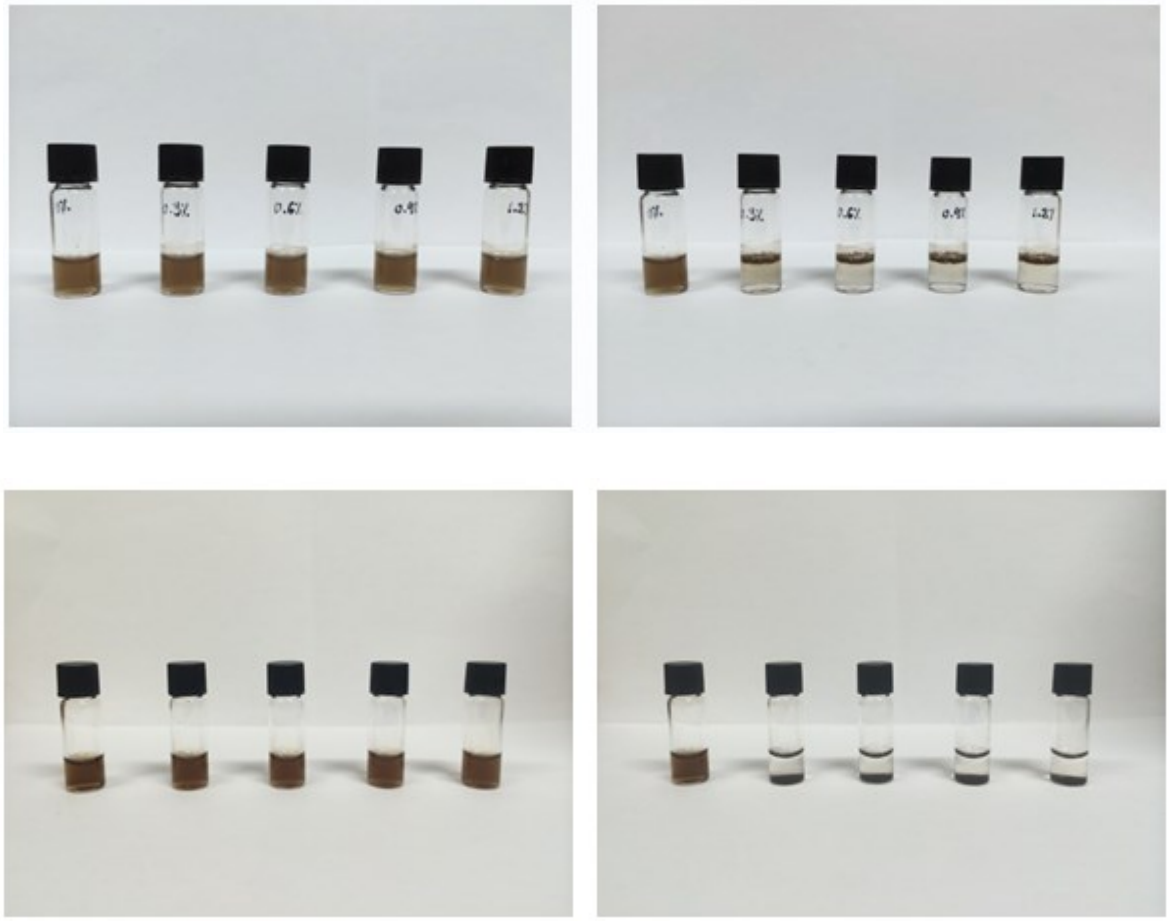

Figure 2.24 Stability of nanoparticles in NaCl solution, from L to R 0 % solution, 0.3 %, 0.6 %, 0.9 % and 1.2 %. Top **NP1,** bottom **NP2** (alendronate).

However, this is a relatively high concentration of nanoparticles for the volume of salt solution. A typical dose for a human is 0.56 mg Fe/kg of body weight diluted in 100 mL of saline. This would

equate to 0.034 mg and is lower than the concentrations used here (0.15 mg Fe) which would not be used *in vivo*. Nevertheless, the nanoparticles are still stable in the salt solutions for a short period of time and would be stable in the time period used in a clinical setting.

c) Toxicity in blood

As an application of the iron oxide nanoparticles is to act as imaging contrast agents in the body, it was necessary to determine the toxicity of the nanoparticles in blood. The assay used here is based on literature protocol.[79] A known concentration of the nanoparticles was incubated with whole blood for 90 min at 37 °C in a shaker. Then, the samples were centrifuged at 600 g for 5 min, the pellet discarded and the supernatant incubated at room temperature for a further 30 min to allow haemoglobin oxidation. Finally, the absorbance of the samples was recorded at 560 nm. If a high signal at this wavelength is observed, it indicates that the red blood cells have burst and the sample is toxic to blood. Water is used here as a positive control, where a definite UV-Vis signal would be expected due to movement of water by osmosis into the red blood cells causing lysis.

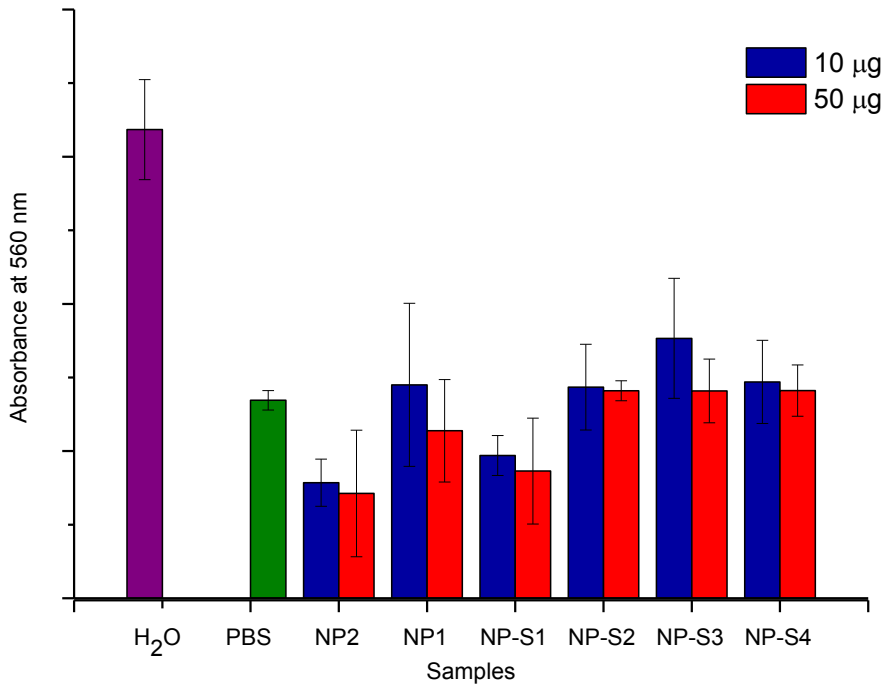

Figure 2.25 Graph showing the uptake of nanoparticles by red blood cells in blood.

Phosphate buffered saline (PBS), having a comparable solute concentration to red blood cells should not cause a large amount of cells to burst and therefore the absorbance in UV-Vis measurement would correlate to a non-toxic effect on red blood cells. From the graph in **Figure 2.25**, all the nanoparticle samples do not appear to be toxic as their UV-Vis signals at 560 nm are all below that of water, and are comparable to that of the PBS sample.

2.3.5 Conclusion

Based on the above results, the most stable of the nanoparticles synthesised is **NP2**, the alendronate coated nanoparticles. The **NP1** particles were also stable in solution, with no signs of aggregation or precipitation, after several months. The sulfonate-coated nanoparticles (**NP-S1 to NP-S4**) were soluble in DMSO but were less stable in solution, as precipitation of the nanoparticles occurred after about one week. As the size of the ligands coating the nanoparticles in each of the species were approximately the same, the hydrodynamic diameters of the resultant nanoparticles were expected to be similar to each other. However sizes were not directly comparable due to the different nature of the solvent the nanoparticles were suspended in during DLS. TGA measurements for **NP2** and the sulfonate coated nanoparticles correlated well with the rhodamine coupling data obtained, but this was not the case for **NP1**. Removal of excess ligand is important during work up to ensure that only bound ligand remains on the nanoparticle surface, but this can be difficult to achieve as the solubility of the nanoparticle and ligand have a significant effect on the success of the work up procedure.

The stability of the nanoparticles in physiological conditions was also investigated, where **NP1** and **NP2** were found to be not very stable in the presence of high salt concentration. This was attributed to the high concentration used in the saline incubation. All the nanoparticles were shown to be non-toxic to red blood cells.

2.4 Experimental

General procedures and characterisation techniques

The synthesis of the core nanoparticles was carried out under nitrogen, while the ligand exchanges were performed under ambient conditions. Nanocrystals were characterised by low and high resolution TEM on a JEOL JEM 2000F microscope. Magnetic data from the nanoparticles were recorded with a QD magnetometer MPMS-7T. Thermogravimetric analysis (TGA) was carried out on a Perkin Elmer Pyris 1 TGA instrument. UV-Vis spectra were recorded on a Perkin-Elmer Lambda 25 UV-Vis system. FT-IR spectra were acquired on a Perkin-Elmer Spectra 100 FT-IR spectrometer, neat on ATR plates. Z-measurements were obtained on a Beckman Coulter Delsa™ Nano. ^{1}H, $^{13}C\{^{1}H\}$ and $^{31}P\{^{1}H\}$ NMR spectra were obtained on a Bruker DRX400 MHz spectrometer. Mass spectrometry was carried out by Mr. J. Barton (2010 – 2012) and Dr. L. Haigh (2012 onwards) at the Department of Chemistry, Imperial College London. Microanalyses were carried out by Mr. S. Boyer, London Metropolitan University.

Syntheses of the ligands were carried out under nitrogen unless stated otherwise. All reagents were purchased from Sigma-Aldrich or TCI-UK (sodium alendronate and sulfonates 2, 3 and 4), and were used as received without further purification. Dry solvents were obtained from the Imperial College Chemistry Department dry solvent towers, which dried the solvents over alumina beads. All other solvents were analytical grade and were obtained from VWR. Water was purified by the PURITE system.

2.4.1 Synthesis of bulk iron oxide nanoparticles

a) Fe_3O_4 nanoparticles via the hydrothermal method [5,6]

a) $FeCl_2.4H_2O$ (0.05 g, 0.25 mmol) was dissolved in distilled water (8 mL). Under vigorous stirring, ammonia solution (1 mL) was added which turned the mixture black. The mixture was stirred for a further 10 minutes before citric acid (0.10 g, 0.52 mmol) was added. The total reaction mixture was placed in a Parr reactor and sealed, then heated in an oven at 134 °C for 3 h. After cooling, the mixture was centrifuged, supernatant decanted and the black precipitate dried to give a black powder.

b) A 0.1 M $FeSO_4.6H_2O$ aqueous solution (2.5 mL, 1 eq) and n-decylamine (0.17 mL, 1.0 mmol, 4 eq) were added to a Parr reactor, sealed and heated in an oven at 200 °C for 10 min. The reaction was

stopped by quenching the reactor in a water bath at room temperature. The reactor was rinsed with ethanol then water and the solid nanoparticles were collected by 5 cycles of centrifugation-decantation.

b) Fe_3O_4 nanoparticles via co-precipitation [8]

$FeCl_3.6H_2O$ (1.17 g, 4.33 mmol) and $FeCl_2.4H_2O$ (0.43 g, 2.16 mmol) were dissolved in deionised water (40 mL) that was purged with nitrogen gas for 1 h. The mixture was stirred vigorously under nitrogen at 90 °C. Aqueous ammonia (1.5 mL) was added to the iron solution which resulted in a colour change from orange to black immediately. The as-formed nanoparticles were isolated using a magnet and washed 3 times with deionised water, and 3 times with ethanol. The nanoparticles were dispersed in ethanol (40 mL), and 20 mL of this solution was used in the following reaction. The remainder had the ethanol decanted and the nanoparticles dried.

c) Fe_3O_4 via high temperature thermal decompositions [24]

$Fe(acac)_3$ (2 mmol), 1,2-hexadecanediol (10 mmol), oleic acid (6 mmol), oleylamine (6 mmol), and benzyl ether (20 mL) were placed in a round bottomed flask under nitrogen, and stirred. The mixture was heated to 200 $^{\circ}$C for 2 h, then heated to reflux (approx 300 $^{\circ}$C) for 1 h. The mixture was a black-coloured solution after heating and was left to cool to room temperature. Under ambient conditions, ethanol (40 mL) was added to the reaction mixture until a black precipitate formed and this was separated by centrifugation. The black product was redispersed in hexane (approx 30 mL) and the mixture centrifuged to remove undispersed particles. The hexane layer was precipitated with ethanol, centrifuged then redispersed into hexane (in a typical synthesis, the final solution was made up to approximately 20 mL hexane).

2.4.2 Silica coated nanoparticles [10]

This reaction was carried out in a non-glass vessel: To the 20 mL of the above solution of nanoparticles in ethanol, was added ultrapure water (5 mL), and aqueous ammonia (0.25 mL). The mixture was sonicated for 5 min. Then, tetraethylorthosilicate (TEOS, 0.5 mL) was added to the reaction mixture, and sonicated for a further 5 min. The reaction mixture was stirred for 4 h, then magnetic separation was carried out to separate the nanoparticles which were washed with ethanol

and DMF three times. The isolated nanoparticles were immersed in 1 M HCl for 20 min to dissolve any uncoated IONPs. After separating the silica coated NPs from the HCl solution, the coated NPs were washed again with ethanol then dried under vacuum.

2.4.3 Synthesis of phosphate-PEG$_6$-amine ligand

A mathematical shorthand is used to denote the positions of oxygen atoms in the elongated PEG chains, in this case 17-tosyloxy-3n$_{15}^{3}$-pentaoxaheptadecan-1-ol represents 17-tosyloxy-3,6,9,12,15-pentaoxaheptadecan-1-ol.

a) Synthesis of 17-tosyloxy-3n$_{15}^{3}$-pentaoxaheptadecan-1-ol (1) [31]

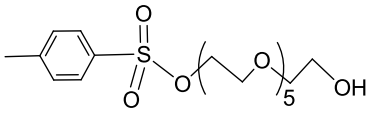

1 was synthesised according to a literature method.[31] To a chilled (0 °C) solution of hexaethylene glycol (5.00 g, 17.7 mmol, 1.0 eq) in DCM (50 mL), were added Ag_2O (6.15 g, 26.6 mmol, 1.5 eq), TsCl (3.70 g, 19.5 mmol, 1.1 eq), and KI (0.59 g, 3.54 mmol, 0.2 eq). After stirring for 30 min, the silver salts were removed by filtration through a pad of celite, which was washed thoroughly with EtOAc. The combined filtrated was concentrated, and the residue purified by silica column chromatography with DCM/acetone (3:2) as eluent, R_f 0.35. The product was obtained as a colourless oil (5.37 g, 12.3 mmol, 70 % yield). ^{1}H NMR (400 MHz, $CDCl_3$): δ 2.45 (3H, s, Me H's on Ts), 2.68 (1H, br s, O*H*), 3.58 – 3.71 (22H, m, C*H*$_2$-C*H*$_2$-O), 4.14 (2H, t, $^3J_{H\text{-}H}$ = 4.6 Hz, -C*H*$_2$-O-Ts), 7.34 (2H, d, $^3J_{H\text{-}H}$ = 7.8 Hz, Ts ring H), 7.79 (2H, d, $^3J_{H\text{-}H}$ = 7.8 Hz, Ts ring H). ^{13}C{^{1}H} NMR (100 MHz, $CDCl_3$): δ 144.8, 133.0, 130.0, 128.0, 72.5, 70.7, 70.6, 70.5, 70.3, 69.3, 68.7, 61.7, 21.6. ESI-HRMS calc. for $C_{19}H_{32}O_9SNa$ 459.1665 found (m/z): 459.1656 $[M + Na]^+$. Anal. Calc. for $C_{19}H_{32}O_9S$: C, 52.28; H, 7.39. Found: C, 52.10; H, 7.50.

b) Synthesis of 17-azido-3n$_{15}^{3}$-pentaoxaheptadecan-1-ol (2) [33,34]

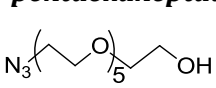

2 was synthesised via a modification of literature methods.[33,34] 17-Tosyloxy-3n$_{15}^{3}$-pentaoxaheptadecan-1-ol (1.00 g, 2.29 mmol) was dissolved in dry acetonitrile (20 mL) under nitrogen. Sodium azide (0.74 g, 11.46 mmol) was added in one portion and the mixture heated at 60 °C overnight. Once cooled, the reaction mixture was filtered over celite and washed with more

MeCN and EtOAc. The combined filtrates were evaporated to give **2** as a pale yellow oil (0.69 g, 2.25 mmol, 98 % yield). ^{1}H NMR (400 MHz, $CDCl_3$): δ 2.83 (1H, br s, O*H*), 3.41 (2H, t, $^{3}J_{H\text{-}H}$ = 5.15 Hz, -C*H*$_2$-N_3), 3.62 – 3.73 (22H, m, C*H*$_2$-C*H*$_2$-O). ^{13}C{^{1}H} NMR (100 MHz, $CDCl_3$): δ 72.5, 70.7, 70.6, 70.5, 70.3, 70.0, 61.7, 50.6. ESI-HRMS calc. for $C_{12}H_{26}N_3O_6$ 308.1822 found (m/z): 308.1823 $[M + H]^+$. IR (ν/cm^{-1}): 2102 (N≡N). Anal. Calc. for $C_{12}H_{25}N_3O_6$: C, 46.89; H, 8.20; N, 13.67. Found: C, 46.90; H, 8.10; N, 13.52.

c) Synthesis of phosphate-PEG-azide (3) [35]

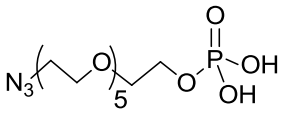

3 was synthesised following a similar phosphorylation reaction in the literature.[35] 17-Azido-3n-pentaoxaheptadecan-1-ol (1.00 g, 3.25 mmol) and triethylamine (0.36 g, 3.58 mmol) was dissolved in dry THF (20 mL). The mixture was cooled to 0 °C and $POCl_3$ (0.55 g, 0.33 mL, 3.58 mmol) was added dropwise. The reaction mixture was stirred for 3 h at room temperature, then quenched with H_2O. After checking that the solution had a pH < 2, the product was extracted into $CHCl_3$ (3 x 15 mL). The combined organic extracts were dried over $MgSO_4$ and solvent evaporated to give a colourless oil (0.55 g, 1.42 mmol, 44 % yield). ^{1}H NMR (400 MHz, $CDCl_3$): δ 3.41 (2H, t, $^{3}J_{H\text{-}H}$ = 6.50 Hz, -C*H*$_2$-N_3), 3.60 – 3.80 (22H, m, C*H*$_2$-C*H*$_2$-O), 9.17 (s, -PO(O*H*)$_2$). ^{13}C {^{1}H} NMR (100 MHz, $CDCl_3$): δ 70.6, 70.5, 70.4, 70.0, 50.7. ^{31}P{^{1}H} NMR (162 MHz, $CDCl_3$): δ 1.32. ESI-HRMS calc. for $C_{12}H_{27}N_3O_9P$ 388.1485 found (m/z): 388.1478 $[M + H]^+$. IR (ν/cm^{-1}): 2113 (N≡N), 1115 (P=O). Anal. Calc. for $C_{12}H_{26}N_3O_9P$: C, 37.21; H, 6.77; N, 10.85. Found: C, 37.35; H, 6.85; N, 10.69.

d) Synthesis of phosphate-PEG-amine (4) [36]

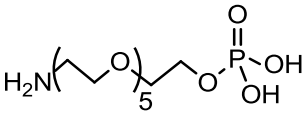

4 was synthesised following the reduction of an azide to an amine via similar literature protocols.[36] Phosphate-PEG-azide (0.50 g, 1.29 mmol) was dissolved in methanol (3.87 mL) and stirred with 10 % Pd-C (10 % by weight). Neat triethylsilane (1.50 g, 12.9 mmol) was added dropwise and the reaction mixture left to stir at room temperature for 6 h. At the end of the reaction, the mixture was filtered over celite, and washed through with methanol. The solvent was evaporated to give the product as a pale yellow oil which was dried overnight under vacuum (0.39 g, 1.08 mmol, 85 % yield). ^{1}H NMR

(400 MHz, $CDCl_3$): δ 3.24 (2H, t, $^3J_{H-H}$ = 5.15 Hz, -C*H*$_2$-NH$_2$), 3.50 – 3.90 (22H, m, -C*H*$_2$-C*H*$_2$-O), 8.13 (s, -PO(O*H*)$_2$ or N*H*$_2$). $^{13}C\{^1H\}$ NMR (100 MHz, $CDCl_3$): δ 70.6, 70.4, 70.2, 70.0, 67.3. $^{31}P\{^1H\}$ NMR (162 MHz, $CDCl_3$): δ 0.6. ESI-HRMS calc. for $C_{12}H_{29}NO_9P$ 362.1580 found (m/z): 362.1595 $[M + H]^+$. IR (v/cm^{-1}): 1115 (P=O). Anal. Calc. for $C_{12}H_{28}NO_9P$: C, 39.89; H, 7.81; N, 3.88. Found: C, 37.38; H, 8.34; N, 3.45. *values are slightly awry due to possible salt contamination.

2.4.4 Synthesis of alkyne and thiol bisphosphonates

a) Methylmethoxy intermediate (5) [70]

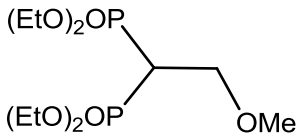

5 was synthesised according to a literature method.[70] Diethylamine (0.29 g, 4.00 mmol) and paraformaldehyde (0.61 g, 20.0 mmol) were dissolved in dry methanol (12 ml) and warmed until clear. Tetraethylmethylene bisphosphonate (1.16 g, 1.00 ml, 4.00 mmol) was added and the mixture heated to reflux for 24 h. The methanol was removed under vacuum, toluene (15 ml) added and then concentrated. This was repeated four times to ensure all the methanol was removed. The methylmethoxy intermediate was isolated as a colourless oil (1.00 g, 3.00 mmol, 75 % yield). ^1H NMR (400 MHz, $CDCl_3$): δ 4.18 (8H, m), 3.88 (2H, td, $^3J_{H-H}$ = 5.60 and 16.0 Hz), 3.37 (3H, s), 2.69 (1H, tt, $^3J_{H-H}$ = 5.30 and 24.0 Hz), 1.32 (12H, t, $^3J_{H-H}$ = 7.00 Hz). $^{31}P\{^1H\}$ NMR (162 MHz, $CDCl_3$): δ 21.2.

b) Vinylidene bisphosphonate ester (6) [70]

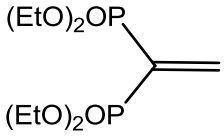

6 was synthesised according to a literature method.[70] The methylmethoxy intermediate (1.00 g, 3.00 mmol) was diluted with toluene (25 mL) and *p*-toluenesulfonic acid monohydrate (0.1 g) added. The reaction was heated to reflux over CaH_2 in a Soxhlet attachment for 14 h, then cooled and toluene removed. DCM (25 mL) was added and washed with water (3 x 15 mL). The combined organic layers were dried over $MgSO_4$, filtered and solvent removed under vacuum to yield a light yellow oil (0.86 g, 2.87 mmol, 96 % yield). ^1H NMR (400 MHz, $CDCl_3$): δ 7.01 (2H, dd, $^3J_{H-H}$ = 33.8 and 37.7 Hz), 4.17 (8H, m), 1.37 (12H, t, $^3J_{H-H}$ = 7.03 Hz). $^{31}P\{^1H\}$ NMR (162 MHz, $CDCl_3$): δ 13.1.

c) Conversion of phosphonate ester to free acid (7) [75,76]

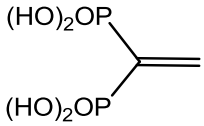

7 was synthesised according to a literature method.[75,76] Vinylidene bisphosphonate ester (0.50 g, 1.67 mmol) was dissolved in DCM (10 mL) and reacted with $BrSi(CH_3)_3$ (2.4 mL, 18.3 mmol) which was added dropwise at 0 °C. The mixture was then stirred at room temperature for 48 h. DCM was evaporated off and the free acid extracted into water (2 mL) and neutralised with 40 % aqueous tetrabutylammonium hydroxide to pH 4. The solution was dried *in vacuo* at 50 – 60 °C and again under the same conditions with 1-butanol (4 mL) to give a thick sticky mass which still contained butanol after drying under vacuum for 2 days (1.20 g crude yield. Assuming 100 % conversion and from NMR integration, 0.30 g of this was the free acid). ^{1}H NMR (400 MHz, D_2O): δ 6.50 (2H, dd, $^{3}J_{H\text{-}H}$ = 33.4 and 36.7 Hz). $^{31}P\{^{1}H\}$ NMR (162 MHz, D_2O): δ 9.2.

d) Synthesis of thiol bisphosphonate via 1,3-propane-dithiol (8a) [70]

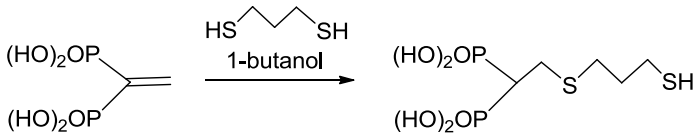

Alkene bisphosphonic acid **7** (0.30 g, 1.60 mmol) was dissolved in 1-butanol (2 mL) then 1,3-propane-dithiol (0.86 mL, 8.00 mmol) added. The mixture was heated to reflux under nitrogen for 2.5 h. After the mixture was cooled, water (25 mL) was added then washed with hexane (3 x 15 mL). The aqueous layer was concentrated under vacuum to give a yellow oil **8a**. Again, a large amount of butanol was still present after drying under vacuum (1.00 g crude yield. Assuming 100 % conversion and from NMR integration, 0.05 g of this was the free acid, 0.17 mmol, 10 % yield). ^{1}H NMR (400 MHz, D_2O): δ 2.90 (2H, td, $^{3}J_{H\text{-}H}$ = 6.50 and 15.5 Hz), 2.60 (2H, t, $^{3}J_{H\text{-}H}$ = 7.19 Hz), 2.52 (2H, t, $^{3}J_{H\text{-}H}$ = 6.89 Hz), 2.27 (1H, tt, $^{3}J_{H\text{-}H}$ = 6.60 and 19.9 Hz), 1.79 (2H, p, $^{3}J_{H\text{-}H}$ = 7.02 Hz). $^{31}P\{^{1}H\}$ NMR (162 MHz, D_2O): δ 18.8.

e) Synthesis of thiol bisphosphonate via cystamine (8b) [71]

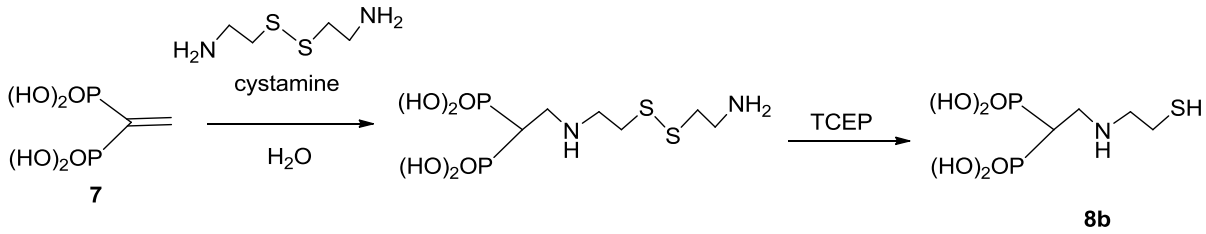

Preparation of cystamine base: Cystamine dihydrochloride (10.00 g, 0.044 mol) was dissolved in water (13 mL). To this was added Et_2O (50 mL) and THF (20 mL). The mixture was cooled to 0 °C, and the temperature maintained during the slow addition of 40 % NaOH solution (60 mL, 0.622 mol). The layers were separated and the aqueous layer extracted with Et_2O (20 mL), and THF (15 mL). The combined organic layers were dried over solid NaOH at 4 °C, and then filtered. The residue was washed with Et_2O (20 mL) and THF (10 mL), and the combined filtrate dried *in vacuo* to give the crude product as a pale yellow residue (6.86 g). The crude residue was purified by vacuum distillation (0.05 mm Hg, b.p. 85 – 90 °C) to give the cystamine base as a thick colourless syrup (3.62 g, 0.024 mol, 54 %). The free base decomposes at room temperature and should be stored at -20 °C. ^{1}H NMR (400 MHz, $CDCl_3$): δ 1.24 (4H, br s), 2.73 (4H, t, $^3J_{H\text{-}H}$ = 6.30 Hz), 2.98 (4H, t, $^3J_{H\text{-}H}$ = 6.30 Hz).

Alkene bisphosphonic acid **7** (0.25 g, 1.329 mmol) was added to cystamine base (0.20 g, 1.329 mmol) in water. The mixture was dried over a steam bath until a clear syrup was obtained. The resultant syrup was heated at 100 ^{o}C for 5 h at which point the mixture turned a dark brown colour. After cooling, the residue was dissolved in water (10 mL) and acetic acid (0.15 mL, 2.66 mmol) was added. The reaction was protected with nitrogen gas and cooled to 15 ^{o}C. Tris(2-carboxyethyl)phosphine (0.50 g, 2.00 mmol) was added in two portions and stirred at room temperature for 2 h. The mixture was filtered by cannula, the filtrate diluted with water and concentrated to half the volume under reduced pressure. This was then passed through an ion-exchange resin in H-form, and eluted with water until neutral. The water was removed under vacuum to give a yellow syrup of **8b** (0.31 g, 1.17 mmol, 88 % yield). ^{1}H NMR (400 MHz, D_2O): δ 2.48 (1H, tt, $^3J_{H\text{-}H}$ = 7.00 Hz and $^2J_{P\text{-}H}$ = 20.0 Hz), 2.80 (2H, t, $^3J_{H\text{-}H}$ = 6.00 Hz), 3.24 (2H, t, $^3J_{H\text{-}H}$ = 6.00 Hz), 3.42 (2H, td, $^3J_{H\text{-}H}$ = 7.00 Hz and $^3J_{P\text{-}H}$ = 14.00 Hz).

f) Synthesis of alkyne bisphosphonate (10) [69]

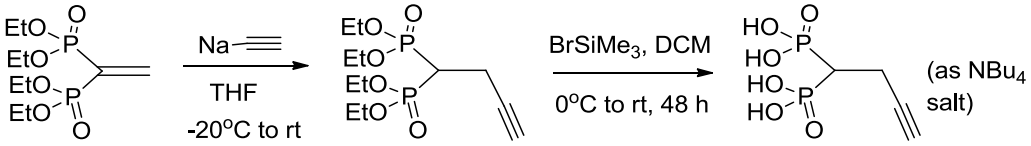

6 **9** **10**

Alkene bisphosphonate ester **6** (0.25 g, 0.833 mmol) was dissolved in dry THF (2.50 mL). A slurry of sodium acetylenide in xylene (0.23 mL, 18 % solution) was added dropwise at -15 °C. The reaction mixture was allowed to warm to room temperature and stirred for 48 h. After this time, ether (5 mL) and 1M HCl (5 mL) was added to the reaction mixture. The organic layer was washed with 1M HCl (5 mL), brine (2 x 5 mL) and dried over magnesium sulphate. The solvent was removed under reduced pressure to give a yellow oil **9** (0.21 g, 0.627 mmol, 75 % yield). ^{1}H NMR (400 MHz, $CDCl_3$): δ 1.39 (12H, t, $^{3}J_{H-H}$ = 7 Hz), 2.09 (1H, s), 2.50 – 2.90 (3H, m), 4.10 – 4.30 (8H, m). $^{31}P\{^{1}H\}$ NMR (162 MHz, $CDCl_3$): δ 21.4.

Alkyne bisphosphonate ester **9** (0.10 g, 0.306 mmol) was dissolved in dry DCM (3 mL). The mixture was cooled in an ice bath and $BrSiMe_3$ (0.28 mL, 2.15 mmol) was added dropwise. The reaction mixture was allowed to warm to room temperature and stirred for 48 h. The solvent was removed *in vacuo*, dissolved in water (2 mL) and neutralised with 40 % tetrabutylammonium hydroxide to pH 4. The solution was dried *in vacuo* at 60 °C to give a sticky white solid with oily residues **10** (0.24 g, 0.205 mmol, 67 % yield). ^{1}H NMR (400 MHz, D_2O): δ 1.98 (1H, s), 2.39 – 2.73 (3H, m). $^{31}P\{^{1}H\}$ NMR (162MHz, D_2O): δ 18.0.

2.4.5 Ligand exchanges

a) Sulfonate 1 (NP-S1)

7-Amino-1,3-naphthalenedisulfonic acid monopotassium salt monohydrate (50 mg) was dissolved in DMSO (5 mL). To this, bulk oleic acid-capped nanoparticles (2 mL from 20 mL hexane stock) which were precipitated out of hexane and resuspended in toluene (2 mL), were added. The reaction mixture was stirred for 2 days after which time the mixture was centrifuged. The supernatant was decanted and the pellet taken up in basic H_2O to remove any remaining ligand. The nanoparticles were separated by a magnet and the supernatant again decanted. DMSO was added and the solution treated with 1 M HCl, quickly sonicated and acetone added to precipitate the particles. It was important to ensure that this acid step took no more than 1 – 2 minutes to prevent the

digestion of the nanoparticles. Separation of the nanoparticles by magnet yielded a black solid that was resuspended in DMSO.

b) Sulfonate 2 (NP-S2)

6-Amino-2-naphthalenesulfonic acid monohydrate (50 mg) was dissolved in water (5 mL) and the pH adjusted to 9/10 with 1 M KOH. To this, bulk oleic acid-capped nanoparticles (2 mL from 20 mL hexane stock) which were precipitated out of hexane and resuspended in THF (2 mL), were added. The reaction mixture was stirred for 2 days after which time the mixture was centrifuged. The supernatant was decanted and the pellet taken up in basic H_2O to remove any remaining ligand. The nanoparticles were separated by a magnet and the supernatant again decanted. DMSO was added and the solution treated with 1 M HCl, quickly sonicated and acetone added to precipitate the particles. It was important to ensure that this acid step took no more than 1 – 2 minutes to prevent the digestion of the nanoparticles. Separation of the nanoparticles by magnet yielded a black solid that was resuspended in DMSO.

c) Sulfonate 3 (NP-S3)

This ligand exchange followed the same method as for **NP-S2** above but with sodium 4-amino-5-hydroxy-2,7-naphthalene disulfonate hydrate as the ligand. Workup was as before.

d) Sulfonate 4 (NP-S4)

This ligand exchange followed the same method as for **NP-S2** and **NP-S3** above but with 6-amino-4-hydroxy-2-naphthalenesulfonic acid as the ligand. Workup was as before.

e) Monodentate phosphate-PEG$_6$-amine (NP1)

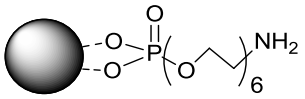

Bulk oleic acid-capped nanoparticles (2 mL from 20 mL stock) were precipitated out of hexane and redissolved in chloroform (2 mL). Monophosphate-PEG$_6$-amine (100 mg) was dissolved in chloroform

(4 mL). The two solutions were combined and stirred at room temperature in a sealed vial for 3 days. Following this, some of the solvent was evaporated to leave a concentrated nanoparticle solution that was precipitated with hexane. The black solid was isolated by a magnet, resuspended in DCM and again precipitated with hexane. This was repeated 3 times in total before the nanoparticles were suspended in ethanol.

f) Bidentate bisphosphonate alendronate (NP2)

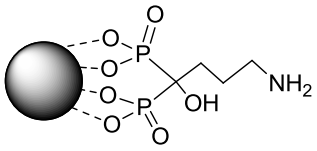

Bulk oleic acid-capped nanoparticles (2 mL from 20 mL stock) were precipitated out of hexane and redissolved in THF (2 mL). Sodium alendronate trihydrate (50 mg) was dissolved in water (5 mL) and the pH adjusted to 9 with 1 M KOH. The THF solution of the nanoparticles was added to the ligand solution, and stirred for 2 days. Then, the stirrer bar was removed and the nanoparticles isolated by a magnet. The supernatant was decanted and the black solid suspended in water. Acetone was added to wash out any remaining ligand and this was repeated a further two times. Finally, the nanoparticles were resuspended in water (approximately 5 mL for this scale of reaction) and the pH checked to ensure it was around 8 (adjusted accordingly with KOH solution).

2.4.6 Determination of iron concentration in nanoparticle samples by the Ferrozine assay

Prior to any coupling reactions with the nanoparticles, the iron concentration in a sample of nanoparticles was determined by a modified protocol of the original Ferrozine assay as described by Stookey.[80] The Ferrozine assay detailed below is based on a literature protocol by Viollier *et al*.[81]

The ferrozine reagent (monosodium salt hydrate of 3-(2-pyridyl)-5,6-diphenyl-1,2,4-triazine-*p,p'*-disulfonic acid) reacts with Fe^{2+} to form a stable purple complex species. This purple colour can be measured by UV-Vis spectroscopy, where the maximum absorbance is recorded at 562 nm. This method of determining iron concentration is used for all nanoparticles in solution and carried out prior to all coupling reactions on the relevant nanoparticles. As an example, typical iron concentration for alendronate coated nanoparticles is approximately 0.5 mg/mL.

Iron calibration standards between 0 – 50 µg/mL Fe(III) were prepared from a 1 mg/mL Fe(III) stock solution of $FeCl_3$ in deionised water. The following solutions were prepared for use in the assay:

a) Reducing agent solution was a 1.4 M hydroxylamine hydrochloride solution in 2 M HCl.
b) Ferrozine solution was 0.01 M Ferrozine in a 0.1 M ammonium acetate solution.
c) Final buffer was a 10 M ammonium acetate solution adjusted to pH 9.5 with NH_4OH solution.

10 µL of iron sample (calibration standard or NP sample) was diluted with deionised water (90 µL) and with 0.5 M HCl (900 µL) to bring the total volume to 1000 µL. The nanoparticle solutions were heated for 45 min at 70 °C to digest the nanoparticles. An aliquot of the heated solution (100 µL) was diluted with deionised water (750 µL) and the reducing agent solution (150 µL). The mixture was allowed to react for 30 min to complete the reduction of Fe(III). Ferrozine solution (100 µL) was added to the mixture, followed by the final buffer (150 µL). The absorbance of the solution at 562 nm was then recorded.

2.4.7 Protocols for further stability measurements

Experiment using healthy volunteers was approved by the local research ethics committee (P/00/029 East London and The City Local Research Ethics Committee 1). Informed written consent was provided according to the Declaration of Helsinki. Blood was collected into 3.2% sodium citrate and diluted 1:1 in RPMI-1640 before separation through a double-density gradient using Histopaque® 1077 and 1119 (Sigma-Aldrich).

a) In H_2O at different pH's

Water at different pH's (pH 1, 3, 5, 7, 9, 11, 13) were prepared by adjusting the pH of ultrapure water (5 mL) with 0.5 M HCl or 0.5 M KOH, and monitoring with a pH meter. 100 µL of prepared **NP1** (100 µL ethanol stock diluted with 100 µL H_2O to give a concentration of 0.75 mg/mL Fe) and **NP2** (1.0 mg/mL Fe in water) were added to vials containing 1 mL of the water at different pH. The stabilities of the particles were visually observed over time.

b) In NaCl solutions

NaCl solutions (10 mL each) of varying concentrations were prepared (0 %, 0.3 %, 0.6 %, 0.9 % and 1.2 % w/v) by dissolving NaCl (12.0 g) in water (10 mL) for a 1.2 % stock solution and diluting accordingly. 100 µL of prepared **NP1** (100 µL ethanol stock diluted with 100 µL H_2O to give a concentration of 0.75 mg/mL Fe) and **NP2** (1.0 mg/mL Fe in water) were added to vials containing 1 mL of the water at different pH. The stabilities of the particles were visually observed over time.

c) Toxicity in blood

Whole blood (750 µL) were incubated for 90 min at 37 °C in an orbital shaker with 10 mM PBS buffer (250 µL) solutions of the nanoparticles at 2 different concentrations (10 µg and 50 µg of each NP sample). Then the samples were centrifuged at 600 g for 5 mins, the pellet was discarded and the supernatant was incubated at room temperature for 30 more min to allow haemoglobin oxidation. Finally the absorbance of the samples was recorded at 560 nm.

2.5 References

1. S. Laurent, D. Forge, M. Port, A. Roch, C. Robic, L. Vander Elst, and R. N. Muller, *Chem. Rev.*, 2008, **108**, 2064–2110.
2. T. J. Daou, S. Begin-Colin, J. M. Grenèche, F. Thomas, A. Derory, P. Bernhardt, P. Legaré, and G. Pourroy, *Chem. Mater.*, 2007, **19**, 4494–4505.
3. T. J. Daou, G. Pourroy, J. M. Greneche, A. Bertin, D. Felder-Flesch, and S. Begin-Colin, *Dalton Trans.*, 2009, 4442–4449.
4. D. Portet, B. Denizot, E. Rump, J.-J. Lejeune, and P. Jallet, *J. Colloid Interf. Sci.*, 2001, **238**, 37–42.
5. S. Takami, T. Sato, T. Mousavand, S. Ohara, M. Umetsu, and T. Adschiri, *Mater. Lett.*, 2007, **61**, 4769–4772.
6. S. Ge, X. Shi, K. Sun, C. Li, J. R. Baker, M. M. Banaszak Holl, and B. G. Orr, *J. Phys. Chem. C*, 2009, **113**, 13593–13599.
7. U. Schwertmann and R. M. Cornell, *Iron oxides in the laboratory: Preparation and characterisation*, WILEY-VCH Verlag, 2000.
8. U. S. Patil, H. Qu, D. Caruntu, C. J. O'Connor, A. Sharma, Y. Cai, and M. A. Tarr, *Bioconjugate Chem.*, 2013, **24**, 1562–9.
9. C. Vogt, M. S. Toprak, M. Muhammed, S. Laurent, J.-L. Bridot, and R. N. Müller, *J. Nanopart. Res.*, 2009, **12**, 1137–1147.
10. C.-W. Lu, Y. Hung, J.-K. Hsiao, M. Yao, T.-H. Chung, Y.-S. Lin, S.-H. Wu, S.-C. Hsu, H.-M. Liu, C.-Y. Mou, C.-S. Yang, D.-M. Huang, and Y.-C. Chen, *Nano Lett.*, 2007, **7**, 149–154.
11. W. Stöber, A. Fink, and E. Bohn, *J. Colloid Interf. Sci.*, 1968, **26**, 62–69.
12. Y.-H. Deng, C.-C. Wang, J.-H. Hu, W.-L. Yang, and S.-K. Fu, *Colloid Surf. A*, 2005, **262**, 87–93.
13. S. H. Im, T. Herricks, Y. T. Lee, and Y. Xia, *Chem. Phys. Lett.*, 2005, **401**, 19–23.
14. Y. Lu, Y. Yin, B. T. Mayers, and Y. Xia, *Nano Lett.*, 2002, **2**, 183–186.
15. Y. A. Barnakov, M. H. Yu, and Z. Rosenzweig, *Langmuir*, 2005, **21**, 7524–7.
16. L. Yao, G. Xu, W. Dou, and Y. Bai, *Colloid Surf. A*, 2008, **316**, 8–14.
17. K. Osseo-Asare and F. J. Arriagada, *Colloid Surf.*, 1990, **50**, 321–339.
18. F. J. Arriagada and K. Osseo-Asare, *Colloid Surf.*, 1992, **69**, 105–115.
19. F. J. Arriagada and K. Osseo-Asare, *Colloid Surf. A*, 1999, **154**, 311–326.
20. S. Santra, R. Tapec, N. Theodoropoulou, J. Dobson, A. Hebard, and W. Tan, *Langmuir*, 2001, **17**, 2900–2906.
21. A.-H. Lu, E. L. Salabas, and F. Schüth, *Angew. Chem. Int. Ed.*, 2007, **46**, 1222–44.
22. M. Zhang, B. L. Cushing, and C. J. O'Connor, *Nanotechnology*, 2008, **19**, 85601.
23. A. Narita, K. Naka, and Y. Chujo, *Colloid Surf. A*, 2009, **336**, 46–56.
24. S. Sun, H. Zeng, D. B. Robinson, S. Raoux, P. M. Rice, S. X. Wang, and G. Li, *J. Am. Chem. Soc.*, 2004, **126**, 273–279.
25. X. Sun, C. Zheng, F. Zhang, Y. Yang, G. Wu, A. Yu, and N. Guan, *J. Phys. Chem. C*, 2009, **113**, 16002–16008.
26. D. Zhang, A. B. Karki, D. Rutman, D. P. Young, A. Wang, D. Cocke, T. H. Ho, and Z. Guo, *Polymer*, 2009, **50**, 4189–4198.
27. S. A. Corr, Y. K. Gun'ko, R. Tekoriute, C. J. Meledandri, and D. F. Brougham, *J. Phys. Chem. C*, 2008, **112**, 13324–13327.

28. K. V. P. M. Shafi, A. Ulman, X. Yan, N.-L. Yang, C. Estournès, H. White, and M. Rafailovich, *Langmuir*, 2001, **17**, 5093–5097.
29. F. Benyettou, I. Milosevic, J. Olsen, L. Motte, and A. Trabolsi, *J. Bioanal. Biomed.*, 2012, 006.
30. H.-K. Mao, T. Takahashi, W. A. Bassett, G. L. Kinsland, and L. Merrill, *J. Geophys. Res.*, 1974, **79**, 1165–1170.
31. F. A. Loiseau, K. K. Hii, and A. M. Hill, *J. Org. Chem.*, 2004, **69**, 639–47.
32. A. Bouzide and G. Sauvé, *Tetrahedron Lett.*, 1997, **38**, 5945–5948.
33. Y. Ju, D. Kumar, and R. S. Varma, *J. Org. Chem.*, 2006, **71**, 6697–700.
34. M. J. Linman, J. D. Taylor, H. Yu, X. Chen, and Q. Cheng, *Anal. Chem.*, 2008, **80**, 4007–13.
35. M. A. White, J. A. Johnson, J. T. Koberstein, and N. J. Turro, *J. Am. Chem. Soc.*, 2006, **128**, 11356–11357.
36. P. K. Mandal and J. S. McMurray, *J. Org. Chem.*, 2007, **72**, 6599–6601.
37. C. Boyer, M. R. Whittaker, V. Bulmus, J. Liu, and T. P. Davis, *NPG Asia Mater.*, 2010, **2**, 23–30.
38. A. Hofmann, S. Thierbach, A. Semisch, A. Hartwig, M. Taupitz, E. Ruhl, and C. Graf, *J. Mater. Chem.*, 2010, **20**, 7842–7853.
39. H. Fleisch, R. G. G. Russell, B. Simpson, and R. C. Muhlbauer, *Nature*, 1969, **223**, 211–212.
40. M. D. Francis, R. Graham, G. Russell, and H. Fleisch, *Science*, 1969, **165**, 1264–1266.
41. H. Fleisch, R. Graham, G. Russell, and M. D. Francis, *Science*, 1969, **165**, 1262–1264.
42. D. Fernández, D. Vega, and A. Goeta, *Acta Crystallogr. C*, 2003, **59**, m543–m545.
43. R. G. G. Russell, M. J. Rogers, J. C. Frith, S. P. Luckman, F. P. Coxon, H. L. Benford, P. I. Croucher, C. Shipman, and H. A. Fleisch, *J. Bone Miner. Res.*, 1999, **14**, 53–65.
44. G. H. Nancollas, R. Tang, R. J. Phipps, Z. Henneman, S. Gulde, W. Wu, A. Mangood, R. G. G. Russell, and F. H. Ebetino, *Bone*, 2006, **38**, 617–27.
45. A. Fitton and D. McTavish, *Drugs*, 1991, **41**, 289–318.
46. L. Widler, K. A. Jaeggi, M. Glatt, K. Muller, R. Bachmann, M. Bisping, A.-R. Born, R. Cortesi, G. Guiglia, H. Jeker, R. Klein, U. Ramseier, J. Schmid, G. Schreiber, Y. Seltenmeyer, and J. R. Green, *J. Med. Chem.*, 2002, **45**, 3721–3738.
47. H. Fleisch, *Endocr. Rev.*, 1998, **19**, 80–100.
48. S. Kunnas-Hiltunen, M. Haukka, J. Vepsäläinen, and M. Ahlgrén, *Dalton Trans.*, 2010, **39**, 5310–8.
49. S. Kunnas-Hiltunen, M. Matilainen, J. J. Vepsäläinen, and M. Ahlgrén, *Polyhedron*, 2009, **28**, 200–204.
50. E. Gumienna-Kontecka, R. Silvagni, R. Lipinski, M. Lecouvey, F. Cesare Marincola, G. Crisponi, V. M. Nurchi, Y. Leroux, and H. Kozlowski, *Inorg. Chim. Acta*, 2002, **339**, 111–118.
51. E. Gumienna-Kontecka, J. Jezierska, M. Lecouvey, Y. Leroux, and H. Kozlowski, *J. Inorg. Biochem.*, 2002, **89**, 13–17.
52. P. Yin, L.-M. Zheng, S. Gao, and X.-Q. Xin, *Chem. Commun.*, 2001, 2346–2347.
53. M. Kontturi, E. Laurila, R. Mattsson, S. Peräniemi, J. J. Vepsäläinen, and M. Ahlgrén, *Inorg. Chem.*, 2005, **44**, 2400–6.
54. D.-K. Cao, S. Gao, and L.-M. Zheng, *J. Solid State Chem.*, 2004, **177**, 2311–2315.
55. L. Wang, Z. Yang, J. Gao, K. Xu, H. Gu, B. Zhang, X. Zhang, and B. Xu, *J. Am. Chem. Soc.*, 2006, **128**, 13358–9.
56. Q. Jin, L. Ricard, and F. Nief, *Polyhedron*, 2005, **24**, 549–555.
57. G. Franc, C.-O. Turrin, E. Cavero, J.-P. Costes, C. Duhayon, A.-M. Caminade, and J.-P. Majoral, *Eur. J. Org. Chem.*, 2009, **2009**, 4290–4299.

58. W. Gao, L. Dickinson, C. Grozinger, F. G. Morin, and L. Reven, *Langmuir*, 1996, **12**, 6429–6435.
59. S. Marcinko and A. Y. Fadeev, *Langmuir*, 2004, **20**, 2270–2273.
60. G. Lecollinet, N. Delorme, M. Edely, A. Gibaud, J.-F. Bardeau, F. Hindré, F. Boury, and D. Portet, *Langmuir*, 2009, **25**, 7828–35.
61. I. Řehoř, V. Kubíček, J. Kotek, P. Hermann, I. Lukeš, J. Száková, L. Vander Elst, R. N. Muller, and J. A. Peters, *J. Mater. Chem.*, 2009, **19**, 1494.
62. G. Busch, E. Jaehne, X. Cai, S. Oberoi, and H.-J. P. Adler, *Synth. Met.*, 2003, **137**, 871–872.
63. M. Cinier, M. Petit, M. N. Williams, R. M. Fabre, F. Pecorari, D. R. Talham, B. Bujoli, and C. Tellier, *Bioconjugate Chem.*, 2009, **20**, 2270–7.
64. G. Fonder, J. Delhalle, M. Essahli, B. Ameduri, and Z. Mekhalif, *Surf. Interface Anal.*, 2008, **40**, 85–96.
65. R. Torres Martin de Rosales, R. Tavarel, A. Glaria, G. Varma, A. Protti, and P. J. Blower, *Bioconjugate Chem.*, 2011, **22**, 455–465.
66. R. Torres Martin de Rosales, R. Tavaré, R. L. Paul, M. Jauregui-Osoro, A. Protti, A. Glaria, G. Varma, I. Szanda, and P. J. Blower, *Angew. Chem. Int. Ed.*, 2011, **50**, 5509–13.
67. Y. Sahoo, H. Pizem, T. Fried, D. Golodnitsky, L. Burstein, C. N. Sukenik, and G. Markovich, *Langmuir*, 2001, **17**, 7907–7911.
68. D. Portet, B. Denizot, E. Rump, F. Hindre, J.-J. Le Jeune, and P. Jallet, *Drug Dev. Res.*, 2001, **54**, 173–181.
69. H. Skarpos, S. N. Osipov, D. V Vorob'eva, I. L. Odinets, E. Lork, and G.-V. Roschenthaler, *Org. Biomol. Chem.*, 2007, **5**, 2361–2367.
70. G. Bansal, J. E. I. Wright, S. Zhang, R. F. Zernicke, and H. Uludag, *J. Biomed. Mater. Res. A*, 2005, **74A**, 618–628.
71. I. S. Alferiev, J. M. Connolly, and R. J. Levy, *J. Organomet. Chem.*, 2005, **690**, 2543–2547.
72. I. S. Alfer'ev, I. L. Kotlyarevskii, N. V. Mikhalin, and V. M. Novikova, *B. Acad. Sci. USSR Ch+*, 1983, **32**, 2515–2518.
73. I. S. Alfer'ev and N. V. Mikhalin, *Bull. Russ. Acad. Sci. Div. Chem. Sci.*, 1992, **41**, 1709–1711.
74. D. W. Hutchinson and D. M. Thornton, *J. Org. Chem.*, 1988, **346**, 341–348.
75. C. McKenna, M. Higa, N. Cheung, and M. McKenna, *Tetrahedron Lett.*, 1977, 155–158.
76. C. R. Degenhardt and D. C. Burdsall, *J. Org. Chem.*, 1986, **51**, 3488–3490.
77. J. H. Lin, I.-W. Chen, and F. A. Deluna, *J. Pharm. Sci.*, 1994, **83**, 1741–1746.
78. M. A. Dobrovolskaia, A. K. Patri, J. Zheng, J. D. Clogston, N. Ayub, P. Aggarwal, B. W. Neun, J. B. Hall, and S. E. McNeil, *Nanomed.*, 2009, **5**, 106–17.
79. M. A. Dobrovolskaia, J. D. Clogston, B. W. Neun, J. B. Hall, A. K. Patri, and S. E. McNeil, *Nano Lett.*, 2008, **8**, 2180–7.
80. L. L. Stookey, *Anal. Chem.*, 1970, **42**, 779–781.
81. E. Viollier, P. . Inglett, K. Hunter, A. . Roychoudhury, and P. Van Cappellen, *Appl. Geochem.*, 2000, **15**, 785–790.

CHAPTER 3

Further functionalisation of the nanoparticles

3 Further functionalisation of the nanoparticles

3.1 Introduction

This chapter discusses the functionalisation of **NP2** (alendronate coated nanoparticles) with PEG for improving water-solubility and for biocompatibility. The main focus was to synthesise a dual-modal MRI/PET imaging agent incorporating iron oxide nanoparticles for the MRI moiety, and Ga-68 as the PET moiety.

With the nanoparticle surface coated with sodium alendronate (**NP2**), the surface of the nanoparticles was further functionalised by coating the nanoparticles with i) polyethylene glycol (PEG) to enhance blood lifetime, ii) a targeting moiety, in this case an antibody for plaque imaging, and, iii) a strained alkyne for copper-free click reaction with a Ga-68 moiety to give a dual-modal MRI/PET imaging agent. The terminal functional group at each step is typically a chemical group that can be reacted further by moderately simple chemistry. The use of peptide coupling chemistry using 1-ethyl-3-(3-dimethylaminopropyl)carbodiimide (EDC) to react amines and carboxylic acids together is exploited. In this case, the amine functional group was the terminal reactive group on the nanoparticle surface with the carboxylic acid group on each of the PEG, the strained alkyne and the targeting moiety.

The dual-modal MRI/PET imaging agent can be assembled in two ways. The first would be to carry out the cycloaddition reaction between the azide and alkyne to form a single probe prior to injection. This method can be further broken down into two routes, with the azide-DOTA moiety being radiolabelled with the Ga-68 either before or after the cycloaddition reaction. Both routes have disadvantages; gallium chelation typically requires elevated temperatures and an acidic environment, both of which affect nanoparticle stability and thus radiolabelling after the cycloaddition reaction would not be ideal. However, radiolabelling before the cycloaddition reaction prior to injection into the patient would result in diminished radioactivity, which is also less than ideal. Another disadvantage of having a single pre-combined nanoparticle MRI/PET probe is the large size that would slow down *in vivo* movement, diminishing radioactivity before reaching its target. Therefore, an alternative route would be to carry out the cycloaddition reaction *in vivo*, with the administration of the two contrast agents separately. Pre-targeting using a magnetic nanoparticle followed by the injection of the radio-labelled molecule at the correct time will ensure radioactivity remains sufficiently high. The functionalisation of the nanoparticles begins with PEGylation, followed by the strained alkyne and the targeting moiety (**Scheme 3.1**), followed by the copper-free cycloaddition reaction *in vivo*.

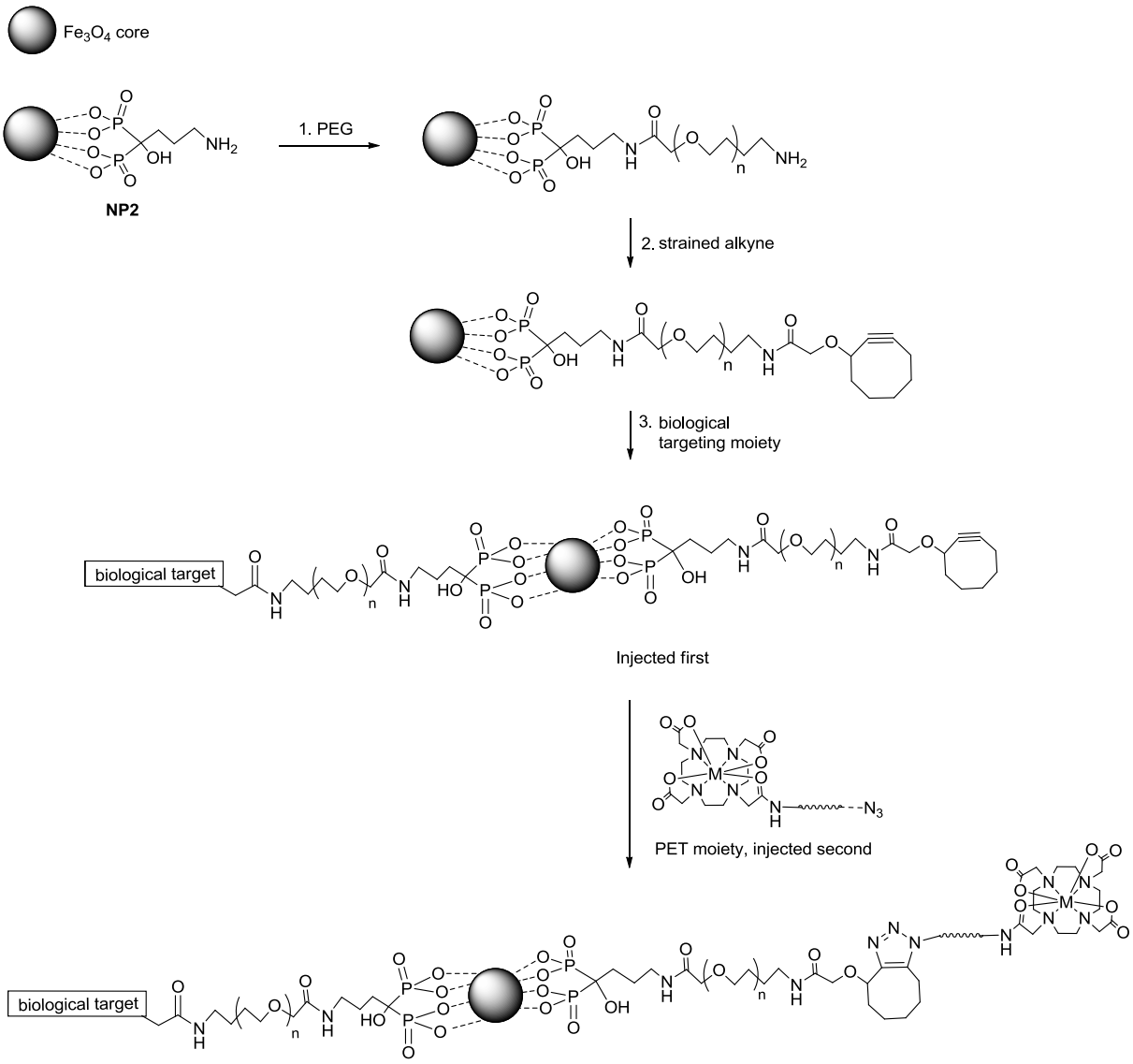

Scheme 3.1 General synthetic scheme for the decoration of nanoparticle surface with PEG, strained alkyne and targeting moiety, followed by reaction between the alkyne (on NP) and azide (on PET moiety) *in vivo*.

Herein, the synthesis and characterisation of the nanoparticles during the PEGylation and coupling of the strained alkyne will be discussed. Prior to using radioactive gallium, model copper-free click reactions with the lanthanide complexes to confirm the success of the click reactions were carried out.

3.2 PEGylation of nanoparticles

Nanoparticles are highly advantageous for use as imaging and therapy agents as they are able to carry high payloads, have high stability, and are able to carry out multiple, simultaneous applications as a result of their high surface area to volume ratio.[1] Despite these advantages, nanoparticle use in medicine has been hampered by several factors, the most significant of which is the ability of the particles to remain in the body long enough to reach the targeted site of action. Nanoparticles are readily cleared from the body by a variety of mechanisms, one of which is elimination by phagocytes in the mononuclear phagocyte system (MPS).[2] Plasma proteins attach to the nanoparticles and are recognised as foreign material by phagocytes in the blood and other tissues. The nanoparticles are engulfed and sent to the liver and spleen for excretion. The nanoparticles can accumulate in the MPS and there have been concerns of toxicity if the nanoparticle aggregates are trapped in the lungs or elsewhere due to capillary obstruction.[3]

Polyethylene glycol (PEG) has been used extensively in the literature to coat nanoparticle surfaces and is undeniably one of the most popular methods to improve blood lifetimes and introduce stealth properties.[3–6] PEG is a coiled, hydrophilic polymer consisting of repeating ethylene ether units which can be attached onto the surface of nanoparticles. The addition of PEG to the nanoparticle surface has been shown to reduce MPS uptake and increase blood circulation time, compared to uncoated nanoparticles.[7]

Circulation half-time ($t_{½}$) is the time period over which more than 50 % of the injected nanoparticles remain in the blood stream, similar to that of the half-life of a drug.[8] In order for nanoparticles to be effective at its application, be it imaging or drug delivery, the $t_{½}$ should be long enough that the particles reach their intended target, as well as remaining there in sufficient concentration for a certain amount of time before image capture or drug delivery. The ideal $t_{½}$ is dependent on application. 2 – 6 h is optimal in imaging for the injection, accumulation of the particles at targeted site, clearance from non-targeted areas and data collection.[9] For therapeutic NPs, the ideal $t_{½}$ is longer, usually days, to allow repeated exposure to the affected area.[9] To avoid exposure of healthy cells to the drug, targeted NPs should allow for the preferential accumulation in diseased cells.

PEG chains increase the circulation time of nanoparticles by modifying the surface of the nanoparticle that interacts with the environment or solvent. In the body, the MPS works by circulating macrophages and monocytes to remove foreign material such as bacteria and viruses.[10] Macrophages and bacteria (and viruses) have similar negative surface charges, so to prevent repulsion between the two, plasma proteins called opsonins attach to the foreign entities to reduce the surface charge before the macrophages engulf them and transport to the liver or spleen for

degradation and excretion.[11] PEG chains reduce the process of opsonin attachment, thus enabling concealment of PEG-coated nanoparticles from the phagocytes and therefore increasing the $t_{½}$.[11–14]

Besides the interaction between NP and the MPS, NP-NP interactions (leading to aggregation) also result in low $t_{½}$. NPs aggregate due to the stronger interaction between particles than the interaction between the nanoparticle and solvent.[15] Spherical nanoparticles have a greater tendency to aggregate when they have a high surface energy, and this interaction potential is associated with the electrostatic repulsion potential and the van der Waals attraction potential.[16,17] PEG molecules minimise the van der Waals attraction and hence decrease the surface energy, resulting in less aggregation.[18–20]

The ideal particle size for *in vivo* applications is between 10 and 100 nm. Particles smaller than 10 nm have increased chances of renal filtration, while those larger than 100 nm are more likely to be taken up by the MPS and will find it more difficult to accumulate in tumour tissue.[13] PEGylation of nanoparticles can help modify the size of the particles, by varying chain length with the size of the nanoparticle core.

PEGylation of nanoparticles has been extensively covered in the literature, with the NP cores ranging from magnetic iron oxide nanoparticles,[21] gold NPs,[22] and quantum dots (QD)[23–25] employed in the imaging field. PEGylated gold NPs have also been used in catalysis and optics.[26–29] Iron oxide nanoparticles however, were one of the first nanoparticles to be used in imaging.[30,31] It has been shown that PEGylation or dextran coating of iron oxide nanoparticles extends $t_{½}$ by up to 200 min and improves image quality.[32–34]

3.2.1 Synthesis of PEGylated NP2

In this project, **NP2** (IONP coated with sodium alendronate) are further coated with PEG molecules of various lengths, and with various terminal groups. According to literature, in general, larger NPs (between 50 and 100 nm) are usually coated with smaller PEG chains (3400 – 10000 M_W) as further increases to the hydrodynamic diameter can reduce $t_{½}$.[3] However, the hydrodynamic diameter is affected by the arrangement and conformation of the PEG chains on the NP surface which can be either mushroom or brush.[35,36] This is discussed further in Section 3.2.3. The terminal functional group on the PEG chain also influences *in vivo* behaviour. Different terminal functional groups will alter the overall surface charge on the nanoparticle. This in turn, will affect whether the particles are detected by opsonins and therefore phagocytic cells.

The PEG molecules chosen here were all linear and their M_W were approximately 800, 3000 and 5000 (PEG units 12, 58 and 96 respectively). At these molecular weights, coupled with the size of the core (6 nm diameter), it was expected that the hydrodynamic diameter of the PEGylated NP be no greater than 50 nm for the highest M_W PEG, assuming linearity is maintained. This is based on average bond lengths and the average length of a PEG monomer unit (0.35 nm),[37,38] where a PEG chain with 96 units, is roughly 33 nm.

In this project, carboxylic acid, amine and hydroxyl terminal groups were investigated. All the PEGs have a carboxylate on one end which react with the terminal amine on **NP2** (**Scheme 3.2**). The amine-terminated PEGs were initially protected with an Fmoc group to prevent reaction with itself. The Fmoc group was cleaved after the coupling reaction to free the amine group. The hydroxyl-terminated PEG was used as obtained. The carboxylate-terminated PEG was produced by reacting the amine-PEGylated **NP2** with succinic anhydride once on the nanoparticle.

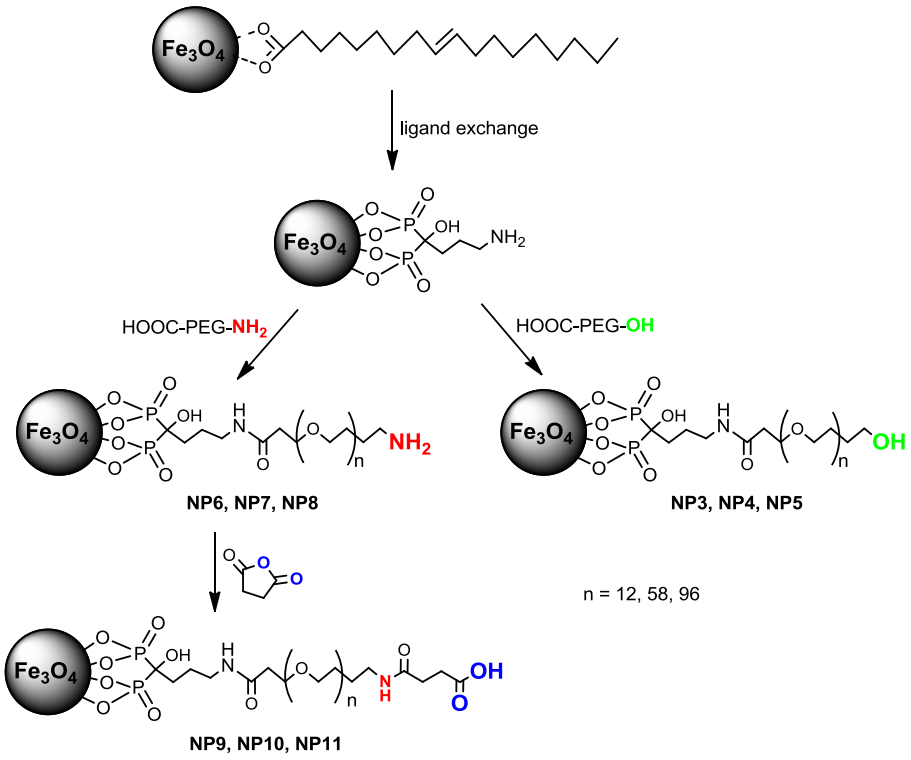

Scheme 3.2 Synthetic scheme showing PEGylation of **NP2**

As it was determined previously that there are approximately 145 free amine groups on the surface of **NP2,** the PEG molecules were added in 300 equivalents relative to the nanoparticle. This equivalence is in a slight excess in order to maximise the yield of the reaction and to maximise the number of PEG molecules coating the surface of the nanoparticle. In a typical experiment, the

nanoparticles were reacted with 300 equivalents of PEG molecules in the presence of EDC to activate the carboxylic acid. After reacting overnight, the mixture was centrifuged and the supernatant decanted. For the OH-terminated particles (**NP-PEG$_n$-OH**; **NP3, NP4, NP5**), the mixture was washed three times by precipitation with acetone, and finally the nanoparticles were resuspended in water. For the amine-terminated particles (**NP-PEG$_n$-NH$_2$**; **NP6, NP7, NP8**), the black pellet was suspended in a piperidine/DMF (20/80) mixture for 15 mins, to remove the Fmoc group on the amine. This was repeated three times to finally give the free amine. The carboxylate-terminated particles (**NP-PEG$_n$-COOH**; **NP9, NP10, NP11**) were obtained by reacting **NP-PEG$_n$-NH$_2$** with 300 equivalents of succinic anhydride for 3 hours. At the end of the reaction, the mixture was washed three times by precipitation with acetone, and finally the nanoparticles were resuspended in water. The OH and COOH terminated nanoparticles were not very soluble in water compared to the NH_2 particles, resulting in a cloudy suspension.

3.2.2 Characterisation of PEGylated nanoparticles

The PEGylated nanoparticles were characterised by infrared spectroscopy, run as neat samples on an ATR plate. For the NH_2 and OH terminated PEG chains, a sharp peak at 1649 cm^{-1} was observed which corresponds to a C=O amide stretch. The infrared spectrum for NP-PEG$_{96}$-NH$_2$ (**NP8**) (M_W 5000) is shown below (**Figure 3.1**).

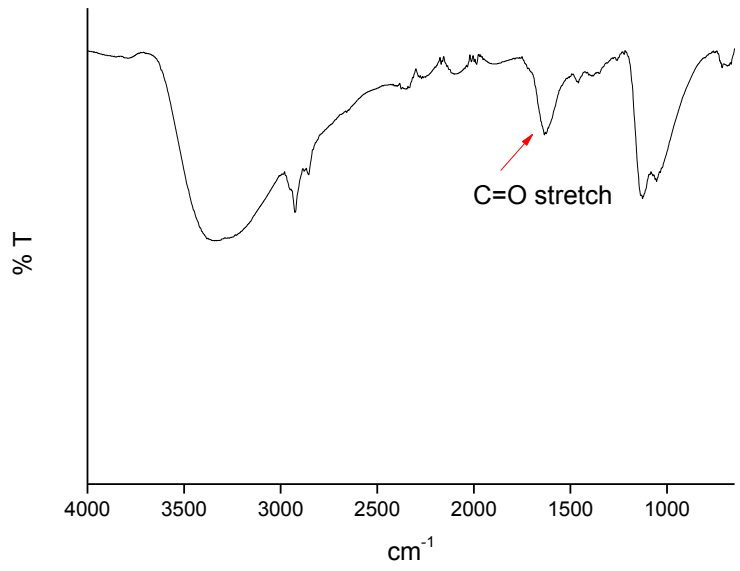

Figure 3.1 Infrared spectrum (neat, ATR plate) of NP-PEG$_{96}$-NH$_2$ **(NP8)**.

The particles were also characterised by DLS measurements to obtain the hydrodynamic size and surface charge of the nanoparticles (**Table 3.1**). All the measurements were carried out at pH 7.4 at 298 K in water. Assuming the PEG molecules remain relatively straight on the nanoparticle surface, it was expected that the higher M_W PEG would have a larger hydrodynamic size. A longer PEG chain will extend further out from the surface of the nanoparticles than a shorter PEG chain, creating a thicker PEG layer, as illustrated in **Figure 3.2**. This trend is observed for the NH_2 and OH functionalised PEGs when the M_W of the PEG is increased. However the COOH functionalised PEGs gave variable size measurements (between 10 and 200 nm over repeats). This could be due to the poor water solubility of the particles making sizing measurements of a suspension difficult to obtain.

Sample	Core	PEG length	Surface group	Surface charge (mV)	Size (nm)
NP2	**NP2**	No PEG	NH_2	-25	30.0
NP6	**NP2**	12 (ca 800 Da)	NH_2	-14	31.0
NP7	**NP2**	58 (ca 3000 Da)	NH_2	-12	33.3
NP8	**NP2**	96 (ca 5000 Da)	NH_2	-12	39.8
NP3	**NP2**	12 (ca 800 Da)	OH	+3	34.3
NP4	**NP2**	58 (ca 3000 Da)	OH	+10	58.5
NP5	**NP2**	96 (ca 5000 Da)	OH	+18	89.4
NP9	**NP2**	12 (ca 800 Da)	COOH	-27	n/a*
NP10	**NP2**	58 (ca 3000 Da)	COOH	-25	n/a*
NP11	**NP2**	96 (ca 5000 Da)	COOH	-25	n/a*

Table 3.1 DLS data detailing the size and surface charges of the various PEGylated **NP2**. *Nanoparticles were not very soluble in water, measurements of the suspensions gave increasingly larger values suggesting aggregation.

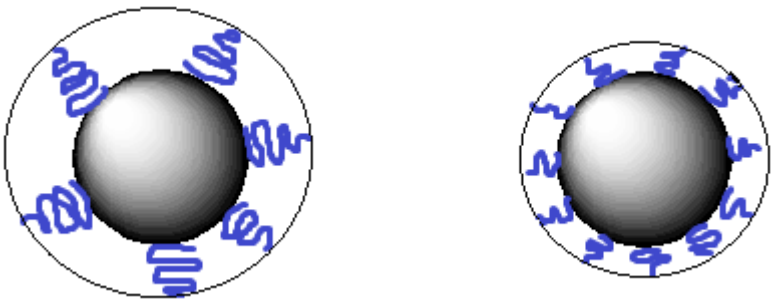

Figure 3.2 Illustration showing PEGylated nanoparticles with a long (left) and short (right) PEG chain. The longer PEG chain extends further out from the surface of the nanoparticles, increasing the thickness of the PEG layer.

The different terminal functional groups should also affect the surface charge on the nanoparticles. In theory, the terminal amine groups would be protonated at pH 7.4, resulting in a positive surface charge. However, an overall negative charge, albeit less negative than **NP2** was observed. This was

expected due to the negative charges from the OH and phosphonate oxygen atoms on the alendronate ligand, countering the positive charge from the amine resulting in an overall smaller negative charge (as previously explained in Chapter 2). The COOH terminal groups on the other hand, would be deprotonated at pH 7.4, resulting in a negative charge, and therefore an overall more negative charge compared to **NP2** and this is indeed what is observed. OH groups have a higher pKa than carboxylic acids (OH approximately 16 compared to 5 for COOH), so the OH terminal group on the PEG would also be deprotonated at pH 7.4 but to a lesser degree than the COOH. However, this would still mean that an overall negative surface charge is expected but a slightly positive charge is observed instead.

The amine terminated PEGylated particles were reacted with rhodamine-NHS to determine the number of free amines on the surface of the nanoparticle after PEGylation. Assuming that no rhodamine reacts with any remaining amines on the alendronate ligand, due to steric hindrance from the PEG chains, the results from the rhodamine coupling after PEGylation should give the number of amine groups on the surface which are from the PEG molecules only. This can then be correlated back to the number of PEG molecules present per nanoparticle.

Sample	No. of amine groups reacted
NP6 (PEG600)	71
NP7 (PEG3000)	72
NP8 (PEG5000)	57

Table 3.2 Number of amine groups that reacted to rhodamine after PEGylation of **NP2**.

From the results (**Table 3.2**), the **NP8** (PEG5000) had fewer amine groups that reacted with rhodamine compared to the **NP6** (PEG600) and **NP7** (PEG3000), which suggests that there are fewer PEG5000 molecules on the nanoparticle surface. Besides extending further out from the nanoparticle surface, a longer PEG molecule would also bind with lower density due to the bulkiness of the larger PEG. A longer PEG would also have a more flexible chain than can coil and therefore render the terminal NH_2 groups less readily accessible for reaction.

3.2.3 Estimation of PEG density and surface conformation

As mentioned previously, PEG molecules on the surface of a nanoparticle can adopt either a mushroom or brush conformation, based on a model by de Gennes.[35,36] The polymer conformation can be determined by comparing the relative polymer size or Flory radius (R_F) of the polymer to the

distance between PEG chains on the nanoparticle surface. The Flory radius (R_F) can be found using the following equation:

$$R_F = aN^{3/5}$$

where a = the length of the monomer unit (which is 0.35 nm for PEG)[37,38], and N = number of monomer units in the polymer.

The distance between PEG chains, D, on a nanoparticle surface is related to the density of polymer on the nanoparticle surface. If there is a low density of polymers on the surface, the distance between the PEG chains will be larger and if this value for D is greater than the R_F value, the polymers adopt a mushroom conformation. When D is smaller than R_F, the polymers adopt a brush conformation. This is illustrated in **Figure 3.3**.

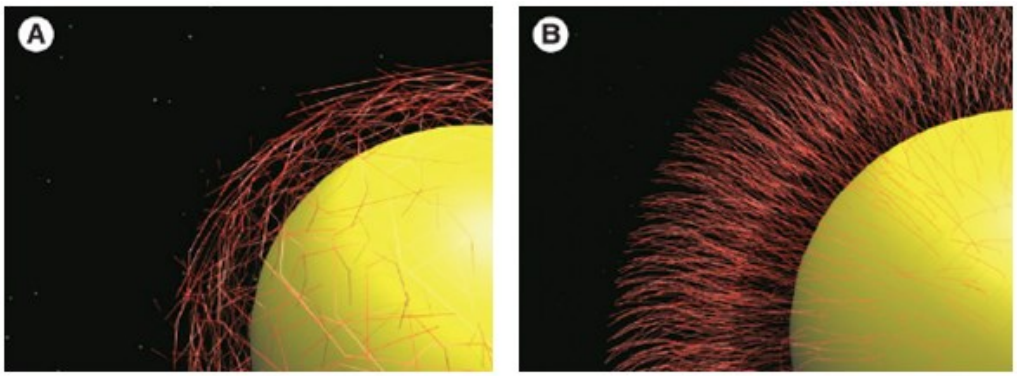

Figure 3.3 Simplified diagram showing the low-density mushroom configurations (A) and high-density brush-type arrangements (B) of polymers on nanoparticle surface. Image taken from ref [9].

The number of amine groups that reacted with rhodamine can be correlated to the number of PEG molecules on the surface of the nanoparticle (assuming that little to no rhodamine reacts with any free amines from the alendronate). From the rhodamine coupling results, the PEG molecules of M_W 600 and 3000 have similar number of PEG molecules on the surface (71 and 72 respectively) while the PEG 5000 has 57 PEG molecules on the surface (**Table 3.2**). From this and the total surface area of the nanoparticle (assuming a sphere), the area that one PEG molecule occupies on the nanoparticle surface (A_{PEG}) can be determined.

$$A_{PEG} = \frac{Surface\ Area\ (NP)}{number\ of\ PEG\ per\ NP}$$

Assuming that the area covered by one PEG chain is a circle, the distance between two PEG molecules on the nanoparticle surface (D) is the diameter of this circle.

$$D = 2 \times \sqrt{\frac{A_{PEG}}{\pi}}$$

Taking into consideration all of these assumptions, equations and rhodamine coupling results in mind, the Flory radius (R_F), PEG density and distance between each PEG molecule can be calculated (**Table 3.3**).

Sample	PEG units	A_{PEG} (nm^2)	R_F (nm)	D (nm)	Conformation
NP6	12	1.59	1.6	1.42	brush
NP7	58	1.59	4.0	1.42	brush
NP8	96	1.98	5.4	1.59	brush

Table 3.3 Summary of values for the surface area of one PEG molecule on the NP (A_{PEG}), Flory radius (R_F) and the distance between each PEG molecule (D), for the different PEG lengths to give the expected PEG conformation on the NP surface.

In theory, larger molecular weight PEG molecules on a nanoparticle surface are expected to adopt a mushroom conformation due to longer distances between the PEG molecules. However, comparison of the D to R_F value for PEG5000 indicates that the PEG conformation is brush. This was due to increasing PEG molecular weight having a weak effect on the number of PEG surface groups, which in turn resulted in a relatively slow increase in D compared to R_F.

3.3 Coupling to cyclooctyne for copper-free click reaction in vivo to give a dual modal MRI/PET contrast agent

3.3.1 'Click' reactions

In 2001, Sharpless, Kolb, and Finn, published a review that described in detail the criteria required for a series of reactions to be referred to as 'Click Chemistry'.[39] These criteria state that the reactions should be high-yielding, stereospecific, be simple to perform by making use of readily available starting materials in environmentally friendly conditions such as water as a solvent, and the byproducts should be removable without the need for chromatographic separation.[39,40] They also described that reactions that fall under the click chemistry group of reactions should have a large thermodynamic energy, and these usually involve carbon-heteroatom bond formation. These types of reactions that fulfil the click chemistry criteria include the opening of strained rings such as

epoxides,[41] epoxidation reactions (addition of oxygen to C=C bonds),[42] and cycloaddition reactions such as Diels-Alder[43] and 1,3-dipolar cycloadditions.

One of the reactions which has seen a large success from the utilisation of click chemistry is the Huisgen cyclisation reaction to prepare 1,2,3-triazoles by a 1,3-dipolar cycloaddition between azides and alkynes. The original reaction involved reacting both reagents at elevated temperature and produced triazoles with a lack of regioselectivity, a 1:1 mixture of the 1,4 and 1,5 regioisomers (**Scheme 3.3**).[44] This in itself meant that this cyclisation reaction was not suitable to be regarded as a click reaction.

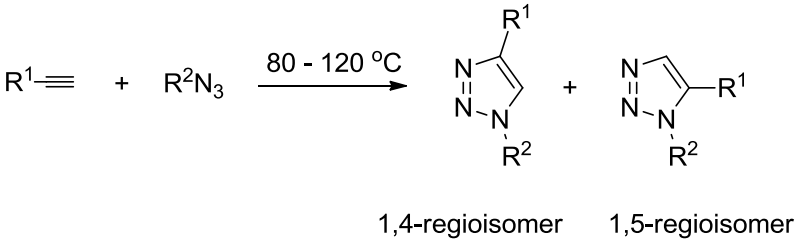

Scheme 3.3 Original reaction between azide and alkyne giving the 1,4 and 1,5 regioisomer in 1:1 mix.

However, it was found that this cyclisation reaction can be catalysed by copper(I) salts to give the 1,4 regioisomer exclusively.[40,45] The copper-catalysed cycloaddition is also carried out in aqueous media at room temperature, and is still compatible when other functional groups are present on both reagents. The copper(I) source is usually obtained through the reduction of copper(II) sulphate in the presence of sodium ascorbate.[45] Other catalyst systems have also been reported, these include organic-soluble copper(I) complexes such as $CuBr.(PPh_3)_3$ and $CuI.P(OEt)_3$,[46] and copper(I) stabilised with ligands such as tris-(benzyltriazolylmethyl)amine (TBTA).[47] These types of modifications which results in the exclusive regioselectivity and experimental simplicity has made this reaction the gold standard among the click reactions.[48–51]

The triazole moiety has found an abundance of applications in biological and pharmaceutical settings, with many examples in the recent literature showcasing the synthesis of triazole-containing peptides, oligosaccharides[52,53] and natural product analogues.[54,55] Through the copper-catalysis of the alkyne-azide cyclisation, it has been possible to synthesise new materials in other fields such as polymers,[56] liquid crystals[57,58] and biological macromolecules.[59] The alkyne-azide cycloaddition has therefore become synonymous as a model click reaction even though Sharpless' initial description covers a variety of syntheses.

The copper-catalysed reaction has a postulated mechanism (**Scheme 3.4**) that involves the initial formation of a copper-alkyne complex which lowers the pK_a value of the alkyne and the proton on the alkyne can then be deprotonated in aqueous medium.[44,60] The copper(I) acetylide complex is attacked by the azide to form a copper(I) adduct and intramolecular cyclisation results in a copper-containing 1,2,3-triazole. Protonation regenerates the copper catalyst and the 1,4-regioisomer of the triazole.

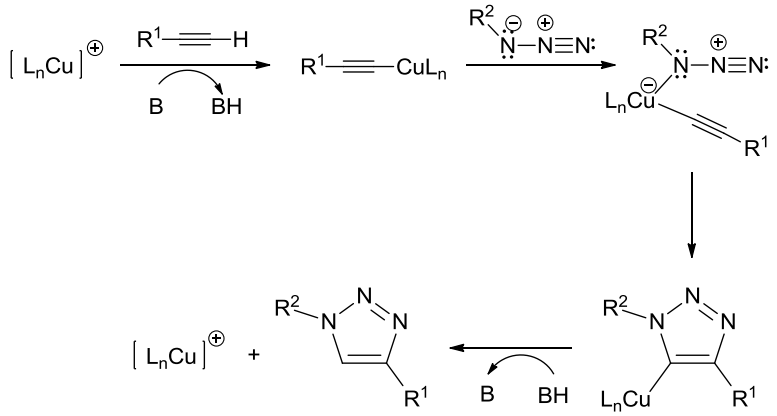

Scheme 3.4 Postulated mechanism of the copper-catalysed cyclisation between alkyne and azide.[44,60]

Out of the various click reactions, the azide-alkyne cycloaddition has been shown to be the most biologically relevant as both the azide and alkyne functionalities are either absent or relatively rare in biological systems.[61] In order to utilise this highly efficient reaction *in vivo*, the cycloaddition reaction between an alkyne and an azide has to be copper-free as copper is toxic.[62] To achieve this, a modification where the alkyne is in a strained ring system has been employed by Bertozzi.[63–68] Prior to Bertozzi, the reaction between cyclooctyne, the smallest of the stable cycloalkynes, and phenyl azide, had already been observed by Wittig and Krebs in 1961 to proceed extremely quickly giving the triazole as a single product.[69] The rate of reaction when the strained alkyne is utilised is dramatically higher than unstrained alkynes due to the acetylene bond angle deformation in the ring.[70,71]

The first generation cyclooctyne synthesised by Bertozzi *et al* was a substituted cyclooctyne (**Figure 3.4**) synthesised according to a modified method originally carried out by Reese and Shaw.[72] However, model reactions of this substituted cyclooctyne with simple azides showed that the reaction suffered from slower kinetics compared to the copper-catalysed reactions. Incorporation of electron-withdrawing groups on alkynes had been shown previously by Ju *et al* to improve reaction rates for catalyst-free alkyne-azide cycloadditions.[73]

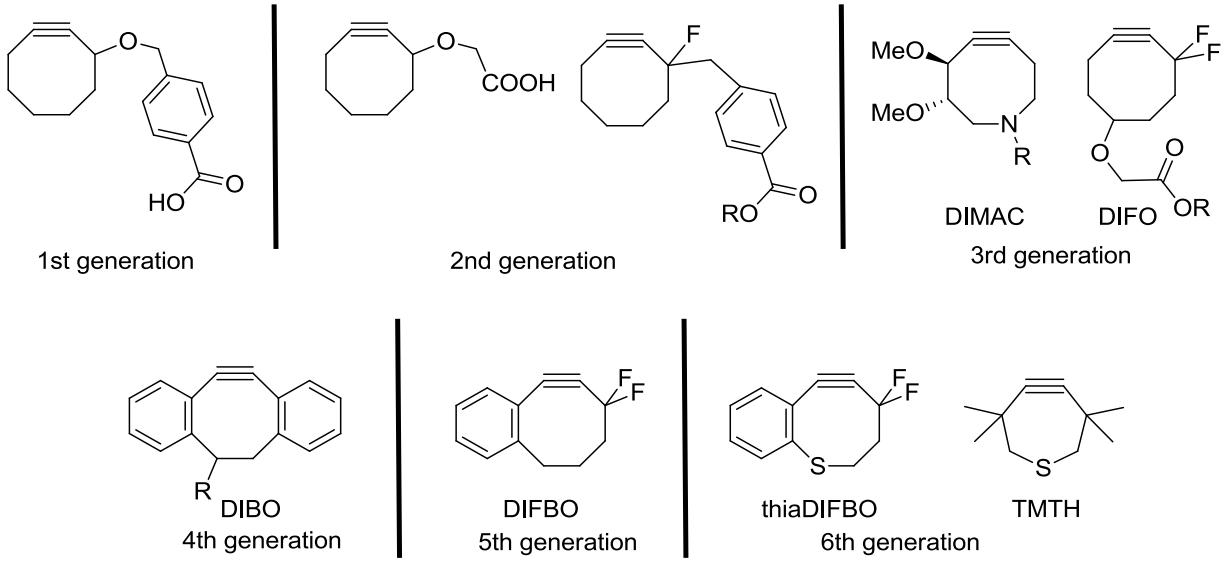

Figure 3.4 Examples of the different cyclooctynes showing the progression in modifications to the compounds.

The Bertozzi group therefore introduced electron-withdrawing fluorine atoms adjacent to the alkyne which would lower the LUMO energy of the alkyne and promote reaction with the azide.[74] One drawback of the original cyclooctynes was the low water-solubility, thereby making it less than ideal for biological applications. Removal of the phenyl ring improved the solubility, as well as decreased steric bulk around the reactive centre, allowing for improved reaction rates (2nd generation, **Figure 3.4**). Further investigations to incorporate two fluorine atoms (DIFO), or with methoxy groups (DIMAC, 3rd generation, **Figure 3.4**) also showed improved kinetics, and no apparent toxicity when used *in vitro* for biomolecule labelling.[64,66,75] The nitrogen atom within the ring in the methoxy substituted cyclooctyne also improved the solubility brought about by the nitrogen atom disrupting the hydrophobicity of the molecule.

To improve the reaction rates even further, steric interaction in the form of phenyl rings fused on either side of the cyclooctyne was added (DIBO, 4th generation). The added rings impart extra strain and the cyclooctynes were shown to have vastly increased reaction kinetics.[76] This dibenzocyclooctyne has been used by El-Sagheer *et al* to join DNA fragments together and they found that the reaction was very fast, completing in 1 minute.[77]

A hybrid of the difluoro-substituted cyclooctyne and the fused aryl cyclooctyne was subsequently synthesised in the Bertozzi group which possessed even greater kinetic reactivity (DIFBO, 5th generation).[78] However, all these modifications have also shown to give unwanted side reactions, as well as oligomerisation of the molecules in solution. Incorporation of a sulfur atom into the ring

(thiaDIFBO, 6th generation) was shown to result in a much more stable molecule that did not undergo oligomerisation, but had very low reaction rate. Contraction of the ring as in the cycloheptyne TMTH, still gave a stable molecule but with the fastest rate constant for an azide-alkyne cycloaddition to date.[79] Unfortunately, a benzene fused TMTH (akin to DIFBO's structure) has not yet been possible to isolate.

Cyclooctynes have found a variety of uses, and in a biological setting, have been shown to successfully be applied *in vitro* and *in vivo*. Site-specific surface functionalisation via the anchoring of proteins, fluorescent tags or other biomolecules to glass surfaces and magnetic beads has been made possible through the use of the copper-free azide-alkyne reaction.[80] Modification of quantum dots (QD) to obtain biomolecule-conjugated QDs while maintaining the luminescent properties of the QDs has also been achieved by "copper-free click".[81] Feringa *et al* have shown that ^{18}F can radiolabel a peptide called bombesin that targets a receptor overexpressed in tumour cells by conjugating bombesin with a cyclooctyne (in this case they used a modified dibenzocyclooctyne). The radiolabelled peptide can then be used as a cancer diagnosis and imaging radioligand.[82] Bertozzi's work has been primarily with glycans. Glycans in cells have been successfully labelled with DIFO (3rd gen), and because the alkynes were also conjugated to fluorophores, imaging of the glycans being internalised into cells was possible.[66] They have also shown that use in a live mouse has been promising. Cells in the mouse were metabolically labelled with azides, and conjugation to cyclooctynes (DIFO and DIMAC among others) was confirmed by detection of glycoconjugates in the isolated cells and other organs *ex vivo*.[75]

Despite the modifications to the cyclooctyne structure to improve reaction rates, most of the cyclooctynes have poor water-solubility. The synthetic routes to these cyclooctynes are also highly demanding, usually between 7 and 10 steps, and giving low final yields. In this work, the simple cyclooctyne (non-fluorinated 2nd gen) was chosen as it can be synthesised in four steps according to a literature method. It is methanol-soluble but still stable after dilution with water. The successful initial use *in vitro* and *in vivo* by Bertozzi *et al* and others, is promising and shows that this system would be ideal for use in this work to produce a dual-modal MRI/PET contrast agent which combines together via copper-free alkyne-azide cycloaddition *in vivo*.

The idea then is to label the iron oxide nanoparticles with the cyclooctyne, and a suitable biological targeting moiety to localise the nanoparticles to a particular location *in vivo*. Subsequent injection of the azide on a ^{68}Ga-DOTA complex (the PET agent), would then see the azide selectively target the cyclooctyne on the nanoparticle, resulting in the dual-modal probe forming *in vivo* (**Figure 3.5**).

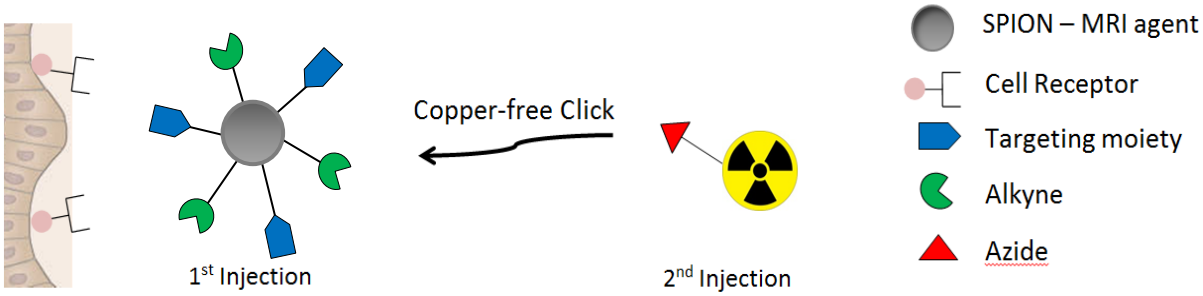

Figure 3.5 Simplified schematic of the copper-free click reaction *in vivo* to form the dual modal MRI/PET probe.

3.3.2 Synthesis of cyclooctyne

As the majority of the cyclooctynes in literature suffer from poor water-solubility and require demanding synthetic preparation procedures, one of the earlier cyclooctynes (**13**, **Scheme 3.5**) was chosen as it was water-soluble. The cyclooctyne **13** is not commercially available and so was synthesised according to literature method.[81]

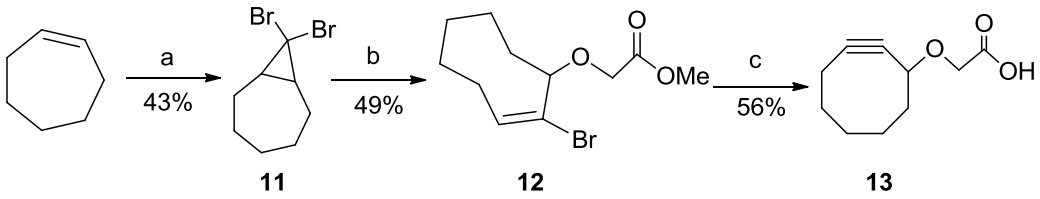

Scheme 3.5 Synthesis of **13** from cycloheptene. Reagents and conditions: a) bromoform, ^{t}BuOK, anhydrous pentane, RT; b) $AgClO_4$, methyl glycolate, anhydrous toluene, RT; c) NaOMe, DMSO, RT.

The synthesis of the strained alkyne was not trivial. As with almost all the literature preparations of the cyclooctyne which can take up to 10 synthetic steps, some of these steps are complex and give low final yields. This 3 step procedure at first glance appears to be relatively simple. However, large loss of yield was encountered at every step after column chromatography, with only about 20 – 50 mg of pure **13** obtained from 1 g of cycloheptene. Isolation of **13** in the final step was difficult as the DMSO used in the reaction was never completely removed during the workup, and co-eluted during the column. The yield of pure **13** relative to DMSO was calculated by running a ^{1}H NMR with an internal standard. From repeat reactions, an average yield of about 20 % of the total mass obtained was pure product. **13** was characterised by NMR, MS and elemental analysis, and was in accordance with literature.[81] There were initial concerns that the low yield of the reaction was due to the level of dryness of the solvents. However, this factor was eliminated with the use of freshly distilled methanol which did not improve yields.

3.3.3 Functionalisation of nanoparticles with cyclooctyne 13

The alendronate coated nanoparticles **NP2** were functionalised with the cyclooctyne **13** by EDC coupling (**Scheme 3.6**), for subsequent copper-free cycloaddition reaction with the ^{68}Ga-DOTA-azide complex.

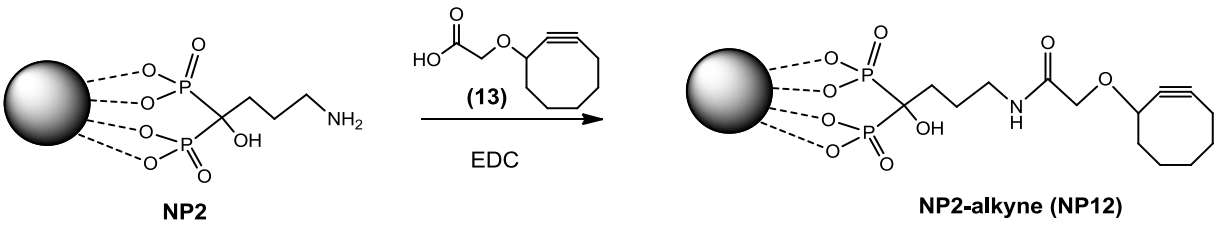

Scheme 3.6 Synthetic scheme showing the coupling of strained alkyne to **NP2** to give **NP12**.

In a typical reaction, 200 equivalents of strained alkyne were reacted with **NP2** in the presence of EDC. It was previously determined in Chapter 2 that **NP2** has on average 115 ± 30 ligands on the surface. To maximise the yield of the alkyne coupling reaction, a slight excess of the ligand **13** was reacted with **NP2. NP2-alkyne (NP12)** was characterised by both infrared spectroscopy and DLS measurements.

To quantify the number of cyclooctyne molecules reacted with **NP2**, a known quantity of rhodamine was reacted with the **NP12** particles and the unreacted rhodamine measured and correlated to a calibration graph, to determine the number of free amine groups left on the surface of the nanoparticle after the alkyne coupling.

Sample	Number of amine groups reacted to rhodamine
NP2 + alkyne 100 eq	193 ± 86
NP2 + alkyne 200 eq	171 ± 94

Table 3.4 Number of amine groups that reacted with rhodamine, after cyclooctyne coupling.

The number of amine groups reacted when rhodamine was added is quite large (**Table 3.4**), but the error in measurements over the repeats is also high. However, some general observations can be deduced from these results. For the 100 eq of alkyne added, the amount of rhodamine reacted was between 107 and 279 molecules per nanoparticle. For the 200 eq of alkyne added, the amount of rhodamine reacted was less, between 74 and 265 molecules. This suggests that there are more cyclooctyne molecules per nanoparticle when 200 eq is used, which is as expected. However, using

200 eq does not result in 100 % coupling yield for the cyclooctyne. When a much higher equivalence of cyclooctyne was used (400 eq or higher), the nanoparticles precipitated out during the reaction, usually very quickly (within 30 min) of the cyclooctyne addition. The resultant nanoparticles were no longer soluble in water. This suggests that at 400 eq, the coupling yield was much higher, maybe even being close to 100 %, but the trade-off is the loss of water-solubility. The loss of water solubility made rhodamine coupling quantification for the 400 eq of cyclooctyne addition difficult and no reproducible or comparable results were obtained.

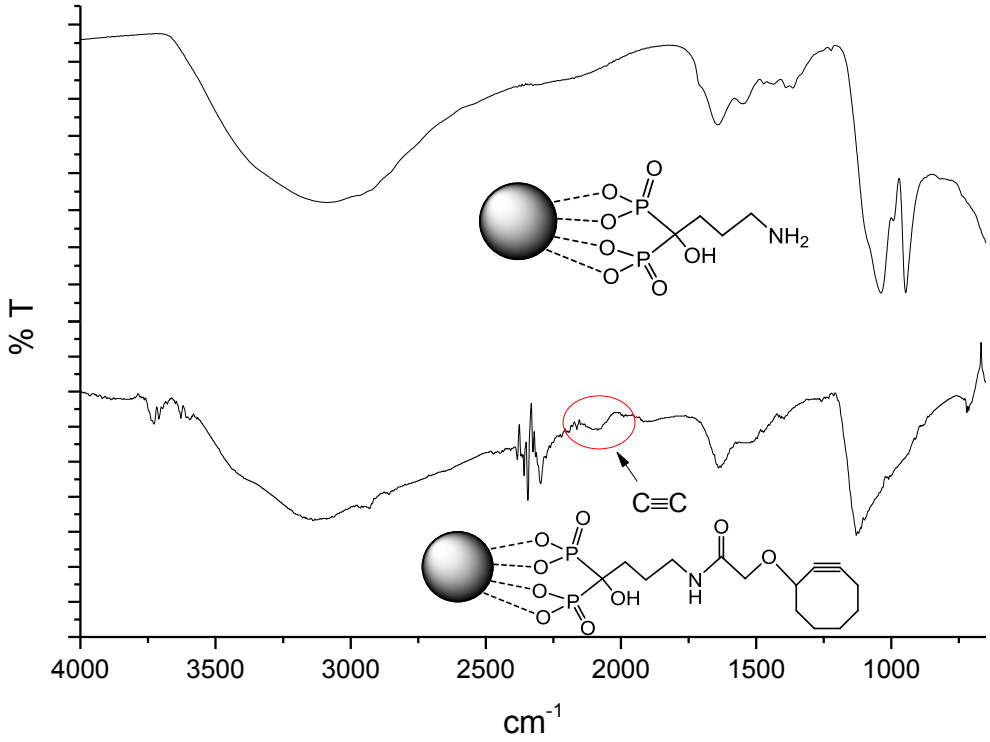

Figure 3.6 Infrared spectrum of **NP12** (below, neat on ATR plate) compared to **NP2** (above, neat on ATR plate).

Infrared spectrum of **NP12** (**Figure 3.6**) showed a weak alkyne stretch at around 2100 cm^{-1} which was not present in **NP2** prior to the alkyne coupling. Some weak NH amide stretches between 3500 and 3700 cm^{-1} are also present, indicative of successful cyclooctyne coupling to **NP2**.

There was no significant change in the hydrodynamic diameter of the **NP12** compared to **NP2**, remaining at approximately 30 nm. This was as expected as the cyclooctyne is a small molecule and so would not significantly change the hydrodynamic diameter of the resultant nanoparticle after coupling. The **NP12** had a similar surface charge when compared to the **NP2**, of -25 mV. This result

was also as expected, for the same reason there was no change to the hydrodynamic diameter after coupling.

3.4 Click reactions with lanthanide azide-DOTA complexes

3.4.1 Lanthanides – properties and luminescence

The azide functional group on the PET moiety (Ga-68), was designed to be on a DOTA macrocycle. DOTA was preferred over NOTA as DOTA is approved for *in vivo* use whereas NOTA is not. Prior to complexation with radioactive gallium, complexations to non-radioactive gallium as well as selected lanthanides were carried out. As both gallium and lanthanides bind similarly well to hard donor atoms (N and O on DOTA-type chelates), lanthanides were used to provide confirmation of complex formation.

The lanthanides are a series of elements in the same period between the *s*- and *d*-blocks of the periodic table, from lanthanum (atomic number 57) to lutetium (atomic number 71). The *4f* electron shell is filled gradually across the period, but is shielded from the outer 5*s* and 5*p* subshells, resulting in the *f*-orbitals being unavailable for bonding. Like the other series in the periodic table, such as the halogens, or alkali metals, the lanthanides share many similar characteristics to each other. These include having a common oxidation state of +3 in aqueous solutions, the adoption of 8 or 9 coordinate complexes, a preference for 'hard' donor atoms (such as O and N), and paramagnetic properties due to having unpaired *f*-electrons.[83] This paramagnetism leads to spectral broadening and resonance shifts in the NMR spectrum for the NMR active nuclei on the ligand coordinated to the Ln(III) ion, and have thus been used as lanthanide shift reagents to determine macromolecular structures such as proteins and nucleic acids.[84]

Another characteristic property of lanthanides is their luminescence. Other than La(III), Gd(III) and Lu(III), the Ln(III) ions emit in the visible and near IR regions of the electromagnetic spectrum. Gd(III) has the largest ground state to excited state energy gap (ΔE) of about 32,000 cm^{-1} therefore the maximum emission wavelength, λ_{max}, occurs in the UV region, which would overlap with the emission of organic chromophores that may be present in solution.[85] Hence, Gd(III) cannot be used in luminescence studies. Analogues using Eu(III) or Tb(III) can be used in place of Gd(III) as they have similar ionic radii, chemical properties and also smaller ΔE values of 12,300 cm^{-1} and 14,800 cm^{-1} respectively. This allows structural properties of Eu(III) and Tb(III) complexes to be deduced from luminescence and NMR spectroscopic studies and then applied to the Gd(III) analogue with

considerable confidence.[86] These results for the lanthanides can then be extrapolated for the non-luminescent gallium analogue.

There are two types of luminescence, one of which is fluorescence, which involves the emission of light from an electronically excited singlet state (S_1) to the ground singlet state (S_0). Another type of luminescence is phosphorescence, which involves the emission from the excited triplet state (T_1) to the ground singlet state (S_0).[85] As there is a change in spin during phosphorescence, this process is forbidden by the selection rule $\Delta S = 0$, and therefore is usually slow in comparison to fluorescence. Lanthanide luminescence is due to three types of electronic transitions. The first is via ligand-to-metal and/or metal-to-ligand charge transfer, which are high in energy and therefore rarely observed. Secondly, transition of an electron between a 4*f* and 5*d* subshell, can result in luminescence where the energy is largely dependent on the nature of the interactions between the ligand and the Ln(III) 5*d* orbitals. As this transition occurs between orbitals that have opposing symmetries with respect to the centre of inversion, it is allowed according to the Laporte selection rule. Finally, although the Laporte rule forbids *f-f* transitions, interactions between the 4*f* wavefunction and the ligand field or its vibrational states allows this rule to be relaxed and therefore give weak and narrow emission bands that are unique to each lanthanide. Although the emission wavelengths for these bands are unaffected by the coordination environment as the 4*f* orbitals are not involved in bonding, the intensities of these bands can be affected. The redistribution of the electrons within the 4*f* orbitals can be spread over many energy levels. The nature of the 4*f* orbitals which can be split into $^{(2S+1)}L$ spectroscopic terms by Coulombic interaction arising from interelectronic repulsion, where $(2S+1)$ is the spin multiplicity, and L = S, P, D and F when the total orbital angular momentum quantum number equals 0, 1, 2 and 3 respectively. These terms are further split into J levels by spin-orbit coupling where J is the total angular momentum. These splittings are illustrated in **Figure 3.7**.

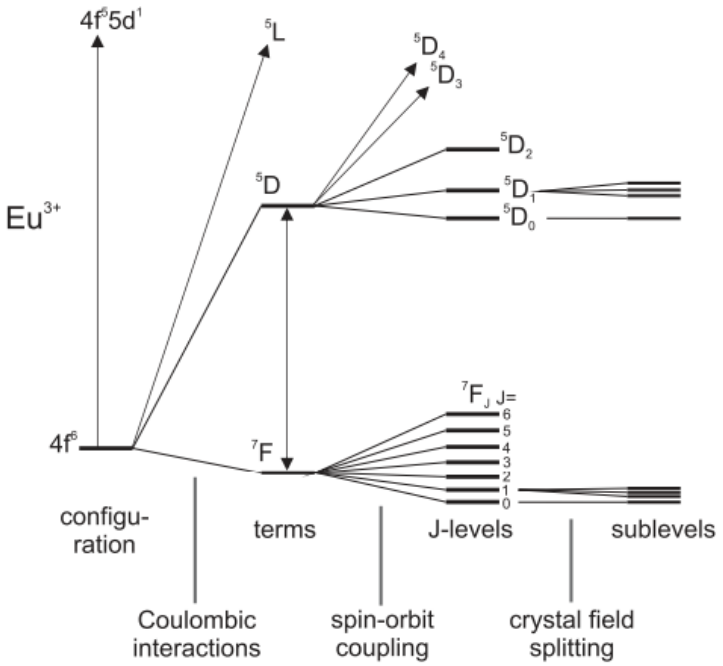

Figure 3.7 Diagram representing the interactions leading to the splitting of the electronic energy levels of a Eu^{3+} ion. Increase in energy is in the upwards direction. Image from ref [87].

Direct excitation of the lanthanides is difficult due to the forbidden *f-f* transitions, and usually results in weak luminescence, which is also quenched by nearby OH and NH oscillators. To increase the intensity of the lanthanide luminescence, organic chromophores (with higher extinction coefficients than lanthanides) are introduced to the ligand, to indirectly excite the lanthanide by acting as an antenna, allowing for energy transfer to the lanthanide.[88] This energy transfer occurs over several steps (**Figure 3.8**). Firstly, the ligand absorbs energy and electrons are excited into the ligand singlet excited state. The large size of the lanthanide ions allows for intersystem crossing (ISC) of the electron from the singlet to the triplet excited state of the ligand. As long as this triplet excited state is higher than the excited state of the lanthanide ion, energy transfer from the ligand to the lanthanide can occur, resulting in increased emission intensity. The efficiency of this energy transfer however, is affected by the rate of energy transfer which has a $1/r^6$ distance-dependence (and r is the distance between the organic chromophore and the Ln(III) centre).[89] Minimising this distance therefore will ensure a more efficient energy transfer and therefore enhanced emission.

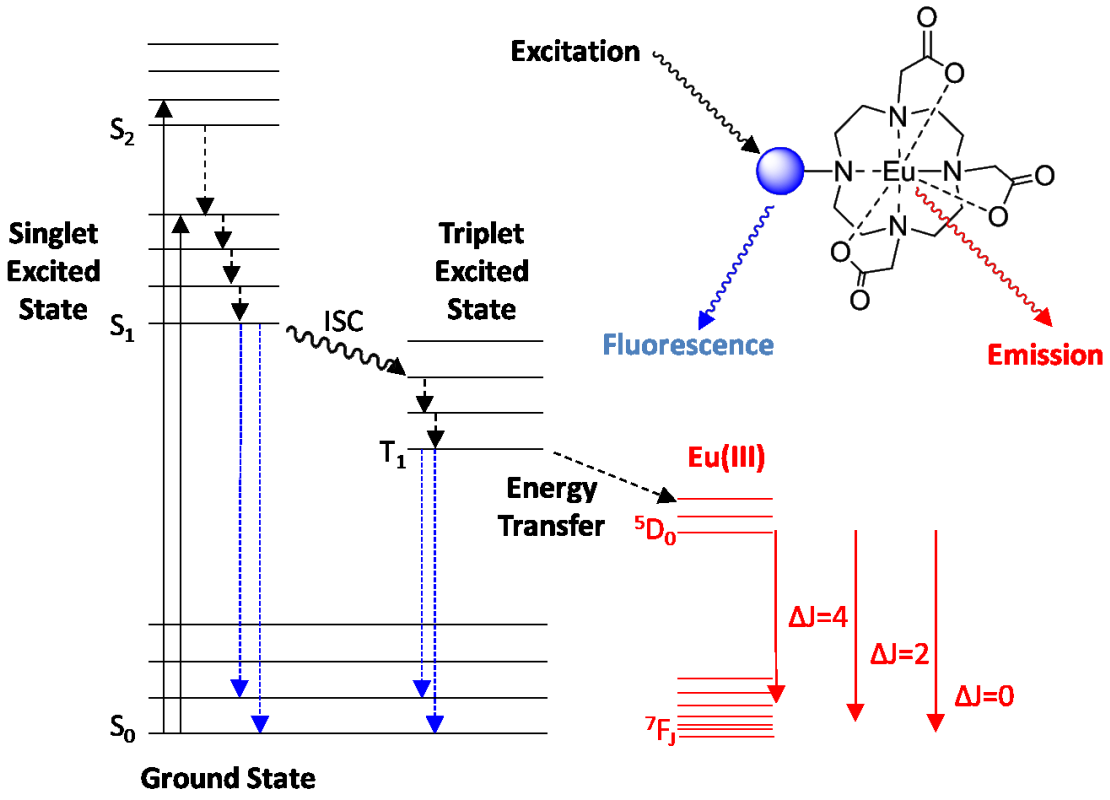

Figure 3.8 Jabloński diagram demonstrating Eu(III) sensitised emission. Excitation of the organic chromophore to its singlet excited state is followed by intersystem crossing (ISC) to the triplet excited state (lines and arrows in black). Energy transfer from T_1 state to Eu(III) results in emission (red arrows).

Emission from the lanthanide via sensitisation with an organic chromophore also results in a large Stokes shift between the chromophore absorption and the Ln(III) emission. For example, aromatic groups usually have λ_{ex} of 250 – 300 nm and λ_{em} of 350 – 400 nm, whereas lanthanides such as Eu(III) emit in the visible light region, λ_{em} of 570 – 720 nm, and so the Eu(III) emission spectrum is red shifted (**Figure 3.9**). Each individual band in a Eu(III) emission spectrum corresponds to the respective transitions from $^5D_0$ to ^7F_J (J = 0 – 6), see **Table 3.5**.

ΔJ	λ_{em} range (nm)	Intensity
0	577 – 581	Very weak
1	585 – 600	Strong
2	610 – 625	Strong to very strong
3	640 – 655	Very weak
4	680 – 710	Medium to strong

Table 3.5 Wavelength ranges and intensities for Eu(III) *ΔJ* transitions.

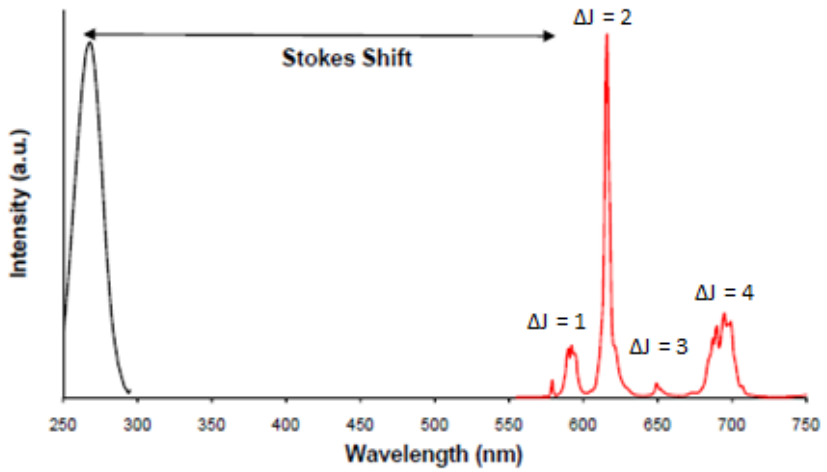

Figure 3.9 Typical Eu(III) emission spectrum of a Eu-DO3A species bearing an organic antenna (red line). Excitation of the organic chromophore (black line) occurs at much shorter wavelengths resulting in a large Stokes shift from the Eu(III) emission in the visible light region.

3.4.2 Synthesis and characterisation of M.L1 complexes and small molecule copper-free click to cyclooctyne

3-Azidopropyl-mono-amide-DOTA (**L1**) was purchased from Macrocyclics. The Eu, Gd and Ga complexes for **L1** have been synthesised and discussed in the literature but no detailed synthetic procedures were outlined. The complexation reactions to europium, terbium, gadolinium, and gallium were carried out in mildly acidic conditions (**Scheme 3.7**), analogous to those outlined for similar complexes.[90,91] Besides NMR and MS characterisation of the gallium complex, the luminescence of the Eu and Tb complexes serve to provide further evidence of the successful complexations.

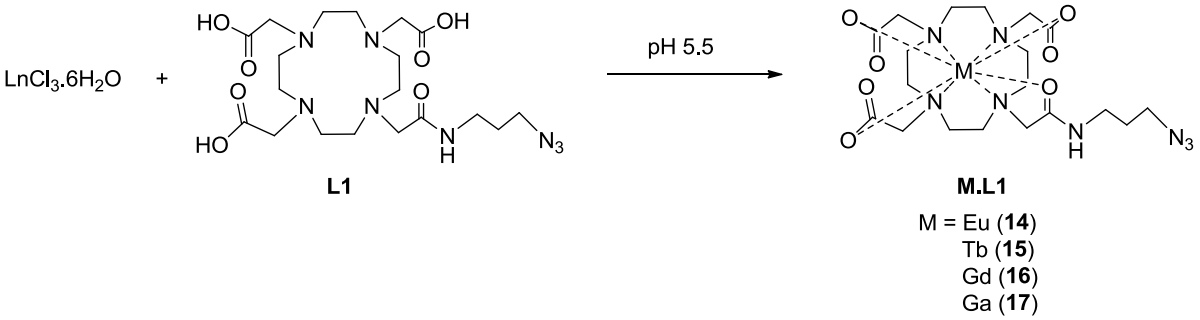

Scheme 3.7 Complexation of azido-mono-amide-DOTA **L1** to M = Eu, Tb, Gd, Ga.

In a typical complexation reaction (for the lanthanides), a slight excess (1.2 eq) of the metal salt was added to the DOTA ligand and the pH of the solution adjusted to 5.5. The reaction mixture was left to stir overnight. The pH of the solution was raised to about 10 to precipitate any unreacted metal

which is filtered off. The filtrate was concentrated and then purified by passing through a sephadex G-10 column to remove any salts. The gallium complex was formed by a similar method, but with the pH adjusted to 4.5 instead. All other steps remained the same.

The europium complex **Eu.L1** (**14**) was isolated as a white solid. High resolution ESI-MS gave a $[M + H]^+$ peak at *m/z* = 637.1610 with the correct isotope splitting pattern for a Eu(III) complex. The terbium complex **Tb.L1** (**15**) was isolated as a white solid and characterised by high resolution ESI-MS with a peak at *m/z* = 643.1656 $[M + H]^+$.

a) Fluorescence spectroscopy of 14 and 15 (Eu.L1 and Tb.L1)

Fluorescence spectroscopy of **14** (**Figure 3.10**) and **15** (**Figure 3.11**) were recorded. A weak peak at 395 nm in the excitation spectrum of **14** corresponded to the wavelength required for pseudo direct excitation of the Eu(III) ion. In the range 575 – 710 nm of the emission spectrum, four weak emission bands, arising from the $^5D_0 \rightarrow {}^7F_J$ (J = 1 – 4), were observed when the complex was excited at 395 nm, with a gate time of 5 ms. The most intense of the peaks observed were at ΔJ = 1, ΔJ = 2 and ΔJ = 4 transitions. The emission spectrum is typical of a Eu(III) emission, but is weak due to the absence of a chromophore to act as a sensitiser for the Eu centre.

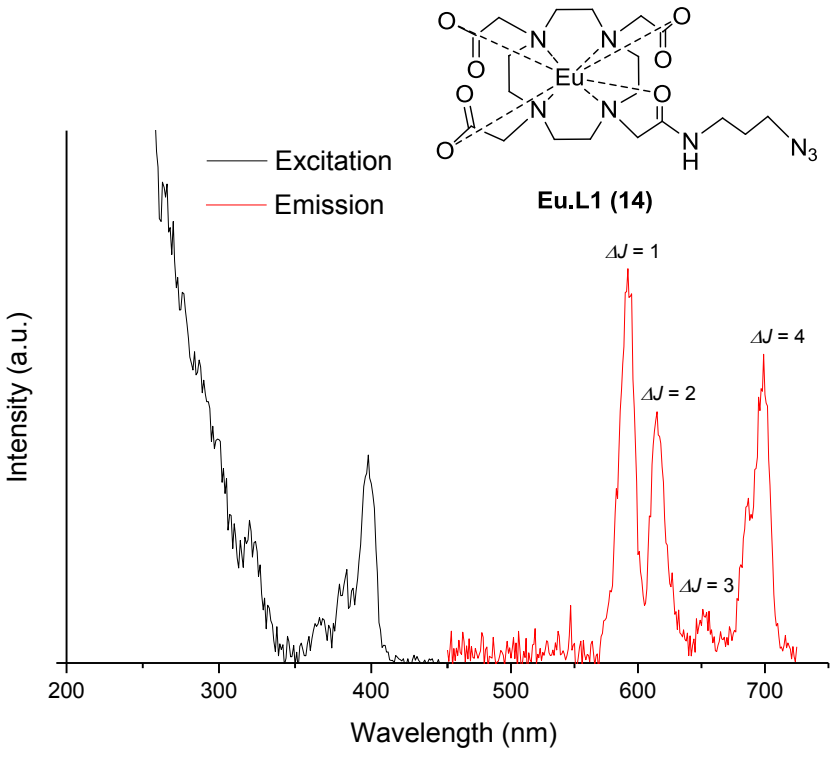

Figure 3.10 Excitation and emission spectrum of **Eu.L1** (**14**) (λ_{ex} = 395 nm, 100 µM, H_2O, 298 K, pH 7.4).

The excitation spectrum of **15** showed peaks at 320, 355 and 375 nm, corresponding to the pseudo direct excitation of the Tb(III) ion. The peak at 355 nm had the highest intensity, so this wavelength was used to excite the complex and obtain an emission spectrum. In the range 450 – 650 nm, four emission bands, arising from the $^5D_4 \rightarrow {}^7F_J$ (J = 3 - 6), were observed when the complex was excited at 355 nm. The emission spectrum is typical of Tb(III) emission but weak due to the absence of a chromophore to act as a sensitiser.

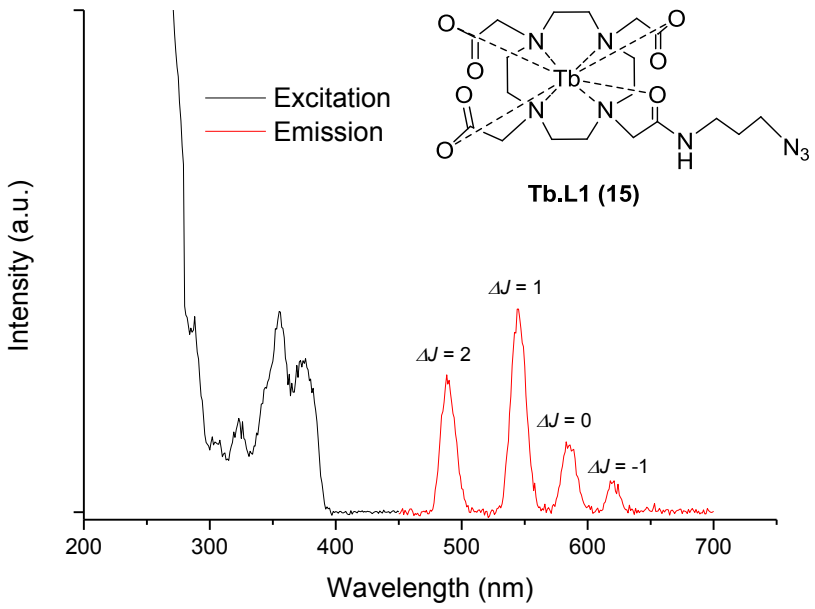

Figure 3.11 Excitation and emission spectrum of **Tb.L1** (**15**) (λ_{ex} = 355 nm, 100 µM, H_2O, 298 K, pH 7.4).

Hydration state, *q,* of the Eu(III) and Tb(III) complexes can also be determined and related back to the Gd(III) analogue, which is useful for relaxivity. A higher hydration state will result in better relaxivity and therefore more intense MRI signal. The usual way to determine hydration state is by growing a crystal of the complex, however this is often very difficult. The crystal structure is also in the solid state and is hence a less than exact measure of the hydration state. The luminescence lifetimes (τ) of both Eu(III) and Tb(III), in H_2O and D_2O differ, due to differences in energy transfer between the vibrational energy levels of H_2O/D_2O and the Ln(III) centre (**Figure 3.12**).

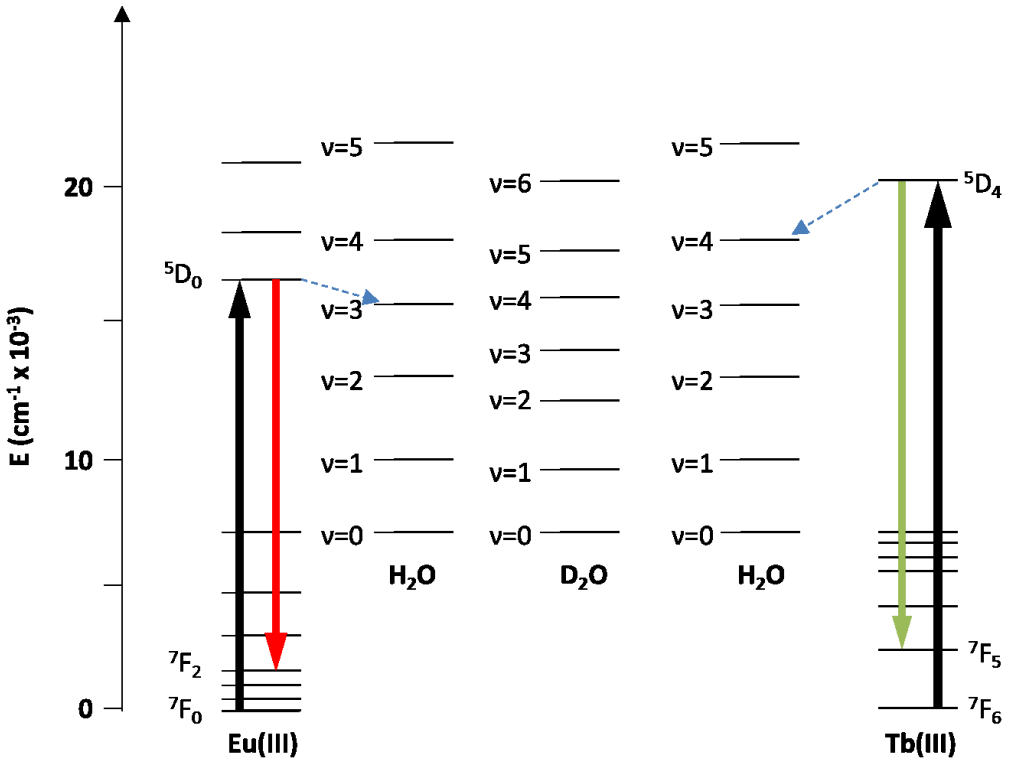

Figure 3.12 Vibrational energy levels of H_2O and D_2O with respect to the ground and excited states of Eu(III) and Tb(III). There is good overlap between $^5D_0$ excited state of Eu(III) and v = 3 vibrational level of H_2O, compared to $^5D_4$ excited state of Tb(III) and the same v = 3 vibrational level of H_2O.

There is a faster rate of decay in H_2O (k_{H2O}) due to less efficient energy transfer between the Ln(III) centre and the energy levels for D_2O. Eu(III) is also more sensitive to quenching than Tb(III) and so has shorter lifetimes in both H_2O and D_2O compared to Tb(III). From these differences in lifetimes and decay rates, the hydration state, q of each complex can be calculated from the following equations.[86]

$$q_{Eu} = 1.2\left[\left(k_{H_2O} - k_{D_2O}\right) - 0.25 - 0.075\right]$$

$$q_{Tb} = 5\left[\left(k_{H_2O} - k_{D_2O}\right) - 0.06\right]$$

where the 0.25 and 0.06 terms reflect the quenching effect of unbound water molecules, and in the case of Eu complexes, the 0.075 term reflects the quenching from a coordinated amide NH group. Luminescence decays of both **14** and **15** in H_2O and D_2O were measured, and the q values calculated (**Table 3.6**). From the lifetime measurements, **14** has a hydration state close to 1 (q of 0.94) meaning that the Eu complex forms an eight coordinate complex with the macrocycle and will bind one water molecule. The determined hydration state of **15** was lower than for **14** (q of 0.67). This could be due to less efficient energy transfer from the Tb(III) centre to the OH and OD oscillators. However, the

value is still acceptable and within error, and confirms that the Tb complex is also eight coordinate and binds one water molecule.

Complex	τ_{H2O}/ms	k_{H2O}/ms^{-1}	τ_{D2O}/ms	k_{D2O}/ms^{-1}	*q*
14	0.63	1.58	2.13	0.47	0.94
15	1.95	0.51	3.08	0.32	0.67

Table 3.6 Lifetimes, rate constants and derived hydration states for **14** and **15**.

b) Eu complex 14 – NMR studies

^{1}H NMR studies of the Eu complex can be used to deduce information regarding the Gd analogue. Both Eu and Gd have ^{1}H NMR spectra that have wide chemical shift range, due to the paramagnetism of the metal ion. ^{1}H NMR of Gd however cannot be studied to deduce structural characterisation due to the extreme line broadening as a result of highly efficient proton relaxation.[92] This proton relaxation is less efficient with europium and therefore, the spectral lines are less broadened. An extended sweep-width ^{1}H NMR spectrum for **14** was recorded and showed signals between -20 and +36 ppm and is as expected for Eu-DOTA-type complexes (**Figure 3.13**).

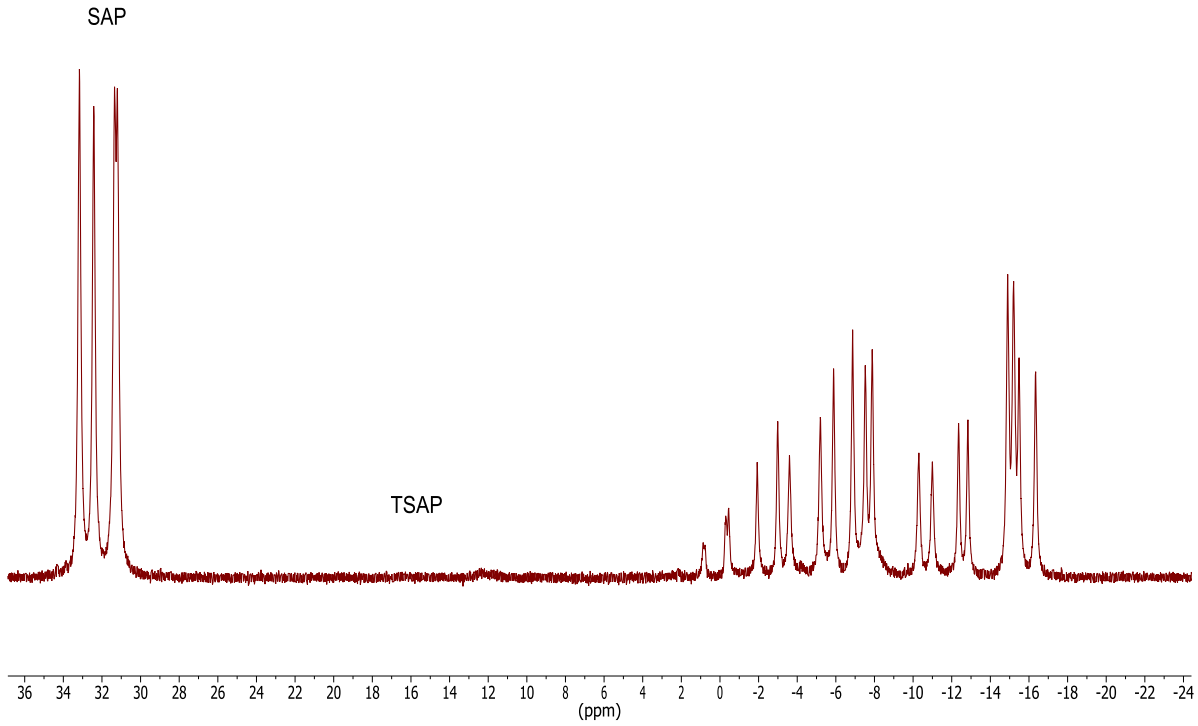

Figure 3.13 Extended sweep-width ^{1}H NMR of **14** (D_2O, 400 MHz, 250 to -250 ppm, with Watergate water suppression).

Previous crystal structure and NMR studies carried out on Ln-DOTA complexes by Botta *et al,* and Roth and Hoeft, have shown that DOTA-type complexes can adopt the structure of one of four stereoisomers once chelated.[93,94] The metal centre is held between the four coplanar nitrogen atoms in the macrocycle, and the four coplanar oxygen atoms of the arms. The macrocycle forms a square conformation that is slightly distorted and which defines the geometry of the complex. There are two main geometries the complex can adopt, the square-antiprismatic isomer (SAP or "major" *M*) and the twisted-square-antiprismatic isomer (TSAP or "minor" *m*), depending on the angle of distortion. These two isomers can be interconverted by flipping the macrocycle ring, or by rotating the arm. The ethylene group conformation around the metal centre can be either a δ or λ configuration therefore the macrocycle conformation is either δδδδ or λλλλ. The acetate arms can also be arranged into two positions, Δ or Λ. The combination of ring interconversion (δ ↔ λ) and arm rotation (Δ ↔ Λ) leads to four stereoisomers, related as two pairs of diastereomers (Δ(δδδδ)/Λ(λλλλ), and Δ(λλλλ)/Λ(δδδδ) (**Figure 3.14**).[95]

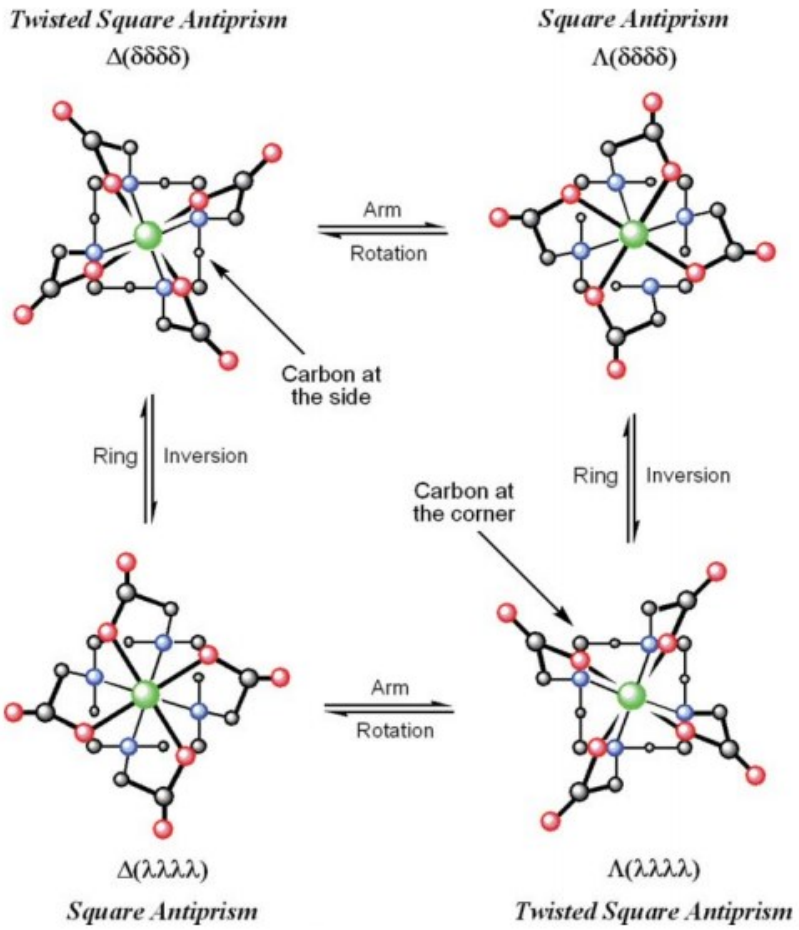

Figure 3.14 The four stereoisomeric complexes of LnDOTA−complexes, related as two enantiomeric pairs. These stereoisomers interconvert by ring inversion or arm rotation. Sequential ring inversion and arm rotation interconverts enantiomers. Figure taken from ref [96].

The two different isomers can be distinguished by differences in chemical shifts in the NMR spectrum, especially for the axial proton closest to the metal centre. In the SAP isomer, this axial proton has a more downfield shift in the range of 30 – 50 ppm, while in the TSAP isomer this same proton appears in the range of 15 – 20 ppm.[97] In the ^{1}H NMR spectrum of **14** (**Figure 3.13**), the signals observed between +30 and +35 ppm in the spectrum corresponds to the axial protons closest to the metal centre, for a complex that is a SAP isomer. Resonances for the TSAP isomer which usually occur between 15 and 20 ppm are not present in the NMR of **14**.

c) Gadolinium and Gallium complexes

The Gd complex **Gd.L1** (**16**) was isolated as a white solid and characterised by high resolution mass spectrometry. ESI-MS of the complex gave a molecular ion peak at *m/z* = 642.1655 $[M + H]^+$ with the correct isotope pattern for a Gd(III) complex.

From the hydration state measurements for the Eu(III) and Tb(III) analogues, it can be deduced that **16** also has a hydration state of 1. $1/T_1$ measurements were carried out and the r_1 relaxivity for **16** was found to be 4.02 mM^{-1} s^{-1}, which is comparable to the relaxivity of Gd-DOTA (r_1 = 4.20 $mM^{-1}s^{-1}$).[98] This value of 4.02 is slightly lower than the 4.20 of Gd-DOTA due to the amide N-H that slows water exchange rates. SAP isomers are known to have slower water exchange rates, and the Eu analogue of this complex (**14**) was found to be predominantly in the SAP isomer which means that **16** is most likely also present as the SAP isomer, and is another reason for the lower r_1 measured.[96,99]

The gallium complex **Ga.L1** (**17**) was isolated as a white solid. High resolution ESI-MS was obtained with a molecular ion peak at *m/z* = 553.1637. ^{1}H NMR of the ligand and complex showed slight differences, with the NMR of the complex showing sharper signals for the CH_2 macrocycle protons (between 3 and 4 ppm) compared to the broadened peaks for the same protons in the NMR of the ligand. This sharpening of said signals is a result of the metal holding the ligand in a constrained conformation preventing bond rotation on the NMR timescale, and is further proof that the complexation was a success.

d) Small molecule cycloaddition reaction of M.L1 complexes to cyclooctyne

Prior to carrying out the cycloaddition reactions with **NP2-alkyne (NP12)**, the complexes were also reacted with the cyclooctyne **13** (**Scheme 3.8**) as confirmation that the cycloaddition reaction is successful. In a typical reaction, the same equivalence of both the cyclooctyne (in the minimum

volume of MeOH) and the complex (in water) were added together in a vial and left to shake. The resulting complexes were characterised without further purification such as column chromatography or aqueous workup.

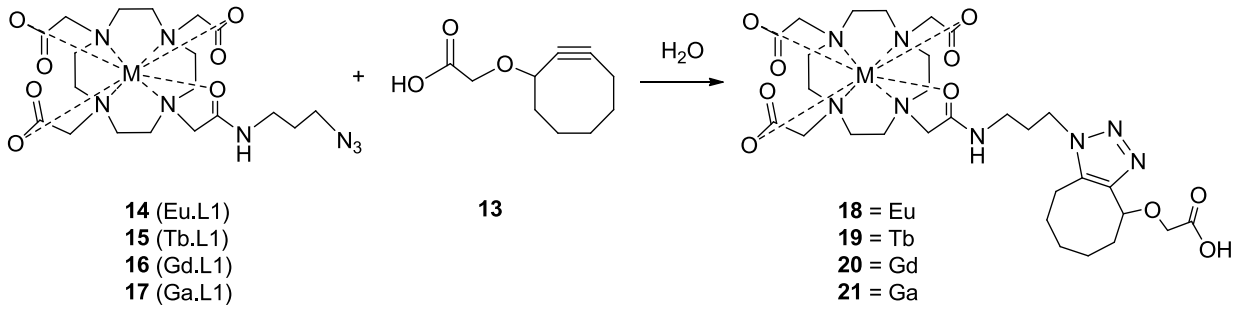

14 (Eu.L1)
15 (Tb.L1)
16 (Gd.L1)
17 (Ga.L1)

13

18 = Eu
19 = Tb
20 = Gd
21 = Ga

Scheme 3.8 Cycloaddition reaction between **M.L1** and cyclooctyne **13.**

The excitation spectrum for both the **18** and **19** (Eu and Tb cyclised complexes respectively) no longer had peaks at 395 nm and 355 nm respectively, which corresponds to the pseudo direct excitation of the respective Ln(III) centres, and instead both excitation spectra had a peak at 255 nm which corresponds to an aromatic group, most likely from the triazole formed during the cycloaddition reaction. As a general rule, when aromatic groups are present near the europium or terbium ion, they can act as an antennae which enhances the lanthanide based emission by harvesting light and transferring the energy to the lanthanide ion.[88] The emission spectra of **18** and **19** showed the same emission spectral lines but at higher intensities when excited at 255 nm. Additionally, the emission spectrum of **18** (**Figure 3.15**) showed more defined spectral lines compared to **14** (before cycloaddition reaction), due to the energy transfer from the triazole to the Eu(III) centre, resulting in an enhanced emission.

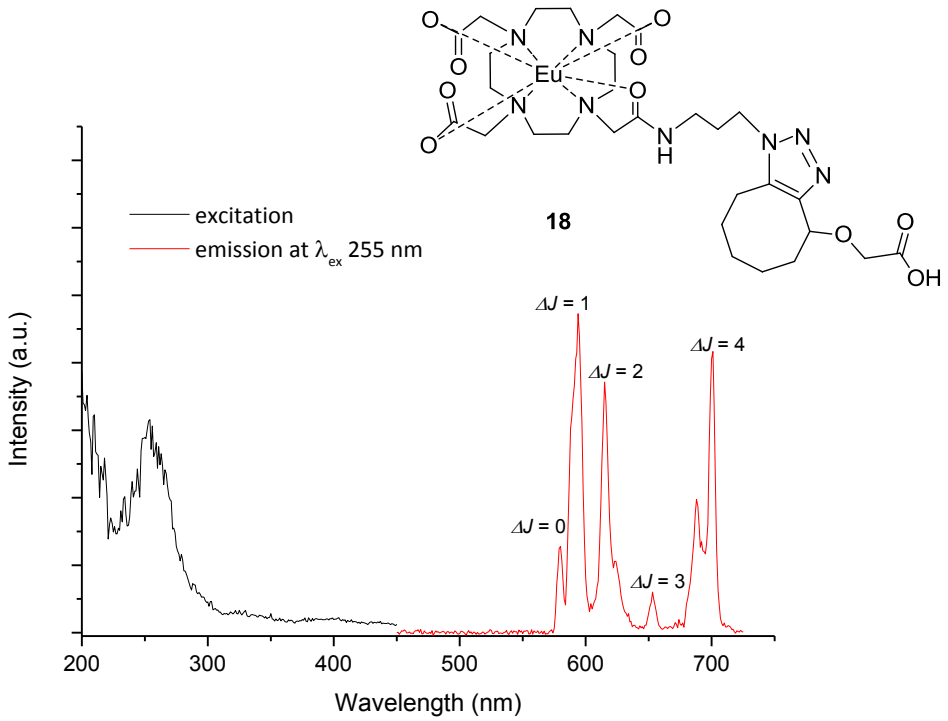

Figure 3.15 Excitation and emission spectrum of **18** (λ_{ex} = 255 nm, 100 µM, H_2O, 298 K, pH 7.4).

The complexes were also characterised by high resolution ESI-MS, with each showing their respective molecular ion peaks at *m/z* = $[M + H]^+$ (**Table 3.7**), confirming the successful click reactions.

Complex	*Calc. m/z*	*Found m/z*
18	817.2536	817.2574
19	825.2590	825.2612
20	824.1989	824.2003
21	735.2593	735.2628

Table 3.7 *m/z* values for the cyclised complexes **18 - 21**.

3.4.3 Copper-free cycloaddition reaction between Ln.L1 to NP-alkyne

In order to confirm further that the azide-alkyne cycloaddition reaction with the nanoparticles would be successful before carrying on with radioactive gallium, it was decided to carry out the cycloaddition reactions on the nanoparticles with the lanthanide complexes as well (more specifically the europium and terbium complexes), in order to observe the fluorescence, if any, once clicked to the nanoparticle (**Scheme 3.9**).

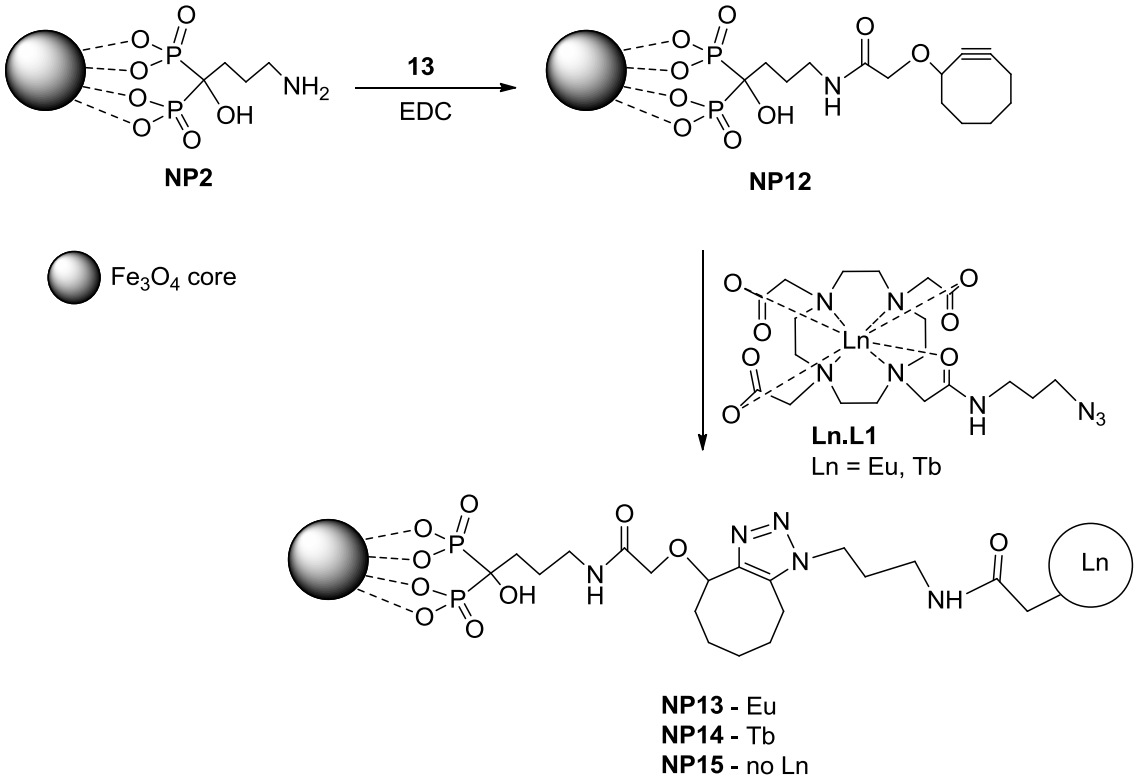

Scheme 3.9 Reactions to couple the alkyne to the nanoparticle followed by copper-free click to Ln-azido-DOTA (Ln = Eu, Tb), as well as with **L1** (no Ln).

In a typical experiment, 200 equivalents of the complex relative to **NP12** were reacted in water for two hours. The nanoparticles were purified by three cycles of precipitation with acetone, with the nanoparticles finally resuspended in water.

Emission spectra for **NP13** (Eu) showed that there was an unexpected well defined emission from the nanoparticles when excited at 395 nm, but not the expected emission from europium metal centre (blue curve, **Figure 3.16**).

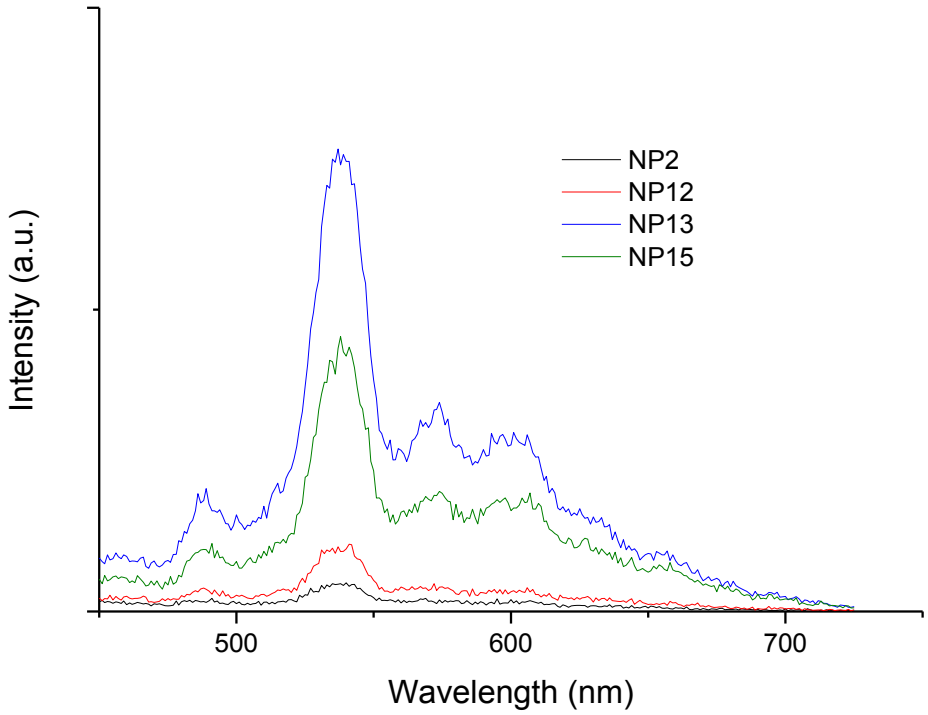

Figure 3.16 Emission spectra of **NP2** (alendronate), **NP12** (alkyne), **NP13** (Eu), and **NP15** (no M). All measurements λ_{ex} = 395 nm, H_2O, 0 ms delay, slits 10:10, 1 mg/mL Fe, pH 7, 25 ^{o}C.

The unexpected emission was further investigated with the nanoparticles at each stage of the synthesis (**NP2** – alendronate, original surface ligand; and **NP12** – alkyne) (**Scheme 3.9**) to confirm the unexpected emission (**Figure 3.16**). The intensity increases from **NP2**, to **NP12** to **NP13** species, suggesting an energy transfer from the ligand to the iron oxide nanoparticle, providing a preferred energy pathway to that of the europium centre. The emission is weak though as the excitation spectrum shows a low intensity peak at 395 nm.

When excited at 395 nm, **NP14** (Tb species) also showed a similar emission, i.e. only the emission from the iron oxide nanoparticle (black curve, **Figure 3.17**). When excited at 375 nm (pseudo direct excitation of Tb centre), the emission spectrum of **NP14** has a slight resemblance to that of a regular Tb complex such as **15** (**Tb.L1**) (with signals at 490 and 545 nm corresponding to the ΔJ = 2 and ΔJ = 1 transitions, red curve **Figure 3.17**). The intensity of these signals are also higher than when excited at 395 nm, which is as expected as 375 nm is a better wavelength for exciting Tb(III) than 395 nm. The emission observed when the nanoparticles are excited at 395 nm suggests that an energy level in the nanoparticle is being accessed and is excited more efficiently than the Eu(III) centre at 395 nm.

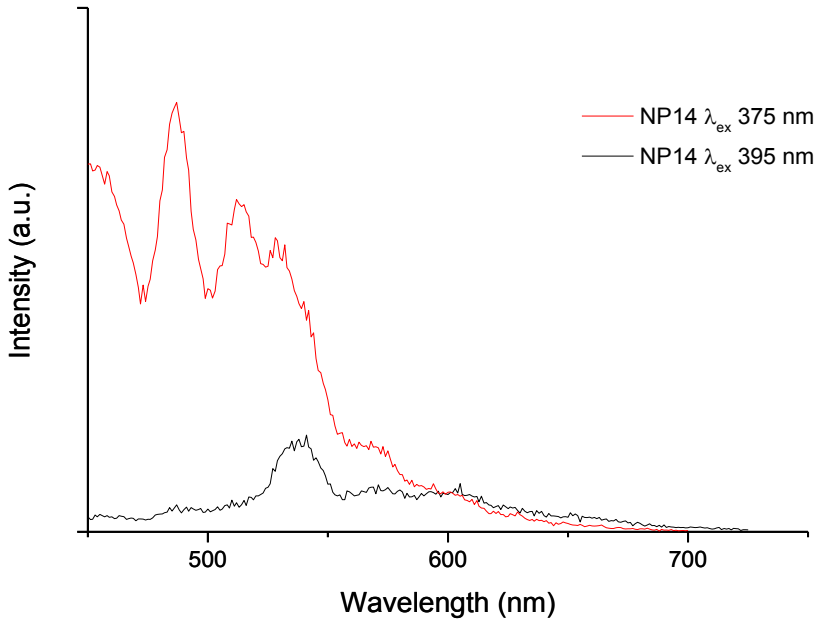

Figure 3.17 Emission spectrum of **NP14** (Tb). Red curve λ_{ex} = 375 nm; black curve λ_{ex} = 395 nm; Both measurements in H_2O, 0 ms delay, slits 10:10, 1 mg/mL Fe, pH 7, 25 ^{o}C.

To determine whether the nanoparticles were indeed emitting a weak fluorescence, the experiment was repeated both with a control set of nanoparticles (cycloaddition without a metal centre, **NP15** no M), as well as a different ligand on the surface of the nanoparticle (11-aminoundecanoate, **NP16**, provided by Dr Juan Gallo). Again, a similar emission spectrum was observed for both **NP15** (green curve, **Figure 3.16**) and **NP16** (**Figure 3.18**), with **NP15** still showing an increased emission intensity from the precursors. Blanks with water and DMSO were confirmed that the emission was not an artefact of the fluorimeter as no emission spectral lines were observed.

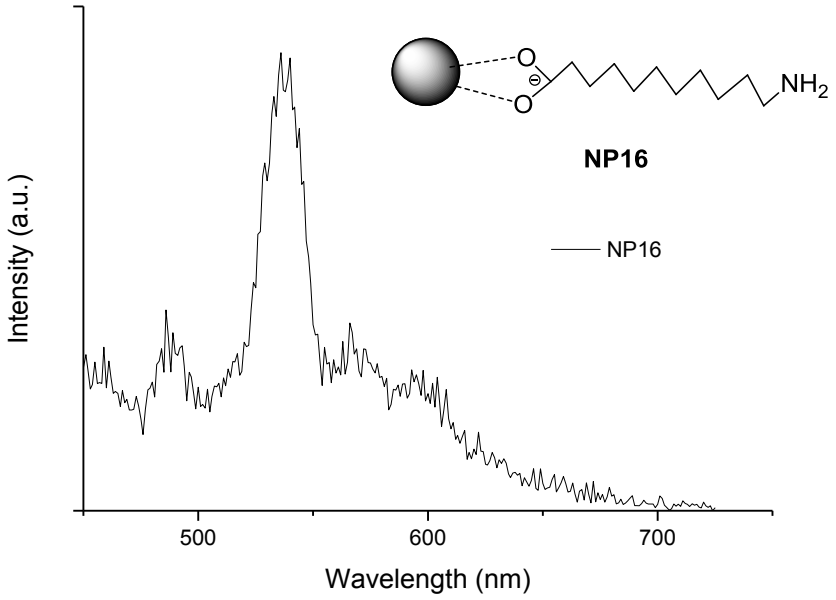

Figure 3.18 Emission spectrum of **NP16** (NP-aminoundecanoate). λ_{ex} = 395 nm, DMSO, 0 ms delay, slits 10:10, 1 mg/mL Fe, pH 7, 25 ^{o}C.

The emission spectrum of **NP16** (NP-aminoundecanoate) suggests that a different ligand system does not change the spectral outcome of the nanoparticle. These results strongly suggest that there is a definite but weak emission from the nanoparticle core. Emission from iron oxide nanoparticles however, has not been reported much in the literature with only one known example of luminescence observed directly from the nanoparticle reported.[100] Fei *et al* postulated that lattice defects on the nanoparticle surface, and the binding of molecules on the nanoparticle surface, cause changes in the electronic structure of the entire molecule, resulting in a weak emission from the nanoparticle between 400 and 600 nm, depending on the excitation wavelength. Most examples in the literature of fluorescent or luminescent nanoparticles involve hybrid or nanocomposite systems, with the fluorescent moiety coming from non-iron oxide nanoparticle species. These include hybrid luminescent non-iron oxide nanoparticles such as mixed lanthanide oxide nanoparticles (Dy/Eu, Ho/Eu and Ho/Tb systems) synthesised by Xu *et al* and lanthanide conjugated to InP quantum dots by Stasiuk *et al*.[101,102] The incorporation of both α-Fe_2O_3 and quantum dots into silica shells is a popular way to form bifunctional nanoparticles with both magnetic and fluorescent properties.[103–105] Another way to synthesise bifunctional luminescent nanoparticles is to conjugate the nanoparticles to a fluorescent complex such as the iridium complex functionalised Fe_3O_4/SiO_2 core shell nanoparticle system synthesised by Hsiao *et al.*[106] The iridium complex after incorporation onto the nanoparticle showed phosphorescent properties. Lanthanide complexes conjugated to iron oxide

nanoparticles have been synthesised and studied in the literature, but are fewer in number, despite the attractive luminescent properties of lanthanides (long lifetimes and sharp emission bands). Yang *et al* showed that terbium emission is observed after conjugation of terbium to the IONP surface.[107] Similar results were shown by Liu *et al* and Choi *et al* where the lanthanide luminescence was observed after conjugation to the iron oxide surface.[108,109] However, the concentrations of the nanoparticle solutions were not always described within the paper, so it is not possible to directly compare their results to those obtained here. Nevertheless, the absence of lanthanide emission from our studies could be due to one of or a combination of the following: 1) a low concentration of lanthanide on the surface of the nanoparticle, 2) absence of an antennae on the Ln complexes to enhance Ln emission, and 3) there is an excited energy level within the nanoparticle core that is accessible allowing a stronger emission from the nanoparticle core to be observed.

As the fluorescence spectroscopy of the NP-Ln species (**NP13** and **NP14**) did not definitively confirm whether the cycloaddition reaction was a success on the nanoparticle surface, ICP-MS analysis was carried out by Dr Stanislav Strekopytov at the Natural History Museum, London to determine the concentration of lanthanide in the nanoparticle samples after the reaction. This can be compared to the amount of Ln complex added per reaction to give the yield of the cycloaddition reaction (**Table 3.8**). The amount of Ln(III) in the respective samples after the reaction was quite low, giving a yield of between 10 and 15 %. This could explain why no lanthanide emission is observed on the nanoparticles. Nevertheless, the fact that the relevant lanthanides are still present in the respective nanoparticle samples after the cycloaddition reaction have shown that the azide-alkyne reaction on the nanoparticles were successful.

Sample	Ln	Amount of Ln in submitted sample (mg)	Amount added during reaction of submitted sample (mg)	% yield of "click" reaction
NP13	Eu	0.16	1.59	10
NP14	Tb	0.20	1.61	13

Table 3.8 Amounts of lanthanide in **NP13** and **NP14** determined by ICP-MS.

With respect to the reaction *in vivo* with Ga-68, this low yield should not be detrimental as PET imaging is more sensitive and therefore only a small amount of the radioisotope would be required to give a significant signal.

3.4.4 Synthesis of modified azido-DOTA and the Ln complexes

To determine if the fluorescence observed after the cycloaddition reaction to the nanoparticles could be enhanced if there was a chromophore on the Ln complex, the DOTA ligand was modified to incorporate a benzyl group which can act as a weak chromophore for the lanthanide. For indirect excitation of Ln(III) to occur, there has to be energy transfer from the sensitising moiety to the Ln(III). This energy transfer is more efficient when the energy level of the sensitising moiety is higher than that of the Ln(III). In the case of Eu(III), which has a $^5D_0$ excited state energy of 17,277 cm^{-1}, a phenyl group's triplet excited state is usually between 20,000 and 30,000 cm^{-1}, and therefore sensitised emission would be expected.[86]

Based on the availability of starting materials for the benzyl moiety, it was decided to utilise a benzyl compound, (4-aminomethyl-phenyl)methanol (**22**). The synthesis of the novel ligand **L2** is outlined in **Scheme 3.10**. 4-Aminomethyl-phenyl-methanol is a costly starting material (£325.39/mmol from Sigma Aldrich, August 2014), however, it can be synthesised from 4-cyanobenzaldehyde (£0.76/mmol from Sigma) via the reduction with $LiAlH_4$ according to a literature protocol.[110,111] This reaction gave **22** in moderate yields (60 – 85 %), slightly lower than in literature (96 %). Characterisation by ^1H and $^{13}C\{^1H\}$ NMR were comparable to the literature, with EI-MS also confirming successful preparation of **22**. Protection of the alcohol group with *tert*-butyl dimethyl silyl (TBDMS) to give **23** was carried out, with the protocol based on similar literature methods to protect alcohols.[112] **23** was characterised by ^1H and $^{13}C\{^1H\}$ NMR and ESI-MS and were in accordance with literature. Reaction of the amine with chloroacetyl chloride gave a reactive chloroacetyl amide species **24** characterised by ^1H and $^{13}C\{^1H\}$ NMR which was assigned by 2D HMQC spectroscopy. However, mass spectrometry of **24** did not give the molecular ion, possibly due to the highly reactive nature of the chloroacetyl moiety.

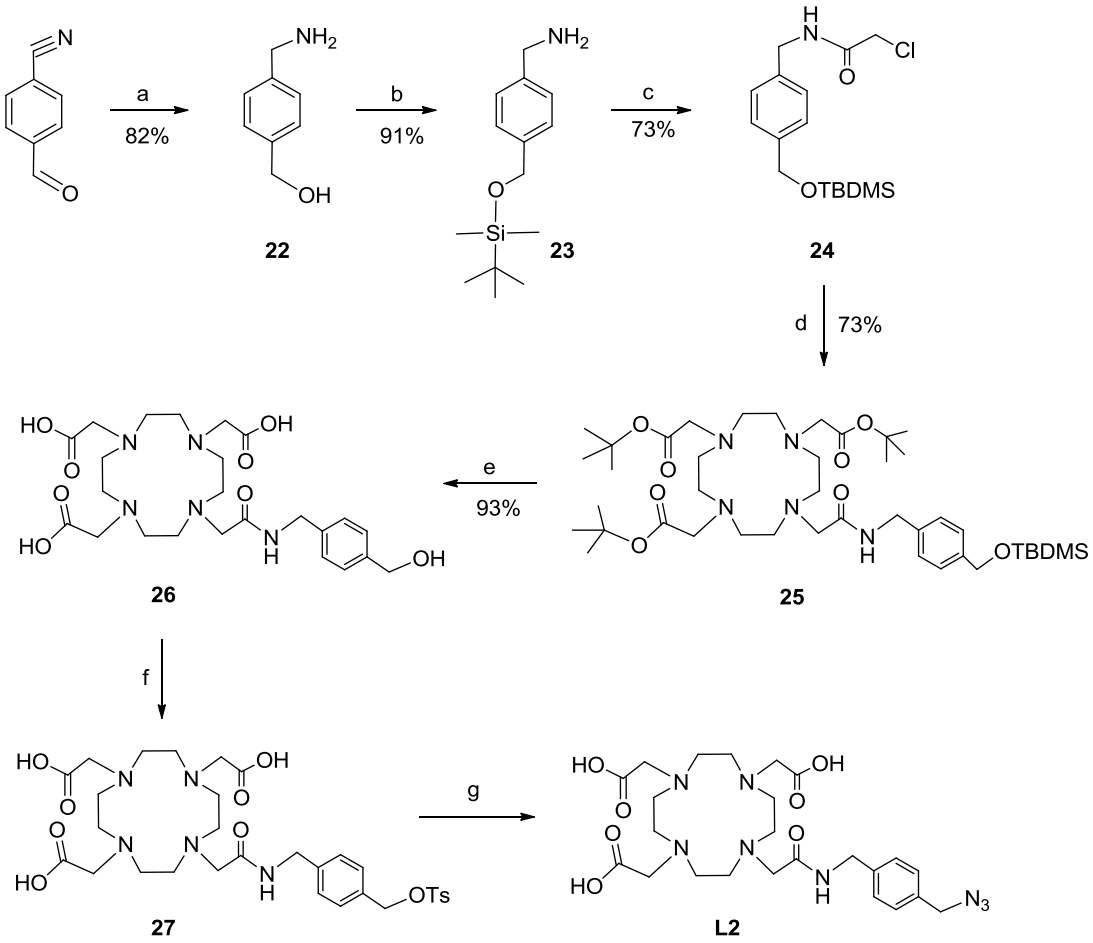

Scheme 3.10 Synthesis of **L2** via (4-aminomethyl-phenyl)methanol. Reagents and conditions: a) $LiAlH_4$, THF, reflux. b) TBDMS-Cl, imidazole, DMF, 0 °C. c) chloroacetyl chloride, NEt_3, DCM, RT. d) DO3A-^{t}Bu, K_2CO_3, MeCN, reflux. e) TFA, DCM, RT. f) TsCl, pyridine, RT. g) NaN_3, DMF, 60 °C.

The addition of **24** to DO3A-^{t}Bu was based on literature protocols,[91] and gave **25**, which was characterised by ^{1}H NMR and ESI-MS. Deprotection of the TBDMS and *tert*-butyl groups with trifluoroacetic acid (TFA) gave the macrocycle **26** which was water-soluble. ^{1}H NMR of **26** showed loss of the *tert*-butyl signals from the protecting groups and the ESI-MS spectrum showed the molecular ion peak at 524.27 $[M + H]^+$. The reaction to convert the OH to a tosylate group to allow for subsequent azide substitution proved difficult due to solubility issues. The macrocycle was not soluble in DCM or most other water immiscible organic solvents, so the reaction was carried out in pyridine. However, purification was difficult as the pyridine removal was purely by evaporation *in vacuo* and was never fully removed even after extended drying. Characterisation by ^{1}H NMR showed traces of pyridine, as well as the product peaks, but also traces of unreacted starting material. Attempts at washing away the unreacted starting materials and pyridine with DCM, as well as passing the compound down a sephadex column were unsuccessful. The azidation reaction was

attempted on crude **27** but this was also unsuccessful as the unreacted azide was not possible to be removed with an aqueous work up.

Due to the difficulties in synthesising **L2** via this method, the azide benzyl arm synthesis via dibromobenzene was investigated (**Scheme 3.11**). Conversion of 1,4-bis(bromomethyl)benzene (or dibromo xylene) to a diazide species (**28**) was followed by mono reduction of an azide to an amine (**29**) using literature methods.[113] The amine is then reacted with chloroacetyl chloride to form a reactive chloro-alkyl amide species (**30**) that can be attached to DO3A.

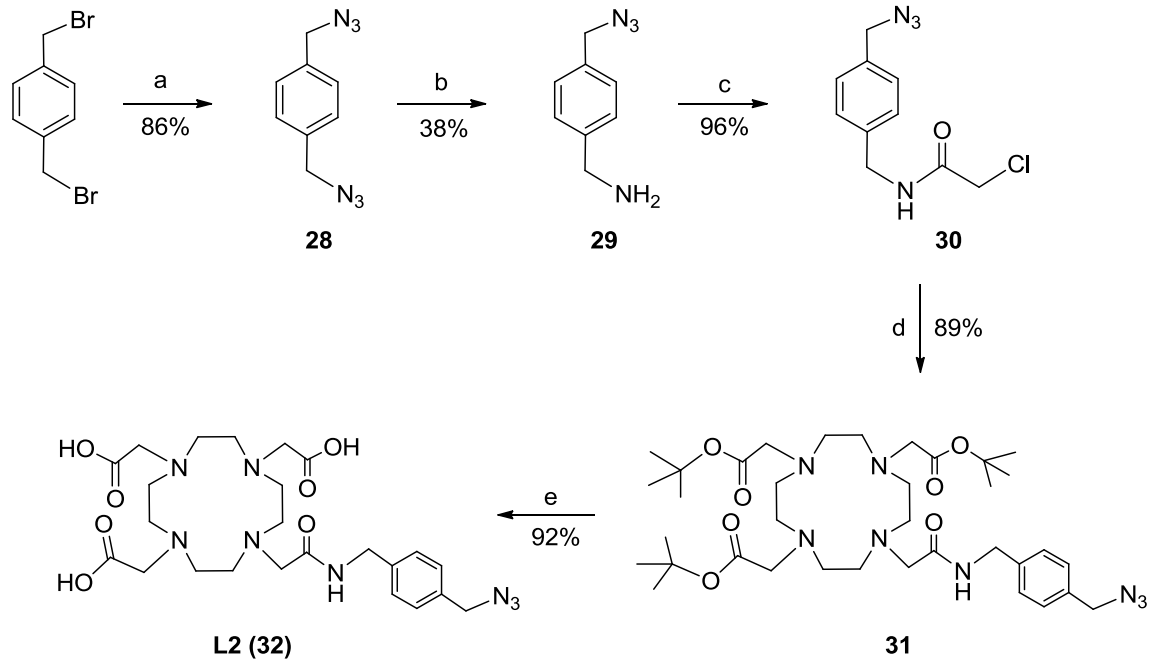

Scheme 3.11 Synthetic route towards the modified azido-DOTA target macrocycle via 1,4-bis(bromomethyl)benzene. Reagents and conditions: a) NaN_3, DMF, 60 °C. b) PPh_3, 1M HCl/Et_2O, RT. c) chloroacetyl chloride, NEt_3, DCM, RT. d) DO3A-^{t}Bu, K_2CO_3, MeCN, reflux. e) TFA, DCM, RT.

Using a literature method where two equivalents of sodium azide was used, 1,4-bis(bromomethyl)benzene species was converted to the diazido species (**28**).[114] The reaction was high yielding (86 %) and did not require further purification after aqueous workup. Characterisation by ^{1}H NMR and ESI-MS was in accordance with literature. The subsequent reaction to convert one of the azide groups to an amino group was also carried out according to literature, via the Staudinger reaction.[113] It involved a two phase reaction with diethyl ether and 1 M HCl, and 1.3 equivalents of triphenylphosphine as a reducing agent. As the reduction of one azide was completed, the desired product (**29**) was taken up into the HCl layer. This reaction to give **29** gave moderate yields (38 % compared to literature yield of 60 %) but after an aqueous workup, no further purification of the

product obtained was required. Purity was confirmed by ^{1}H NMR and ESI-MS as well as elemental analysis, and these data were in accordance with literature.

The next stage was to react **29** with chloroacetyl chloride to give **30**, which has not previously been reported. The reaction was extremely high yielding (>90 %), needing no further purification after workup. The purity of **30** was confirmed by CI-MS and elemental analysis. Finally, 1.5 equivalents of **30** was reacted with DO3A-^{t}Bu in the presence of K_2CO_3 to give **31**. From the ^{1}H and ^{13}C{^{1}H} NMR spectra, the desired product was successfully synthesised. High resolution ESI-MS shows the molecular ion peak at 717.4674 $[M + H]^+$, and purity was confirmed by elemental analysis. Subsequent deprotection of the ^{t}Bu groups with TFA gave **L2** (**32**) which was characterised by the loss of the ^{t}Bu signals in the ^{1}H NMR, and high resolution ESI-MS with the molecular ion peak for $[M+H]^+$ at *m/z* = 549.2788. Elemental analysis was attempted but did not give satisfactory values most likely due to the presence of salts after the deprotection with TFA.

Complexation of **L2** with Eu and Tb was carried out. In a typical complexation reaction, a slight excess (1.2 eq) of the metal salt was added to the DOTA ligand and the pH of the solution adjusted to 5.5. The reaction mixture was left to stir overnight. The pH of the solution was raised to around 10 to precipitate any unreacted metal which was filtered off. The filtrate was concentrated and then purified by passing through a sephadex G-10 column to remove any salts.

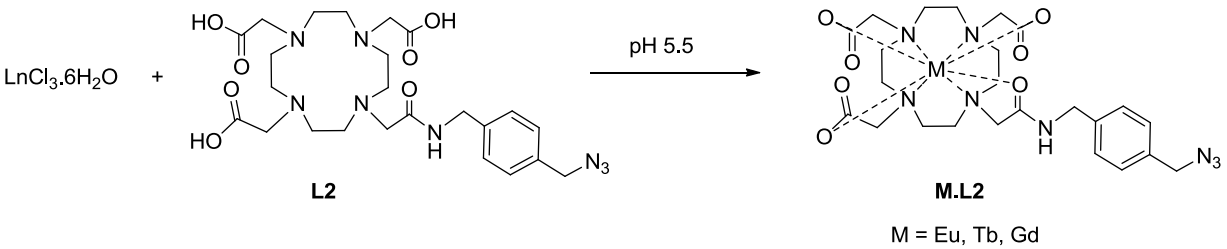

Scheme 3.12 Complexation of the modified azido-DOTA **L2** with M = Eu, Tb, Gd.

a) Characterisation of the Ln.L2 complexes

The gadolinium complex **Gd.L2** (**35**) was isolated as a pale yellow solid. High resolution ESI-MS gave an $[M + H]^+$ peak at *m/z* = 704.1820 with the correct isotope splitting pattern for a Gd(III) complex. Relaxivity for **35** was found to be 4.70 mM^{-1} s^{-1}, and is comparable to the relaxivity of **16** (**Gd.L1**) and Gd-DOTA.

The europium complex **Eu.L2** (**33**) was isolated as a pale yellow solid. High resolution ESI-MS gave an $[M + H]^+$ peak at *m/z* = 697.1766 with the correct isotope splitting pattern for a Eu(III) complex. An

extended sweep-width ^{1}H NMR of the complex was recorded (**Figure 3.19**) showing signals between -20 and +36 ppm and is as expected for Eu-DOTA-type complexes. Like **Eu.L1** (**14**), the SAP isomer was again predominantly present.

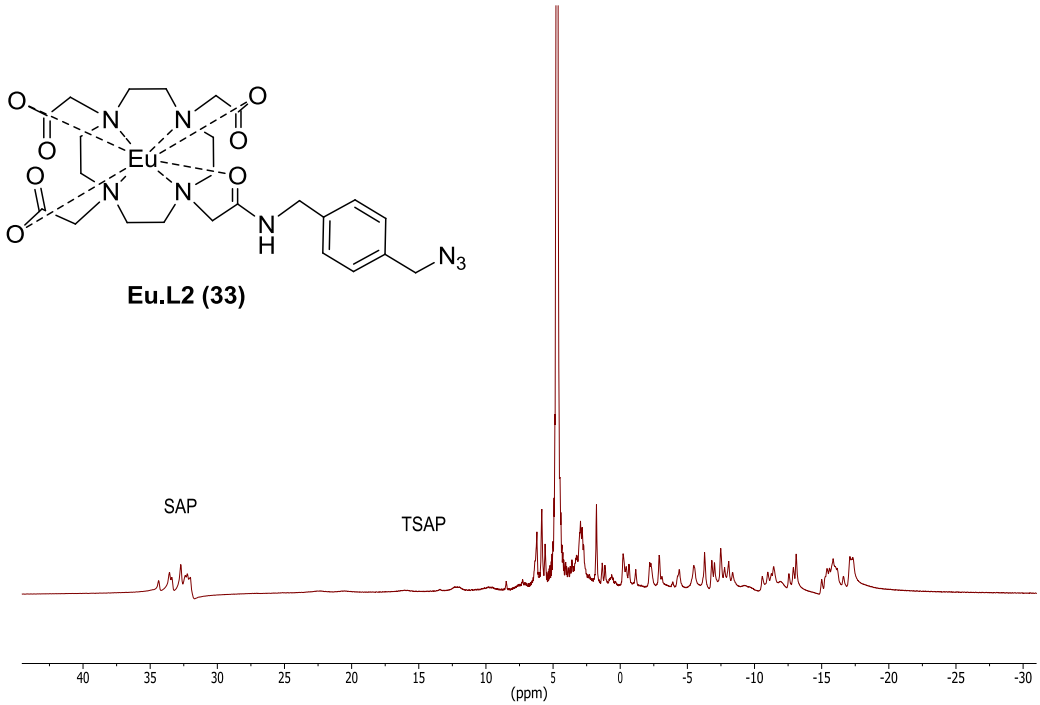

Figure 3.19 Extended sweep-width ^{1}H NMR spectrum of **Eu.L2** (D_2O, 400 MHz, 250 to -250 ppm).

As with the triazole formed with the cyclised **Eu** and **Tb L1** complexes (**18** and **19**), the benzyl group in **L2** is also expected to act as an antenna for the lanthanide emission. The excitation spectrum was monitored at λ_{em} = 595 nm (ΔJ = 1 transition) and showed an intense indirect sensitisation at λ_{ex} 255 nm, with a much weaker peak at λ_{ex} 395 nm. The emission spectrum of **33** (**Figure 3.20**) was recorded at both excitation wavelengths, 255 nm (excitation of the benzyl group) and 395 nm (pseudo direct excitation of the Eu(III) centre). Both emission spectra gave the spectral lines for a Eu(III) complex, with the 255 nm emission having more defined spectral lines than at 395 nm. The signal intensity at 255 nm is also higher than when excited at 395 nm, confirming that there is energy transfer from the benzyl group to the Eu centre.

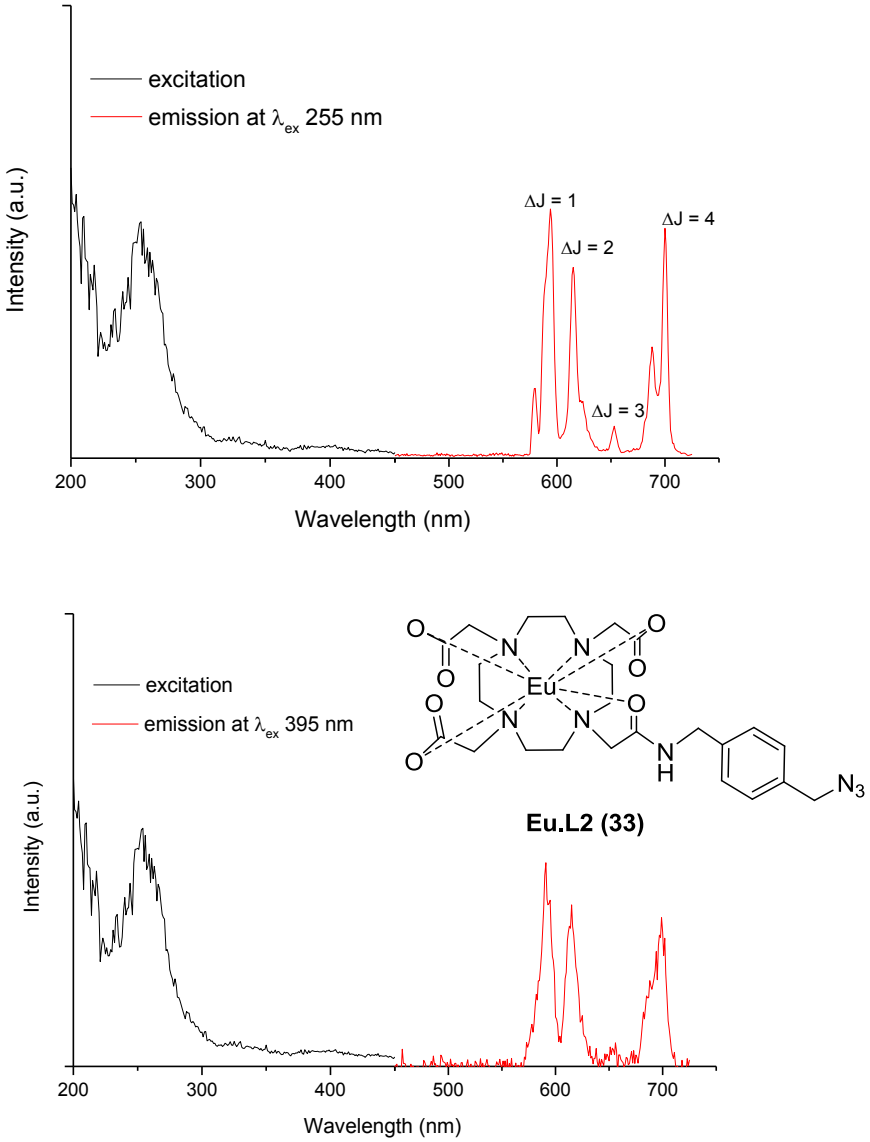

Figure 3.20 Emission spectra of **33** at λ_{ex} 255 nm (top) with 2.5/2.5 slits, and 395 nm (bottom) 10/10 slits. The excitation spectrum corresponds to λ_{em} 595 nm. The 255 nm spectrum was recorded at smaller slits as higher slit gave a signal intensity >1000 that was not plottable. Samples recorded in H_2O, 100 µM, 298 K, pH 7.4.

The terbium complex **Tb.L2** (**34**) was isolated as a pale yellow solid. High resolution ESI-MS gave an $[M + H]^+$ peak at *m/z* = 705.1802. The excitation spectrum was monitored at λ_{em} = 545 nm (ΔJ = 1 transition) and showed a maximum at λ_{ex} 255 nm, but no peak at 355 nm. Nevertheless, the emission spectrum of **34** (**Figure 3.21**) was recorded at both wavelengths, 255 nm (excitation of the benzyl group) and 355 nm (pseudo direct excitation of the Tb(III) centre). Both emission spectra gave the expected spectral shape for Tb complex, with the various $^5D_4 \rightarrow {}^7F_J$ (J = 3 – 6) transitions. The emission spectrum at 255 nm has a higher intensity emission than 355 nm for the same slit (10/10) with the 255 nm emission going over the range (>1000) of recorded intensity. Therefore for the

255 nm graph (**Figure 3.21**), it is a plot of the emission at slit 2.5/2.5 which reduced the maximum intensity of the emission spectrum to an intensity that was plottable. This increase in intensity confirms that there is energy transfer from the benzyl group to the Tb centre.

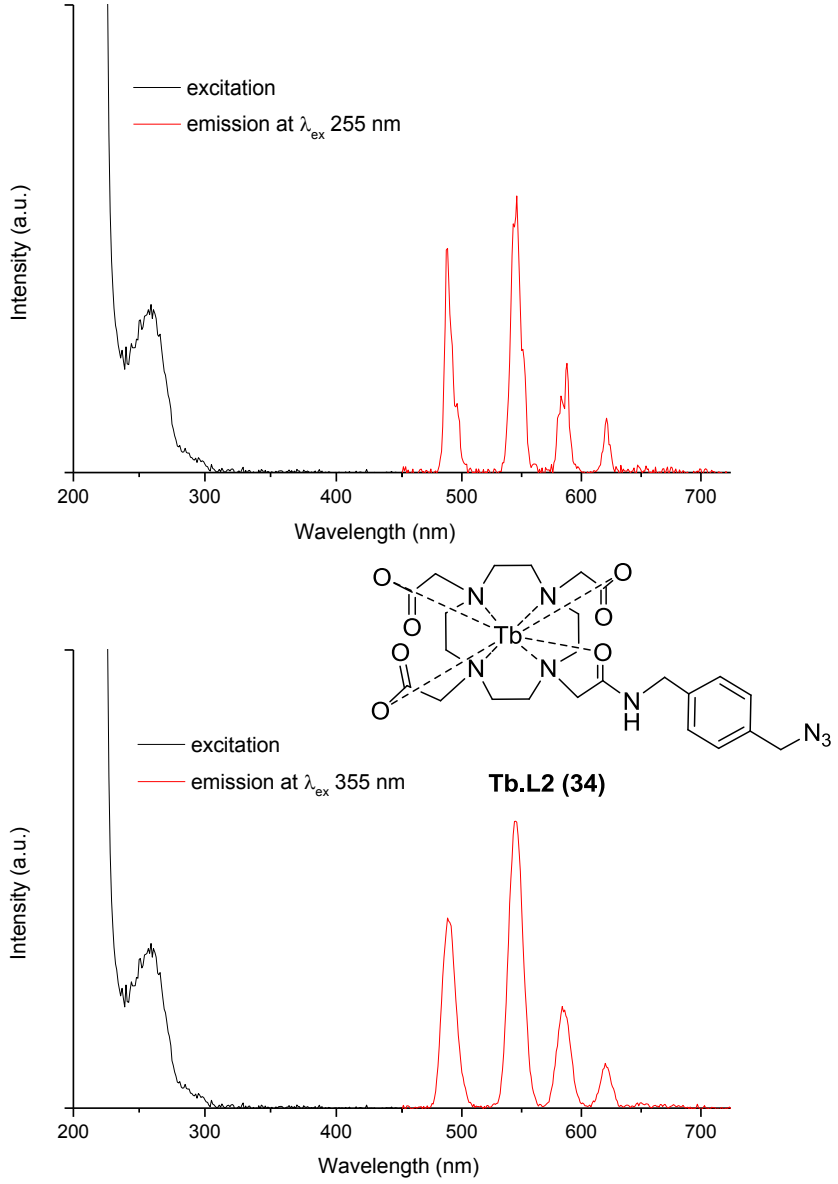

Figure 3.21 Emission spectra of **34** at λ_{ex} 255 nm (top) with 2.5/2.5 slits, and 355 nm (bottom) 10/10 slits. The excitation spectrum corresponds to λ_{em} 545 nm. The 255 nm spectrum was recorded at smaller slits as higher slit gave a signal intensity >1000 that was not plottable. Samples recorded in H_2O, 100 µM, 298 K, pH 7.4.

Luminescence decays of both **33** and **34** in H_2O and D_2O were measured. From the lifetime measurements, both **33** and **34** have hydration states close to 1 (**Table 3.9**), showing that both complexes are eight coordinate and will bind one water molecule.

Complex	τ_{H2O}/ms	k_{H2O}/ms^{-1}	τ_{D2O}/ms	k_{D2O}/ms^{-1}	*q*
33	0.63	1.59	1.93	0.52	0.90
34	1.98	0.51	3.32	0.30	0.72

Table 3.9 Lifetimes, rate constants and derived hydration states for **33** and **34**.

b) Small molecule cycloaddition reaction of M.L2 complexes to cyclooctyne

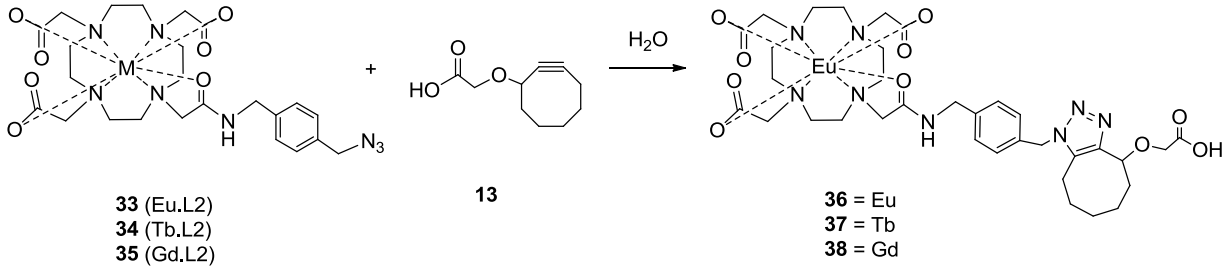

33 (Eu.L2)
34 (Tb.L2)
35 (Gd.L2)

13

36 = Eu
37 = Tb
38 = Gd

Scheme 3.13 Cycloaddition reaction between **M.L2** and cyclooctyne **13.**

Like the **M.L1** complexes, **M.L2** were also reacted with **13** in a copper-free cycloaddition reaction (**Scheme 3.13**). Fluorescence spectroscopy of **36** (**Figure 3.22**) and **37** (**Figure 3.23**) showed little to no change after the cycloaddition reaction, in both the excitation and emission spectra. The excitation spectra for **36** was obtained by monitoring at λ_{em} 595 nm, while for **37** this was at λ_{em} 545 nm. Both showed increased intensity for the λ_{ex} 255 nm peak, which is most likely a contribution from the aromatic benzyl unit and possibly the triazole too. The emission spectra for both **36** and **37** at 255 nm, and also at 395 nm (for **36 - Eu**) and 355 nm (for **37 - Tb**), were similar to the pre-cyclised species, with the 255 nm emission spectrum for **36** having higher intensity and more defined spectral shape. As previously discussed, sensitised emission is affected by the distance between the chromophore and the Ln(III) centre, and if the triazole formed during the cycloaddition reaction is far enough away from the Ln(III) centre, the spectra of the cyclised species should see very little change.

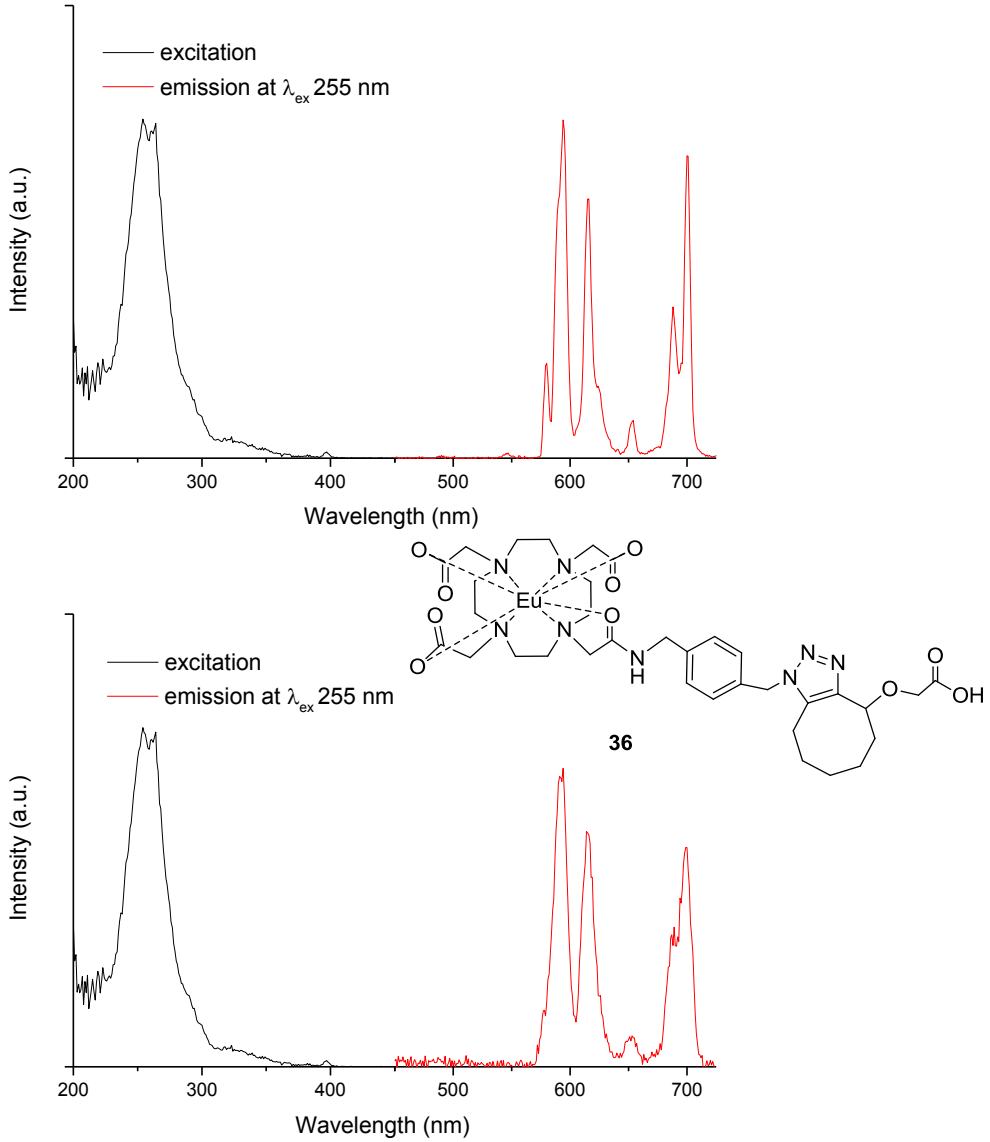

Figure 3.22 Emission spectra of **36** at λ_{ex} 255 nm (top), and λ_{ex} 395 nm (bottom). Excitation spectra in both were recorded for λ_{em} 595 nm. Samples recorded in H_2O, 100 µM, 298 K, pH 7.4.

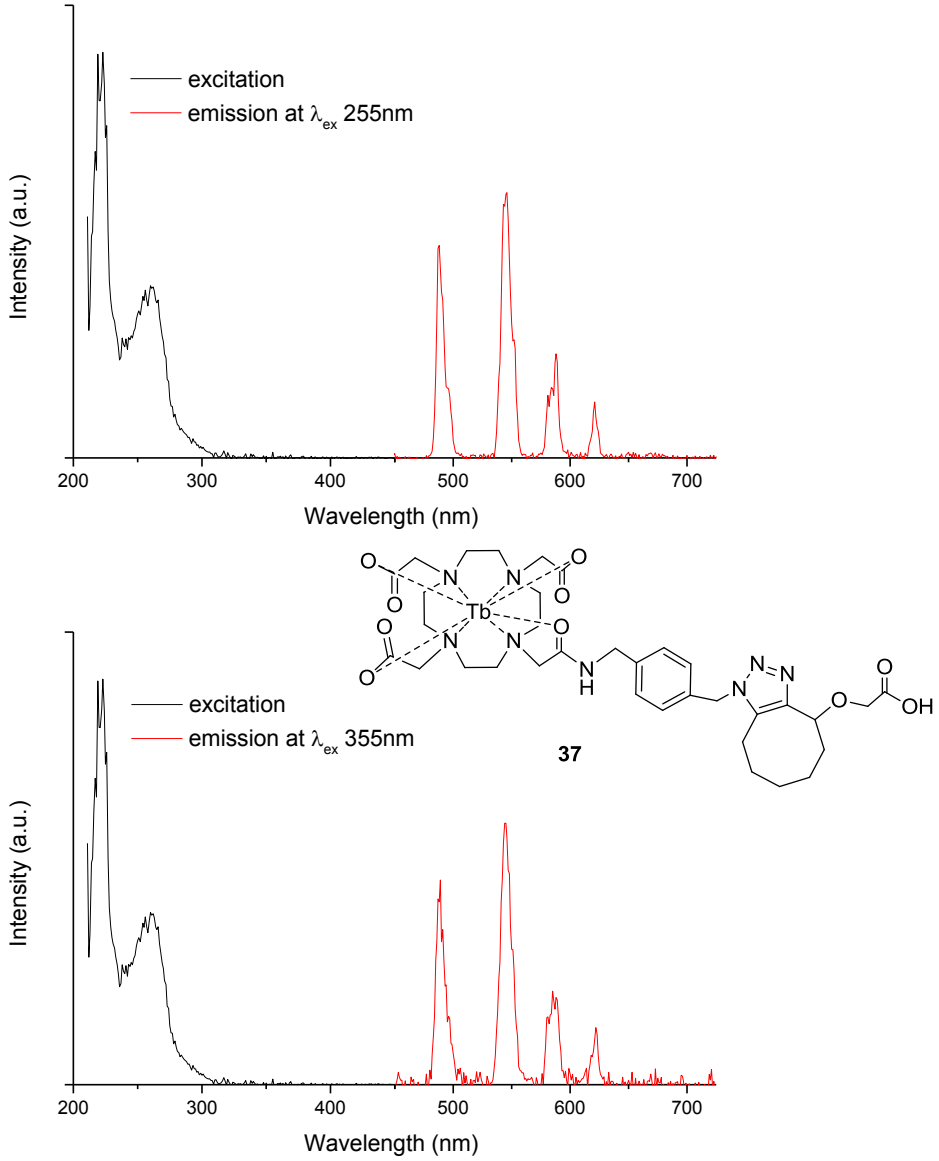

Figure 3.23 Emission spectra of **37** at λ_{ex} 255 nm (top), and λ_{ex} 395 nm (bottom). Excitation spectra in both were recorded for λ 545 nm. Samples recorded in H_2O, 100 μM, 298 K, pH 7.4.

36, 37 and **38** were also characterised by MALDI-MS (T**able 3.10**). High resolution ESI-MS was attempted, but no molecular ion or fragment peaks were observed.

Complex	*Calc. m/z*	*Found m/z*
36	880.3	881.3
37	886.3	887.3
38	885.4	886.4

T**able 3.10** *m/z* values for the cyclised complexes **36 - 38**.

3.4.5 Copper-free cycloaddition reaction between Ln.L2 to NP-alkyne

The copper-free cycloaddition reaction between the **Ln.L2** complexes (Ln = Eu, Tb, Gd) and **NP12** (**NP-alkyne**) were carried out (**Scheme 3.14**), as previously with **Ln.L1** and **NP12**, and fluorescence spectroscopy of the nanoparticles recorded, to determine if there would be any enhanced emission from the lanthanide conjugated to the nanoparticle.

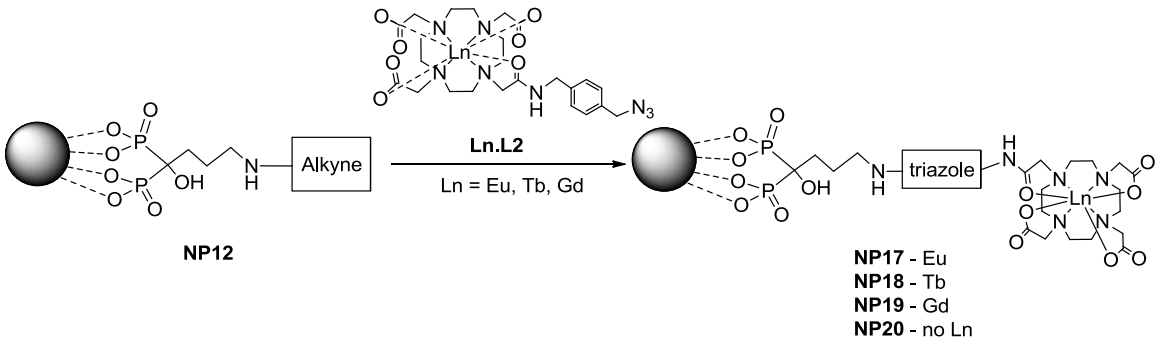

Scheme 3.14 Copper-free cycloaddition reactions between **NP12** and **Ln.L2** (Ln = Eu, Tb, Gd).

As before, emission spectra for **NP17** (Eu species) showed that there was an unexpected well defined emission from the nanoparticles when excited at 395 nm, but not the expected emission from the Eu(III) centre (**Figure 3.26**). When excited at 375 nm (**Figure 3.25**), the spectra show some similarities to the expected emission from a terbium metal centre (transitions at 490, 545, 580 and 610 nm), although much less defined. When the NPs were excited at 255 nm (**Figure 3.24**), neither the Eu nor Tb spectral shape was observed. The same spectral pattern was observed for all the NP species at the specific wavelengths, including when the lanthanide centre was gadolinium, when there was no Ln centre, as well as for **NP2** (alendronate) and **NP12** (alkyne).

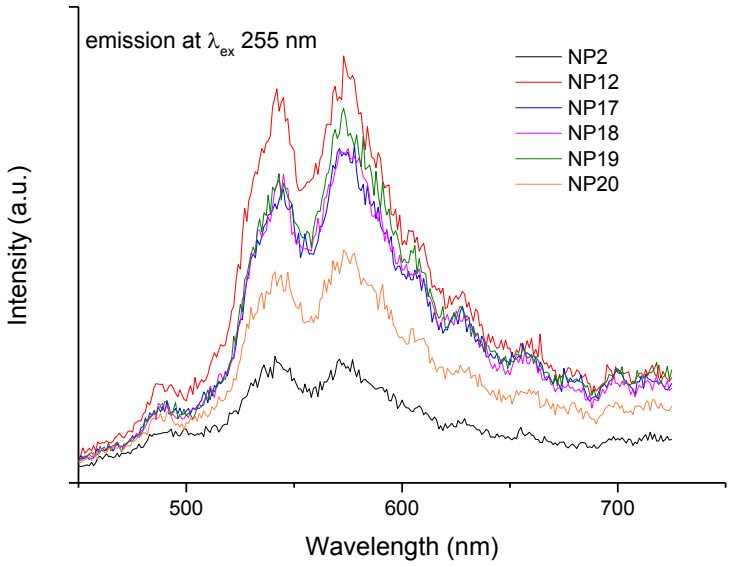

Figure 3.24 Emission spectrum of all the NP species at λ_{ex} 255 nm, H_2O, 0 ms delay, slits 10:10, 0.5 mg/mL Fe, pH 7, 25 °C.

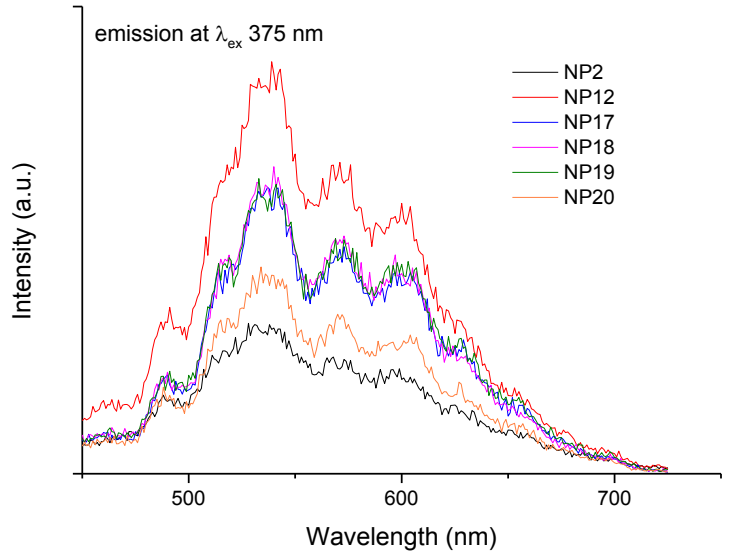

Figure 3.25 Emission spectrum of all the NP species at λ_{ex} 255 nm, H_2O, 0 ms delay, slits 10:10, 0.5 mg/mL Fe, pH 7, 25 °C.

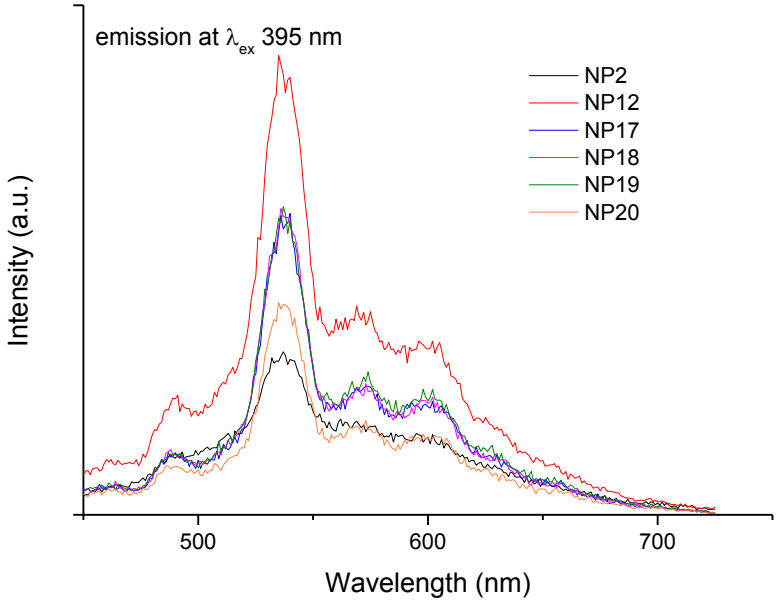

Figure 3.26 Emission spectrum of all the NP species at λ_{ex} 395 nm, H_2O, 0 ms delay, slits 10:10, 0.5 mg/mL Fe, pH 7, 25 ^{o}C.

The same emission spectral shape was observed for each NP species at a specific wavelength, and this emission spectral shape changes in the same way for all the NP species when the excitation wavelength applied is changed. This suggests that the emission observed is most likely not due to the lanthanide complex conjugated to the nanoparticle, but rather emission from the nanoparticle itself. This is similar to results observed by Fei *et al* where shifts in the emission peaks are observed for different excitation wavelengths.[100] They describe nanosized particles as having a large number of lattice defects on the particle surface and when organic molecules are bound to the surface the electronic structure of the whole particle changes. As a result, the 4*s* and 4*p* states (over the 3*d* states) have an increased probability of being populated, and of being involved in energy transition to give emission. This could explain the spectral patterns observed for all the nanoparticle species, even when the surface molecules differ. However, in order to confirm this, further experiments on more sophisticated instruments with a high powered laser are required.

3.5 Conclusion

The functionalisation of **NP2** with PEG for biocompatibility purposes, and also with a cyclooctyne for pretargeted click reaction, were carried out. The PEGylated and alkyne functionalised nanoparticles were characterised by IR spectroscopy and colourimetric assays to determine yields and availability of reactive functional groups on the NP surface. Both **NP2-PEG** (**NP3** – **NP11**) and **NP2-alkyne** (**NP12**) were successful but with variable yields. Even with an excess of reactants, the coupling yield of the alkyne was quite low, but this was due to the resultant low-solubility of the nanoparticle when a large excess was utilised.

Copper-free cycloaddition reactions of the **NP2-alkyne** species with the azide-DOTA (**L1**) were characterised by following the luminescence of the Eu(III) and Tb(III) **L1** complexes once on the nanoparticle. Unexpected results were obtained which suggested the emission observed was from the nanoparticles as opposed to the lanthanide, even though presence of the lanthanide was confirmed by ICP-MS. Modification to the DOTA chelate (to give the novel compound **L2**) and subsequent click reactions with the **Ln.L2** complexes to **NP2-alkyne** still gave emission spectra that suggests nanoparticle luminescence. Unfortunately, due to time constraints, conjugation of the nanoparticles to the gallium-68 analogue of the azide-DOTA macrocycles (**L1** and **L2**) were not carried out.

3.6 Experimental

Syntheses of ligands were carried out under nitrogen unless stated otherwise. Chemical reagents were purchased from Sigma-Aldrich, TCI-UK, or VWR (Alfa Aesar). dPEG's were obtained from both Quanta Biodesign and Iris Biotech. All the reagents were used as received without further purification. Dry solvents were obtained from the Imperial College Chemistry Department dry solvent towers which dried the solvents over alumina beads. All other solvents were analytical grade and were obtained from VWR. EDC couplings were carried out in MilliQ water under ambient conditions. Composition analysis of the nanoparticles was carried out by Dr Stanislav Strekopytov at the Natural History Museum, London on an ICP-MS (Agilent 7700x ICP-MS). UV-Vis spectra were recorded in a Perkin-Elmer Lambda 25 UV-Vis system. Fluorescence spectra were recorded in aqueous solutions on a Cary Varian luminescence spectrometer. Samples were held in 10 mm × 4 mm quartz Hellma cuvettes. FT-IR spectra were acquired in a Perkin-Elmer Spectra 100 FT-IR spectrometer, neat on ATR plates. ^{1}H NMR spectra and T_1/T_2 inversion recovery data were obtained in a Bruker DRX400 MHz spectrometer. Z-measurements were obtained in a Beckman Coulter Delsa™ Nano.

3.6.1 Synthesis of PEGylated NP2

a) NP-PEG$_n$-NH$_2$ (NP6, NP7, NP8)

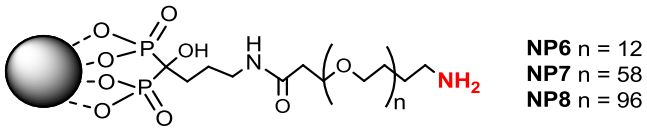

NP6 n = 12
NP7 n = 58
NP8 n = 96

To **NP2** in MilliQ water (0.5 mg NP, 1.43 nmol, typically about 250 µL from a 2.0 mg/mL NP solution) was added HOOC-PEG$_n$-NH(fmoc) (300 eq) in the presence of EDC (excess). After overnight reaction, the mixture was centrifuged and the supernatant decanted. The black pellet was suspended in a piperidine/DMF (20/80) mixture for 15 mins, to remove the Fmoc group on the amine. This was followed by addition of acetone to precipitate the nanoparticles. The alternating piperidine/DFM and acetone steps were repeated three times in total to give the free amine, and the final nanoparticles were resuspended in water (250 µL).

b) NP-PEG$_n$-OH (NP3, NP4, NP5)

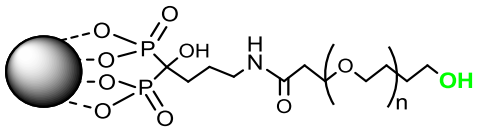

To **NP2** in MilliQ water (0.5 mg NP, 1.43 nmol, typically about 250 µL from a 2.0 mg/mL NP solution) was added HOOC-PEG$_n$-OH (300 eq) in the presence of EDC (excess). After overnight reaction, the mixture was centrifuged and the supernatant decanted. The black pellet was suspended in water and washed by precipitation with acetone. This was repeated three times and the resultant nanoparticles were resuspended in water (250 µL).

c) NP-PEG$_n$-COOH (NP9, NP10, NP11)

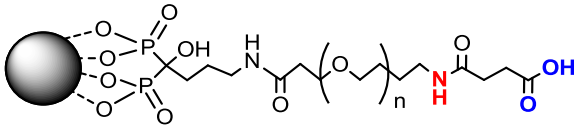

Succinic anhydride (5 – 10 mg, excess) in water (250 µL) was adjusted to pH 8 with KOH. To this was added **NP-PEG$_n$-NH$_2$** in water (0.5 mg NP, 250 µL). The pH was adjusted again to pH 8 and the mixture left to react for 1 hour. At the end of the reaction, the mixture was washed three times by precipitation with acetone, and the resultant nanoparticles were resuspended in water.

3.6.2 Synthesis of the strained alkyne

The following procedures to synthesise **11, 12** and **13** were according to a literature method, with no modifications.[81]

a) 8,8-Dibromobicyclo[5.0.1]octane (11)

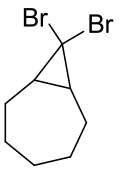

Cycloheptene (1.00 g, 10.40 mmol) was dissolved in dry pentane (5 mL). Potassium *tert*-butoxide (2.33 g, 20.80 mmol, 2.0 eq) was added under nitrogen. The mixture was cooled to -10 °C and the addition of bromoform (3.94 g, 15.60 mmol, 1.5 eq) gave a brown mixture which was stirred at room temperature overnight. Water (50 mL) was then added and neutralised with 1 M HCl (approx. 1 mL).

The aqueous phase was washed with pentane (3 x 20 mL), the pentane layers combined and washed with water (3 x 20 mL), dried over $MgSO_4$ and concentrated *in vacuo* to give a yellow-orange oil. This was purified by passing through a short silica column (95:5 cyclohexane/EtOAc) to give a clear oil (1.20 g, 4.51 mmol, 43 % yield). ^{1}H NMR (400 MHz, $CDCl_3$): δ 2.24 – 2.31 (2H, m), 1.80 – 1.95 (3H, m), 1.69 – 1.79 (2H, m), 1.32 – 1.41 (2H, m), 1.10 – 1.28 (3H, m). EI-MS (m/z): 266 $[M]^+$.

b) Methyl 2-bromocyclooct-1-en-3-glycolate (12)

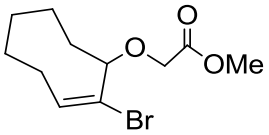

8,8-Dibromobicyclo[5.0.1]octane (1.00 g, 3.76 mmol) and methyl glycolate (2.61 mL, 33.84 mmol) were dissolved in anhydrous toluene (5 mL) and protected from light by aluminium foil and N_2. $AgClO_4$ (1.56 g, 7.52 mmol) was added under N_2 flow and stirred at room temperature for 1.5 h. Silver salts were then filtered and washed with EtOAc. The filtrate was concentrated and the residue purified immediately by column chromatography on silica (2-15 % EtOAc/cyclohexane) to give the product as a yellow oil (0.51 g, 1.83 mmol, 49 % yield). ^{1}H NMR (400 MHz, $CDCl_3$): δ 6.25 (1H, dd, $^3J_{H\text{-}H}$ = 4.06, 11.56 Hz), 4.27 (1H, d, $^2J_{H\text{-}H}$ = 16.1 Hz), 4.15 (1H, dd, $^3J_{H\text{-}H}$ = 4.83, 10.17 Hz), 4.01 (1H, d, $^2J_{H\text{-}H}$ = 16.1 Hz), 3.79 (3H, s), 0.79 – 2.81 (10H, m). ESI-MS (m/z): 299 $[M + 23]^+$.

c) Cyclooct-1-yn-3-glycolic acid (13)

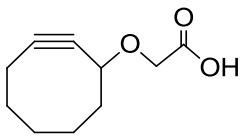

Methyl 2-bromocyclooct-1-en-3-glycolate (0.50 g, 1.81 mmol) was dissolved in anhydrous DMSO (2 mL and 0.5 M NaOMe solution (24 mL) and stirred overnight. The methanol was removed *in vacuo* and the dark yellow residue taken up in DCM and 1 M HCl added until the solution was pH 4. The phases were separated and the aqueous phase extracted further with DCM. The combined DCM layers were concentrated and purified by column chromatography (silica, 0-8 % MeOH/DCM) to yield a pale yellow oil (0.18 g, 1.01 mmol, 56 % yield). ^{1}H NMR (400 MHz, $CDCl_3$): δ 9.10 (1H, br s, H_{acid}), 4.30 – 4.63 (1H, m), 4.19 (1H, d, $^2J_{H\text{-}H}$ = 16.8 Hz), 4.03 (1H, d, $^2J_{H\text{-}H}$ = 16.8 Hz), 1.30 – 2.30 (10H, m). $^{13}C\{^1H\}$ NMR (100 MHz, $CDCl_3$): δ 172.29, 101.06, 91.72, 72.67, 65.89, 42.17, 40.78, 34.23, 29.62, 26.24, 20.65. CI-MS (m/z): 200 $[M + NH_4]^+$.

3.6.3 Synthesis of NP2-alkyne (NP12)

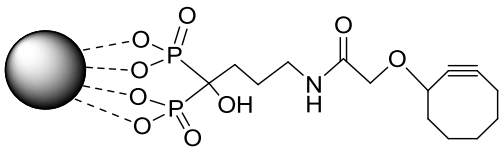

NP2 (0.5 mg NP, 1.43 nmol, typically about 250 µL from a 2.0 mg/mL NP solution) was adjusted to pH 8. The cyclooctyne **2.3** (0.078 mg, 0.43 µmol) was dissolved in MeOH (20 µL) and added to the nanoparticle solution. EDC (about 5 mg, excess) was added and the mixture left to shake overnight. The nanoparticles were precipitated out with acetone, centrifuged, and the supernatant decanted. This was repeated three times. Finally, the resultant nanoparticles were resuspended in water (250 µL).

3.6.4 Complexation of L1 to M (M = Eu, Tb, Gd, Ga)

a) Synthesis of Eu.L1(14)

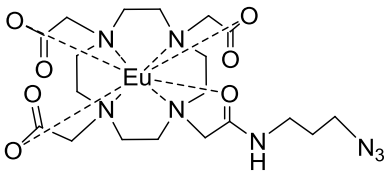

Eu.L1 (14)

Ligand **L1** (11.10 mg, 0.0186 mmol) was dissolved in MilliQ water (1 mL) and the pH adjusted to 5.5 with 0.5 M KOH. $EuCl_3.6H_2O$ (8.87 mg, 0.024 mmol, 1.3 eq) was added slowly, while maintaining the pH at 5.5. The mixture was stirred overnight. Unreacted Eu^{3+} was precipitated as $Eu(OH)_3$ by the addition of 0.5 M KOH (pH of mixture at 10). The precipitate was separated from the supernatant by centrifugation. The supernatant was concentrated *in vacuo*, and the residue passed down a Sephadex G-10 column. Fractions containing the compound were tested for free metal by the xylenol orange test.[115] Metal-free fractions were combined and the solvent removed by lyophilisation. **Eu.L1** was obtained as a white solid (8.50 mg, 0.013 mmol, 72 %). ESI-HRMS calc. for $C_{19}H_{31}EuN_8O_7$ 637.1606 found (m/z): 637.1610 $[M + H]^+$.

b) Synthesis of Tb.L1(15)

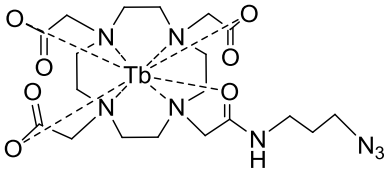

Tb.L1 (15)

Tb.L1 was synthesised according to the same method as the Eu analogue. **L1** (12.30 mg, 0.021 mmol) and $TbCl_3.6H_2O$ (10.02 mg, 0.026 mmol, 1.3 eq) were used. The complex was obtained as a white solid (9.50 mg, 0.0148 mmol, 72 %). ESI-HRMS calc. for $C_{19}H_{31}N_8O_7Tb$ 643.1647 found (m/z): 643.1656 $[M + H]^+$.

c) Synthesis of Gd.L1(16)

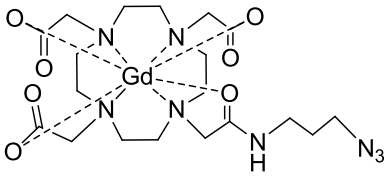

Gd.L1 (16)

Gd.L1 was synthesised according to the same method as the Eu analogue. **L1** (11.60 mg, 0.019 mmol) and $GdCl_3.6H_2O$ (9.41 mg, 0.025 mmol, 1.3 eq) were used. The complex was obtained as a white solid (12.00 mg, 0.0187 mmol, 96 %). ESI-HRMS calc. for $C_{19}H_{31}GdN_8O_7$ 642.1635 found (m/z): 642.1655 $[M + H]^+$.

d) Synthesis of Ga.L1(17)

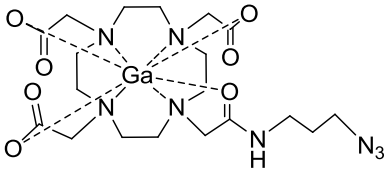

Ga.L1 (17)

Ga.L1 was synthesised according to the same method as the Eu analogue, with the exception that the pH was adjusted to 4.5 instead. **L1** (10.00 mg, 0.017 mmol) and anhydrous $GaCl_3$ (5.90 mg, 0.034 mmol, 2.0 eq) were used. The complex was obtained as a white solid (7.50 mg, 0.014 mmol, 80 %). ESI-HRMS calc. for $C_{19}H_{31}GaN_8O_7$ 553.1650 found (m/z): 553.1637 $[M + H]^+$. ^1H NMR (400 MHz, D_2O): δ 8.34 (1H, t, $^3J_{H\text{-}H}$ = 6.22 Hz, N*H*), 3.94 – 4.10 (4H, m, CH_2 propyl chain), 3.91 (4H, m, macrocycle CH_2

adjacent to propyl azide arm), 3.70 (2H, s, α-CH_2 on azide arm), 3.57 (4H, s, CH_2 on carboxylate arm trans to each other), 3.55 (2H, s, CH_2 on carboxylate arm trans to azide arm), 3.26 – 3.45 (12H, m, macrocycle ring CH_2), 1.82 (2H, m, middle CH_2 on propyl chain).

3.6.5 Synthesis of modified azido-DOTA

a) Synthesis of 1,4,7-Tris(tert-butoxycarbonylmethyl)-1,4,7,10-tetraazacyclododecane hydrobromide (DO3A-tBu ester) [116,117]

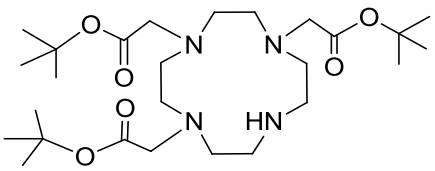

DO3A-tBu ester was synthesised according to literature method.[116,117] Cyclen (1.00 g, 5.81 mmol) and sodium acetate (1.57 g, 19.16 mmol) was suspended in *N,N*-dimethylacetamide (15 mL). The mixture was cooled to -20 °C. In a separate flask, *tert*-butyl bromoacetate (3.74 g, 4.31 mL, 19.16 mmol) was dissolved in DMA (4 mL) and added dropwise over 30 min to the suspension of cyclen after which the reaction mixture was allowed to warm to room temperature and stirred for 24 h. A white precipitate formed during the reaction. After 24 h, the reaction mixture was added to water (90 mL) to give a clear yellow solution. $NaHCO_3$ was added with stirring. Effervescence was observed and an off-white precipitate formed over time. This was filtered under suction and the solid dissolved in chloroform (50 mL). The yellow solution was washed with water (2 x 30 mL), dried over $MgSO_4$, filtered then concentrated to about 2-3 mL. Ether (approx. 50 mL) was added which precipitated a white solid that was filtered under suction to give DO3A-tBu.HBr (1.71 g, 2.88 mmol, 83 % yield). ^{1}H NMR (400 MHz, $CDCl_3$): δ 10.05 (1H, br s, NH), 3.39 (4H, s, CH_2 ^{t}Bu arms), 3.30 (2H, s, CH_2 middle ^{t}Bu arm), 3.12 (4H, m, CH_2 ring H), 2.92 (12H, m, CH_2 ring H), 1.47 (27H, s, ^{t}Bu H). ^{13}C{^{1}H} NMR (100 MHz, $CDCl_3$): δ 171.3, 162.5, 80.9, 57.3, 52.1, 50.7, 47.6, 36.5, 31.4, 28.3. ESI-MS (m/z): 515 $[M – HBr + H]^+$, 459 $[M – HBr – {}^tBu + H]^+$.

b) Synthesis of 4-(aminomethyl)benzyl alcohol (22)[110,111]

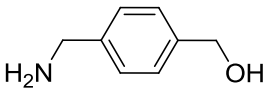

22 was synthesised according to literature method.[110,111] 4-Cyanobenzaldehyde (1.0 g, 7.67 mmol, 1 eq) in dry THF (10 mL) was added dropwise via a pressure-equalising funnel under nitrogen to a

suspension of $LiAlH_4$ (1.75 g, 46.02 mmol, 6 eq) in THF (20 mL) at 0 °C. The mixture was heated to reflux and stirred for 5 hours, before cooling again to 0 °C and quenching with H_2O (2 mL), 15 % NaOH (4 mL) and H_2O again (6 mL). After stirring overnight at room temperature, the mixture was filtered on a pad of celite and washed through with EtOAc. Solvent was evaporated to give the desired compound 4-(aminomethyl)benzyl alcohol as a white solid (0.85 g, 6.21 mmol, 82 %). ^{1}H NMR (400 MHz, $CDCl_3$): δ 7.28 (4H, m, aromatic H), 4.65 (2H, s, -C*H*$_2$-OH), 3.82 (2H, s, C*H*$_2$-NH_2). $^{13}C\{^1H\}$ NMR (100 MHz, $CDCl_3$): 127.3, 65.2, 46.2. EI-MS (m/z): 137 $[M + H]^+$.

c) Synthesis of 4-(aminomethyl)benzyl TBDMS ether (23) [112,117]

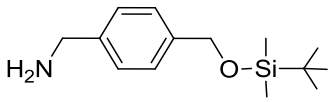

23 was synthesised by a variation of literature methods.[112,117] A solution of 4-(aminomethyl)benzyl alcohol (0.25 g, 1.82 mmol) and imidazole (0.31 g, 4.56 mmol) in DMF (10 mL) was cooled to 0 °C and TBDMS-Cl (0.30 g, 2.00 mmol) was added. The mixture was stirred at room temperature overnight. The reaction mixture was diluted with ethyl acetate, washed with H_2O (3 x 15 mL) and brine (2 x 20 mL). The organic layer was dried over anhydrous magnesium sulphate, filtered and concentrated in vacuo, to give **15** as a yellow oil (0.63 g, 2.76 mmol, 91 %). ^{1}H NMR (400 MHz, $CDCl_3$): δ 7.29 (4H, m, aromatic H), 4.75 (2H, s, -C*H*$_2$-OTBDMS), 3.87 (2H, s, C*H*$_2$-NH_2), 1.60 (2H, br s, N*H*$_2$), 0.96 (9H, s, ^{t}Bu *H*'s TBDMS), 0.12 (6H, s, Me *H*'s TBDMS). $^{13}C\{^1H\}$ NMR (100 MHz, $CDCl_3$): 142.0, 140.0, 127.0, 126.3, 64.8, 46.3, 26.0, 18.4 , -5.2. ESI-HRMS calc. for $C_{14}H_{25}NOSi$ – MeCN adduct 293.2049 found (m/z): 293.2044 $[M\text{-MeCN adduct} + H]^+$.

d) Synthesis of 4-(2-chloro-N-methylacetamide)benzyl TBDMS ether (24)

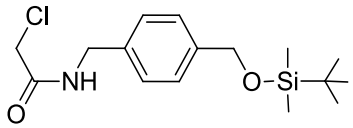

24 is a new compound, and was formed by reacting **23** with the acylating agent chloroacetyl chloride. **23** (0.35 g, 1.37 mmol) and NEt_3 (0.15 g, 0.21 mL, 1.51 mmol) were dissolved in DCM (10 mL) and cooled to 0 °C. This mixture was added dropwise, cold, to a solution of chloroacetyl chloride (0.17 g, 0.12 mL, 1.51 mmol) in DCM (3 mL). The reaction mixture was stirred for 2 hours, after which solvent and volatiles were evaporated *in vacuo*. The residue was dissolved in DCM and

washed with H_2O (10 mL). The organic layer was dried over $MgSO_4$, filtered and solvent evaporated to give **24** as a white solid (0.33 g, 1.00 mmol, 73 %). ^{1}H NMR (400 MHz, $CDCl_3$): δ 7.31 (4H, m, aromatic H), 6.87 (1H, br s, N*H*), 4.76 (2H, s, CH_2-OTBDMS), 4.51 (2H, d, $^3J_{H-H}$ = 5.60 Hz, -CH_2-Cl), 4.13 (2H, s, -CH_2-NH_2), 0.96 (9H, s, ^{t}Bu *H*'s TBDMS), 0.12 (6H, s, Me *H*'s TBDMS). ^{13}C{^{1}H} NMR (100 MHz, $CDCl_3$): 165.9, 141.2, 135.7, 127.8, 126.5, 64.6, 43.7, 42.6, 26.0 18.4, -5.2. IR (ν/cm^{-1}): 1651 (C=O), 3278 (NH). ESI-HRMS calc. for $C_{16}H_{27}NO_2Si$ 293.2049 found (m/z): 293.2086 $[M + H]^+$.

e) Synthesis of 25[91]

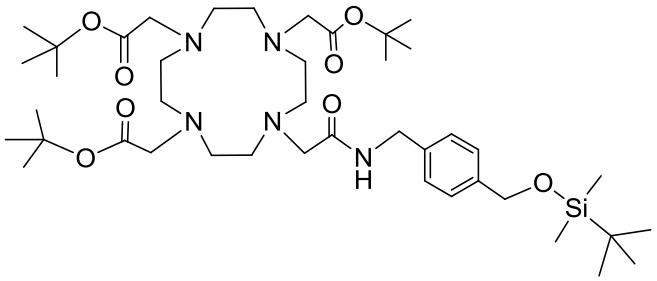

25 is a new compound, and was synthesised following similar protocols from literature.[91] 1,4,7-Tris(*tert*-butoxycarbonylmethyl)-1,4,7,10-tetraazacyclododecane hydrobromide (0.36 g, 0.61 mmol) was dissolved in acetonitrile (20 mL). K_2CO_3 (0.42 g, 3.05 mmol) was added and the suspension stirred for 30 mins before the addition of **24** (0.30 g, 0.92 mmol). The reaction mixture was heated to reflux overnight. When cooled to room temperature, the base and salts were filtered off, and the filtrate evaporated. The residue was dissolved in DCM, washed with water then dried over $MgSO_4$, filtered and solvent evaporated to give **25** as a pale yellow oil (0.36 g, 0.44 mmol, 73 %). ^{1}H NMR (400 MHz, $CDCl_3$): δ 7.29 (4H, m, aromatic H), 4.68 (2H, m, -NH-CH_2-benzyl), 4.38 (2H, m, -CH_2-OTBDMS), 2.40 – 3.44 (24H, m, CH_2 backbone and those closest to the macrocycle, on arms), 1.45 (18H, s, ^{t}Bu on arms trans to each other), 1.43 (9H, s, ^{t}Bu on arm trans to chromophore arm), 0.91 (9H, s, ^{t}Bu on TBDMS), 0.08 (6H, s, Me H's on TBDMS). ^{13}C{^{1}H} NMR (100 MHz, $CDCl_3$): 171.8, 171.7, 128.0, 127.8, 127.1, 126.0, 82.0, 81.9, 81.6, 64.8, 58.0, 56.4, 42.7, 28.2, 28.0, 26.0, 18.4, -5.2. ESI-HRMS calc. for $C_{42}H_{76}N_5O_8Si$ 806.5463 found (m/z): 806.5482 $[M + H]^+$.

f) Synthesis of 26

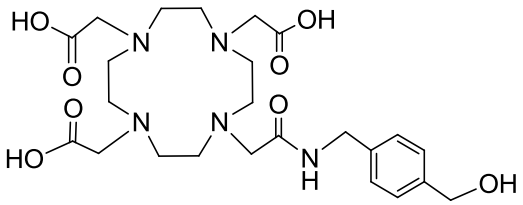

25 (0.30 g, 0.37 mmol) was dissolved in DCM (2 mL) and trifluoroacetic acid added dopwise. The solution was stirred under nitrogen for 24 h. The solvents were removed *in vacuo*. The residue was taken up in DCM and then evaporated. This was repeated with ether, and again with DCM to give **26** as a pale yellow sticky solid (0.18 g, 93 %). ^{1}H NMR (400 MHz, D_2O): δ 7.38 (4H, m, aromatic H), 3.85 – 4.24 (6H, m, C*H*$_2$ on benzyl arm), 2.62 – 3.83 (22H, C*H*$_2$ on backbone and on COOH arms). ^{13}C{^{1}H} NMR (100 MHz, D_2O): 173.7, 163.0, 162.6, 162.3, 139.4, 127.7, 120.4, 117.4, 114.6, 63.5, 52.0, 42.8. ESI-HRMS calc. for $C_{24}H_{38}N_5O_8$ 524.2720 found (m/z): 524.2709 $[M + H]^+$.

g) Synthesis of 1,4-bis(azidomethyl) benzene (28) [114]

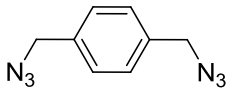

28 was synthesised according to a literature method.[114] 1,4-Bis(bromomethyl)benzene (0.50 g, 1.89 mmol, 1 eq) was dissolved in dry DMF (10 mL) and NaN_3 (0.25 g, 3.79 mmol, 2 eq) added. The mixture was heated at 60 °C overnight. At the end of the reaction, water (20 mL) was added to quench the reaction. The product was extracted with diethyl ether (3 x 15 mL). The combined organic extracts were washed with water (3 x 15 mL), then dried over $MgSO_4$ and evaporated to dryness to give **28** as a pale yellow oil (0.31 g, 1.64 mmol, 86 %). No further purification was necessary. ^{1}H NMR (400 MHz, $CDCl_3$): δ 7.38 (4H, s, aromatic H), 4.39 (4H, s, -C*H*$_2$-N_3). ^{13}C{^{1}H} NMR (100 MHz, $CDCl_3$): 135.5, 128.7, 54.4. IR (v/cm^{-1}): 2086 (N_3). EI-MS (m/z): 188 $[M]^+$. Anal. Calc. for $C_8H_8N_6$: C, 51.06; H, 4.28; N, 44.66. Found: C, 51.15 H, 4.21; N, 44.48.

h) Synthesis of 1-(aminomethyl)-4-(azidomethyl)benzene (29) [113]

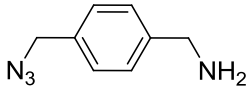

29 was synthesised according to literature method.[113] **20** (0.30 g, 1.59 mmol) was suspended in a mixture of diethyl ether (8 mL) and 1 M HCl (6 mL). PPh_3 (0.54 g, 2.08 mmol) was added and the heterogenous mixture stirred vigorously for 24 h. The layers were then separated and the aqueous layer extracted with ether (3 x 20 mL) to remove PPh_3O and any remaining starting materials. The aqueous layer was basified to pH 10 by adding KOH solution (1 M), then extracted with DCM (4 x 20 mL). The combined DCM extracts were washed with brine, dried over $MgSO_4$, filtered and evaporated *in vacuo* to give the product **21** as a pale yellow oil (0.10 g, 0.62 mmol, 38 %). ^{1}H NMR (400 MHz, $CDCl_3$): δ 7.37 (2H, d, $^3J_{H\text{-}H}$ = 8.14 Hz, aromatic H), 7.32 (2H, d, $^3J_{H\text{-}H}$ = 8.14 Hz, aromatic H), 4.35 (2H, s, -C*H*$_2$-N_3), 3.91 (2H, s, -C*H*$_2$-NH_2), 1.46 (2H, s, N*H*$_2$). ^{13}C{^{1}H} NMR (100 MHz, $CDCl_3$): 143.5 (-*C*-CH_2-NH_2), 133.8 (-*C*-CH_2-N_3), 128.5 (aromatic C), 127.6 (aromatic C), 54.6 (-*C*H_2-N_3), 46.2 (-*C*H_2-NH_2). IR (ν/cm^{-1}): 2095 (N_3), 3341 (NH_2). CI-MS (m/z): 163 $[M + H]^+$, 180 $[M + NH_4]^+$. Anal. Calc. for $C_8H_{10}N_4$: C, 59.24; H, 6.21; N, 34.54. Found: C, 59.35 H, 6.25; N, 34.41.

i) Synthesis of 1-(azidomethyl)-4-(2-chloro-N-methylacetamide)benzene (30)

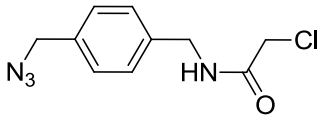

30 is a new compound, and was formed by reacting **29** with the acylating agent chloroacetyl chloride. **29** (0.14 g, 0.86 mmol) and NEt_3 (0.10 g, 0.13 mL, 0.95 mmol) were dissolved in DCM (10 mL) and cooled to 0 °C. This was added dropwise, cold, to chloroacetyl chloride (0.11 g, 76 μL, 0.95 mmol) in DCM (3 mL). The reaction mixture was stirred for 2 hours, after which solvent and volatiles were evaporated *in vacuo*. The residue was dissolved in DCM, washed with H_2O (10 mL), organic layer dried over $MgSO_4$, filtered and solvent evaporated to give **30** as a white solid (0.19 g, 0.83 mmol, 96 %). ^{1}H NMR (400 MHz, $CDCl_3$): δ 7.33 (4H, s, aromatic H), 7.00 (1H, br s, N*H*), 4.52 (2H, d, $^3J_{H\text{-}H}$ = 5.88 Hz, C*H*$_2$-NH_2), 4.35 (2H, s, -C*H*$_2$-N_3), 4.12 (2H, s, -C*H*$_2$-Cl). ^{13}C{^{1}H} NMR (100 MHz, $CDCl_3$): 165.9 (-*C*=O), 137.5 (quaternary C), 135.0 (quaternary C), 128.7 (aromatic C), 128.3 (aromatic C), 54.4 (-*C*H_2-N_3), 43.5 (-*C*H_2-NH-CO), 42.7 (-*C*H_2-Cl). IR (ν/cm^{-1}): 1651 (C=O), 2091 (N_3), 3278 (NH). CI-MS (m/z): 239 $[M + H]^+$, 256 $[M + NH_4]^+$. Anal. Calc. for $C_{10}H_{11}N_4OCl$: C, 50.32; H, 4.65; N, 23.47. Found: C, 50.40 H, 4.79; N, 23.31.

j) Synthesis of 31

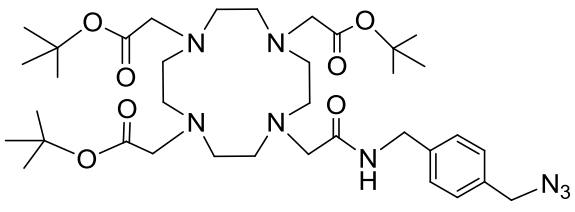

31 is a new compound, and was synthesised following similar protocols from literature.[91] 1,4,7-Tris(*tert*-butoxycarbonylmethyl)-1,4,7,10-tetraazacyclododecane hydrobromide (0.68 g, 1.15 mmol) was dissolved in acetonitrile (20 mL). K_2CO_3 (0.24 g, 1.72 mmol) was added and the suspension stirred for 30 mins before the addition of **30** (0.30 g, 1.26 mmol). The reaction mixture was heated to reflux overnight. When cooled to room temperature, the base and salts were filtered off, and the filtrate evaporated. The residue was dissolved in DCM, washed with water then dried over $MgSO_4$, filtered and solvent evaporated to give **23** as a pale orange oil (0.80 g, 1.12 mmol 89%). ^{1}H NMR (400 MHz, $CDCl_3$): δ 9.12 (1H, t, $^3J_{H-H}$ = 6.00 Hz, N*H*), 7.32 (2H, d, $^3J_{H-H}$ = 7.89 Hz, aromatic H), 7.27 (2H, d, $^3J_{H-H}$ = 7.89 Hz, aromatic H), 4.50 (2H, d, $^3J_{H-H}$ = 6.30 Hz, -C*H*$_2$-NH-CO-CH$_2$-macrocycle), 4.31 (2H, s, -C*H*$_2$-N$_3$), 3.16 (2H, s, macrocycle-C*H*$_2$-CONH-), 3.07 (4H, s, -C*H*$_2$-COO^{t}Bu trans to each other), 3.04 (2H, s, -C*H*$_2$-COO^{t}Bu trans to chromophore arm), 2.67 – 2.79 (12H, m, C*H*$_2$ backbone), 2.48 – 2.56 (4H, m, CH$_2$ backbone), 1.45 (27H, s, ^{t}Bu H). ^{13}C{^{1}H} NMR (100 MHz, $CDCl_3$): 172.2 (-*C*ONH), 170.7 (-*C*OO^{t}Bu), 139.7 (quaternary C), 133.9 (quaternary C), 128.4 (aromatic C), 128.1 (aromatic C), 57.9 (macrocycle-*C*H$_2$-CONH-), 56.5 (-*C*H$_2$-COO^{t}Bu trans to chromophore arm), 56.0 (-*C*H$_2$-COO^{t}Bu trans to each other), 55.1 (*C*H$_2$ backbone), 54.5 (-*C*H$_2$-N$_3$), 53.6 (*C*H$_2$ backbone), 52.5 (*C*H$_2$ backbone), 51.9 (*C*H$_2$ backbone), 42.6 (HN-*C*H$_2$-aromatic), 28.2 (^{t}Bu C). IR (ν/cm^{-1}): 1651 (C=O), 2091 (N$_3$), 3278 (NH). ESI-HRMS calcd. for $C_{36}H_{61}N_8O_7$ 717.4663 found m/z 717.4674 $[M + H]^+$. Anal. Calc. for $C_{36}H_{60}N_8O_7$: C, 60.31; H, 8.44; N, 15.63. Found: C, 60.11; H, 8.32; N, 15.58.

k) Synthesis of modified azide-DOTA [L2 (32)]

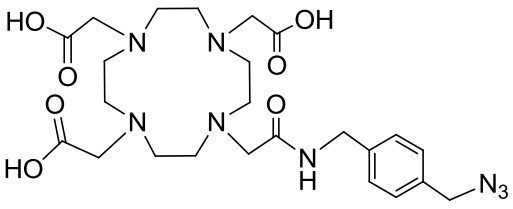

31 (0.50 g, 0.697 mmol) was dissolved in DCM (2 mL) and trifluoroacetic acid added dopwise. The solution was stirred under nitrogen for 24 h. The solvents were removed *in vacuo*. The residue was taken up in DCM and then evaporated. This was repeated with ether, and again with DCM to give **L2**

(**32**) as a pale yellow sticky solid (0.35 g, 0.638 mmol, 92 %). ^{1}H NMR (400 MHz, D_2O): δ 7.32 (4H, m), 2.81 – 3.97 (24H, m), 4.00 – 4.13 (2H, m), 4.22 – 4.39 (2H, m). $^{13}C\{^{1}H\}$ NMR (100 MHz, D_2O): 173.4, 168.8, 163.0, 162.6, 162.3, 130.1, 129.0, 128.1, 54.8, 53.9, 53.0, 51.9, 51.1, 49.1, 47.6, 42.7, 42.2. ESI-HRMS calcd. for $C_{24}H_{36}N_8O_7$ 549.2785 found m/z 549.2788 $[M + H]^+$.

3.6.6 Complexation of L2 to M (M = Eu, Tb, Gd)

a) Synthesis of Eu.L2(33)

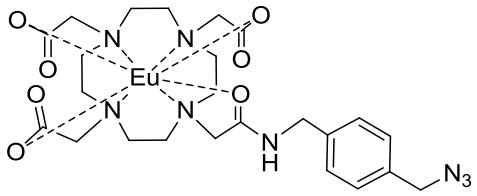

Eu.L2 (33)

Ligand **L2** (57.00 mg, 0.104 mmol) was dissolved in MilliQ water (1 mL) and the pH adjusted to 5.5 with 0.5 M KOH. $EuCl_3.6H_2O$ (41.80 mg, 0.114 mmol) was added slowly, while maintaining the pH at 5.5. The mixture was stirred overnight. Unreacted Eu^{3+} was precipitated out as $Eu(OH)_3$ by the addition of 0.5 M KOH (pH of mixture at 10). The precipitate was separated from the supernatant by centrifugation. The supernatant was concentrated *in vacuo*, and the residue passed down a Sephadex G-10 column. Fractions containing the compound were tested for free metal by the xylenol orange test. Metal-free fractions were combined and the solvent removed by lyophilisation. **Eu.L2** (**33**) was obtained as a pale yellow solid (19.90 mg, 0.028 mmol, 30 %). ESI-HRMS calc. for $C_{24}H_{33}EuN_8O_7$ 697.1749 found (m/z): 697.1766 $[M + H]^+$.

b) Synthesis of Tb.L2(34)

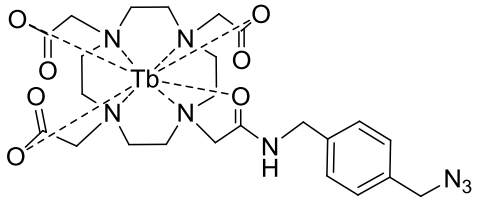

Tb.L2 (34)

Tb.L2 (**34**) was synthesised according to the same method as the Eu analogue. **L2** (56.50 mg, 0.104 mmol) and $TbCl_3.6H_2O$ (42.70 mg, 0.114 mmol) were used. The complex was obtained as a pale yellow solid (23.30 mg, 0.033 mmol, 32 %). ESI-HRMS calc. for $C_{24}H_{33}N_8O_7Tb$ 705.1848 found (m/z): 705.1802 $[M + H]^+$.

c) Synthesis of Gd.L2(35)

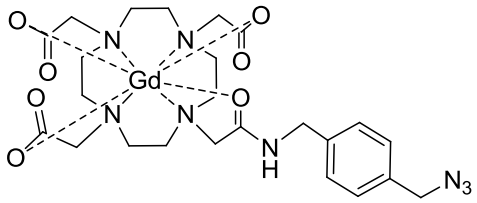

Gd.L2 (35)

Gd.L2 (**35**) was synthesised according to the same method as the Eu analogue. **L2** (57.50 mg, 0.104 mmol) and $GdCl_3$ (42.50 mg, 0.114 mmol) were used. The complex was obtained as a pale yellow solid (30.10 mg, 0.043 mmol, 41 %). ESI-HRMS calc. for $C_{24}H_{33}GdN_8O_7$ 704.1792 found (m/z): 704.1802 $[M + H]^+$.

3.6.7 Click procedures

a) Cyclooctyne to Ln.L1/Ln.L2

To **Ln.L1** or **Ln.L2** (1 mg) in water (1 mL), was added cyclooctyne **13** (1 eq, usually approximately 0.25 mg dissolved in 50 µL methanol). The mixture was left to react for 6 hours. Without further purification, the reaction mixture was submitted for mass spectrometry.

b) NP2-alkyne to Ln.L1/Ln.L2

To **NP2-alkyne** (0.5 mg NP) in water (250 µL), was added **Ln.L1** or **Ln.L2** (200 eq with respect to **NP-alkyne**). The mixture was left to shake for 6 hours, then centrifuged and the supernatant decanted. The pellet was resuspended in water, and washed by precipitating with acetone, and again centrifuged to isolate the nanoparticles. The nanoparticles were finally resuspended in water.

The nanoparticle samples for fluorescence spectroscopy were made up to 1 mg/mL Fe concentration (1.67 mg/mL NP concentration).

3.7 References

1. P. K. Jain, X. Huang, I. H. El-Sayed, and M. A. El-Sayed, *Acc. Chem. Res.*, 2008, **41**, 1578–86.
2. R. Gref, Y. Minamitake, M. Peracchia, V. Trubetskoy, V. Torchilin, and R. Langer, *Science*, 1994, **263**, 1600–1603.
3. K. Knop, R. Hoogenboom, D. Fischer, and U. S. Schubert, *Angew. Chem. Int. Ed.*, 2010, **49**, 6288–308.
4. R. Gref, M. Lück, P. Quellec, M. Marchand, E. Dellacherie, S. Harnisch, T. Blunk, and R. . Müller, *Colloid Surf. B*, 2000, **18**, 301–313.
5. V. C. F. Mosqueira, P. Legrand, J.-L. Morgat, M. Vert, E. Mysiakine, R. Gref, J.-P. Devissaguet, and G. Barratt, *Pharm. Res.*, 2001, **18**, 1411–1419.
6. S. M. Moghimi and J. Szebeni, *Prog. Lipid Res.*, 2003, **42**, 463–478.
7. L. E. van Vlerken, T. K. Vyas, and M. M. Amiji, *Pharm. Res.*, 2007, **24**, 1405–14.
8. G. Prencipe, S. M. Tabakman, K. Welsher, Z. Liu, A. P. Goodwin, L. Zhang, J. Henry, and H. Dai, *J. Am. Chem. Soc.*, 2009, **131**, 4783–7.
9. J. V Jokerst, T. Lobovkina, R. N. Zare, and S. S. Gambhir, *Nanomed.*, 2011, **6**, 715–28.
10. T. M. Saba, *Arch. Int. Med.*, 1970, **126**, 1031.
11. D. E. Owens and N. A. Peppas, *Int. J. Pharm.*, 2006, **307**, 93–102.
12. S. M. Ryan, G. Mantovani, X. Wang, D. M. Haddleton, and D. J. Brayden, *Expert Opin. Drug Deliv.*, 2008, **5**, 371–83.
13. F. Alexis, E. Pridgen, L. K. Molnar, and O. C. Farokhzad, *Mol. Pharm.*, 2008, **5**, 505–15.
14. S.-D. Li and L. Huang, *Biochim. Biophys. Acta*, 2009, **1788**, 2259–66.
15. B. S. Zolnik and N. Sadrieh, *Adv. Drug Deliv. Rev.*, 2009, **61**, 422–7.
16. K. A. D. Guzman, M. P. Finnegan, and J. F. Banfield, *Environ. Sci. Technol.*, 2006, **40**, 7688–93.
17. P. Yang, M. Ando, and N. Murase, *Langmuir*, 2011, **27**, 895–901.
18. Y.-W. Jun, M. F. Casula, J.-H. Sim, S. Y. Kim, J. Cheon, and A. P. Alivisatos, *J. Am. Chem. Soc.*, 2003, **125**, 15981–5.
19. S. Förster and M. Antonietti, *Adv. Mater.*, 1998, **10**, 195–217.
20. W. Zhao, M. A. Brook, and Y. Li, *Chembiochem*, 2008, **9**, 2363–71.
21. D. Artemov, N. Mori, B. Okollie, and Z. M. Bhujwalla, *Magn. Reson. Med.*, 2003, **49**, 403–8.
22. M. Geso, *Brit. J. Radiol.*, 2007, **80**, 64–5; author reply 65.
23. L. A. Bentolila, Y. Ebenstein, and S. Weiss, *J. Nucl. Med.*, 2009, **50**, 493–6.
24. X. Michalet, F. F. Pinaud, L. A. Bentolila, J. M. Tsay, S. Doose, J. J. Li, G. Sundaresan, A. M. Wu, S. S. Gambhir, and S. Weiss, *Science*, 2005, **307**, 538–44.
25. M. M. van Schooneveld, E. Vucic, R. Koole, Y. Zhou, J. Stocks, D. P. Cormode, C. Y. Tang, R. E. Gordon, K. Nicolay, A. Meijerink, Z. A. Fayad, and W. J. M. Mulder, *Nano Lett.*, 2008, **8**, 2517–25.
26. W. P. Wuelfing, S. M. Gross, D. T. Miles, and R. W. Murray, *J. Am. Chem. Soc.*, 1998, **120**, 12696–12697.
27. M. Möller, J. P. Spatz, and A. Roescher, *Adv. Mater.*, 1996, **8**, 337–340.
28. M. Fathalla, S.-C. Li, U. Diebold, A. Alb, and J. Jayawickramarajah, *Chem. Commun.*, 2009, 4209–11.
29. A. B. R. Mayer and J. E. Mark, *Eur. Polym. J.*, 1998, **34**, 103–108.
30. J. C. A. and B. Donovan, *Proc. Phys. Soc. Lond.*, 1960, **75**, 149.

31. R. Weissleder, G. Elizondo, J. Wittenberg, C. A. Rabito, H. H. Bengele, and L. Josephson, *Radiology*, 1990, **175**, 489–493.
32. S. A. Schmitz, M. Taupitz, S. Wagner, K. J. Wolf, D. Beyersdorff, and B. Hamm, *J. Magn. Reson. Imaging*, 2001, **14**, 355–61.
33. A. K. Gupta and M. Gupta, *Biomaterials*, 2005, **26**, 3995–4021.
34. J. Xie, C. Xu, N. Kohler, Y. Hou, and S. Sun, *Adv. Mater.*, 2007, **19**, 3163–3166.
35. P. G. de Gennes, *Adv. Colloid Interface Sci.*, 1987, **27**, 189–209.
36. P. G. de Gennes, *Macromolecules*, 1980, **13**, 1069–1075.
37. A. K. Kenworthy, K. Hristova, D. Needham, and T. J. McIntosh, *Biophys. J.*, 1995, **68**, 1921–36.
38. P. L. Hansen, J. A. Cohen, R. Podgornik, and V. A. Parsegian, *Biophys. J.*, 2003, **84**, 350–5.
39. H. C. Kolb, M. G. Finn, and K. B. Sharpless, *Angew. Chem. Int. Ed.*, 2001, **40**, 2004–2021.
40. C. W. Tornøe, C. Christensen, and M. Meldal, *J. Org. Chem.*, 2002, **67**, 3057–3064.
41. I. Pastor and M. Yus, *Curr. Org. Chem.*, 2005, **9**, 1–29.
42. T. Siu and A. K. Yudin, *J. Am. Chem. Soc.*, 2002, **124**, 530–531.
43. B. Gacal, H. Durmaz, M. A. Tasdelen, G. Hizal, U. Tunca, Y. Yagci, and A. L. Demirel, *Macromolecules*, 2006, **39**, 5330–5336.
44. Q. Wang, S. Chittaboina, and H. Barnhill, *Lett. Org. Chem.*, 2005, **2**, 293–301.
45. V. V Rostovtsev, L. G. Green, V. V Fokin, and K. B. Sharpless, *Angew. Chem. Int. Ed.*, 2002, **41**, 2596–9.
46. F. Pérez-Balderas, M. Ortega-Muñoz, J. Morales-Sanfrutos, F. Hernández-Mateo, F. G. Calvo-Flores, J. A. Calvo-Asín, J. Isac-García, and F. Santoyo-González, *Org. Lett.*, 2003, **5**, 1951–4.
47. T. R. Chan, R. Hilgraf, K. B. Sharpless, and V. V Fokin, *Org. Lett.*, 2004, **6**, 2853–5.
48. Q. Wang, T. R. Chan, R. Hilgraf, V. V Fokin, K. B. Sharpless, and M. G. Finn, *J. Am. Chem. Soc.*, 2003, **125**, 3192–3.
49. A. E. Speers, G. C. Adam, and B. F. Cravatt, *J. Am. Chem. Soc.*, 2003, **125**, 4686–7.
50. F. Fazio, M. C. Bryan, O. Blixt, J. C. Paulson, and C.-H. Wong, *J. Am. Chem. Soc.*, 2002, **124**, 14397–14402.
51. A. J. Link and D. A. Tirrell, *J. Am. Chem. Soc.*, 2003, **125**, 11164–5.
52. L. Marmuse, S. A. Nepogodiev, and R. A. Field, *Org. Biomol. Chem.*, 2005, **3**, 2225–7.
53. D. P. Temelkoff, M. Zeller, and P. Norris, *Carbohyd. Res.*, 2006, **341**, 1081–90.
54. H. Lin and C. T. Walsh, *J. Am. Chem. Soc.*, 2004, **126**, 13998–4003.
55. J. Yang, D. Hoffmeister, L. Liu, X. Fu, and J. S. Thorson, *Bioorgan. Med. Chem.*, 2004, **12**, 1577–1584.
56. D. T. S. Rijkers, G. W. van Esse, R. Merkx, A. J. Brouwer, H. J. F. Jacobs, R. J. Pieters, and R. M. J. Liskamp, *Chem. Commun.*, 2005, 4581–3.
57. G. Conte, F. Ely, and H. Gallardo, *Liq. Cryst.*, 2005, **32**, 1213–1222.
58. H. Gallardo, F. Ely, A. J. Bortoluzzi, and G. Conte, *Liq. Cryst.*, 2005, **32**, 667–671.
59. H. C. Kolb and K. B. Sharpless, *Drug Discov. Today*, 2003, **8**, 1128–1137.
60. F. Himo, T. Lovell, R. Hilgraf, V. V Rostovtsev, L. Noodleman, K. B. Sharpless, and V. V Fokin, *J. Am. Chem. Soc.*, 2005, **127**, 210–6.
61. J.-F. Lutz, *Angew. Chem. Int. Ed.*, 2008, **47**, 2182–4.
62. D. C. Kennedy, C. S. McKay, M. C. B. Legault, D. C. Danielson, J. A. Blake, A. F. Pegoraro, A. Stolow, Z. Mester, and J. P. Pezacki, *J. Am. Chem. Soc.*, 2011, **133**, 17993–8001.
63. N. J. Agard, J. A. Prescher, and C. R. Bertozzi, *J. Am. Chem. Soc.*, 2005, **127**, 11196–11196.
64. E. M. Sletten and C. R. Bertozzi, *Org. Lett.*, 2008, **10**, 3097–9.

65. J. A. Codelli, J. M. Baskin, N. J. Agard, and C. R. Bertozzi, *J. Am. Chem. Soc.*, 2008, **130**, 11486–93.
66. J. M. Baskin, J. A. Prescher, S. T. Laughlin, N. J. Agard, P. V Chang, I. A. Miller, A. Lo, J. A. Codelli, and C. R. Bertozzi, *P. Natl. Acad. Sci. USA*, 2007, **104**, 16793–7.
67. N. J. Agard, J. A. Prescher, and C. R. Bertozzi, *J. Am. Chem. Soc.*, 2004, **126**, 15046–7.
68. N. J. Agard, J. M. Baskin, J. A. Prescher, A. Lo, and C. R. Bertozzi, *ACS Chem. Biol.*, 2006, **1**, 644–648.
69. G. Wittig and A. Krebs, *Chem. Ber.*, 1961, **94**, 3260–3275.
70. H. Meier, H. Petersen, and H. Kolshorn, *Chem. Ber.*, 1980, **113**, 2398–2409.
71. K. J. Shea and J. S. Kim, *J. Am. Chem. Soc.*, 1992, **114**, 4846–4855.
72. C. B. Reese and A. Shaw, *J. Chem. Soc. D, Chem. Comm.*, 1970, 1172.
73. Z. Li, T. S. Seo, and J. Ju, *Tetrahedron Lett.*, 2004, **45**, 3143–3146.
74. N. Agard, J. Baskin, J. Prescher, A. Lo, and C. Bertozzi, *ACS Chem. Biol.*, 2006, **1**, 644–648.
75. P. V Chang, J. A. Prescher, E. M. Sletten, J. M. Baskin, I. A. Miller, N. J. Agard, A. Lo, and C. R. Bertozzi, *P. Natl. Acad. Sci. USA*, 2010, **107**, 1821–6.
76. X. Ning, R. P. Temming, J. Dommerholt, J. Guo, D. B. Ania, M. F. Debets, M. A. Wolfert, G.-J. Boons, and F. L. van Delft, *Angew. Chem. Int. Ed.*, 2010, **49**, 3065–8.
77. M. Shelbourne, X. Chen, T. Brown, and A. H. El-Sagheer, *Chem. Commun.*, 2011, **47**, 6257–9.
78. E. M. Sletten, H. Nakamura, J. C. Jewett, and C. R. Bertozzi, *J. Am. Chem. Soc.*, 2010, **132**, 11799–805.
79. G. de Almeida, E. M. Sletten, H. Nakamura, K. K. Palaniappan, and C. R. Bertozzi, *Angew. Chem. Int. Ed.*, 2012, **51**, 2443–7.
80. A. Kuzmin, A. Poloukhtine, M. A. Wolfert, and V. V Popik, *Bioconjugate Chem.*, 2010, **21**, 2076–85.
81. A. Bernardin, A. Cazet, L. Guyon, P. Delannoy, F. Vinet, D. Bonnaffé, and I. Texier, *Bioconjugate Chem.*, 2010, **21**, 583–588.
82. L. S. Campbell-Verduyn, L. Mirfeizi, A. K. Schoonen, R. A. Dierckx, P. H. Elsinga, and B. L. Feringa, *Angew. Chem. Int. Ed.*, 2011, **50**, 11117–20.
83. S. Cotton, *Lanthanides and Actinides*, Wiley, 1991.
84. J.-C. G. Bünzli and C. Piguet, *Chem. Soc. Rev.*, 2005, **34**, 1048–77.
85. J.-C. G. Bünzli, *Acc. Chem. Res.*, 2006, **39**, 53–61.
86. J. I. Bruce, M. P. Lowe, and D. Parker, in *The Chemistry of Contrast Agents in Medical Magnetic Resonance Imaging*, eds. A. E. Merbach and E. Toth, Wiley, 2000, pp. 438–458.
87. J. Vuojola and T. Soukka, *Methods Appl. Fluoresc.*, 2014, **2**, 012001.
88. D. Parker, R. S. Dickins, H. Puschmann, C. Crossland, and J. A. K. Howard, *Chem. Rev.*, 2002, **102**, 1977–2010.
89. A. Dossing, *Eur. J. Inorg. Chem.*, 2005, **2005**, 1425–1434.
90. P. Caravan, J. J. Ellison, T. J. McMurry, and R. B. Lauffer, *Chem. Rev.*, 1999, **99**, 2293–2352.
91. D. J. Mastarone, V. S. R. Harrison, A. L. Eckermann, G. Parigi, C. Luchinat, and T. J. Meade, *J. Am. Chem. Soc.*, 2011, **133**, 5329–37.
92. P. Lebdusková, P. Hermann, L. Helm, E. Tóth, J. Kotek, K. Binnemans, J. Rudovský, I. Lukes, and A. E. Merbach, *Dalton Trans.*, 2007, 493–501.
93. S. Aime, M. Botta, and G. Ermondi, *Inorg. Chem.*, 1992, **31**, 4291–4299.
94. S. Hoeft and K. Roth, *Chem. Ber.*, 1993, **126**, 869–873.

95. S. Aime, M. Botta, M. Fasano, M. P. M. Marques, C. F. G. C. Geraldes, D. Pubanz, and A. E. Merbach, *Inorg. Chem.*, 1997, **36**, 2059–2068.
96. M. Woods, M. Botta, S. Avedano, J. Wang, and A. D. Sherry, *Dalton Trans.*, 2005, 3829–37.
97. M. Woods, S. Aime, M. Botta, J. A. K. Howard, J. M. Moloney, M. Navet, D. Parker, M. Port, and O. Rousseaux, *J. Am. Chem. Soc.*, 2000, **122**, 9781–9792.
98. L. N. Goswami, L. Ma, P. J. Kueffer, S. S. Jalisatgi, and M. F. Hawthorne, *Molecules*, 2013, **18**, 9034–48.
99. M. Woods, Z. Kovacs, S. Zhang, and A. D. Sherry, *Angew. Chem. Int. Ed.*, 2003, **42**, 5889–92.
100. H. Fei, X. Ai, M. Gao, Y. Yang, T. Zhang, and J. Shen, *J. Lumin.*, 1995, **66-67**, 345–348.
101. W. Xu, B. A. Bony, C. R. Kim, J. S. Baeck, Y. Chang, J. E. Bae, K. S. Chae, T. J. Kim, and G. H. Lee, *Sci. Rep.*, 2013, **3**, 3210.
102. G. J. Stasiuk, S. Tamang, D. Imbert, C. Poillot, M. Giardiello, C. Tisseyre, E. L. Barbier, P. H. Fries, M. de Waard, P. Reiss, and M. Mazzanti, *ACS Nano*, 2011, **5**, 8193–201.
103. D. K. Yi, S. T. Selvan, S. S. Lee, G. C. Papaefthymiou, D. Kundaliya, and J. Y. Ying, *J. Am. Chem. Soc.*, 2005, **127**, 4990–1.
104. F. Erogbogbo, K.-T. Yong, R. Hu, W.-C. Law, H. Ding, C.-W. Chang, P. N. Prasad, and M. T. Swihart, *ACS Nano*, 2010, **4**, 5131–8.
105. F. Zhan and C. Zhang, *J. Mater. Chem.*, 2011, **21**, 4765.
106. C.-W. Lai, Y.-H. Wang, C.-H. Lai, M.-J. Yang, C.-Y. Chen, P.-T. Chou, C.-S. Chan, Y. Chi, Y.-C. Chen, and J.-K. Hsiao, *Small*, 2008, **4**, 218–24.
107. B. Wang, J. Hai, Q. Wang, T. Li, and Z. Yang, *Angew. Chem. Int. Ed.*, 2011, **50**, 3063–6.
108. Z. Liu, B. Li, B. Wang, Z. Yang, Q. Wang, T. Li, D. Qin, Y. Li, M. Wang, and M. Yan, *Dalton Trans.*, 2012, **41**, 8723–8.
109. J. Choi, J. C. Kim, Y. B. Lee, I. S. Kim, Y. K. Park, and N. H. Hur, *Chem. Commun.*, 2007, 1644–6.
110. G. J. L. Bernardes, G. Casi, S. Trüssel, I. Hartmann, K. Schwager, J. Scheuermann, and D. Neri, *Angew. Chem. Int. Ed.*, 2012, **51**, 941–4.
111. J. Lee, J. Lee, M. Kang, M. Shin, J.-M. Kim, S.-U. Kang, J.-O. Lim, H.-K. Choi, Y.-G. Suh, H.-G. Park, U. Oh, H.-D. Kim, Y.-H. Park, H.-J. Ha, Y.-H. Kim, A. Toth, Y. Wang, R. Tran, L. V Pearce, D. J. Lundberg, and P. M. Blumberg, *J. Med. Chem.*, 2003, **46**, 3116–26.
112. R. S. Portoa, M. L. A. A. Vasconcellosb, E. Venturab, and F. Coelho, *Synthesis*, 2005, **14**, 2297–2306.
113. K.-N. Lau, H.-F. Chow, M.-C. Chan, and K.-W. Wong, *Angew. Chem. Int. Ed.*, 2008, **47**, 6912–6.
114. J. R. Thomas, X. Liu, and P. J. Hergenrother, *J. Am. Chem. Soc.*, 2005, **127**, 12434–5.
115. A. Barge, G. Cravotto, E. Gianolio, and F. Fedeli, *Contrast Media Mol. I.*, 2006, **1**, 184–8.
116. B. Jagadish, G. L. Brickert-Albrecht, G. S. Nichol, E. A. Mash, and N. Raghunand, *Tetrahedron Lett.*, 2011, **52**, 2058–2061.
117. N. Naganna and N. Madhavan, *Org. Lett.*, 2013, **15**, 5870–3.

CHAPTER 4

Dual-weighted T_1/T_2 MR agents

4 Dual-weighted T_1/T_2 MR agents

4.1 Introduction

In the previous chapter, **Gd.L1** and **Gd.L2** conjugated to the nanoparticle surface were not possible to be characterised by fluorescence as Gd(III) does not have an emission in the visible range unlike the Eu(III) and Tb(III) analogues. However, an interesting consequence of having a T_1 agent (the Gd chelate) conjugated to the iron oxide nanoparticle surface (T_2 agent) is that the relaxivities of both moieties can be affected, as discussed below. To investigate this, a range of Gd-chelate conjugated nanoparticles with various modifications were synthesised, and their relaxivities measured. Instead of utilising a copper-free alkyne-azide cycloaddition reactions to form the Gd-NP conjugates, as was previously carried out with the Eu/Tb chelates, the Gd-NP conjugates here were synthesised by direct conjugation of DOTA to **NP2** by stoichiometric activation of one carboxylic acid on the DOTA, followed by the Gd complexation (**Scheme 4.1**). The reason for this was two-fold, i) unsubstituted DOTA is considerably cheaper than **L1** (azido-mono-amide-DOTA) for the large number of nanoparticle species to be synthesised here; and ii) the cyclooctyne is synthetically demanding and it was difficult to produce a substantial quantity for the whole series.

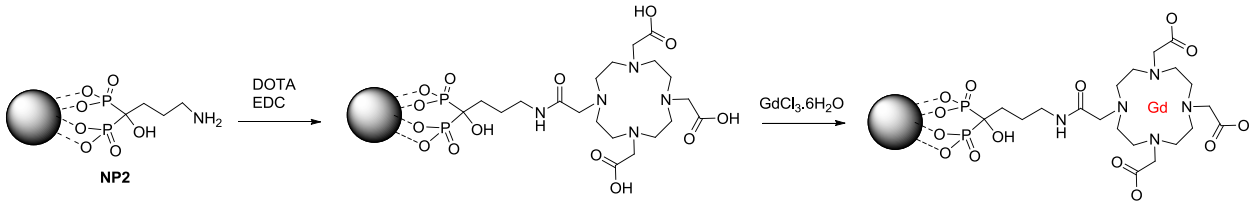

Scheme 4.1 General scheme to conjugate mono-activated DOTA to **NP2**, followed by Gd complexation.

As discussed in Chapter 1, T_1 is the time constant for longitudinal or spin-lattice relaxation, and T_2 is the time constant for transverse or spin-spin relaxation. Contrast agents (CA) work by reducing both T_1 and T_2 relaxation times of protons via the interaction between the electron spins of the contrast agent and the spins of the water protons in its surroundings. The inverse of the relaxation time constants ($1/T_1$ and $1/T_2$) gives the relaxation rates (R_1 and R_2) respectively. Both T_1/T_2 and R_1/R_2 are concentration dependent, so another term known as the relaxivity constant (r_1 and r_2) that is independent of concentration can be derived from the linear relationship between R and the concentration of CA. The r_1/r_2 value therefore allows different species to be compared directly.

Gadolinium-containing T_1 contrast agents are the preferred CA for MR imaging as the enhanced signal produced is more favourable. T_2 agents on the other hand give a darkened signal which can be misinterpreted as bleeding, calcification or other anomalies. Nevertheless, iron oxide nanoparticles

as T_2 agents are more biocompatible compared to Gd due to its lower toxicity. Thus, having a dual contrast T_1/T_2 MRI probe can overcome the drawbacks of both MRI techniques, with compatible T_1 and T_2 acquisitions allowing for artefacts to be reduced and diagnostics to be doubly verified.

The earliest example of dual contrast T_1/T_2 MR imaging was carried out by Weissleder *et al* to image liver tumours in rats, whereby administration of both Gd-DTPA and ferrite together showed enhanced tumour signal from the Gd-DTPA while the liver showed a negative signal intensity from the accumulation of ferrite, compared to when they were administered separately.[1] Their results show an increase in r_1 but no effect on r_2 when both agents are present at the same time. The same effect was observed when the contrast agents were administered sequentially in humans, in studies carried out by Semelka *et al* and Kubaska *et al*.[2,3] More recently, there have been studies to integrate both T_1 and T_2 moieties into a single contrast agent, typically conjugating Gd chelates onto iron oxide nanoparticles.

Besides iron oxide nanoparticles, Gd- and Mn-based nanoparticles have also been utilised to form dual T_1/T_2 contrast agents even though Gd and Mn nanoparticles (and their small molecule counterparts) have primarily been used as T_1 contrast agents. Hybrid nanoparticle systems combining either Gd or Mn nanoparticles with iron oxide nanoparticles have recently been shown to exhibit both T_1 and T_2 relaxivity. Theoretically, integration of the T_1 and T_2 contrast as a single entity as opposed to having the T_1 on the external part of the T_2 moiety would result in the T_1 spins aligning in the same direction as the magnetic field induced by the T_2 material, enhancing the T_1 effect while maintaining the T_2 signal.[4,5] This is illustrated in **Figure 4.1**.[5]

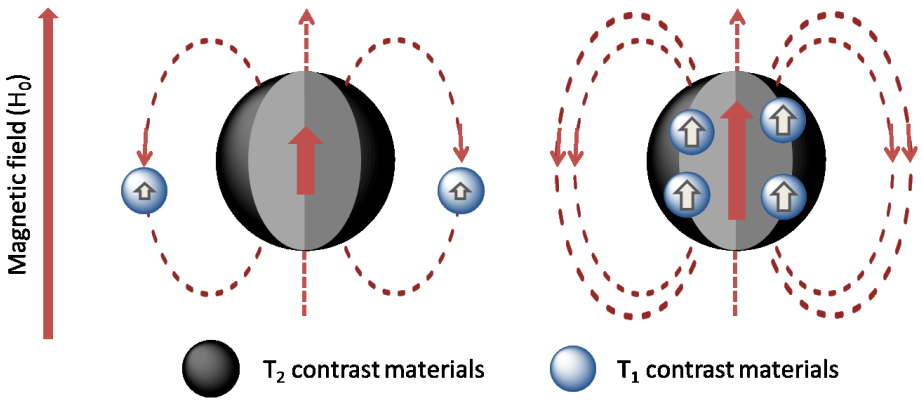

Figure 4.1 Spin interaction difference between T_1 and T_2 contrast agents in different locations. Left: When T_1 is on the outside of T_2, the magnetic field from T_2 opposed the T_1 field, reducing the T_1 relaxivity. Right: The magnetic field of both contrast agents are simultaneously enhanced when both T_1 and T_2 are a single entity.

This was confirmed by experimental evidence from Gao *et al*.[5] They synthesised Gd_2O_3-embedded Fe_3O_4 nanoparticles (GdIO) which had enhanced T_1 and T_2 relaxivities. The GdIO had a higher r_2 than

Fe_3O_4 as well as higher r_1 than Gd_2O_3 and in addition, the Gd_2O_3 nanoparticles on their own showed no enhanced T_2 contrast, while Fe_3O_4 nanoparticles on their own showed no enhanced T_1 contrast. Gao's results demonstrate a synergistic enhancement of r_1 and r_2 in GdIO.

Kim *et al* [6] synthesised Gd-doped iron oxide nanoparticles (**Figure 4.2**) and showed that the Gd-substituted nanoparticles produced both a T_1 and T_2 contrast, from images of a rat's liver. However, they only compared their results to Fe_3O_4 nanoparticles as a control, and there was no comparison to a standard T_1 agent. Im *et al* [7] have also produced a hybrid nanoparticle system of iron oxide and manganese oxide (Fe_3O_4/MnO) with varying Fe_3O_4 sizes, the simplified structures are illustrated in **Figure 4.2**. MR imaging of the liver showed both T_1 and T_2 contrast effects, rationalised by the internalisation of the NP by Kupffer cells in the liver which releases Mn^{2+} ions. The released Mn^{2+} activates the T_1 effect while the Fe_3O_4 retains its negative contrast. The T_2 relaxivity was also shown to increase with Fe_3O_4 size, with no effect on the r_1, although the r_2 values were lower for the hybrids than for unmodified Fe_3O_4.

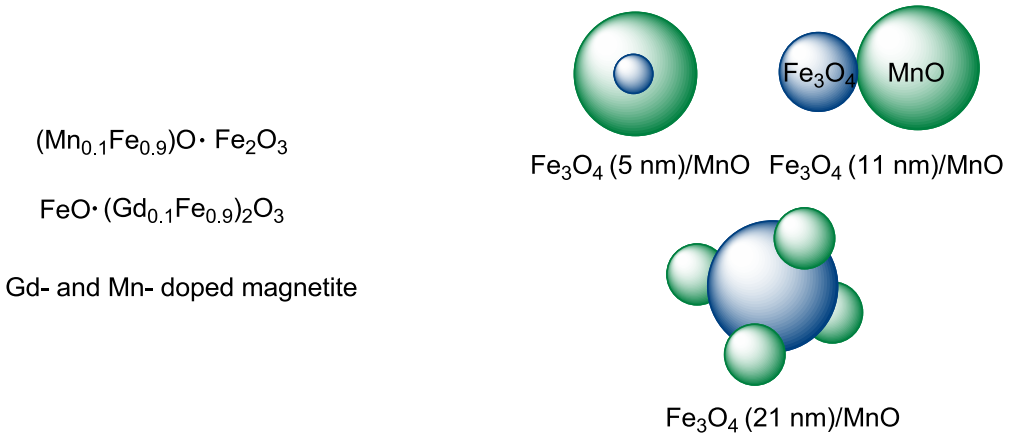

Figure 4.2 Gd- and Mn-doped magnetite structure synthesised by Kim *et al* (left),[6] and the Fe_3O_4/MnO hybrid systems of varying Fe_3O_4 sizes synthesised by Im *et al* (right).[7]

Other systems such as the Mn-loaded silica spheres by Niu *et al* illustrated that the Mn can act as both T_1 and T_2 agents with r_1 and r_2 values of 10.1 and 169.7 $mM^{-1}s^{-1}$ respectively, higher than other reported dual-mode contrast agents, and also higher than conventional T_1 and T_2 agents such as Gd-DTPA (r_1 = 9.6 $mM^{-1}s^{-1}$) and Feridex (r_2 = 108 $mM^{-1}s^{-1}$).[8] They attributed the high r_1 value to the mesoporous silica structure, allowing faster water diffusion into the mesopores, increasing the r_1 relaxivity. The enhanced r_2 relaxivity was postulated to arise from the ultrasmall MnO nanocluster formed during synthesis. Being antiferromagnetic, these ultrasmall nanoclusters with high surface-

to-volume ratio exhibit a larger proportion of uncompensated surface spins and therefore higher magnetisation values, leading to higher r_2.

Although hybrid nanoparticle systems have shown some promising results, simple conjugation of a paramagnetic chelate to the surface of the iron oxide nanoparticle is still an attractive method to produce dual-mode contrast agents. The theoretical assumption is that these simpler combined agents will have an increase in the r_1 without the r_2 being affected greatly. The actual results however are much more complex and four publications were chosen for comparison. Yang *et al* [9] and Bae *et al* [10] showed independently with different T_1/T_2 systems, that r_2 strongly decreases when iron oxide nanoparticles are conjugated to Gd chelates, with an enhancement in the r_1. Choi *et al* [11] also observed the same trend with a possible dependence on distance between the Gd to the magnetic core. Finally, Huang *et al* [12] showed the opposite trend where both r_1 and r_2 increased with Gd concentration when the T_1 and T_2 moieties are coupled. In all these cases, r_1 increases when Gd is incorporated. However, the r_2 trends are not the same for all four publications. These contradicting results (summarised in **Table 4.1**) demonstrate that further studies are required to understand the relationship between the final relaxivities and the design and structure of the T_1/T_2 probes. Thus, in this research, a series of iron oxide nanoparticles functionalised with Gd chelates were prepared, with modifications as follows (overview in **Figure 4.3**):

1) replacing the paramagnetic component for a different metal ion (**Set 1**, **Table 4.2**);
2) changing the chelator for the paramagnetic component (**Set 2**, **Table 4.3**);
3) modifying the distance between the magnetic core and the paramagnetic chelate (**Set 3**, **Table 4.4**);
4) altering the organic coating/anchoring ligand on the nanoparticle cores, while keeping the Gd chelate and at the same time comparing the effect on distance, (**Set 4**, **Table 4.5**); nanoparticles for this set were provided by Dr. Gallo.

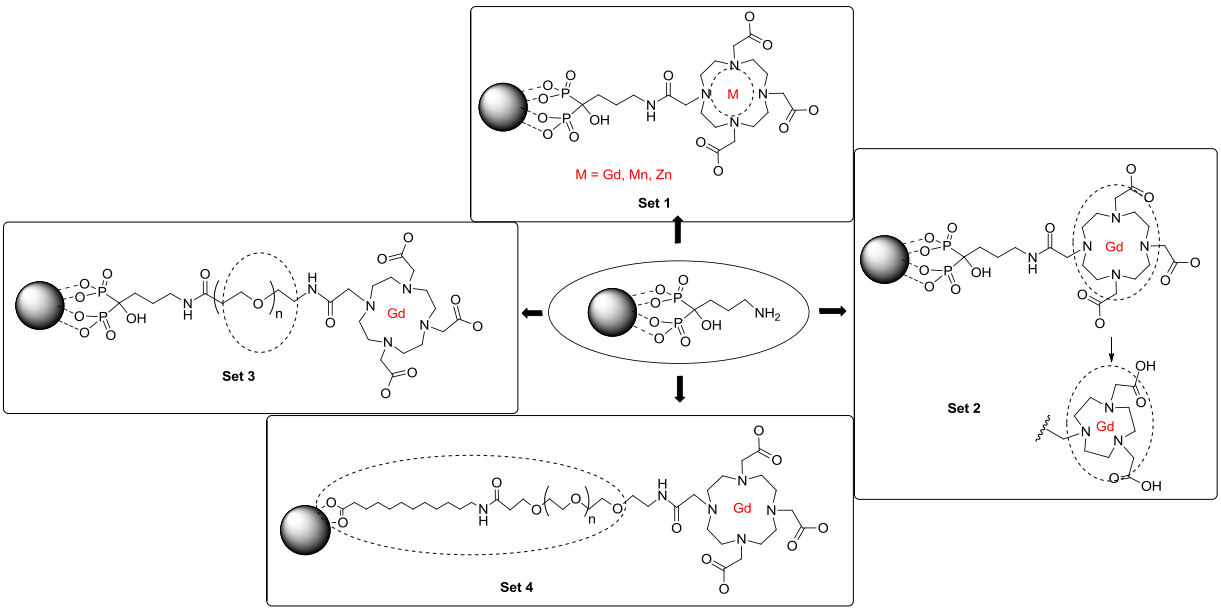

Figure 4.3 Overview of the different modifications to the T_1/T_2 systems, with the particular modification of each set highlighted by the dashed lines.

NP	Core size (nm)	Final size (nm)	Z potential (mV)	r_2 (Fe)	r_1 (Fe)	Ref
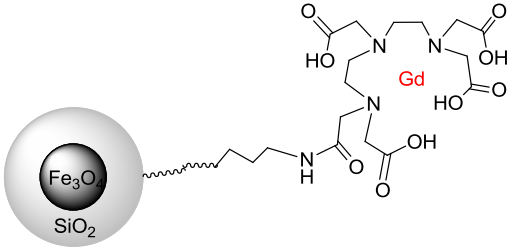	6	27	+16	↓with inc Gd	↑ with inc Gd	9
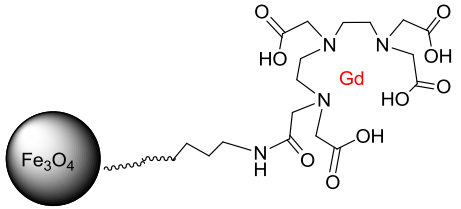	17	73.8*	-5	↓ with inc Gd	↑ with inc Gd	10
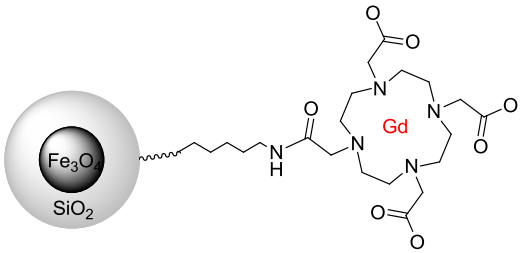	22	40	+17	↑ with inc Gd	↑ with inc Gd	12
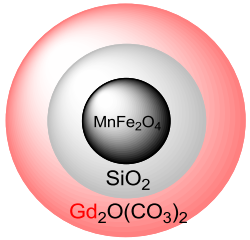	15	20 – 37.5	n/a	↓with inc Si thickness	↑ with inc Si thickness	11

Table 4.1 Literature T_1/T_2 probes with their respective data for comparison.

*hydrodynamic diameter. All other sizes in the table were obtained via TEM measurements in the relevant publications.

NP	Core size/nm	Theoretical size/nm	Z size/nm	Z potential mV	r_2 (Fe)	r_2 (Fe+M)	r_1 (Fe)	r_1 (Gd)	r_1 (Fe+M)
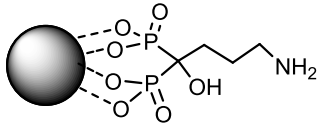 **NP2**	6	8.12	20.15	-13	329.75	-	1.84	-	-
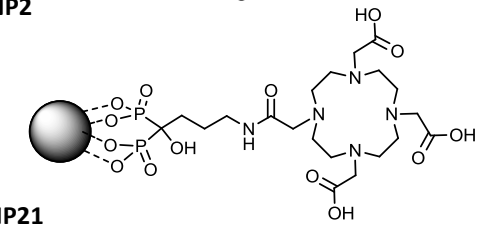 **NP21**	6	8.84	22.40	-12	480.14	-	1.72	-	-
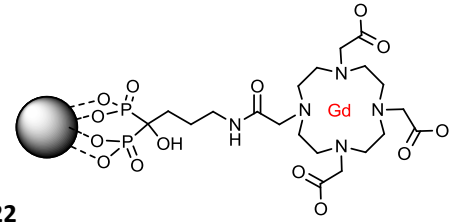 **NP22**	6	9.10	31.87	-16	282.49	267.22	3.14	54.89	2.96
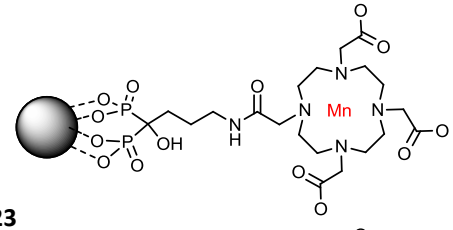 **NP23**	6	9.22	15.70	-16	224.45	212.34	1.51	26.41	1.42
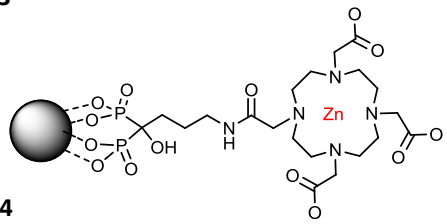 **NP24**	6	9.34	23.90	-17	305.66	289.14	1.49	26.13	1.41

Table 4.2 Set 1 of the T_1/T_2 probes. Modification to the probes is the metal in the DOTA chelate.

NP	Core size/nm	Theoretical size/nm	Z size/nm	Z potential mV	r_2 (Fe)	r_2 (Fe+M)	r_1 (Fe)	r_1 (Gd)	r_1 (Fe+M)
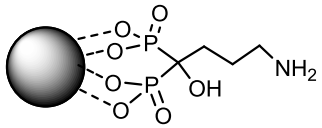 **NP2**	6	8.12	20.15	-13	329.75	-	1.84	-	-
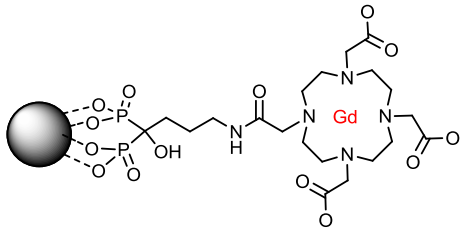 **NP22**	6	9.10	31.87	-16	282.49	267.33	3.14	54.89	2.96
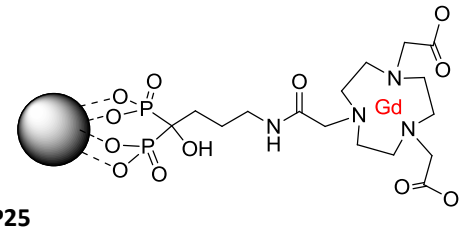 **NP25**	6	9.50	20.84	-12	220.35	212.87	2.06	58.93	1.99

Table 4.3 Set 2 with the replacement of Gd chelate from DOTA to NOTA.

NP	Core size/nm	Theoretical size/nm	Z size/nm	Z potential mV	r_2 (Fe)	r_2 (Fe+M)	r_1 (Fe)	r_1 (Gd)	r_1 (Fe+M)
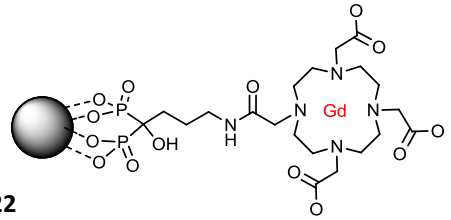 **NP22**	6	9.10	31.87	-16	282.49	267.22	3.14	54.89	2.96
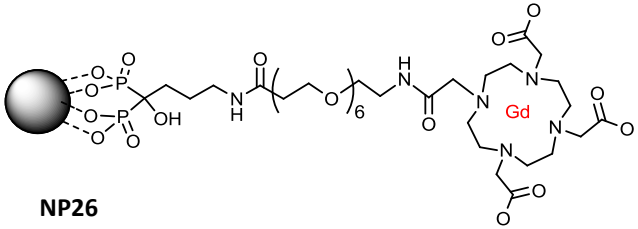 **NP26**	6	12.54	37.70	-10	177.16	167.59	1.83	32.00	1.73
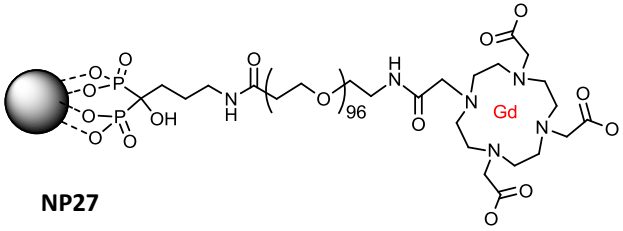 **NP27**	6	79.80	40.70	-15	143.74	135.98	1.21	21.19	1.15

Table 4.4 Set 3 with modifications to the distance between the magnetic core and paramagnetic Gd chelate.

NP	Core size/nm	Theoretical size/nm	Z size/nm	Z potential mV	r_2 (Fe)	r_2 (Fe+M)	r_1 (Fe)	r_1 (Gd)	r_1 (Fe+M)
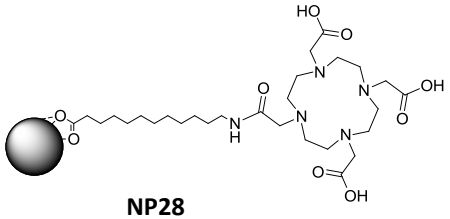 **NP28**	6	11.02	82.91		226.89	-	0.88	-	-
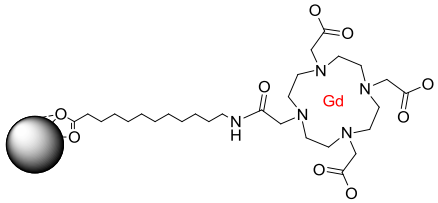 **NP29**	6	11.14	82.91		19.18	18.79	0.69	33.20	0.68
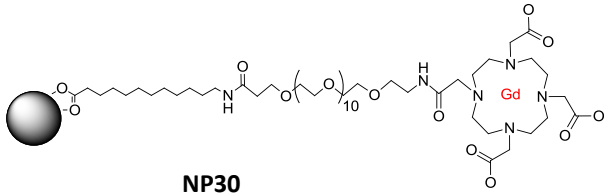 **NP30**	6	14.34	-		98.98		0.70		

Table 4.5 Set 4 alteration of the anchoring ligand from alendronate to 11-aminoundecanoate (bisphosphonate to carboxylate anchor), while at the same time altering the distance between the core and the Gd chelate.

4.2 Synthesis and characterisation of T_1/T_2 conjugate families

NP21 was complexed with different metals in the DOTA cavity (**Set 1**) by reacting the DOTA-functionalised nanoparticles with the respective metal salts. DOTA is the most widely used Gd^{3+} chelator due to its biocompatibility and stability with a range of metals and was therefore used in the majority of the nanoparticles synthesised.[13] NOTA replaced DOTA in one of the samples to observe if there would be an effect on hydration state about the gadolinium centre on the relaxivity (**Set 2**). Both NOTA and DOTA were conjugated to the surface of **NP2** by stoichiometric peptide coupling (**Scheme 4.2**). In a typical experiment, 300 equivalents of DOTA or NOTA relative to the nanoparticle were added to a 0.5 mg solution of the NP in water, and left to react overnight.

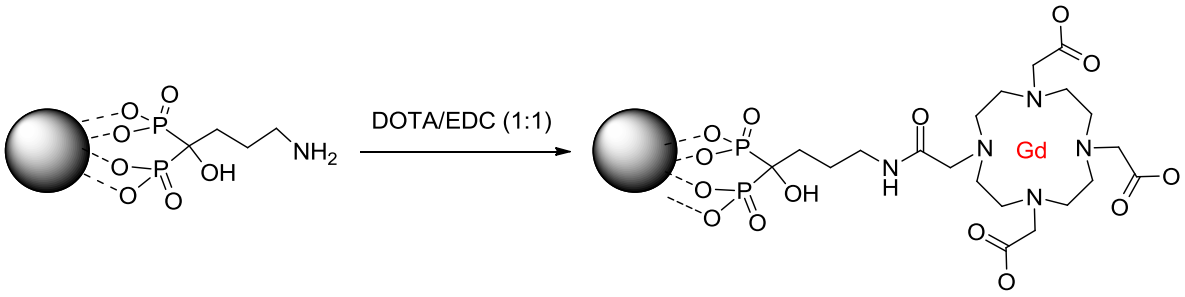

Scheme 4.2 Stoichiometric addition of DOTA (or NOTA) to **NP2**.

The yields of the DOTA (and NOTA) couplings to **NP2** and **NP2-PEG$_n$** were determined via quantification of unreacted chelate by an indirect colorimetric method. The washings from the DOTA coupling reaction were incubated with Gd^{3+} and then a small aliquot added to a fixed volume of 0.017 M xylenol orange solution. Free Gd^{3+} turns the solution from orange to purple, and this colour change can be measured by UV-Vis spectroscopy.[14] Similar to the rhodamine coupling reactions of **NP2** and **NP12** previously, the amount of free and bound Gd^{3+} in the washings can be calculated from the calibration curve, and correlated back to the amount of unreacted DOTA/NOTA in the washings. The DOTA coupling yields for both PEGylated and non-PEGylated particles were > 70 %. The NOTA coupling was slightly lower at 50 % yield. The lower yield for the NOTA coupling could be due to the use of pre-activated NOTA-NHS which deactivates over time, compared to the DOTA coupling where the carboxylic acid was activated with EDC *in situ*.

PEG chains were incorporated between the Gd-DOTA and nanoparticle core to observe the effect of distance between the T_1 and T_2 moieties on the resultant relaxivity (**Set 3**). The PEG molecules were of two different lengths (6 and 96 units) with a carboxylic acid on one end for conjugation by EDC coupling to the amine on the nanoparticle surface, and a protected Fmoc-amine on the other. After

coupling, the Fmoc is removed by treatment with three cycles of piperidine in DMF (20/80) for 15 minutes each, to give the free amine which can be further reacted with DOTA. The same procedure and characterisation methods were employed as before in Section 3.1.

The final nanoparticles were characterised by infrared spectroscopy and NMR relaxivity measurements. The PEGylated nanoparticles were confirmed by the presence of C=O amide stretch in the IR spectrum, as previously discussed in Chapter 3. C=O carboxylic acid stretching frequency in the infrared spectrum of the DOTA coupled nanoparticles further confirmed the coupling, alongside the xylenol orange assay. Further characterisation of the nanoparticles was made by DLS to obtain hydrodynamic size and surface charges. As previously explained in Chapter 2, the surface charge of **NP2** is negative at pH 7.4. This number remains even after PEGylation, DOTA coupling and Gd complexation, as expected from the contribution of the hydroxyl group on the alendronate. Hydrodynamic sizes of the nanoparticles increased with increasing PEG length, as expected. The diameter of **NP2** increased from 20.15 nm to 31.87 nm after DOTA-Gd conjugation and then to 37.70 nm and 40.70 nm after PEGylation with PEG_6 and PEG_{96} respectively. The theoretical diameter of the resultant nanoparticles were also calculated by determining the length of the total ligand on the nanoparticle surface using ChemBio 3D Ultra, and subsequently adding twice this value to the diameter of the nanoparticle core. This number was then compared to the hydrodynamic diameter and any effects they had on the relaxivities.

4.3 Relaxivities

Solutions of each nanoparticle sample of at least three different concentrations were prepared in pure water and placed in an NMR tube, containing a sealed capillary tube of D_2O. NMR T_1 and T_2 experiments to obtain T_1 and T_2 relaxation times respectively were performed on a 400 MHz Bruker NMR instrument. The relaxivity constants (both r_1 and r_2) were calculated through the curve fitting of T_1^{-1} and T_2^{-1} versus the metal concentrations in mM [Fe], [Gd] (or [Mn] or [Zn]), and ([Fe] + [Gd]).

The results obtained were quite difficult to interpret and therefore the trends in r_2 relaxivities will be discussed separately to the r_1 relaxivities. The trend for each modification set will be discussed within each relaxivity effect. The r_2 values with respect to [Fe] and ([Fe] + [Gd]) are very similar for each nanoparticle since the concentration of iron is far greater than that of gadolinium in any sample. Therefore, only the r_2*([Fe])* values were considered and compared for each nanoparticle set, over the r_2*([Fe] + [Gd])* values. For r_1 values, both r_1*([Gd])* and r_1*([Fe] + [Gd])* were considered and compared as Gd is more relevant with respect to r_1 compared to Fe.

4.3.1 T_2 relaxivity

The r_2*([Fe])* value for **NP2** (329.7 $mM^{-1}s^{-1}$) was found to be much higher than other IONP contrast agent coated with carboxylate-based ligands (r_2 = 50 - 150 $mM^{-1}s^{-1}$).[15–17] The relaxivity of the nanoparticles is related to the saturation magnetisation, and the method of nanoparticle preparation and the nature of the coating ligands (depending on the functional group of the anchor) changes the saturation magnetisation, resulting in differing relaxivities. Daou *et al* [18] have found that when nanoparticles are coated with an organic ligand, an oxidised layer is formed on the nanoparticle surface, whereby the nanoparticles consist of a stoichiometric core with an oxidised layer, and this was shown for both carboxylate and phosphate/phosphonate coated nanoparticles. However, the different anchoring functional groups affect the saturation magnetisation within the oxidised layer through spin canting, and therefore affect the net saturation magnetisation of the whole nanoparticle.[18] Spin canting occurs when the spins are tilted slightly about the axis by a small angle resulting in a non-zero net magnetisation. This does not occur for phosphate-based ligands but does for carboxylate-based ligands, and thus the phosphate-coated nanoparticles have a higher magnetisation and therefore higher relaxivity.[18] As previously discussed in Chapters 1 and 2, IONPs synthesised via the high temperature thermal decomposition method have a higher crystallinity which is also correlated to nanoparticle magnetisation.[19,20] These two factors; the lack of spin canting, and the high crystallinity of the core; together justify the exceptionally high relaxivity of **NP2**.

In comparing the r_2 values of **Set 1** (**Table 4.2**)**,** the relaxivities follow the same trend as observed in the literature. The r_2*([Fe])* of **NP2** (329.75 $mM^{-1}s^{-1}$) decreased to 282.49 $mM^{-1}s^{-1}$ in **NP22** when Gd is incorporated into the probe. This is due to the gadolinium interfering with the T_2 relaxation of the nanoparticle.[21,22] When the chelated metal was manganese (**NP23**) instead, the r_2*([Fe])* value also decreased to 224.45 $mM^{-1}s^{-1}$. This is as expected as Mn^{2+} is also a T_1 paramagnetic agent, and will therefore have the same effect as Gd^{3+}.[23,24] The relaxivity of **NP24** [r_2*([Fe])* = 305.66 $mM^{-1}s^{-1}$] is still similar in value to **NP2** and is as expected due to Zn^{2+} not being a paramagnetic ion like Mn^{2+} and Gd^{3+} and therefore should not affect the final relaxivity of the probe. The r_2*([Fe]+[M])* values for **NP22, NP23** and **NP24**, where [M] is [Gd], [Mn] or [Zn], also decreased by the same relative amounts.

When DOTA is replaced with NOTA as the Gd chelator (**Set 2**, **Table 4.3**), there is a decrease in the r_2*([Fe])* for **NP25** (220.35 $mM^{-1}s^{-1}$) compared to the r_2*([Fe])* value of **NP2** (329.75 $mM^{-1}s^{-1}$). Similar results are observed with **NP22** (i.e. a decrease in r_2*([Fe])* to 282.49 $mM^{-1}s^{-1}$ from **NP2**), and is in accordance with observations by Yang *et al* and Bae *et al*.[9,10] The larger decrease for **NP25** (Gd-

NOTA) can be attributed to the gadolinium having one more free coordination site or electron spin availability that results in a larger interference of the magnetic field generated by the magnetic core. Thus, the magnetisation of the resultant nanoparticle is decreased, as was observed.

Within **Set 3** (**Table 4.4**), a decrease in the r_2*([Fe])* of **NP22** (282.49 $mM^{-1}s^{-1}$) to **NP26** (177.16 $mM^{-1}s^{-1}$) is observed when a PEG chain is introduced. A further decrease to 143.74 $mM^{-1}s^{-1}$ was determined when the PEG length increased in **NP27.** This observation is in accordance with those made by Choi *et al*.[11] The same trend is seen across the r_2*([Fe]+[Gd])* value. This decrease can be explained as an interference of the magnetic field generated by the magnetic core and the effect is distance-dependent from the core. This interference in the field interacts with the water in the vicinity of the probe. A larger distance between the two moieties reduces the overall magnetic field that can interact with the water, thus resulting in a reduced T_2 contrast. The larger distance between the T_1 and T_2 moieties is confirmed by both the theoretical calculated size and hydrodynamic size measurement. There is a much larger increase in size for the calculated theoretical size values (9.10 nm for no PEG, 9.50 nm for short PEG and 79.80 for long PEG), compared to the increase in hydrodynamic diameter (31.87 nm when there is no PEG to 37.7 nm and 40.7 nm for the short and longer PEG chains respectively). The measured hydrodynamic diameter however is more accurate as the PEG chains are more likely to be coiled than linear, which is the assumption made for the calculated theoretical size values.

Changing the alendronate anchoring ligand for 11-aminoundecanoate (**Set 4**, **Table 4.5**) resulted in a similar trend in r_2*([Fe])* to that of **Set 1** whereby a decrease in r_2*([Fe])* is observed when Gd is incorporated in accordance with Yang *et al* and Bae *et al's* observations,[9,10] with both the non-PEGylated (**NP29**) and PEGylated conjugates (**NP30**) having lower r_2*[(Fe])* of 19.18 $mM^{-1}s^{-1}$ and 98.98 $mM^{-1}s^{-1}$ respectively compared to the r_2*([Fe])* of **NP28** (226.89 $mM^{-1}s^{-1}$). However, the increase in distance between the T_1 and T_2 moiety by the introduction of PEG had the opposite trend to that observed by Choi *et al*.[11] **NP30** had a higher r_2*([Fe])* value than **NP29**. In this particular case, this could be due to a different reason where the increased water solubility after PEGylation would allow the water molecules better access to the Gd and therefore have an increased effect on the r_2.

4.3.2 T_1 relaxivity

Since **NP2** and **NP2-DOTA** have no r_1*([Gd])* or r_1*([Fe]+[Gd])*, it was not possible to compare them to the values for the Gd-DOTA functionalised nanoparticles. The r_1*([Fe])* values in **Set 1** (**Table 4.2**) only partially follow the general literature trend of increasing when a paramagnetic metal is present.

With **NP22**, there is an increase in the r_1*([Fe])* from 1.84 $mM^{-1}s^{-1}$ (**NP2**) to 3.14 $mM^{-1}s^{-1}$. This is not the case when the metal ion is Mn^{2+} **NP23** (r_1*([Fe])* = 1.51 $mM^{-1}s^{-1}$). Since Mn^{2+} is less strongly paramagnetic than Gd^{3+}, its weaker effect on the relaxivity may be insignificant such that it not observed. The r_1 when the metal ion is Zn^{2+} **NP24** (r_1 = 1.49 $mM^{-1}s^{-1}$) is similar in value to when it is Mn^{2+}. However, this is as expected as it is also similar in value to the non-metal containing **NP2-DOTA** and Zn^{2+} should not have any effect on the final relaxivity of the nanoparticle.

Replacement of DOTA with NOTA as the Gd chelator in **Set 2** (**Table 4.3**) saw an increase in the r_1*([Gd])* relaxivity from 54.89 $mM^{-1}s^{-1}$ to 58.93 $mM^{-1}s^{-1}$. There is no similar correlation to the literature trend for this set. However, the increase in relaxivity is as expected as the extra water coordination site allows water ligands to bind in the NOTA-Gd complex which results in faster water exchange and therefore a higher relaxivity.

When the distance between the Gd chelate and the nanoparticle core was altered (**Set 3**, **Table 4.4**), the results were opposite to that observed by Choi *et al*.[11] All the r_1 values (relative to [Fe], [Gd], and ([Fe]+[Gd])) decreased instead when the Gd was further from the core (i.e. r_1*([Fe])* was 1.83 $mM^{-1}s^{-1}$ for the short PEG chain **NP26** and 1.21 $mM^{-1}s^{-1}$ for the longer chain **NP27**). One reason for the lower relaxivity of **NP27** could be the conformation of the PEG chain. A larger PEG chain is more likely to coil into a mushroom conformation instead of remaining linear, wrapping the Gd chelate within the PEG chain. This can hinder the binding of water to the Gd resulting in lower relaxivities. The hydrodynamic size of **NP27** (40.7 nm) was not much larger than **NP26** (37.7 nm), which indicates that the PEG in **NP26** is most likely linear while in **NP27** the PEG is most likely coiled, even though the theoretical size of the **NP27** was much larger.

Set 4 (**Table 4.5**) r_1 values also do not follow the literature trend of increasing when Gd is present, and there is no considerable effect on the r_1 values with respect to distance between the T_1 and T_2 moieties. The r_1 of **NP30** (0.70 $mM^{-1}s^{-1}$) did not differ from that of **NP29** (0.69 $mM^{-1}s^{-1}$).

4.4 Conclusion

The relaxivities for the nanoparticles synthesised here have not followed one particular trend, and not always the specific trends mentioned in the selected literature. **NP2** was found to have an exceptionally high relaxivity, and is higher than other T_2 contrast agents with similarly sized cores reported in the literature. When the nanoparticles are conjugated to a Gd chelate, although the r_2 values decrease slightly, r_1 values increase in comparison to **NP2.** This result makes these conjugates excellent candidates for dual-weighted T_1/T_2 contrast agents. Modification of the distance between the T_1 and T_2 moieties decreased both r_2 and r_1 with increasing distance and so shorter distances are desirable.

Changing the DOTA macrocycle for NOTA also resulted in a favourable increase in r_1*([Gd])* value compared to **NP22** (DOTA)**.** However the use of NOTA *in vivo* is not currently clinically approved This modification was not discussed in the literature and so a comparison could not be drawn.

Replacing the alendronate ligand for 11-aminoundecanoate decreased the r_2 value due to the difference in functional group for the anchor. When the distance between the T_1 and T_2 centre for the 11-aminoundecanoate functionalised nanoparticles is increased, r_2*([Fe])* values also decreased while r_1*[(Gd)]* values remained similar. Overall, alendronate ligand was found to be an ideal ligand to produce T_1/T_2 contrast agents with excellent relaxivities.

4.5 Experimental

NOTA-NHS ester and DOTA were obtained from CheMatech and used without further purification. The metal salts and xylenol orange were obtained from Sigma-Aldrich and used without further purification. All solvents were analytical grade and were obtained from VWR. EDC couplings were carried out in MilliQ water under ambient conditions. FT-IR spectra were acquired in a Perkin-Elmer Spectra 100 FT-IR spectrometer, neat on ATR plates. ^{1}H NMR spectra and T_1/T_2 inversion recovery data were obtained in a Bruker DRX400 MHz spectrometer. Z-measurements were obtained in a Beckman Coulter Delsa Nano.

4.5.1 Synthesis of NP2-DOTA

To **NP2** in MilliQ water (0.5 mg NP, 1.43 nmol, typically about 250 µL from a 2.0 mg/mL NP solution) was added a solution of DOTA (300 eq) and EDC (1 eq with respect to DOTA). The mixture was left to shake overnight then centrifuged and the supernatant separated and isolated for yield quantification by a xylenol orange assay. The residue was taken up in water (100 µL) and washed by precipitating with acetone and the nanoparticles were isolated by centrifugation. This second supernatant was not used in the xylenol orange assay. The nanoparticles were then resuspended in water (250 µL).

4.5.2 Synthesis of NP2-NOTA

To **NP2** in MilliQ water (0.5 mg NP, 1.43 nmol, typically about 250 µL from a 2.0 mg/mL NP solution) was added NOTA-NHS ester (300 eq). As the NOTA was pre-activated, no additional EDC was added. The mixture was left to shake overnight then centrifuged and the supernatant separated and isolated for yield quantification by a xylenol orange assay. The residue was taken up in water (100 µL) and washed by precipitation with acetone and the nanoparticles were isolated by centrifugation. This second supernatant was not used in the xylenol orange assay. The nanoparticles were then resuspended in water (250 µL).

4.5.3 Synthesis of NP2-PEG$_n$-DOTA

NP2 was PEGylated with HOOC-PEG$_n$-NH$_2$ by the same method as previously reported in Chapter 3. The subsequent DOTA conjugation was the same method as for the synthesis of **NP2-DOTA.**

4.5.4 Gd complexations

NP2-DOTA (0.5 mg NP, in 250 µL water) was adjusted to pH 6 with 0.5 M HCl. $GdCl_3.6H_2O$ in acetate buffer pH 6 (300 eq with respect to NP, 1 eq with respect to DOTA) was added to the nanoparticle solution and the mixture left to shake overnight. After centrifugation, the supernatant was decanted and the residue taken up in water. The nanoparticles were washed by precipitation with acetone and the nanoparticle were isolated by centrifugation. The nanoparticles were then resuspended in water (250 µL).

The same complexation method was used for all the nanoparticle species (PEGylated and non-PEGylated, and for the NOTA chelate) and for the different metals (Mn and Zn).

4.5.5 Xylenol orange assay

The amount of DOTA unreacted after the DOTA coupling reaction was determined by incubating the washings from the DOTA coupling reaction with a known quantity of Gd^{3+} (approximately the same equivalence as the DOTA added to the NP reaction). The amount of free Gd^{3+} remaining after the incubation can be determined by a xylenol orange assay and correlated back to the amount of Gd^{3+} that reacted with the DOTA in the washings, and therefore the amount of DOTA that coupled to the NP can be determined. This assay is based on the method by Barge *et al*.[14]

Gd^{3+} calibration standards (50 µL each) between 0 – 10 µg Gd(III) were prepared from a 1 mg/mL Gd(III) stock solution of $GdCl_3.H_2O$ in deionised water. The xylenol orange solution was prepared by dissolving xylenol orange (3 mg) in acetate buffer (250 mL, 50 mM, pH 5.8) to give a 0.017 mM solution. The 0.017 mM xylenol orange solution (500 µL each) was added to the standards (50 µL) and the UV-Vis of the solution recorded. The calibration curve is a plot of the ratio of the absorbance at 573 nm and 433 nm, against the concentration of Gd^{3+}.

The same volume of xylenol orange (500 µL) was added to an aliquot of the supernatant after incubation with Gd^{3+} (50 µL). UV-Vis of the solution was recorded and the ratio of the absorbance at (573/433) nm was correlated to the concentration of Gd^{3+} in the calibration curve.

4.6 References

1. R. Weissleder, S. Saini, D. D. Stark, J. Wittenberg, and J. T. Ferrucci, *Am. J. Roentgenol.*, 1988, **150**, 561–6.
2. R. C. Semelka, J. K. T. Lee, S. Worawattanakul, T. C. Noone, R. H. Patt, and S. M. Ascher, *J. Magn. Reson. Imaging*, 1998, **8**, 670–674.
3. S. Kubaska, D. V Sahani, S. Saini, P. F. Hahn, and E. Halpern, *Clin. Radiol.*, 2001, **56**, 410–5.
4. F. Hu and Y. S. Zhao, *Nanoscale*, 2012, **4**, 6235–43.
5. Z. Zhou, D. Huang, J. Bao, Q. Chen, G. Liu, Z. Chen, X. Chen, and J. Gao, *Adv. Mater.*, 2012, **24**, 6223–8.
6. J. Kim, C. Lee, and S. Lee, *Bull. Korean Chem. Soc*, 2009, **30**, 6–9.
7. G. H. Im, S. M. Kim, D.-G. Lee, W. J. Lee, J. H. Lee, and I. S. Lee, *Biomaterials*, 2013, **34**, 2069–76.
8. D. Niu, X. Luo, Y. Li, X. Liu, X. Wang, and J. Shi, *Appl. Mater. Interf.*, 2013, **5**, 9942–8.
9. H. Yang, Y. Zhuang, Y. Sun, A. Dai, X. Shi, D. Wu, F. Li, H. Hu, and S. Yang, *Biomaterials*, 2011, **32**, 4584–4593.
10. K. H. Bae, Y. B. Kim, Y. Lee, J. Hwang, H. Park, and T. G. Park, *Bioconjugate Chem.*, 2010, **21**, 505–12.
11. J.-S. Choi, J.-H. Lee, T.-H. Shin, H.-T. Song, E. Y. Kim, and J. Cheon, *J. Am. Chem. Soc.*, 2010, **132**, 11015–7.
12. C.-C. Huang, C.-Y. Tsai, H.-S. Sheu, K.-Y. Chuang, C.-H. Su, U.-S. Jeng, F.-Y. Cheng, C.-H. Su, H.-Y. Lei, and C.-S. Yeh, *ACS Nano*, 2011, **5**, 3905–16.
13. G. Stasiuk and N. Long, *Chem. Commun.*, 2013, **49**, 2732.
14. A. Barge, G. Cravotto, E. Gianolio, and F. Fedeli, *Contrast Media Mol. I.*, 2006, **1**, 184–8.
15. E. D. Smolensky, H.-Y. E. Park, T. S. Berquó, and V. C. Pierre, *Contrast Media Mol. I.*, 2011, **6**, 189–199.
16. S. Tong, S. Hou, Z. Zheng, J. Zhou, and G. Bao, *Nano Lett.*, 2010, **10**, 4607–13.
17. U. Tromsdorf, O. Bruns, and S. Salmen, *Nano Lett.*, 2009, **9**, 4434–4440.
18. T. J. Daou, J. M. Grenèche, G. Pourroy, S. Buathong, A. Derory, C. Ulhaq-Bouillet, B. Donnio, D. Guillon, and S. Begin-Colin, *Chem. Mater.*, 2008, **20**, 5869–5875.
19. D. Margulies, F. Parker, F. Spada, R. Goldman, J. Li, R. Sinclair, and A. Berkowitz, *Phys. Rev. B*, 1996, **53**, 9175–9187.
20. D. Margulies, F. Parker, M. Rudee, F. Spada, J. Chapman, P. Aitchison, and A. Berkowitz, *Phys. Rev. Lett.*, 1997, **79**, 5162–5165.
21. A. Villringer, B. R. Rosen, J. W. Belliveau, J. L. Ackerman, R. B. Lauffer, R. B. Buxton, Y.-S. Chao, V. J. Wedeenand, and T. J. Brady, *Magn. Reson. Med.*, 1988, **6**, 164–174.
22. P. Loubeyre, T. De Jaegere, H. Bosmans, Y. Miao, Y. Ni, W. Landuyt, and G. Marchal, *J. Magn. Reson. Imaging*, 1999, **9**, 447–53.
23. A. C. Silva, J. H. Lee, I. Aoki, and A. P. Koretsky, *NMR Biomed.*, 2004, **17**, 532–43.
24. J. H. Lee, A. C. Silva, H. Merkle, and A. P. Koretsky, *Magn. Reson. Med.*, 2005, **53**, 640–8.

CHAPTER 5

Biological application of the functionalised nanoparticles

5 Biological application of the functionalised nanoparticles

5.1 Introduction

One of the applications of the nanoparticles synthesised in this research, was to utilise them as contrast agents for the imaging of vulnerable plaque. This chapter will introduce the reader to a specific biological target, which when conjugated to the nanoparticle will then be used for the imaging of vulnerable plaque. Much of the work in this chapter is preliminary, and was carried out in collaboration with Dr Takayuki Homma in the Krams group, Bioengineering Department, Imperial College London.

5.2 Fractalkine as a specific target for vulnerable plaque imaging

As previously discussed in Chapter 1, macrophages are present at every stage of atherosclerosis. These macrophages have antigens on their surface, and secrete signalling proteins called chemokines that aid cell migration, as well as other proteins, chemicals and enzymes. One particular chemokine that has been well-documented in the literature to play a significant role in inflammation, including atherosclerosis, is Fractalkine, a CX3CL1 chemokine.[1] First characterised by Bazan *et al,*[2] this chemokine exists in both the membrane-bound and soluble form. When membrane bound, the firm adhesion of monocytes to the endothelial cells are promoted by the chemokine. When soluble, it acts as a chemoattractant for cells that express the Fractalkine receptor (CX3CR1).[3] The two processes are outlined in **Figure 5.1**. The CX3CR1 receptor is expressed on various cells such as monocyte-derived macrophages, smooth muscle cells, and T-cells. Fractalkine (or CX3CL1) interacts with only a single receptor (CX3CR1), unlike other chemokine molecules that have an affinity for multiple receptors. The inflammation process repeats itself continuously, due to the continual presence of the chemokines on the macrophages and other Fractalkine-expressing cells, and this can ultimately result in the formation of vulnerable plaque. Therefore, Fractalkine as a target is an ideal candidate in the imaging of vulnerable plaque.

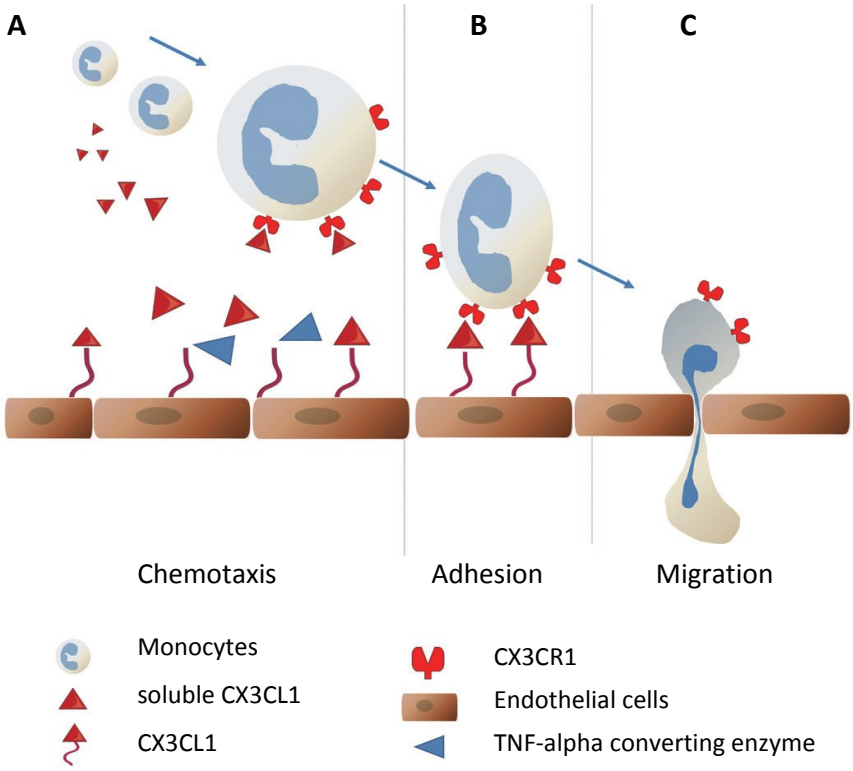

Figure 5.1 Diagram showing the dual-role of Fractalkine (CX3CL1) in atherosclerosis. When bound to the endothelial membrane, it promotes the adhesion of CX3CR1-expressing monocytes in the blood to the vessel wall (B) and subsequently the migration of the monocytes into the endothelial cells (C). CX3CL1 becomes soluble after cleavage by TNF-alpha converting enzyme, and acts as a chemoattractant for CX3CR1-expressing cells (A). Image taken from ref [3].

Both the Fractalkine molecule itself, as well as its receptor can be utilised as targets for the imaging of vulnerable plaque. Therefore, the primary aim of this section of work was to synthesise a single-chain variable fragment (scFv) of an antibody that will be conjugated to the nanoparticles. It is proposed that the scFv will then either be targeted towards macrophages that express the chemokine Fractalkine receptor, or the endothelial cells that express the Fractalkine itself, in order to image vulnerable plaque (**Figure 5.2**).

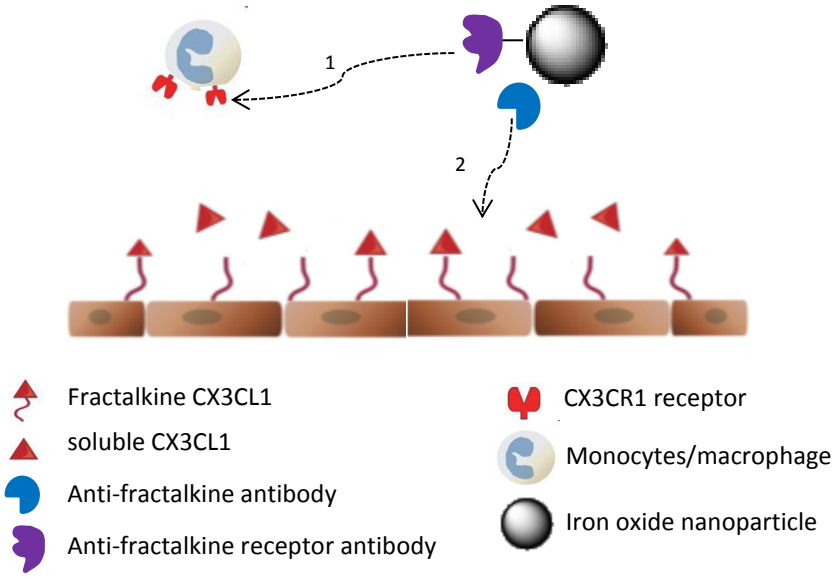

Figure 5.2 Proposed target routes towards the imaging of vulnerable plaque. Route 1 is the targeting of an anti-Fractalkine receptor antibody on the nanoparticle towards the Fractalkine receptor on a macrophage that also has a chemoattraction towards the Fractalkine molecule on the endothelial cells of plaque. Route 2 is the targeting of an anti-Fractalkine antibody on the nanoparticle towards the Fractalkine molecule either soluble or bound to the surface of the endothelial cells.

5.3 Preliminary results

The preparation of antibodies against both Fractalkine and the receptor were attempted – an anti-Fractalkine receptor antibody for the Fractalkine receptor; and an anti-Fractalkine antibody for the Fractalkine protein. As antibodies are very large molecules, the preparation of a shorter chain fragment (single chain variable fragment, scFv) of the desired antibody was attempted, in order to achieve higher selectivities with the target. The anti-Fractalkine receptor antibody was not successfully identified by the Krams group. However, the anti-Fractalkine antibody was successfully identified and plasmid containing scFv against Fractalkine was isolated and provided by the Krams group. The scFv was screened from the Tomlinson I and J library (data not shown) previously within the group, but its specificity towards Fractalkine was not confirmed. Two clones of the scFv were isolated and inserted into plasmids. Both clones had identical protein sequences confirmed from the promoter to terminator region, but may contain differences in the other areas of the plasmid. In order to confirm that these possible differences did not have an effect on the specificity towards Fractalkine, both clones should be used and compared.

5.3.1 Initial macrophage uptake experiments

The uptake of nanoparticles by macrophages before their conjugation to scFv is an undesirable process, since macrophages are present all over the body. Uptake of nanoparticles in this case means a high non-specific uptake. There are two subpopulations of macrophages, M1 and M2, which differentiate from monocytes when the monocytes enter tissue and are exposed to growth factors and other compounds.[4–6] Exposure of the monocytes to granulocyte macrophage colony stimulating factor (GM-CSF) and macrophage colony stimulating factor (M-CSF) differentiate the monocytes into macrophages.[7] Monocytes are polarised into M1 macrophages by GM-CSF while M-CSF polarises monocytes into M2 macrophages. Both M1 and M2 polarised macrophages are present in atherosclerotic plaque, although there is some evidence of a higher population of M1 in vulnerable plaque.[8–10] Therefore, the preferential uptake of the particles by a subpopulation of the macrophages (M1) may still be acceptable.

The nanoparticles tested here were the PEGylated nanoparticles (**NP6**, **NP7** and **NP8**,) synthesised earlier in Chapter 3. The PEG molecules were of three different lengths, but each featuring NH_2 terminal groups as these would be the functional groups utilised for subsequent scFv conjugation.

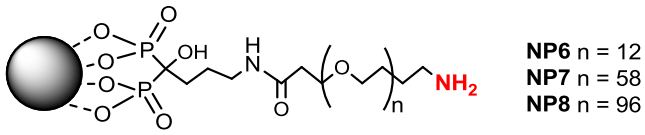

Figure 5.3 Structures of **NP6**, **NP7** and **NP8** tested in the macrophage uptake experiments.

The M1 and M2 macrophages for the uptake experiments were obtained by harvesting white blood cells from the bone marrow of mice, and subsequently polarising the cells by the addition of the respective macrophage colony stimulating factors. HeLa cells, a human cancer cell line, were used as control cells. Despite the need for macrophages in the research of inflammation, no appropriate cell model is available. Therefore macrophage polarisation protocol utilises monocytes which are either bone marrow-derived or blood-derived. Bone marrow-derived monocytes are preferred as the maturity of the cells is at its lowest and therefore can be controlled. Blood-derived monocytes usually contain cells at different stages of maturation.

After incubation of the two subpopulations of macrophages, and the control HeLa cells, with the nanoparticles, the cells were washed to remove any unbound/non-uptaken nanoparticles and the remaining nanoparticles were stained with Prussian blue dye. Prussian blue is a dye that binds to

non-haemoglobin iron.[11] The nuclei of the cells were then counter-stained with nucleus red. The cells were then imaged by microscopy.

From the images (**Table 5.1**), it appears that all the nanoparticle samples were taken up by both the M1 and M2 macrophages. However, it is not possible to definitively distinguish between preferential M1 or M2 uptake. The conditions for this experiment however, have not been fully optimised. The cell density of the M1/M2 macrophages and the amount of nanoparticle used in the incubation still need to be optimised in order to improve the quality of images obtained. Nevertheless, with optimisation, this method can still be used for future screening of nanoparticles.

	M1	M2	HeLa
NP6	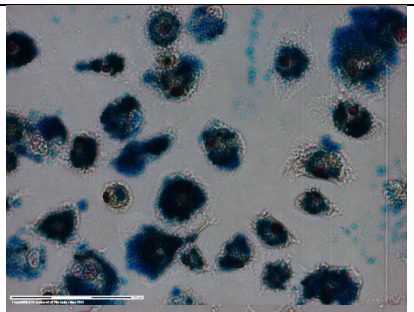	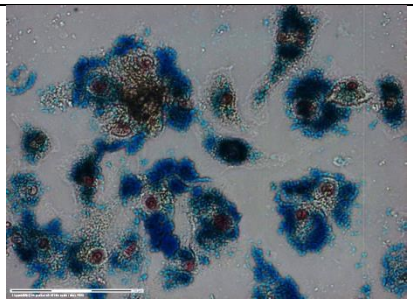	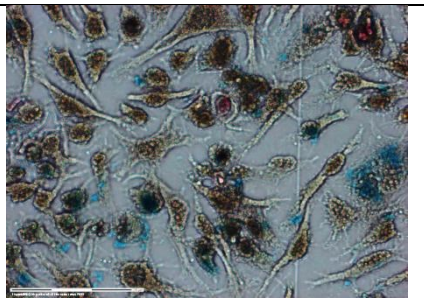
NP7	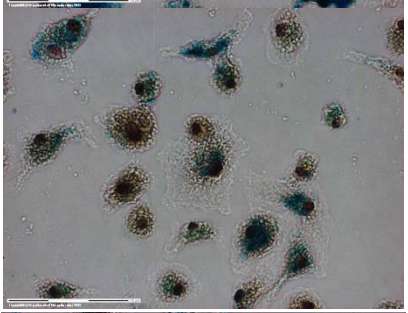	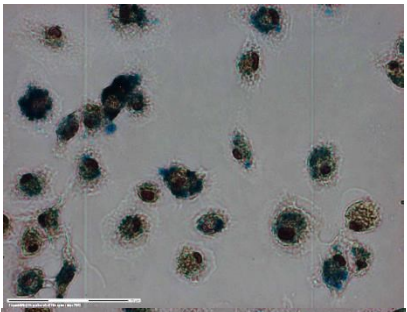	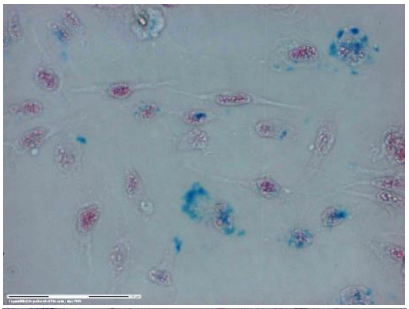
NP8	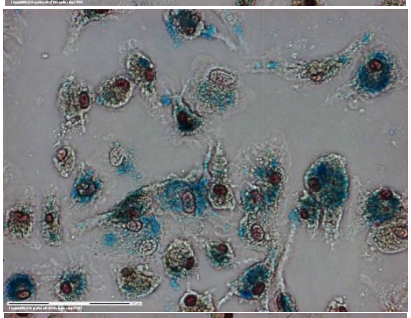	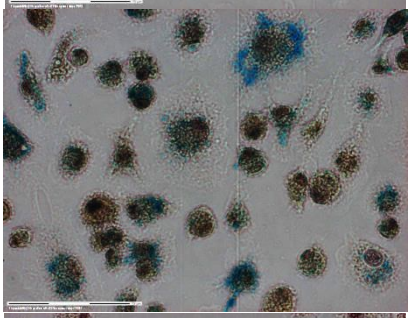	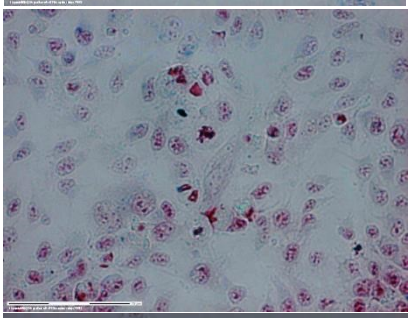
no NP	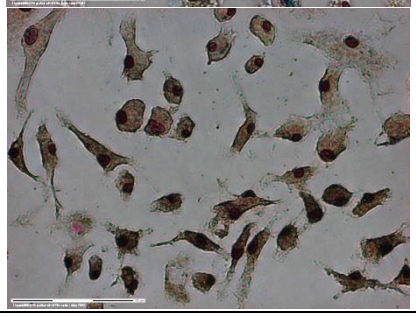	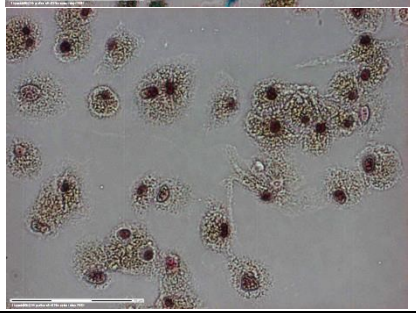	

Table 5.1 Microscopy images of macrophage incubated with nanoparticles, with HeLa cells as a control cell line. Magnification of the images are x40. Iron is stained blue while the nucleus of the cells are stained red. When the cells take up the nanoparticles, the blue colour from the iron should overlap the red nucleus. The above images show nanoparticle uptake by both M1 and M2 macrophages, and no uptake by the control HeLa cells.

5.3.2 scFv preparation and specificity test

In order to produce a candidate of scFv against Fractalkine by *E. coli*, the phage containing the scFv DNA was transformed into *E. coli* then stored as a glycerol stock at -80 °C. A microspatula of the frozen glycerol stock of the bacteria was inoculated into a small volume of the medium to make a preculture. A portion of the preculture was subsequently inoculated into the main culture medium and incubated to produce the scFv. This experiment was run in parallel with three separate protein expressing bacterium; two scFv from different plasmid clones, and a control containing Ubiquitin (which is not Fractalkine specific).

After incubation of the bacteria overnight with IPTG, the scFvs were purified. Purification begins by separating the bacterial cells from the medium, by centrifugation. The media was filtered through 0.45 µm and 0.2 µm syringe filters to remove any last traces of cells. The filtered media was then passed through AcroSep MEP Hyper cell column, a protein purification column. The column retains the protein and prior to elution with a buffer, phosphate buffered saline (PBS) was passed through to wash out any unbound protein. The protein was isolated from the column by elution with a second buffer that reduces the pH of the column. The fractions of eluted buffer containing the scFv were analysed by sodium dodecyl sulfate polyacrylamide gel electrophoresis (SDS-PAGE) to confirm the molecular weight of the protein. At each stage of the purification, a small aliquot of the filtered media (labelled “S” for the sample after the syringe filtration, and labelled “FT” after passing down the column) as well as the PBS washing (W1 – W10) and eluted buffers (E1 – E6), were isolated for SDS-PAGE analysis.

The SDS-PAGE (**Figure 5.4**) of each fraction after purification on column did not show the desired molecular weight of the scFv (expected around 29 kDa). Both scFv had identical SDS-PAGE results. The SDS-PAGE of the Ubiquitin also did not show the expected molecular weight.

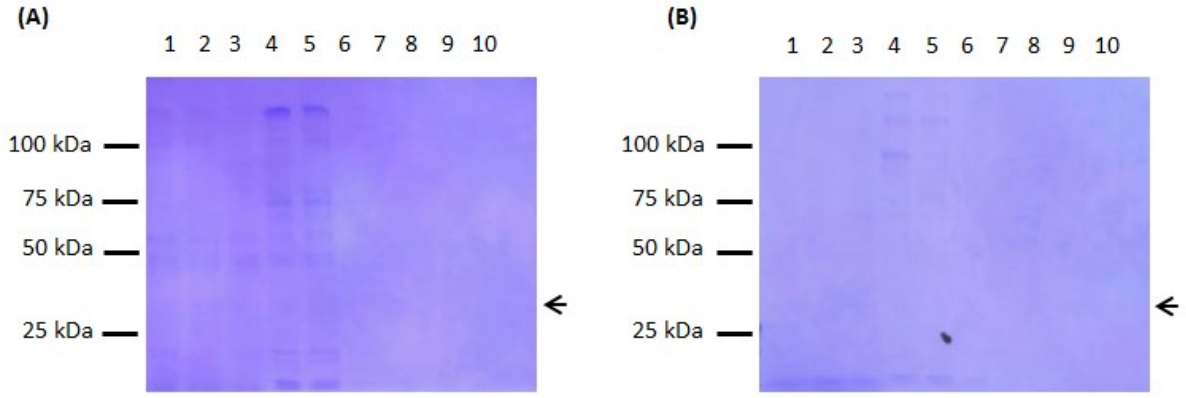

Figure 5.4 SDS-PAGE after initial purification of (A) scFv and (B) Ubiquitin. Arrowheads represent the region where the scFv and Ubiquitin M_W were expected to appear. The following samples were in the labelled wells: 1) filtered supernatant "S", 2) flow through "FT", 3) washing "W1", 4) washing "W10", 5 – 10) elutions "E1 – E6".

Two different hypotheses could account for the results of this experiment: 1) glucose was added to the medium, to minimise the early expression of protein that can be toxic to the bacteria. The glucose can inhibit the action of the IPTG (which was added to allow the *E. coli* to express the proteins); 2) the bacteria did express the proteins, but did not release it into the media.

Therefore, first the scFv preparation was repeated on a small scale with no glucose added, but keeping all other conditions the same. The same results as before were observed, with the desired scFv or Ubiquitin molecular weights not detected on SDS-PAGE (**Figure 5.5**). This suggests that glucose does not have an effect of the bacterial expression of scFv.

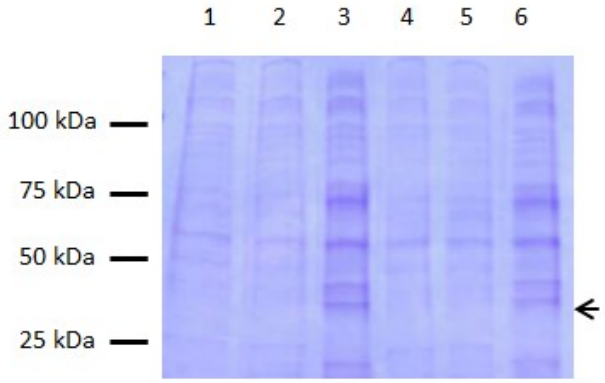

Figure 5.5 SDS-PAGE of scFv preparation with no glucose added. Arrowhead represents the region where the M_W of the proteins were expected to appear. Wells 1, 2 and 3 are the same as 4, 5 and 6 respectively, but at two different concentrations. Wells 1 and 4, and 2 and 5, are the supernatant from scFv samples. Wells 3 and 6 are the supernatant from the Ubiquitin sample.

To examine if reason 2 was the culprit, the pellet from the initial scFv preparation was lysed by sonication. The lysate was separated from the cell debris by centrifugation and the supernatant analysed by SDS-PAGE (**Figure 5.6**). As before, the desired molecular weight was not detected by the SDS-PAGE.

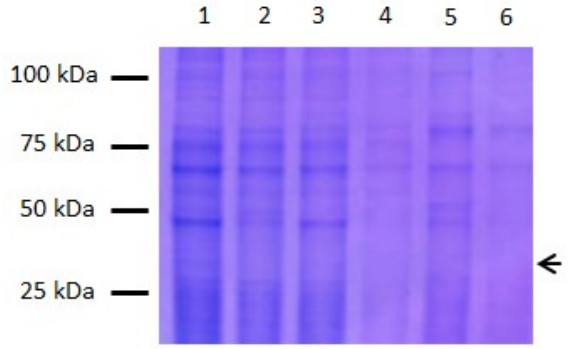

Figure 5.6 SDS-PAGE after the pellet was sonicated. Arrowhead represents the region where the M_W of the proteins were expected to appear. Wells 1, 2 and 3 are identical to wells 4, 5 and 6 respectively, but at two different concentrations. Wells 1 and 4, and 2 and 5, are from scFv samples. Wells 3 and 6 are from the Ubiquitin sample.

The experiment was then repeated with fresh *E. coli* transformant. Newly transformed *E. coli* with monoclonal phage was prepared, from a HB2151 competent cell and scFv coded plasmid. The competent cells are mixed with the plasmids (three different samples; two anti-Fractalkine scFvs and one control anti-Ubiquitin). The transformed bacteria were then plated on petri dishes and incubated overnight. After counting the colonies, one colony from each transformant was selected and added to a preculture medium, and the scFv preparation repeated as before for all three different bacteria. After purification, each fraction was analysed by SDS-PAGE (**Figure 5.7**).

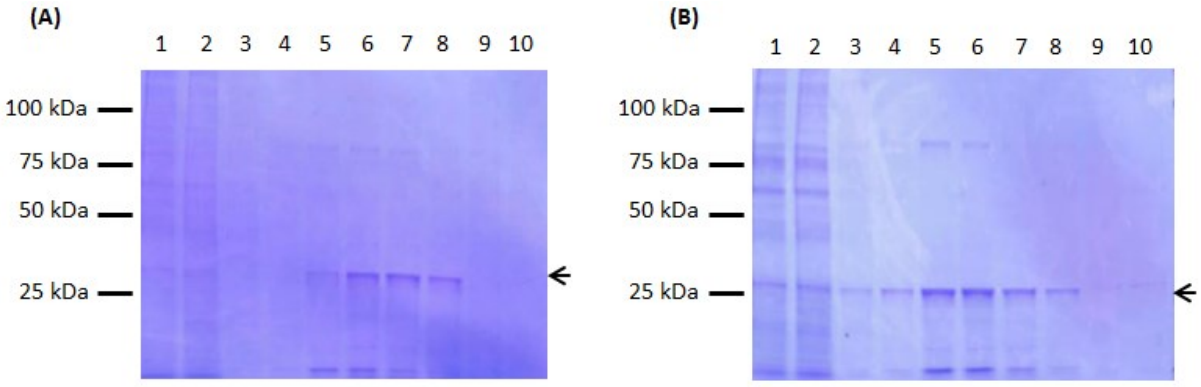

Figure 5.7 SDS-PAGE of (A) scFv and (B) Ubiquitin. Arrowhead represents the region where the M_W of the proteins were expected to appear. The following samples were in the labelled wells: 1) filtered supernatant "S", 2) flow through "FT", 3 – 8) elutions "E1 – E6", 9) washing "W9", 10) washing "W10".

From the SDS-PAGE, the eluted samples (wells 5 – 8) containing the scFv had the expected molecular weight of 29 kDa. This result suggested that the scFv was present. To confirm that the scFv was Fractalkine specific, an enzyme-linked immunosorbent assay (ELISA) test was carried out. The resulting colourimetric indicator can be measured (OD_{450}) and the values obtained used to determine the quantity of scFv binding to the antigen. The scFv (both clones) were tested against the Fractalkine antigen (at two different concentrations), as well as the Ubiquitin antigen. PBS(-) and BSA were used as negative controls. The results from the ELISA was plotted (**Graph 5.1**).

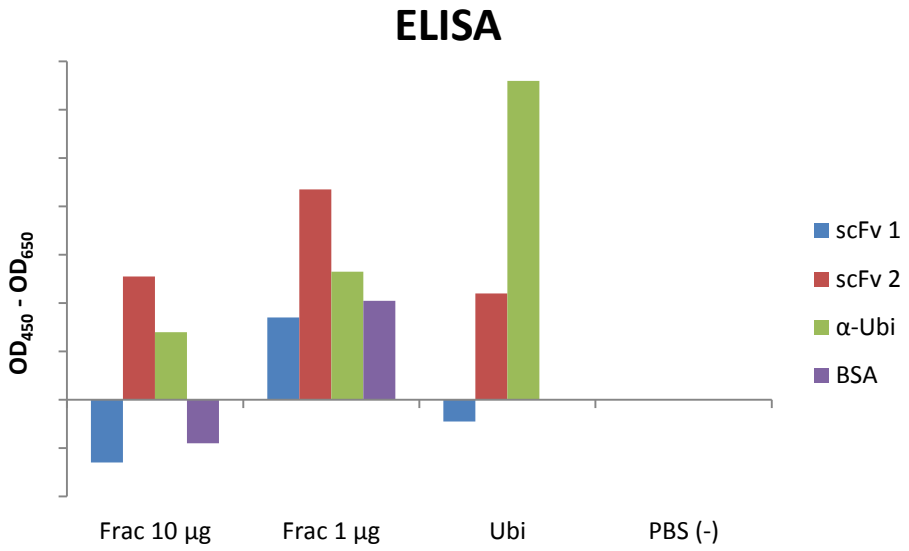

Graph 5.1 Plot of (OD_{450} – OD_{650}) values for the relevant samples (scFv 1 - blue, scFv 2 - red, α-Ubiquitin - green and BSA - purple), against the different antigen coatings (Fractalkine, Ubiquitin and PBS(-)).

The ELISA results are very preliminary and cannot confirm the specificity of the scFv towards Fractalkine. However, scFv 2 does show a degree of specificity towards Fractalkine which is promising. The Ubiquitin antigen coating showed the correct binding results, with the Ubiquitin binding strongly as expected, no binding for scFv 1 and some binding for scFv 2 (potentially a false positive). When the coating was PBS, no binding in all samples were observed, as expected. ELISA measurements are highly susceptible to false positive readings, as cross contamination between wells is very easy.

5.4 Conclusion

Preliminary uptake experiments of non-targeted conjugated nanoparticles with M1 and M2 polarised macrophages showed uptake by both subpopulations of macrophage. It was not possible to distinguish preferential uptake between M1 and M2 macrophage. Optimisation of the method, such as determining the ideal cell density and concentration of nanoparticle during incubation, is required, and will be the subject of future studies.

A human Fractalkine specific scFv fragment was successfully prepared following the transformation of an *E. coli* strain with plasmid containing the scFv DNA. Initial problems in the preparation of the scFv were identified and the protocol improved to obtain the desired scFv. The molecular weight of the scFv was determined by SDS-PAGE. Unfortunately, specificity towards the human Fractalkine was not confirmed by preliminary ELISA. Due to time constraints, further ELISA measurements were not able to be carried out to confirm the specificity of the scFv, and conjugation to nanoparticles were not possible. Once conjugated to the nanoparticles, the specificity of the scFv on the nanoparticles towards Fractalkine would be further tested by histology experiments, as well as by MRI with mice injected with the nanoparticles.

5.5 Experimental

All reagents and media were prepared as sterile and autoclaved, unless otherwise stated. MilliQ water was purified by the PURITE system.

The following reagents were obtained from Sigma: Phosphate buffered saline without calcium or magnesium [PBS(-)] (P4417), D-(+)-Glucose (G8270), Tween20 (P5927), Isopropyl β-D-1-thiogalactopyranoside (IPTG) (I6758-10G), 3,3',5,5'-Tetramethylbenzidine (TMB) (T5525), Red blood cell lysing buffer (R7757). Potassium acetate (60035), RbCl (R2252), $MnCl_2.4H_2O$ (221279), $CaCl_2.2H_2O$ (C3306), 3-(N-morpholino)propanesulfonic acid (MOPS, 69947), glycerol (G7893).

The following reagents were obtained from Invitrogen: SDS-PAGE 10-20 % Tris-Glycine Gel (EC66252), Tris-Glycine SDS Sample Buffer (2x) (LC2676), Tris-Glycine SDS running buffer (10x) (LC2675), Dry Ease Mini-Gel Dryer System (NI2387A), Gel Dry solution (LC4025).

Sodium Chloride was obtained from VWR (BDH, 102415K). Tryptone (VM371131 147), yeast extract (VM077526 919), LB medium (1.10285.0500) and LB agar (1.10283.0500) were obtained from Merck. DMSO (EC200-664-3) and Ampicillin (BP1760-5) were obtained from Fisher Scientific. Macrophage colony-stimulating factor (MCSF, 315-02), Interleukin 4 (IL-4, 214-14), Interleukin 13 (IL-13, 210-13), Interferon gamma (IFN-γ, 315-05), Human Fractalkine (0.1 mg/mL, 300-31) were all obtained from PeproTech EC Ltd. Lipopolysaccharide (LPS) (tlr-pelps) was purchased from Invivogen. Dulbecco's Modified Eagle Medium (DMEM) (BE12-604F) was purchased from Lonza. β-mercaptoethanol (60-24-2) was purchased from Laiwu Hehui Chemical Co.

Labtech Chamber Slide Labtek II 4 pk16 (154526) for nanoparticle incubation with macrophages was purchased from Nalge Nunc International. Petri dishes (90 x 14.2 mm) for growing *E. coli* were obtained from VWR (391-0455). AcroSep MEP Hyper cell column (1 mL capacity, 12035-C001) was obtained from Pall.

25 and 50 mL falcon tubes were centrifuged by Rotanta 460R rotor no. 5624 (Hettich). OD_{600} values were recorded on a BioPhotometer Plus (Eppendorf). Bright field images were captured on a PALM MicroBeam from Zeiss (optical microscope).

Full DMEM was prepared complementing DMEM with 10 % fetal calf serum (FCS) obtained from Gibco and 1 % Penicillin Streptomycin (P11-010) purchased from PAA.

TMB solution was made by dissolving 1 TMB tablet in 1 mL DMSO and adding this into 9 ml of phosphate-citrate buffer aqueous solution (the content of 1 capsule in 100 mL water).

2xYT solution was made by mixing tryptone (8 g), yeast extract (5 g) and NaCl (2.5 g) in water (500 mL).

5.5.1 Polarisation of M1 and M2 macrophages from mouse femurs and tibias

All experimental procedures were performed in accordance with protocols approved by Imperial College Animal Care and Use Committee. Five female C57BL/6 mice aged between 8 - 20 weeks were included in the study.

The femurs and tibias from euthanised mice were harvested and the bones were cleaned from muscle tissues in DMEM for 1 min. Using a sterile razor blade, both ends of the bones were cut. A needle was placed into the cut ends and the bone flushed with DMEM and collected into a 50 mL falcon tube. The alcon tubes were topped up to 50 mL before centrifugation at room temperature for 5 min at 490 g. The cells (pellet) were separated with red blood cell lysing buffer (5 mL) at room temperature and then topped up with DMEM to 50 mL and centrifuged as previously. The cells (pellet) were suspended in full DMEM (3 mL) and counted with hematocytometer under microscope and diluted to a density of 1 x 10^6 cells/mL with full DMEM. To this, a macrophage colony-stimulating factor (M-CSF, 1/1,000 dilution) was added. The solution was plated into T75 and T25 flasks (20 mL and 7 mL respectively), and incubated at 37 °C for 5 days to mature. At the day of the maturation period, the supernatant was removed and fresh DMEM (10 mL) was added, removed, and then more fresh DMEM added (5 mL). The cells were scratched off from the plates and the suspension transferred to a falcon tube, centrifuged, and the pellet suspended in full DMEM (3 mL) and counted as previously before dilution to a density of 0.5 x 10^6 cells/mL with full DMEM. The solution of cells were plated subsequently in the desired wells of Labtech's chamber slides (0.5 – 1.0 mL/well), then left overnight at 37 °C to adhere. HeLa cells (0.5 x 10^6 cells/mL, 0.5 – 1.0 mL/well) were added into desired wells as a non-phagocytic negative control and adherence allowed. For the macrophage cultures, once adhered, the supernatant was removed, and the following polarisation factors added to the relevant wells: for M1 polarisation - 100 ng/mL IFN-γ + LPS (1/1,000 and 1/500 vol., respectively) and M2 polarisation - 50 ng/mL IL-4 + IL-13 (each 1/500 vol.); and left to polarize for 24 hours. Nanoparticle samples (25 μg/well) were added to wells and incubated for 4 to 5 hours at 37 °C. The phagocytosis was stopped by adding ice cold PBS (1 mL) and washed 4 times with PBS. The slides were air dried for 30 min, then the cells fixed in acetone for 30 min on ice, subsequently washed with PBS for 5 min and air dried at room temperature, before being stained with Prussian blue.

5.5.2 Prussian blue staining

No metal components were used (e.g. tweezers/racks) in this stain as the basis of the stain is the reaction between Fe(III) ions and potassium hexacyanoferrate (II) which forms a blue pigment. The following solutions were prepared at room temperature:

(A): Potassium hexacyanoferrate(II) (1.0 g) was dissolved in MilliQ water (50 mL).

(B): 37 % HCl (2.5 mL) diluted with MilliQ water (47.5 mL).

Equal portions of A and B were mixed to form the iron staining solution. Cells fixed on slides (see previous) were suspended in the iron staining solution for 15 min, then rinsed with MilliQ water and counter-stained (nuclei) with neutral red for 5 min. The slides were then rinsed with tap water, dehydrated in 100 % ethanol for 1 min, then cleared in HistoClear for 1 min before mounted on a microscope.

5.5.3 scFv preparation

All procedures with bacterial cell culture were performed under aseptic manipulation.

Day 1: A pre-culture medium was prepared which contained 2YxT (5 mL), 100 µg/mL Ampicillin and 1 % glucose in a 14 mL Falcon tube. A microspatula-full of a stock *E. coli* was inoculated and shaken at 37 °C, 180 rpm overnight.

Day 2: Main culture medium containing 2xYT (300 mL), 50 mg/mL Ampicillin (200 µL) and 40 % glucose (250 µL) was prepared. The pre-culture (2 mL) was inoculated and shaken at 37 °C, 180 rpm until OD_{600} = 0.9 (about 3 hours). OD_{600} was measured on an Eppendorf Biophonate Plus photometer. To the mixture was added 0.1 M isopropyl β-D-1-thiogalactopyronoside IPTG (1 mL so the final concentration was 1 mM) and shaken at 30 °C, 180 rpm overnight.

Day 3: To confirm that the cultured bacteria were successfully grown, the OD_{600} of the "Day 2" prepared solutions were measured. The cultured media were divided into Falcon tubes and centrifuged at 1800 g (2870 rpm) for 10 minutes at 4 °C. Subsequently, the supernatant was stored on ice until purified.

5.5.4 Purification of scFv

The following stock solutions for running of the column were prepared:

a) PBS (-): 1 tablet of PBS (Sigma Aldrich) was dissolved in MilliQ water (200 mL) then filtered with a 0.2 µm syringe filter and stored at 4 °C.
b) Elution buffer: 50 mM sodium acetate at pH 4.96 combined with 50 mM NaCl solution. A stock solution of 1 M sodium acetate was prepared by dissolving sodium acetate (8.02 g) in MilliQ water (100 mL). A stock solution of 1 M NaCl was prepared by dissolving NaCl (5.85 g) in MilliQ water (100 mL). The elution buffer was prepared by combining the 1 M sodium acetate solution (5 mL) and the 1 M NaCl (5 mL) and diluted with MilliQ water up to 100 mL.
c) Tris.HCl: 5.463 g of Tris Base was dissolved in MilliQ water (30 mL) then adjusted to pH 8.8.

The previously obtained supernatant was first filtered with a 0.45 µm syringe filter then with a 0.2 µm syringe filter. The filtered supernatant (250 µL) was combined with 2x sample buffer (250 µl) and β-mercaptoethanol (25 µL) and labelled as sample "S". AcroSep MEP Hyper cell column was equilibrated with PBS(-) (5 mL) using a 20 mL syringe. All filtered supernatant were applied keeping the flow through in an autoclaved bottle. The columned flow through (250 µL) was combined with 2x sample buffer (250 µL) and β-mercaptoethanol (25 µL) and labelled as "FT". The column was then washed with PBS(-) (10 mL), with the flow through isolated as 1 mL fractions each in separate Eppendorf tubes. Each of the 1 mL fractions of the PBS washings (250 µL) was combined with 2x sample buffer (250 µL) and β-mercaptoethanol (25 µl) and labelled as W1 to W10 respectively. Following that, ScFv was eluted from the column with elution buffer (6 mL), with the flow through again isolated as 1 mL fractions in separate Eppendorf tubes. To each fraction, 1.5 M Tris HCl pH 8.8 (50 µl) was added to neutralise the sample. As before, each of the eluted fractions (250 µl each) was combined with 2x sample buffer (250 µl) and β-mercaptoethanol (25 µl) and labelled as sample E1 to E6 respectively. The column was washed with PBS (-) (10 mL) for later use. All the samples S, FT, W1-W10, E1-E6, were stored on ice until the SDS-PAGE.

5.5.5 Preparation of new competent cells (HB 2151 *E. Coli)*

LB media was prepared by dissolving LB powder (25 g) in MilliQ water (1 L), and then autoclaved.

TfbI was prepared by dissolving potassium acetate (0.15 g, 30 mM), RbCl (0.61 g, 100 mM), $CaCl_2.2H_2O$ (0.07 g, 10 mM), $MnCl_2.4H_2O$ (0.50 g, 50 mM), and glycerol (7.5 mL) in MilliQ water

(30 mL). The volume of the solution was topped up with MilliQ water to 50 mL. The pH was adjusted to 5.8 with 0.2 M acetic acid and sterilised by filtration with a 0.2 µm syringe filter.

TfbII was prepared by dissolving 3-(N-morpholino)propanesulfonic acid (MOPS) (0.10 g, 10 mM), $CaCl_2.2H_2O$ (0.55 g, 75 mM), RbCl (0.06 g, 10 mM) and glycerol (7.5 mL) in MilliQ water (30 mL). The volume of the solution was topped up with MilliQ water to 50 mL. The pH was adjusted to 6.5 with 1 M KOH and sterilised by filtration with a 0.2 µm syringe filter.

To an aliquot of the LB broth (2 mL), a spatula of previously frozen HB 2151 *E. Coli* was inoculated and this preculture incubated at 37 °C overnight. A portion of the preculture (1 mL) was added into LB broth (100 mL) and incubated at 37 °C until the OD_{600} = 0.3 (approximately 1.5 h). The media was transferred into two 50 mL falcon tubes and placed on ice for 5 min, then centrifuged at 4200 rpm for 10 min at 4 °C. The pellet was resuspended in TfbI (20 mL per falcon tube), vortexed and placed on ice for 5 min. The solution was centrifuged as before and the pellet resuspended in TfbII (2 mL per falcon tube), vortexed and placed on ice for 15 min. To store the competent cells, the TfbII solutions of the cells were dispensed into ice cold Eppendorf tubes and snap freezed in liquid N_2 before storage at -80 °C.

5.5.6 Transformation (insertion of plasmid into competent cells)

LB agar was prepared by dissolving LB agar powder (37 g) in MilliQ water (1 L). The mixture was autoclaved, then kept at 55 °C until the pouring stage. Prior to pouring into the petri dishes, ampicillin (1 mL) was added. The dishes were allowed to cool until the agar solidified and then labelled, sealed with parafilm and stored at 4 °C.

To the competent cells in TfbII solution (100 µL aliquots) was added the following plasmids separately (0.5 µL each):

a) scFv 1
b) scFv 2
c) Ubiquitin
d) pUC19 vector as a control.

The mixtures were placed on ice for 30 min then heat shocked at 42 °C for 1 min before cooling on ice for 2 min. To each mixture was added LB broth containing 0.4 % glucose and 20 mM $MgSO_4$ (1 mL, where 100 mL LB broth requires 100 µL of 40 % glucose stock and 200 µL $MgSO_4$ 1 M stock). The mixtures were incubated at 37 °C for 1 h, before plating on LB agar plates that were incubated at

37 °C overnight. The colonies were counted and one from each (except the pUC19 control) were incubated in a preculture for scFv synthesis as previously outlined.

5.5.7 SDS-PAGE

All samples "S", "FT", "W1-10", "E1-E6" from the scFv purification, were boiled using Techne Dri-Block DB2D for 5 minutes before application of each (25 µL) onto a 12 well, 1.0 mm, 12 % Tris-glycine gel cassette with a commercial marker (10 µL) applied as a reference in the first and last well. The gel was run in a tank containing Tris-glycine running buffer (x10 dilution), at 185 V (constant voltage), for 1 h, or until the dye has reached the bottom of the gel. The gel was removed from the holder and stained with a Coomassie Brilliant Blue (CBB) dye for 20 min. The stain was discarded and washed with deionised water, then left to destain overnight. Finally the gels were dried overnight according to manufacturer's instructions.

5.5.8 ELISA

All amounts described are per well. A 96 well plate was coated with the relevant antigens: 1) a recombinant Human Fractalkine antigen (100 µL from 10 µg/mL); 2) Ubiquitin (100 µL from 20 µM); 3) PBS (-) as control. After leaving to coat overnight at 4 °C, the wells were washed 3 times with PBS (-). After the final wash, 3 % BSA in PBS (-) (200 µL) were added and incubated at room temperature for 2 h. This acts as a blocking agent for non-specific binding sites. The wells were washed again 3 times with PBS (-), then scFv samples (or anti-Ubiquitin as control) (10 µL) suspended in 3 % BSA/PBS (-) (100 µL) was added. The plate was incubated for 1 h at room temperature. The wells were washed 3 times with PBS (-)/0.1 % Tween 20. Finally, TMB colourimetric substrate (100 µL) was added and left to develop a blue colour for 2 – 15 mins at room temperature. The reaction was stopped by the addition of 1 M H_2SO_4 (50 µL), which turned the solutions varying degrees of yellow. The absorbances of the solutions in each well were recorded at OD_{450} and OD_{650} on a plate reader, and the OD_{650} value subtracted from the OD_{450} value.

5.6 References

1. S. D. Cushing, J. A. Berliner, A. J. Valente, M. C. Territo, M. Navab, F. Parhami, R. Gerrity, C. J. Schwartz, and A. M. Fogelman, *P. Natl. Acad. Sci. USA*, 1990, **87**, 5134–8.
2. J. F. Bazan, K. B. Bacon, G. Hardiman, W. Wang, K. Soo, D. Rossi, D. R. Greaves, A. Zlotnik, and T. J. Schall, *Nature*, 1997, **385**, 640–4.
3. S. Apostolakis and D. Spandidos, *Acta Pharm. Sin.*, 2013, **34**, 1251–6.
4. T. Gui, A. Shimokado, Y. Sun, T. Akasaka, and Y. Muragaki, *Mediat. Inflamm.*, 2012, **12**.
5. A. Mantovani, S. Sozzani, M. Locati, P. Allavena, and A. Sica, *Trends Immunol.*, 2002, **23**, 549–555.
6. S. Gordon and P. R. Taylor, *Nat. Rev. Immunol.*, 2005, **5**, 953–64.
7. M. Jaguin, N. Houlbert, O. Fardel, and V. Lecureur, *Cell. Immunol.*, 2013, **281**, 51–61.
8. J. L. Stöger, M. J. J. Gijbels, S. van der Velden, M. Manca, C. M. van der Loos, E. A. L. Biessen, M. J. A. P. Daemen, E. Lutgens, and M. P. J. de Winther, *Atherosclerosis*, 2012, **225**, 461–8.
9. J. Khallou-Laschet, A. Varthaman, G. Fornasa, C. Compain, A.-T. Gaston, M. Clement, M. Dussiot, O. Levillain, S. Graff-Dubois, A. Nicoletti, and G. Caligiuri, *PLoS One*, 2010, **5**, e8852.
10. A. Seneviratne, M. Hulsmans, P. Holvoet, and C. Monaco, *Cardiovasc. Res.*, 2013, **99**, 284–93.
11. R. D. Sundberg and H. Broman, *Blood*, 1955, **10**, 160–6.

CHAPTER 6

Conclusions and future work

6 Conclusions and future work

6.1 General conclusions

The use of iron oxide nanoparticles as MRI contrast agents has been extensively researched in literature. Their mode of imaging is different to gadolinium-based contrast agents and so would not completely replace them as MRI contrast agents. However, nanoparticles do offer a slight advantage over Gd contrast agents, as they can achieve exceptionally high relaxivities, and due to the large surface area can be decorated with various moieties, enabling multiple functions within one construction.

Dual-modal MRI/PET contrast agents have been synthesised and studied in the literature, mostly with a non-nanoparticle agent as the MRI moiety, and the combined contrast agent as one entity. This poses several problems where a large dual-modal nanoparticulate based contrast agent would move slowly *in vivo* and reduce the lifetime of the PET radioisotope. To overcome this, a pre-targeting concept to bring the two separate contrast agents together *in vivo* was proposed. Conjugation of a cyclooctyne (strained alkyne) to the nanoparticle would enable copper-free azide-alkyne cycloaddition to a PET-moiety (^{68}Ga-azido-DOTA complex).

The surface of the nanoparticles were decorated firstly with a small molecule ligand bearing a strong binding anchor, and subsequently with PEG for improved water solubility and biocompatibility. The two step functionalisation, first with a small molecule and then the PEG allows for a more versatile approach, compared to simply coating the nanoparticles with a biocompatible polymer such as dextran (the binding mode of which is usually by weak electrostatic interactions).

Prior to using the radioactive gallium, luminescent lanthanides were utilised to enable characterisation of the resultant nanoparticles after the cycloaddition reaction by traditional methods. In addition to the luminescent lanthanides, paramagnetic gadolinium was also conjugated to the nanoparticles by the copper-free alkyne-azide cycloaddition reaction. This gave a dual-weighted T_1/T_2 contrast agent with enhanced r_1 relaxivities. This was an interesting area of the nanoparticles to investigate, therefore a range of Gd-conjugated NPs, with various modifications were synthesised, and their physical properties studied.

With respect to biological application, the nanoparticles were intended for use as a contrast agent in the imaging of vulnerable plaque. An attempt was made to functionalise the nanoparticles with a biological targeting agent, by conjugation to a short chain antibody fragment that is specific to a protein called Fractalkine.

Bearing all of this in mind, the general outline of the progression of the project is described again in the scheme below (**Scheme 6.1**).

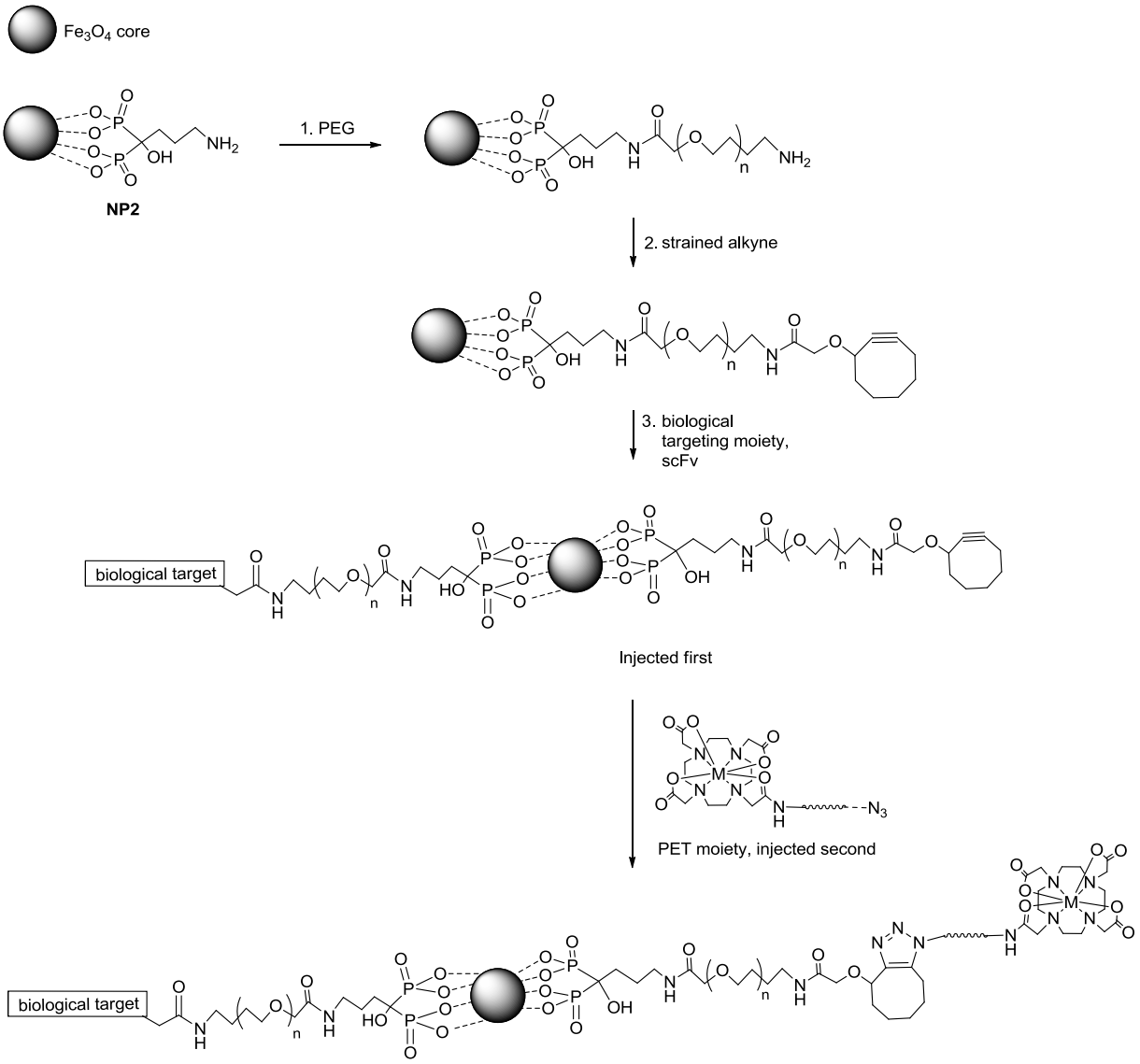

Scheme 6.1 Overview of the synthesis and structure of the final nanoparticle target.

In Chapter 2, several methods to synthesise iron oxide nanoparticles were discussed, however the high temperature thermal decomposition of an iron precursor, iron acetylacetonate, produced the most ideal nanoparticles with a low size dispersion and high crystallinity. The nanoparticles were of 6 nm diameter on average, and coated with hydrophobic oleic acid. Different ligands to replace the oleic acid were investigated to obtain water-soluble nanoparticles. Ligands with sulfonate, phosphonate and bisphosphonate as anchoring groups were investigated. Sodium alendronate, a ligand with a bisphosphonate group as the anchor, was determined to be the most successful as the

resultant nanoparticles (**NP2**) were water-soluble. This excellent stability is due to the strong interaction between the nanoparticle surface and the bisphosphonate group.[1,2]

Chapter 3 described the conjugation of **NP2** to PEG of different lengths with different terminal functional groups, as well as conjugation to a cyclooctyne (**NP12**). Both conjugations were successful and characterised accordingly. Initial copper-free cycloaddition reactions between **NP12** and Ln-azide-DOTA complexes (where Ln = Eu and Tb) were attempted, however unexpected fluorescence results were observed. This led to work investigating the relaxivity effects on nanoparticles when the metal conjugated to the NP surface was Gd (Chapter 4). The T_1/T_2 conjugates gave relaxivities that did not always have a defined trend, nor followed a particular literature trend. However the enhanced r_1 relaxivities on conjugation of the Gd to the NP makes these nanoparticles ideal for use as dual-weighted T_1/T_2 contrast agents. Reaction between **NP12** and ^{68}Ga-azide-DOTA was not achieved in the time available.

In Chapter 5, the preparation of scFv specific towards Fractalkine was attempted using *E. coli*. The scFv was intended to be conjugated to the nanoparticle for vulnerable plaque imaging. Work is still ongoing to determine the specificity of the scFv towards the Fractalkine antigen. Preliminary uptake experiments with macrophages indicate that the nanoparticles are taken up by both M1 and M2 polarised macrophages which is not ideal, and it was not possible to determine preferential uptake between the two macrophage populations.

6.2 Future work

As an extension of work with respect to the synthesis of nanoparticles, hybrid nanoparticles such as manganese ferrite ($MnFe_2O_4$) could be another nanoparticle core to be investigated. $MnFe_2O_4$ nanoparticles have a higher magnetisation than Fe_3O_4 and so would have even higher relaxivities than those already synthesised here.[3–6] $MnFe_2O_4$ can be synthesised via a similar method to the high temperature thermal decomposition of iron(III) acetylacetonate to form Fe_3O_4.[7] Partial substitution of $Fe(acac)_3$ for $Mn(acac)_2$ in a 1:2 ratio at the same conditions gives $MnFe_3O_4$ (**Scheme 6.2**).

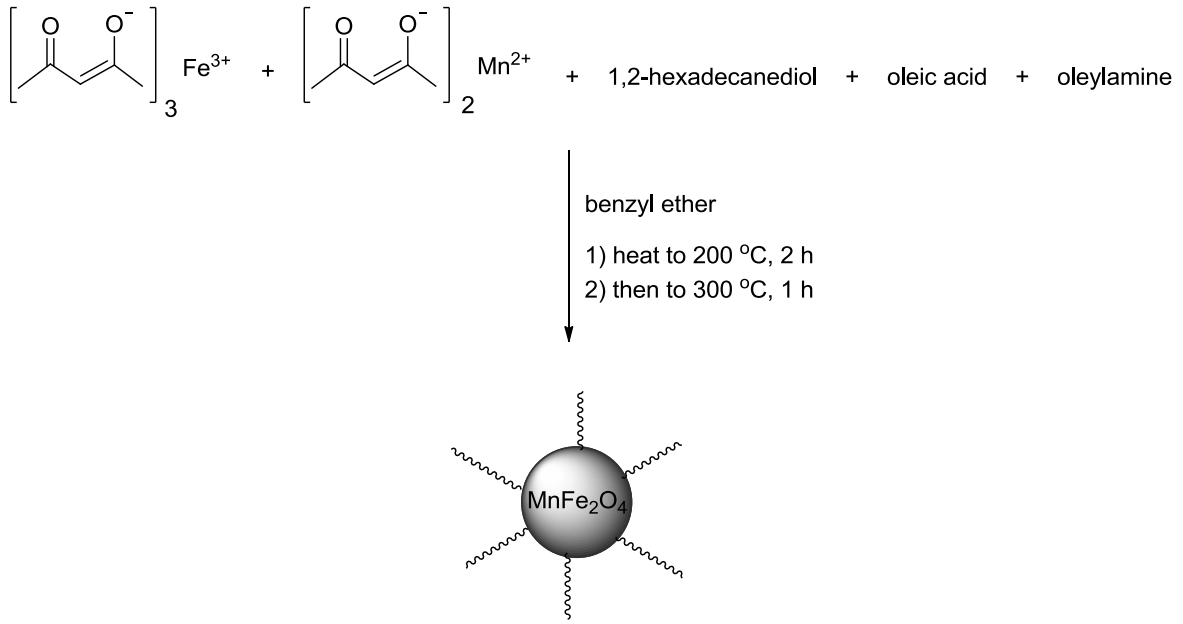

Scheme 6.2 Synthesis of $MnFe_2O_4$ via the high temperature thermal decomposition of $Fe(acac)_3$ and $Mn(acac)_2$.

Various molecules can act as capping agents for a nanoparticle; polymers and inorganic shells among others. Only small molecules were investigated here to allow for versatility in conjugation of further moieties. Polymers such as polyacrylic acid and polyethylenimine could serve as potential polymeric coatings for nanoparticles. The stability of the resultant nanoparticles could then be investigated and compared to those coated by small molecules in this project.

With respect to the fluorescence of the nanoparticles in Chapter 3, further investigation with a higher-powered laser or a fluorimeter capable of measuring shorter gating times would help elucidate the results observed. Lifetime measurements of the Ln-conjugated nanoparticles would also be carried out.

The use of the cyclooctyne here can be improved upon, by the use of the later generation modified cyclooctynes. This would require a more difficult and multi-step synthesis, or directly purchasing the costly cyclooctynes. However, another catalyst-free efficient cycloaddition reaction that has been identified in the literature is between tetrazine (some examples in **Figure 6.1**) and a strained alkene or alkyne.[8–10] This reaction (**Scheme 6.3**) has been suggested to have extremely fast kinetics, and is more tolerant to water.

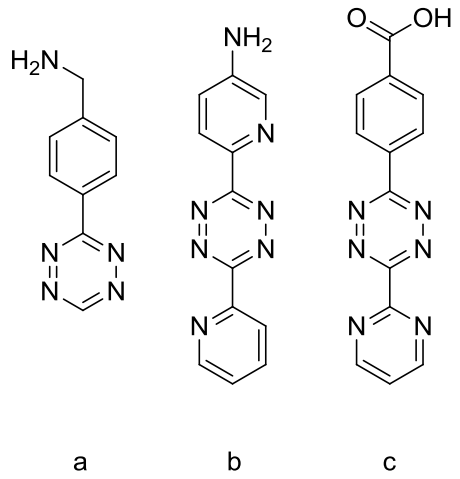

Figure 6.1 Structures of tetrazines that have been used in reported cycloaddition reactions. a) (4-(1,2,4,5-tetrazin-3-yl)phenyl)methanamine, b) 6-(6-pyridin-2-yl)-1,2,4,5-tetrazin-3-yl)pyridine-3-amine, c) 4-(6-pyrimidin-2-yl)-1,2,4,5-tetrazin-3-yl)benzoic acid.

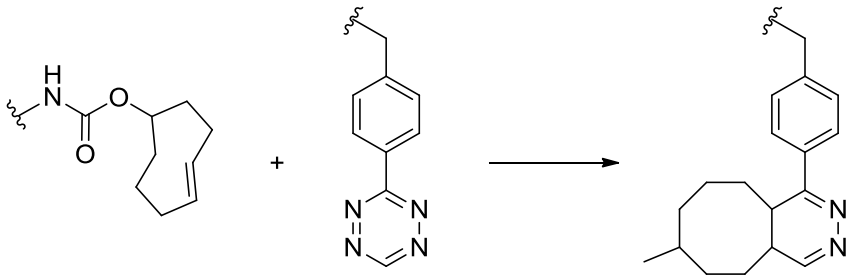

Scheme 6.3 Cycloaddition reaction between a *trans*-cyclooctene and tetrazine.[11]

With respect to the dual-weighted T_1/T_2 nanoparticle conjugates, further modifications such as changing the size of the nanoparticle core as well as the type of nanoparticle core itself, and measuring the relaxivities to understand their effects on the magnetisation of the nanoparticles. Larger nanoparticles are expected to have higher magnetisation and this should be reflected in the T_1 and T_2 measurements.

The biological aspects of this project have not been addressed sufficiently mainly due to time constraints. Radiolabelling experiments with gallium-68 would need to be carried out to form the ^{68}Ga-azido-DOTA complexes and subsequently testing the copper-free cycloaddition reaction with the alkyne functionalised nanoparticles *in vitro* and *in vivo*. If successful, conjugation of tetrazine to the PET moiety or the nanoparticle and subsequently the cycloaddition reaction could be carried out in order to compare the reaction kinetics for the azide-alkyne cycloaddition and the tetrazine-strained alkene/alkyne.

With respect to the preparation of the scFv, confirmation of the specificity against Fractalkine by ELISA is the first step. Once confirmed, conjugation to the nanoparticle will be carried out and the specificity again confirmed, by ELISA as well as histology experiments.

From the macrophage uptake experiments, it has not been possible to distinguish between M1 or M2 macrophage uptake for the nanoparticle not functionalised with scFv. Unfortunately, obtaining bone marrow-derived monocytes are time consuming (and require the euthanisation of mice), and therefore the macrophage polarisation protocol has been slow to optimisation to improve the cell density of the cells. Nevertheless, once optimised, the uptake experiments themselves will also require optimisation. Experimentation with varying concentrations of nanoparticles per well, and different cell densities per well should be carried out.

If all this is successful, MR imaging in live mice and eventually pigs would be ideal, alongside the possible dual-modal MRI/PET imaging. Distribution studies should also be carried out. In the long term, comparison of the imaging of vulnerable plaque by the nanoparticles to that via other imaging modalities such as OCT could be carried out to determine the efficacy and success of this method.

In summary, this work has showcased a promising methodology towards the synthesis of a dual-modal MRI/PET contrast agent with hopes for use in the imaging of vulnerable plaque. However, more work needs to be carried out in order to refine the system and chemistry in order to develop this as a viable tool for the required application.

6.3 References

1. T. J. Daou, S. Begin-Colin, J. M. Grenèche, F. Thomas, A. Derory, P. Bernhardt, P. Legaré, and G. Pourroy, *Chem. Mater.*, 2007, **19**, 4494–4505.
2. T. J. Daou, L. Li, P. Reiss, V. Josserand, and I. Texier, *Langmuir*, 2009, **25**, 3040–4.
3. L. Wei, G. Zhou, Z. Li, L. He, M. Gao, J. Tan, and H. Lei, *Magn. Reson. Imaging*, 2007, **25**, 1442–8.
4. U. I. Tromsdorf, N. C. Bigall, M. G. Kaul, O. T. Bruns, M. S. Nikolic, B. Mollwitz, R. A. Sperling, R. Reimer, H. Hohenberg, W. J. Parak, S. Förster, U. Beisiegel, G. Adam, and H. Weller, *Nano Lett.*, 2007, **7**, 2422–7.
5. J.-H. Lee, Y.-M. Huh, Y. Jun, J. Seo, J. Jang, H.-T. Song, S. Kim, E.-J. Cho, H.-G. Yoon, J.-S. Suh, and J. Cheon, *Nat. Med.*, 2007, **13**, 95–9.
6. H. Yang, C. Zhang, X. Shi, H. Hu, X. Du, Y. Fang, Y. Ma, H. Wu, and S. Yang, *Biomaterials*, 2010, **31**, 3667–73.
7. S. Sun, H. Zeng, D. B. Robinson, S. Raoux, P. M. Rice, S. X. Wang, and G. Li, *J. Am. Chem. Soc.*, 2004, **126**, 273–279.
8. N. K. Devaraj and R. Weissleder, *Acc. Chem. Res.*, 2011, **44**, 816–27.
9. M. R. Karver, R. Weissleder, and S. A. Hilderbrand, *Bioconjug. Chem.*, 2011, **22**, 2263–70.
10. J. D. Thomas, H. Cui, P. J. North, T. Hofer, C. Rader, and T. R. Burke, *Bioconjug. Chem.*, 2012, **23**, 2007–13.
11. C. Tassa, S. Y. Shaw, and R. Weissleder, *Acc. Chem. Res.*, 2011, **44**, 842–52.